Spring 5-14-2022

Multi-scale modeling of dislocation motion and interaction: Theory, Plastic Properties, and Boundary Conditions

Abu Bakar Siddique
University of New Mexico - Main Campus

Abu Bakar Siddique

Candidate

Mechanical Engineering

Department

This dissertation is approved, and it is acceptable in quality and form for publication:

Approved by the Dissertation Committee:

Dr. Tariq A. Khraishi

Chair

Dr. Yu-Lin Shen

Member

Dr. Rafiqul Tarefdar

Member

Dr. Hojun Lim

Member

Multi-scale modeling of dislocation motion and interaction: Theory, Plastic Properties, and Boundary Conditions

by

Abu Bakar Siddique

B.Sc., Mechanical Engineering, Bangladesh University of Engineering and Technology, 2006

M.S., Mechanical Engineering, University of New Mexico, 2016

DISSERTATION

Submitted in Partial Fulfillment of the

Requirements for the Degree of

Doctor of Philosophy

in Engineering

The University of New Mexico

Albuquerque, New Mexico

May, 2022

Dedication

To my parents, wife and daughters.

"Each problem that I solved became a rule which served afterwards to solve other problems."

- Rene Descartes

Acknowledgments

I heartily acknowledge the effort of Dr. Tariq A Khraishi for mentoring my research. I also acknowledge Sandia National Labs and the department of Mechanical Engineering for supporting my research.

I would like to thank the rest of my dissertation committee as well; Dr. Yu-Lin Shen, Dr. Rafiqul Tarefder, and Dr. Hojun Lim for their help and guidance to my research.

Multi-scale modeling of dislocation motion and interaction: Theory, Plastic Properties, and Boundary Conditions

by

Abu Bakar Siddique

B.Sc., Mechanical Engineering, Bangladesh University of Engineering and Technology, 2006

M.S., Mechanical Engineering, University of New Mexico, 2016

Ph.D., Engineering, University of New Mexico, 2022

Abstract

Dislocation theory is the fundamental tool for explaining plasticity in the material. The elastic field of a material is always influenced by the presence of dislocations and other defects independent of the loading configurations. Scientists and researchers have minimal success in solving plasticity problems analytically. And for this reason, the capturing of dislocation dynamics is highly dependent on numerical modeling, which is always a challenge for its inherent multi-scale nature. Current research investigates and develops self-consistent numerical models for different plasticity problems based on the distributed-dislocation technique and the collocation-point method. Numerical methods are developed for different boundary conditions in the presence of crystal dislocations and discontinuities in the material. Boundary conditions due to the discontinuity in the material are satisfied by placing image or fictitious dislocations or dislocations of unknown Burgers vectors at predefined places. On the free surfaces, some designated points are selected (termed as

"collocation points") to enforce the boundary conditions there only. Numerical models are developed to satisfy the boundary conditions at those collocation points, assuming that satisfying the boundary conditions at those collocation points is sufficient to capture the field solution of the problem. Burgers vectors of those fictitious dislocations are solved for using a system of linear equations that ensures the tractions on the collocation points are zero. It is evident from the assumption that the numerical solution improves as the number of collocation points on the free surfaces increases. The developed numerical scheme is implemented in one of the existing Dislocation Dynamics (DD) codes by Zbib et al. to show the free surface effect in a constant strain-rate simulation. The applications extend to free surfaces with complex geometry and can thus capture the interaction of multiple voids of any geometry. Other studies tackled the singular behavior near the dislocation core, the effect of multiple dislocations or multipoles on the plasticity of the material as well as the effect of solute atoms on both the elastic and plastic behavior of metallic crystalline materials.

Contents

List of Figures

List of Figures

List of Tables

Chapter 1

Introduction

Most of mechanical design is done in a material's elastic region but knowledge of plasticity is required to know the failure behavior of a material. Plasticity is the ability of a material to change shape permanently. In crystalline metals, this process mainly takes place by the collective motion and nucleation of dislocations (which also known as line defects in the atomic lattice).

More accurate understanding and better predictive capabilities, and the rise of computational power and numerical methods have enabled a mesoscopic description of dislocations and their dynamics. At length scales on the order of a micrometer and larger, dislocations (which have core regions on the order of nanometers) can be idealized as curved lines or straight segments and the associated crystallographic distortions can be modeled using elasticity theory. At this scale of matter, plastic deformation is described in terms of the dynamics of individual dislocations or segments and is that is often referred to as discrete dislocation (DD) plasticity. Moreover, the outcomes of simulations conducted at the mesoscale can be fed into larger-scale finite element simulations to predict bulk material behavior.

Discrete dislocation dynamics (DDD) simulations can be used to illustrate defect and crystalline physics, which is often not possible to capture during real experiments, by developing appropriate models for the plastic response of crystals. Moreover, simulations do not require expensive testing equipment and materials. An accurate simulation explores the physics of the problem in-depth and brings interesting phenomena to attention to the researchers and scientists. Experts are developing different codes to simulate various problems of dislocation dynamics for the last few decades.

The dislocation is a source of stress in a material. Stress field solutions for a straight dislocation line in an infinite medium is a classic problem in plasticity theory. The stress field solutions need to be adjusted for any discontinuity in the medium. Current research starts with 2D simple boundary-value problems and is extended to more complex 3D boundary-value problems.

In Chapter 2, we have presented the stress field solution for an infinite screw dislocation in an infinitely-wide, constant-thickness plate. In this problem, the presence of the screw dislocation near two free surfaces means that the traction calculated from the classical solution is not negligible on both free surfaces. To satisfy the boundary conditions, we introduce an algorithm to place image (fictitious) dislocations on both sides of the free surfaces to annul traction on the free surfaces. Finally, the field solution is derived by adding contributions from all the image dislocations and the crystal dislocation.

In Chapter 3, we solve the stress field of a screw dislocation near voids of any shape. In this problem, a numerical scheme is developed, padding fictitious image dislocations of unknown Burgers vectors on the void perimeter to satisfy the zero-traction boundary condition. The solution from the numerical scheme produced results comparable to analytical solutions in limiting situations. Moreover, the numerical method is capable of finding the solution in the presence of multiple interacting voids of any shape for which no analytical

solution is available.

In Chapter 4, we have combined our knowledge of Chapter 2 and Chapter 3 in an special problem. We have presented the stress field solution of a screw dislocation in a plate that is voided, i.e. having a cylindrical hole in it. The developed method can be extended for any shaped hole inside the plate. We have also determined the positions of equilibrium for the dislocation in the plate.

In Chapter 5, we develop a numerical methodology for treating static and dynamic dislocation problems near a free surface. First, the algorithm is developed for a dislocation segment near a free surface and then implemented in a 3D Dislocation Dynamics simulation. To annul traction on the free surface, we padded rectangular generally prismatic dislocation loops of unknown Burgers vectors on the free surface in a finite mesh. The geometric center of each loop is selected as a collocation point. Traction-free boundary condition is enforced on each of the collocation points and generated a linear set of equations to be solved for the unknown Burgers vectors of the fictitious padded loops. Once the system of linear equations is solved for the unknown Burgers vectors, the field solution is calculated by adding the contribution from all the fictitious loops and the crystal dislocation segment. The numerical solution is compared with a similar analytical solution to verify the accuracy of the method. The method is implemented in a 3D discrete dislocation dynamics (DDD) code to show the surface effect on the multiplication of a Frank-Read (FR) source under constant strain-rate loading.

In Chapter 6, the methodology developed in Chapter 5 is extended for triangular-loop surface meshes with an intention to apply the same methodology on curved surfaces. The coefficient of the unknown Burgers vector is determined using a generalized method termed the “Brute-force” method, where no prior knowledge of loop stress is required. Solutions are determined using both the rectangular and triangular loops surface meshes and com-

pared with the a similar analytical solution to verify the accuracy of the method. This new method is also implemented in the previous 3D DDD code and a similar problem to that in Chapter 5 was simulated. This new methodology is easy to implement in an existing 3D DDD code since no mathematical formulation is needed to calculate the coefficient of the unknown Burgers vectors. For this reason, the same algorithm applies to any type of surface meshes, which is vital for a curved boundary. We were also motivated to explore the methodology for locally-condensed finer mesh in a generally coarse surface mesh with an intention to save on computational effort in the simulations. This method intends to minimize the surface collocation points for creating similar results produced in a finer uniform mesh throughout the surface. This can make the simulation faster since the number of linear equations is fewer compared to the previous method.

In Chapter 7, we have investigated the stress field solution of a 3D linear dislocation segment extensively with an intention to propose a guideline for calculating the stress field in the core region near the dislocation segment. The purpose of this is to get rid of the infinite nature of the classical solution and thus avoid very high stresses during computations. This regularization process had to be physically-based.

In Chapter 8, we have utilized 3D DDD code to simulate the multiplication phenomenon of multiple FR sources under constant strain-rate loading. The objective of the study was to learn the effect of some parameters, i.e. the number of FR sources, size, and distance between any two neighboring FR sources on the stress-strain curve. We have observed the formation and destruction of dynamic dislocation dipoles in the simulation during dislocation movement, and also the effect of this phenomenon on the plasticity of the material. We have investigated the role of the relative positions of the FR sources on the ensuring flow stress values in the simulated material.

In Chapter 9, we enhanced the capability of the existing DDD code to explore the elas-

tic and plastic behavior in the presence of solute atoms inside the material, i.e. using a binary alloy system. This is a complex problem as it could entail millions or billions of interactions between solute atoms, depending on their weight percent or faction, and the dislocation segments in the simulation. Ultimately, a statistical approach had to be employed to enable homogenization and thus make the run times feasible. An important part of this study is to compare to existing experimental data.

Chapter 2

Screw dislocation in a plate

Abstract

The study of dislocations is very important in material science because it helps us to predict the mechanical behavior of metals in the plastic regime. In past studies, scientists and researchers have shown the analytic solutions of the stress field in the case of the infinite and semi-infinite medium. In this article, we study the stress field of a single screw dislocation in a finite thickness plate considering the presence of the image or virtual dislocations. The solution is verified against known or expected results.

Keywords: Dislocations, Screw Dislocations, Image Dislocations, Stress field

2.1 Introduction

Numerous research has been conducted based on the dislocation theory to characterize material properties. Using the concept of dislocation in materials, Koehler [1] explained the plastic deformation of materials. Hull and Bacon [2], as well as Weertman and Weert-

man [3], described the stress field of a positive screw dislocation in an infinite material. This stress field solution does not apply to a finite plate that has traction-free surfaces. In this article, we ensure the surfaces in a dislocated plate are traction-free by adding fictitious or virtual image dislocations on both sides of the plate. We formulate the coordinates of the image dislocations and use their stress field as a correcting term to be added to the infinite-material solution. Such superposition ensures zero traction on the free surfaces and therefore represents the correct stress solution at any material point in the plate. The image dislocations are added incrementally till an infinite number of them. Results are presented, showing how the correct superposed solution differs in behavior and quantitatively from the infinite-material solution. Results are also shown for solution verification.

2.2 Theory/Solution Development

We know in linear elasticity [4], the ij-th component of the small strain tensor is given by,

$$e_{ij} = \frac{1}{2}\left(\frac{\partial u_i}{\partial j} + \frac{\partial u_j}{\partial i}\right) \tag{2.1}$$

and Hooke's law for isotropic material,

$$\sigma_{ij} = \lambda\left(e_{xx} + e_{yy} + e_{zz}\right)\delta_{ij} + 2Ge_{ij} \tag{2.2}$$

where $i = x, y, z$, $j = x, y, z$ and λ, G are Lamé constant.

From Fig. 2.1 we see there is no deformation along x, y direction i.e. $u_x = 0$, $u_y = 0$ and $u_z = \frac{b}{2\pi}\tan^{-1}(y/x)$. Now from Eq. (2.1) we write,

$$e_{xx} = e_{yy} = e_{zz} = e_{xy} = e_{yx} = 0 \tag{2.3a}$$

$$e_{xz} = e_{zx} = -\frac{b}{4\pi}\frac{y}{x^2 + y^2} \tag{2.3b}$$

$$e_{yz} = e_{zy} = \frac{b}{4\pi}\frac{x}{x^2 + y^2} \tag{2.3c}$$

$$\tag{2.3d}$$

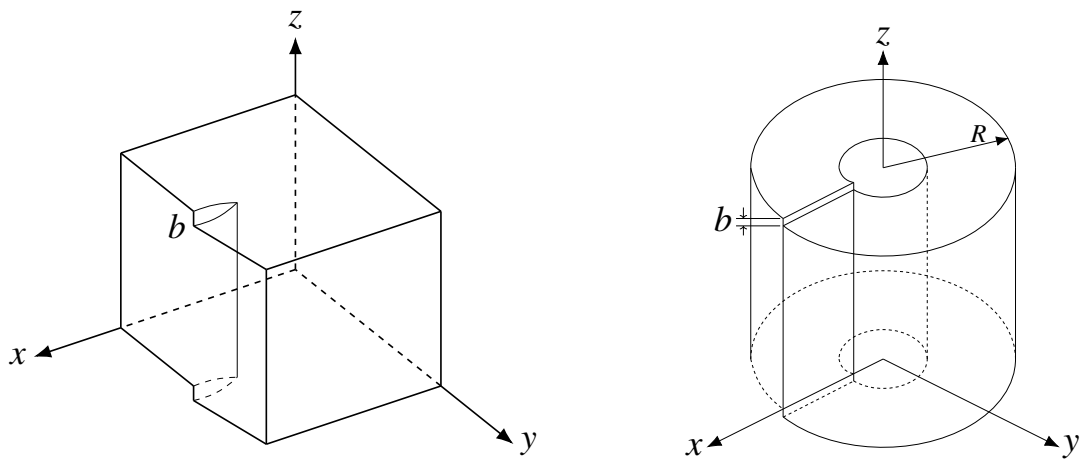

Figure 2.1: Screw dislocation (schematic) shown in Cartesian and Cylindrical coordinate system.

No from eqs. (2.2) and (2.3) we can write,

$$\sigma_{xx} = \sigma_{yy} = \sigma_{zz} = \sigma_{xy} = \sigma_{yx} = 0 \tag{2.4a}$$

$$\sigma_{xz} = \sigma_{zx} = 2Ge_{xz} = 2Ge_{zx} = -\frac{Gb}{2\pi}\frac{y}{x^2+y^2} \tag{2.4b}$$

$$\sigma_{yz} = \sigma_{zy} = 2Ge_{yz} = 2Ge_{zy} = \frac{Gb}{2\pi}\frac{x}{x^2+y^2} \tag{2.4c}$$

Equation (2.4) expresses the stress field in the presence of a positive screw dislocation at the origin. We rewrite Eq. (2.4b) as

$$\sigma_{xz} = \sigma_{zx} = -\frac{G(b)}{2\pi}\frac{y}{((x-D_x)^2+(y-D_y)^2)} \tag{2.5}$$

where, (D_x, D_y) are the coordinates of the dislocation. We set our origin at the positive dislocation $\S_0$ meaning the coordinates $(D_x, D_y) \equiv (0,0)$ for $\S_0$ and (x,y) are the coordinates of any point P in the thin plate. See Fig. 2.2.

Now the stress on surface 1 ($x \equiv -a$) due to $\S_0$ is,

$$\sigma_{xz} = \sigma_{zx} = -\frac{G(b)}{2\pi}\frac{y}{(a^2+y^2)} \tag{2.6}$$

and on surface 2 ($x \equiv d-a$) is

$$\sigma_{xz} = \sigma_{zx} = -\frac{G(b)}{2\pi}\frac{y}{((d-a)^2+y^2)} \tag{2.7}$$

Surfaces 1 and 2 should be traction free surfaces, i.e. σ_{xx}, σ_{xy} and σ_{xz} should be zero at these surfaces.

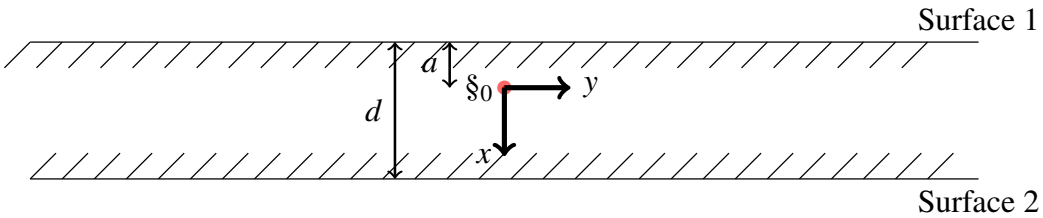

Figure 2.2: Positive screw dislocation on a thin plate

From Eq. (2.4a) we find $\sigma_{xx} = \sigma_{xy} = 0$ and in Eq. (2.4b) $\sigma_{xz} = \sigma_{zx} \neq 0$ on the free surfaces where $y \neq 0$. But we see σ_{xz} and σ_{zx} should be zero to satisfy the condition of traction free surface. To ensure surfaces 1 and 2 to be traction free (i.e. $\sigma_{xz} = \sigma_{zx} = 0$) we add two fictitious negative dislocations §_1 at a distance a from surface 1 (outward) and §_2 at a distance $d-a$ from surface 2 (outward) so the net stress would be zero on the surfaces. Note that the symbol § is used to represent negative screw dislocations and the symbol § is used to represent positive screw dislocations. Now the total stress on surface 1 due to dislocations §$_0$ and §$_1$ is

$$\begin{aligned}\sigma_{xz} = \sigma_{zx} &= -\frac{G(b)}{2\pi}\frac{y}{((-a)^2+y^2)} - \frac{G(-b)}{2\pi}\frac{y}{((-a-(-2a))^2+y^2)} \\ &= -\frac{Gb}{2\pi}\frac{y}{(a^2+y^2)} + \frac{Gb}{2\pi}\frac{y}{(a^2+y^2)} \\ &= 0\end{aligned} \tag{2.8}$$

Similarly the total stress on surface 2 due to dislocations $\S_0$ and $\wr_2$ is

$$\begin{aligned}\sigma_{xz} = \sigma_{zx} &= -\frac{G(b)}{2\pi}\frac{y}{((d-a)^2+y^2)} - \frac{G(-b)}{2\pi}\frac{y}{((d-a-2(d-a))^2+y^2)} \\ &= -\frac{Gb}{2\pi}\frac{y}{((d-a)^2+y^2)} + \frac{Gb}{2\pi}\frac{y}{((d-a)^2+y^2)} \\ &= 0\end{aligned} \tag{2.9}$$

But dislocation $\wr_1$ causes stress on surface 2 and $\wr_2$ on surface 1. Now the total stress σ_{zx} on surface 1 due to $\S_0$, $\wr_1$ and $\wr_2$

$$\begin{aligned}\sigma_{xz} = \sigma_{zx} &= -\frac{G(b)}{2\pi}\frac{y}{((-a)^2+y^2)} - \frac{G(-b)}{2\pi}\frac{y}{((-a-(-2a))^2+y^2)} \\ &\quad - \frac{G(-b)}{2\pi}\frac{y}{((-a-2(d-a))^2+y^2)} \\ &= -\frac{Gb}{2\pi}\frac{y}{(a^2+y^2)} + \frac{Gb}{2\pi}\frac{y}{(a^2+y^2)} + \frac{Gb}{2\pi}\frac{y}{((-2d+a)^2+y^2)} \\ &= \frac{Gb}{2\pi}\frac{y}{((-2d+a)^2+y^2)}\end{aligned} \tag{2.10}$$

Similarly the total stress on surface 2 due to dislocations $\S_0$, $\wr_1$ and $\wr_2$ is

$$\begin{aligned}\sigma_{xz} = \sigma_{zx} &= -\frac{G(b)}{2\pi}\frac{y}{((d-a)^2+y^2)} - \frac{G(-b)}{2\pi}\frac{y}{((d-a-2(-a))^2+y^2)} \\ &\quad - \frac{G(-b)}{2\pi}\frac{y}{((d-a-2(d-a))^2+y^2)} \\ &= -\frac{Gb}{2\pi}\frac{y}{((d-a)^2+y^2)} + \frac{Gb}{2\pi}\frac{y}{((d+a)^2+y^2)} + \frac{Gb}{2\pi}\frac{y}{((d-a)^2+y^2)} \\ &= \frac{Gb}{2\pi}\frac{y}{((d+a)^2+y^2)}\end{aligned} \tag{2.11}$$

Again we can see the stress $\sigma_{zx} \neq 0$ on the surfaces. So we again add two positive dislocations $\S_3$ at a distance $2d-a$ from surface 1 (outward) and $\S_4$ at a distance $d+a$ from surface 2 (outward) so the net stress would be zero on the surfaces. Now the total

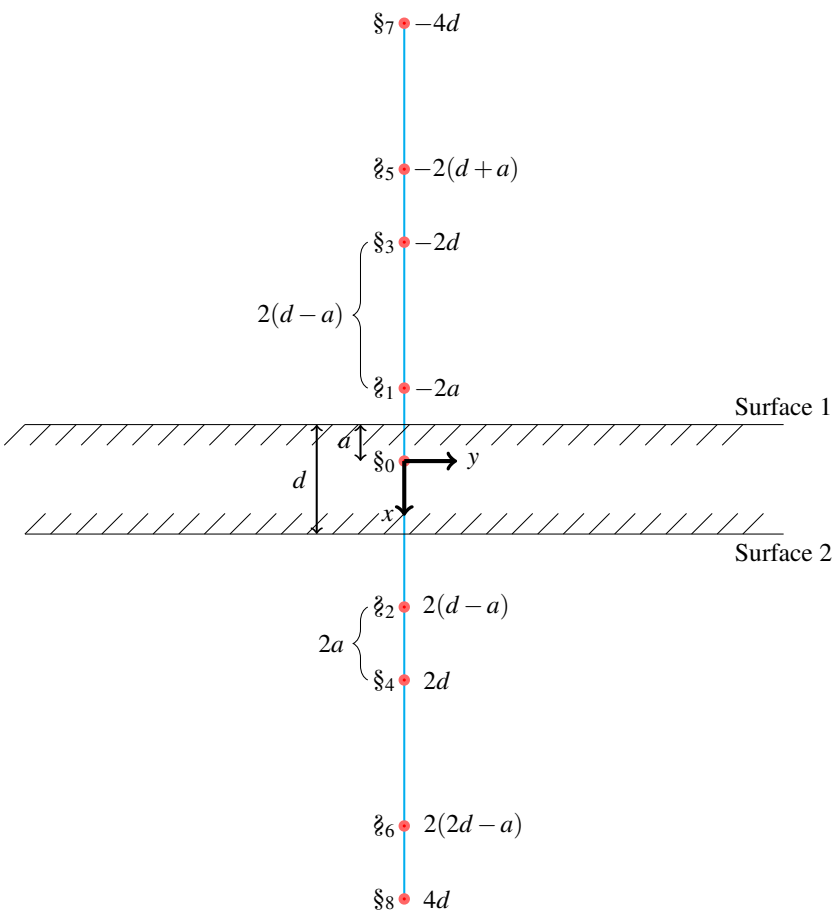

Figure 2.3: Locations of image dislocations

stress on surface 1 due to dislocations §$_0$, §$_1$, §$_2$ and §$_3$ is

$$\begin{aligned}\sigma_{xz} = \sigma_{zx} &= \frac{Gb}{2\pi}\frac{y}{((2d-a)^2+y^2)} - \frac{Gb}{2\pi}\frac{y}{((-a-(-2d))^2+y^2)} \\ &= \frac{Gb}{2\pi}\frac{y}{((2d-a)^2+y^2)} - \frac{Gb}{2\pi}\frac{y}{((2d-a)^2+y^2)} \\ &= 0\end{aligned} \tag{2.12}$$

Similarly the total stress on surface 2 due to dislocations §$_0$, ȣ$_1$, ȣ$_2$ and §$_4$ is

$$\begin{aligned}\sigma_{xz} = \sigma_{zx} &= \frac{Gb}{2\pi}\frac{y}{((d+a)^2+y^2)} - \frac{Gb}{2\pi}\frac{y}{((d-a)-2d)^2+y^2)} \\ &= \frac{Gb}{2\pi}\frac{y}{((d+a)^2+y^2)} - \frac{Gb}{2\pi}\frac{y}{((d+a)^2+y^2)} \\ &= 0\end{aligned} \tag{2.13}$$

Again dislocation §$_3$ causes stress on surface 2 and §$_4$ on surface 1. Now the total stress σ_{zx} on surface 1 due to §$_0$, ȣ$_1$, ȣ$_2$, §$_3$ and §$_4$ is

$$\begin{aligned}\sigma_{xz} = \sigma_{zx} &= -\frac{Gb}{2\pi}\frac{y}{(-a-2d)^2+y^2)} \\ &= -\frac{Gb}{2\pi}\frac{y}{((2d+a)^2+y^2)}\end{aligned} \tag{2.14}$$

Similarly the total stress on surface 2 due to dislocations §$_0$, ȣ$_1$, ȣ$_2$, §$_3$ and §$_4$ is

$$\begin{aligned}\sigma_{xz} = \sigma_{zx} &= -\frac{Gb}{2\pi}\frac{y}{((d-a)-(-2d))^2+y^2)} \\ &= -\frac{Gb}{2\pi}\frac{y}{((3d-a)^2+y^2)}\end{aligned} \tag{2.15}$$

Again we can see the stress $\sigma_{zx} \neq 0$ on the surfaces. So we again add two negative dislocations ȣ$_5$ at a distance $2d+a$ from surface 1 (outward) and ȣ$_6$ at a distance $3d-a$ from surface 2 (outward) so the net stress would be zero on the surfaces. Now the total stress on surface 1 due to dislocations §$_0$, ȣ$_1$, ȣ$_2$, §$_3$, §$_4$ and ȣ$_5$ is

$$\begin{aligned}\sigma_{xz} = \sigma_{zx} &= -\frac{Gb}{2\pi}\frac{y}{((2d+a)^2+y^2)} - \frac{G(-b)}{2\pi}\frac{y}{((-a-(-2d-2a))^2+y^2)} \\ &= -\frac{Gb}{2\pi}\frac{y}{((2d+a)^2+y^2)} + \frac{Gb}{2\pi}\frac{y}{((2d+a)^2+y^2)} \\ &= 0\end{aligned} \tag{2.16}$$

Similarly the total stress on surface 2 due to dislocations §$_0$, ȣ$_1$, ȣ$_2$, §$_3$, §$_4$ and ȣ$_6$ is

$$\begin{aligned}\sigma_{xz} = \sigma_{zx} &= -\frac{Gb}{2\pi}\frac{y}{((3d-a)^2+y^2)} - \frac{G(-b)}{2\pi}\frac{y}{((d-a)-(4d-2a))^2+y^2)} \\ &= -\frac{Gb}{2\pi}\frac{y}{((3d-a)^2+y^2)} + \frac{Gb}{2\pi}\frac{y}{((3d-a)^2+y^2)} \\ &= 0\end{aligned} \tag{2.17}$$

Again dislocation $\beth_5$ causes stress on surface 2 and $\beth_6$ on surface 1. Now the total stress σ_{zx} on surface 1 due to $\S_0$, $\beth_1$, $\beth_2$, $\S_3$, $\S_4$, $\beth_5$ and $\beth_6$ is

$$\begin{aligned}\sigma_{xz} = \sigma_{zx} &= -\frac{G(-b)}{2\pi}\frac{y}{(-a-2(2d-a))^2+y^2)} \\ &= \frac{Gb}{2\pi}\frac{y}{((4d+a)^2+y^2)}\end{aligned} \tag{2.18}$$

Similarly the total stress on surface 2 due to dislocations $\S_0$, $\beth_1$, $\beth_2$, $\S_3$, $\S_4$, $\beth_5$ and $\beth_6$ is

$$\begin{aligned}\sigma_{xz} = \sigma_{zx} &= -\frac{G(-b)}{2\pi}\frac{y}{((d-a)-2(-d-a))^2+y^2)} \\ &= \frac{Gb}{2\pi}\frac{y}{((3d+a)^2+y^2)}\end{aligned} \tag{2.19}$$

We can see a trend in the position of the image dislocations and that is

$$D\big|_{\beth_i} = -2(di+a)+2d,\, 2(di-a) \text{ and } D\big|_{\S_i} = \mp 2di$$

where, $i = 1,2,\ldots\infty$. This is how we can rewrite Eq. (2.5) considering all the image dislocations as,

$$\begin{aligned}\sigma_{xz} = \sigma_{zx} = -\frac{Gby}{2\pi}\Bigg[&\frac{1}{x^2+y^2} - \frac{1}{(x+2a)^2+y^2} - \frac{1}{\{x-2(d-a)\}^2+y^2} \\ &+ \frac{1}{(x+2d)^2+y^2} + \frac{1}{(x-2d)^2+y^2} - \frac{1}{\{x+2(d+a)\}^2+y^2} \\ &- \frac{1}{\{x-2(2d-a)\}^2+y^2} + \frac{1}{(x+4d)^2+y^2} + \frac{1}{(x-4d)^2+y^2} \\ &- \frac{1}{\{x+2(2d+a)\}^2+y^2} - \frac{1}{\{x-2(3d-a)\}^2+y^2} + \frac{1}{(x+6d)^2+y^2} \\ &+ \frac{1}{(x-6d)^2+y^2} - \cdots\Bigg]\end{aligned} \tag{2.20}$$

$$\begin{aligned}\sigma_{yz} = \sigma_{zy} = &\frac{Gb}{2\pi}\left[\frac{x}{x^2+y^2} - \frac{x+2a}{(x+2a)^2+y^2} - \frac{x-2(d-a)}{\{x-2(d-a)\}^2+y^2}\right.\\
&+ \frac{x+2d}{(x+2d)^2+y^2} + \frac{x-2d}{(x-2d)^2+y^2} - \frac{x+2(d+a)}{\{x+2(d+a)\}^2+y^2}\\
&- \frac{x-2(2d-a)}{\{x-2(2d-a)\}^2+y^2} + \frac{x+4d}{(x+4d)^2+y^2} + \frac{x-4d}{(x-4d)^2+y^2}\\
&- \frac{x+2(2d+a)}{\{x+2(2d+a)\}^2+y^2} - \frac{x-2(3d-a)}{\{x-2(3d-a)\}^2+y^2} + \frac{x+6d}{(x+6d)^2+y^2}\\
&\left.+ \frac{x-6d}{(x-6d)^2+y^2} - \cdots\right]\end{aligned} \tag{2.21}$$

We can write the above equations as the summation of infinite series as

$$\begin{aligned}\sigma_{xz} = \sigma_{zx} = -\frac{Gby}{2\pi}&\left[\frac{1}{x^2+y^2} - \sum_{i=1}^{N}\left\{\frac{1}{\{x+2(di-d+a)\}^2+y^2}\right.\right.\\
&- \frac{1}{\{x-2(di-a)\}^2+y^2} + \frac{1}{(x+2di)^2+y^2}\\
&\left.\left.- \frac{1}{(x-2di)^2+y^2}\right\}\right]\end{aligned} \tag{2.22}$$

$$\begin{aligned}\sigma_{yz} = \sigma_{zy} = \frac{Gb}{2\pi}&\left[\frac{x}{x^2+y^2} - \sum_{i=1}^{N}\left\{\frac{x+2(di-d+a)}{\{x+2(di-d+a)\}^2+y^2}\right.\right.\\
&+ \frac{x-2(di-a)}{\{x-2(di-a)\}^2+y^2} - \frac{x+di}{(x+2di)^2+y^2}\\
&\left.\left.- \frac{x-di}{(x-2di)^2+y^2}\right\}\right]\end{aligned} \tag{2.23}$$

where N should be ∞.

2.3 Solution Verification

Equations (2.22) and (2.23) have infinite series summation but in practice we summed up to $N = 10^5$ to get stress $\sigma_{xz} = \sigma_{zx} < G \times 10^{-12}$ on the either surface. Figure 2.4 shows the maximum σ_{zx}/G value on either surface, i.e. the global surface maxima, versus N.

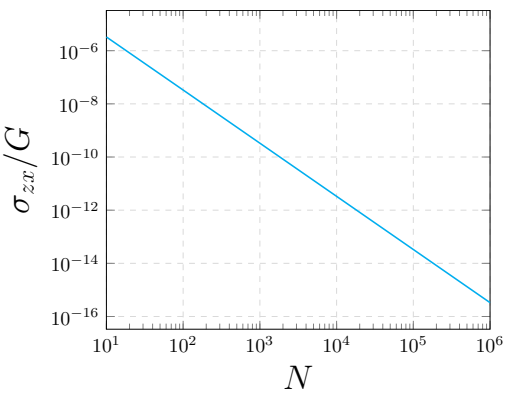

Figure 2.4: Solution convergence plot with N.

In Figs. 2.5 and 2.6, we show the stress field over the finite plate with and without incorporating the image dislocations placing a positive dislocation at 0.1d from surface 1. As we see, in Fig. 2.5(left) where the image dislocations are not incorporated (i.e. stress calculated using Eq. (2.4b)) the σ_{zx} stress is not zero on either surface. But in Fig. 2.5(right) σ_{zx} is essentially zero ($< G \times 10^{-12}$) on the either surface where image dislocations are incorporated in the stress calculation (i.e. stress calculated using Eq. (2.22)).

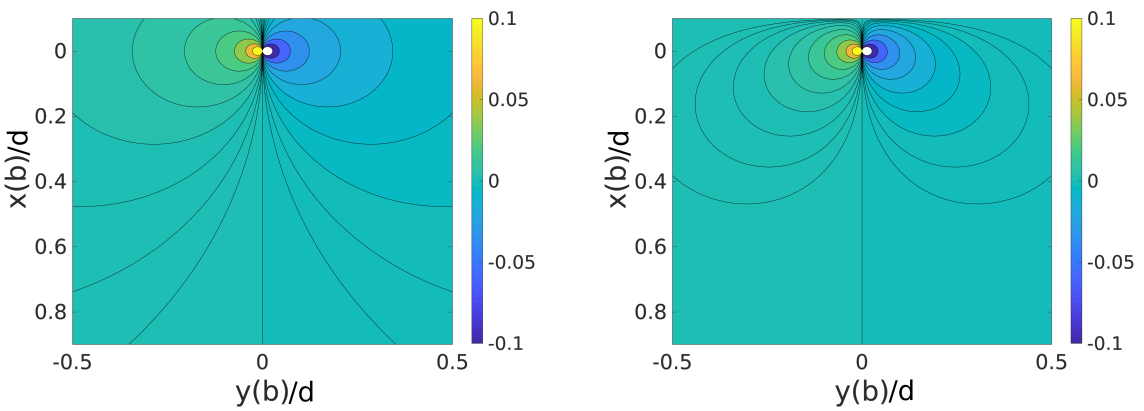

Figure 2.5: Contour plots of σ_{zx}/G. Positive dislocation §$_0$ at $0.1d$ away from top surface. The figure on the right is showing the effect of image dislocations on the stress field

We also show the σ_{zy} stress plotted over the finite plate in Fig. 2.6 (image dislocations

incorporated or not). In Fig. 2.7(a-b) we show the stress σ_{zx} along $y = 4b$ and $y = 10b$. As

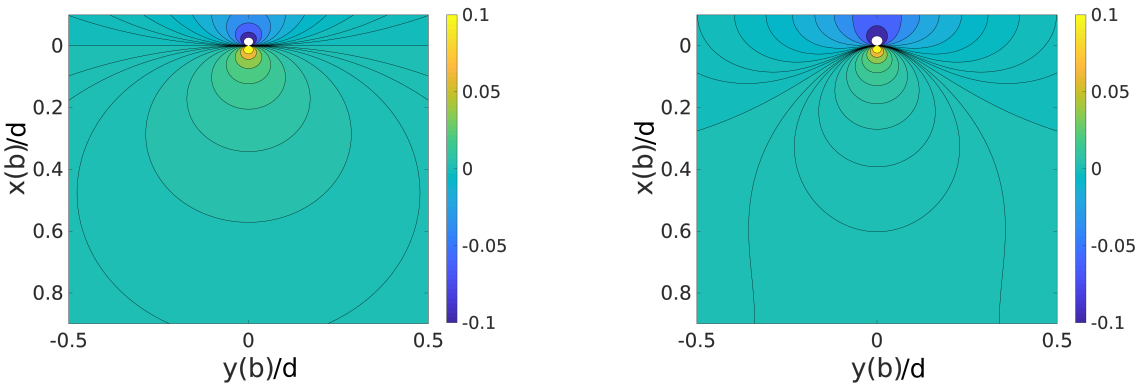

Figure 2.6: Contour plots of σ_{zy}/G. Positive dislocation §$_0$ at $0.1d$ away from top surface. The figure on the right is showing the effect of image dislocations on the stress field

can be seen for a positive dislocation, the difference between the stresses calculated using eqs. (2.4b) and (2.22) is more on the surface near to the dislocation and it diminishes as the dislocation moves far from the surface which is quite intuitive. Equations (2.4b) and (2.22) should produce same stress for a point far from the dislocation. We show similar picture for stress σ_{zy} in Fig. 2.7(c-d).

Finally, in Fig. 2.8 we show the stress σ_{zx} on the free surfaces calculated using Eqs. (2.4b) and (2.22) what confirms that we achieve the traction free surfaces when consider the image dislocations on either side of the plate.

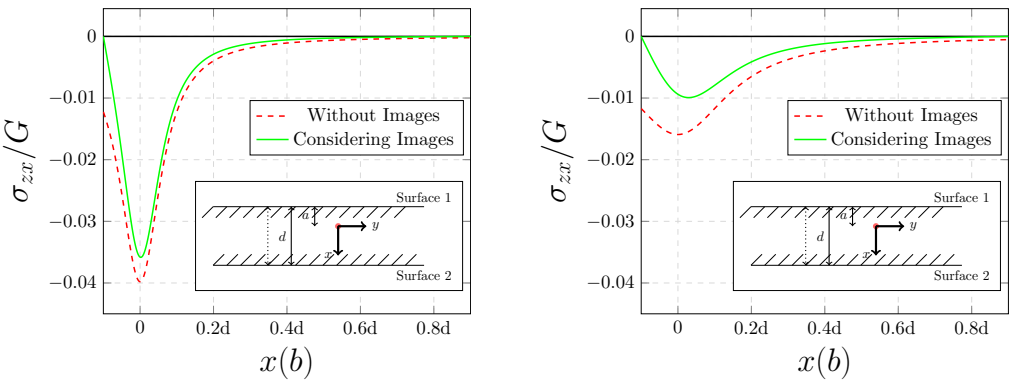

(a) along $y = 4b$

(b) along $y = 10b$

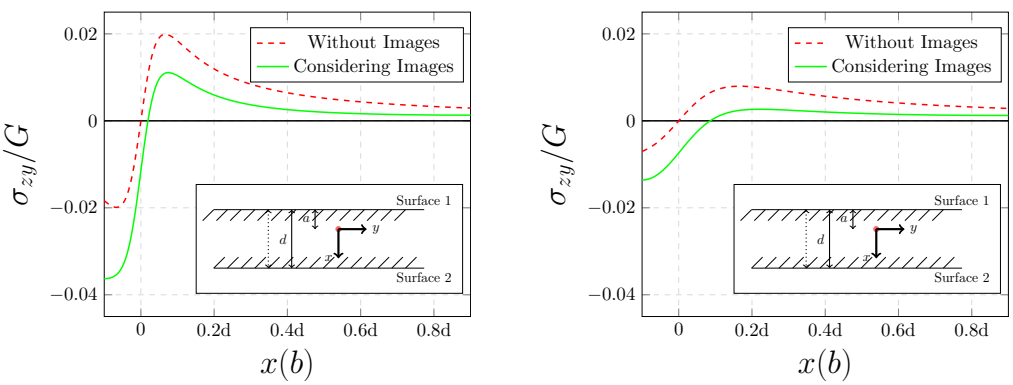

(c) along $y = 4b$

(d) along $y = 10b$

Figure 2.7: Positive dislocation $\S_0$ is at $0.1d$ away from top surface

.

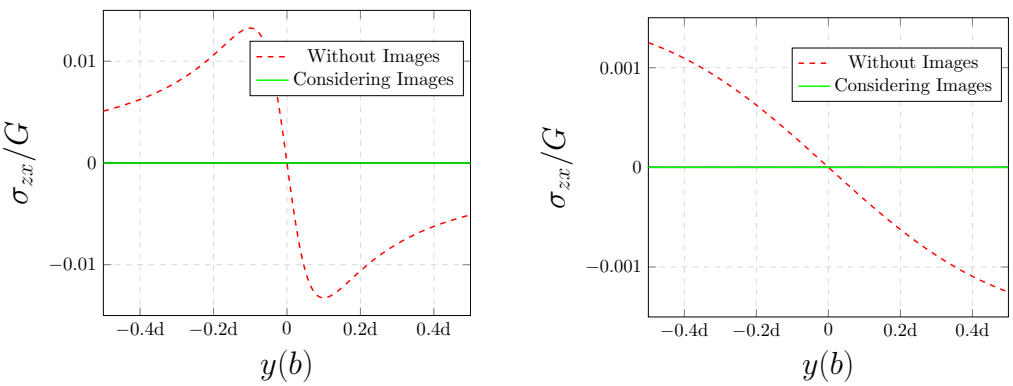

(a) Top surface (b) Bottom surface

Figure 2.8: Stress σ_{zx} on the surfaces when positive dislocation §$_0$ is at $0.1d$ away from top surface

.

2.4 Conclusion

The analytic formulation of stress field for infinite and semi-infinite medium does not satisfy the boundary conditions for the case of a finite medium. In this article, we have introduced the formulation of the stress field over a thin plate in the presence of image dislocations. Moreover, we have shown how the image dislocations are distributed. With the distributed image dislocations, we have confirmed the condition of traction-free surfaces using line and contour plots.

Conference proceedings reference

Siddique, A.B., & Khraishi, T.A. (2019). Stress field of a single screw dislocation in a plate. Proceedings of the 2019 ASEE Gulf-Southwest Annual Conference, Michael McGinnis (ed.), March 10-12, 2019, University of Texas at Tyler, EasyChair Preprint no. 1057.

Chapter 3

Screw dislocation around a void of any shape

Abstract

Analytical solutions for dislocations around multiple interacting free surfaces are strictly case-specific (they depend on the exact dislocation location and number and geometry of voids/free surface). This is because they rely on the precise placement of image (fictitious) dislocations, and thus can end up being very complicated in their formulation. The current article presents a general numerical scheme based on the collocation point method. The proposed method is capable of generating solutions for dislocations around multiple interacting free surfaces of any shapes or geometries. The paper also furnishes verification of the developed methodology and new results.

3.1 Introduction

The stress field around a dislocation [5] in an infinite isotropic medium is a classic problem in linear elastoplasticity. In a semi-infinite medium, the free surface affects the dislocation and also changes the associated stress field from the one developed for an infinite medium. Eshelby et al. formulated the 2D solution for straight screw dislocations of infinite length [6], and Head [7] studied the elastic interaction of a screw dislocation in a semi-infinite isotropic medium with a surface layer (i.e. oxide film). In the case of non-planar (curved) free surfaces, Eshelby [8] solved the stress field for a screw dislocation eccentrically situated in a cylindrical rod, and Friedel presented the analytical solution for a screw dislocation near a cylindrical void [9]. The solutions mentioned above are for a dislocation located inside a medium. Yoffe [10] showed stress field calculations for a straight dislocation terminating at a free surface at an arbitrary angle.

A free surface creates an attractive force [11] on a dislocation, which can affect its motion in a crystal. Lubarda et al. [12], [13], [14], derived the image forces (attractive force by the free surface) on an infinite-length screw dislocation for multiple interacting free surfaces of different geometry/topology in an isotropic medium. Such solutions were strictly case-specific (they depend on the exact dislocation location and number and geometry of voids/free surface). The authors of the current article propose a general numerical solution for straight dislocations near multiple interacting free surfaces of arbitrary geometry/topology. Examples in this article are shown for screw type dislocations. The proposed nu- merical framework is developed based on the concept of the colloca- tion point method implemented by Khraishi et al. [15], [16], [17] and Siddique and Khraishi [18]. The developed method is versatile and adaptive and can be used in 2D dislocation dynamics simulations to model the effect of free surface on dislocation glide and the ensuing crystal plasticity [19], [20]. Complete theoretical development of the algorithm is presented in the Theory section, then a numerical scheme to the solution is discussed in

the Numerical Framework section. The stress field and image force calculations on the dislocation are presented in the Results section for several problem configurations, and the solution is verified where possible.

3.2 Theory

De Wit [21] derived the stress tensor elements, $\sigma_{ij}(\vec{r})$, at a field point $\vec{r} = (x, y, z)$ for an infinite straight dislocation within the framework of isotropic elasticity as,

$$\begin{aligned}\sigma_{ij}(\vec{r}) = &-\frac{\mu b_n}{2\pi r^2}\Bigg[r_m\left(\varepsilon_{jmn}\, t_i + \varepsilon_{imn}\, t_j\right) \\ &-\frac{1}{(1-\nu)}\varepsilon_{kmn}\left\{\left(\delta_{ij} + t_i\, t_j\right) r_m - \delta_{mi}\, r_j - \delta_{jm}\, r_i + \frac{2 r_m r_i r_j}{r^2}\right\} t_k\Bigg]\end{aligned} \tag{3.1}$$

where, $\vec{t}$ and $\vec{b}$ are the line sense (direction) and Burgers vector of an infinite straight dislocation. Equation (3.1) expands following the rules of index notations (textbook by Khraishi and Shen [4] , and one more textbook by George Mase [22]). For an infinite screw dislocation along the z-direction, the Burgers vector is $\vec{b} = (0, 0, b_z)$ and the line sense is $\vec{t} = (0, 0, 1)$. In this case, Eq. (3.1) reduces to,

$$\sigma_{ij}(\vec{r}) = -\frac{\mu b_n}{2\pi r^2}\Bigg[r_m\left(\varepsilon_{jmn}\, t_i + \varepsilon_{imn}\, t_j\right)\Bigg] \tag{3.2}$$

since $\varepsilon_{kmz} t_z = 0$. We write the stress tensor for $i = 1, 2, 3$ and $j = 1, 2, 3$ accordingly,

$$\boldsymbol{\sigma}(\vec{r}) = \begin{bmatrix}\sigma_{xx} & \sigma_{xy} & \sigma_{xz} \\ \sigma_{xy} & \sigma_{yy} & \sigma_{yz} \\ \sigma_{xz} & \sigma_{yz} & \sigma_{zz}\end{bmatrix} = -\frac{\mu b_z}{2\pi r^2}\begin{bmatrix}0 & 0 & y \\ 0 & 0 & x \\ y & x & 0\end{bmatrix} \tag{3.3}$$

Equation (3.3) conforms with the solution presented in [11] and [2]. Similarly, Eq. (3.1) can be reduced for an infinite edge dislocation. Equation (3.3) is independent of z, so it

becomes a 2D problem. Moreover, Eq. (3.3) is linear in b_z and can be written as,

$$\boldsymbol{\sigma}(\vec{r}) = b_z \begin{bmatrix} 0 & 0 & k_{xz} \\ 0 & 0 & k_{yz} \\ k_{xz} & k_{yz} & 0 \end{bmatrix} \tag{3.4}$$

where, $[K]$ is termed the kernel matrix (following [15] and [16]). The stress tensor at any field point $\vec{r} = (x, y, z)$ for any dislocation located at other than the origin of the Cartesian coordinate system can be written as,

$$\boldsymbol{\sigma}(\vec{r}) = -\frac{\mu b_z}{2\pi r^2} \begin{bmatrix} 0 & 0 & y' \\ 0 & 0 & x' \\ y' & x' & 0 \end{bmatrix} \tag{3.5}$$

where x' and y' are the relative distances of that origin-offset dislocation from point $\vec{r}$.

In the framework of linear elasticity, the stress tensor element $\sigma_{\alpha\beta}(\vec{r}_P)$ at any field point P for M dislocations can be expressed using the principle of linear superposition as,

$$\sigma_{\alpha\beta}(\vec{r}_P) = \sum_{m=1}^{M} \sigma^m_{\alpha\beta}(\vec{r}'_P) \tag{3.6}$$

where $\sigma^m_{\alpha\beta}(\vec{r}'_P)$ is the $\alpha\beta$ stress component by dislocation m for stress in an infinite medium (see [11] and [2]). Here $\vec{r}'_P$ represents the relative position vector between dislocation m and the field point in question (point P here). Now in the presence of any discontinuity in the medium, Eq. (3.6) needs to incorporate a "correction term" to account for the existing physical boundary conditions. Discontinuity in the medium can appear, for example, in the form of voids, cracks, or free boundary surfaces. Then Eq. (3.6) can be re-written to incorporate the boundary effects as,

$$\sigma_{\alpha\beta}(\vec{r}_P) = \sum_{m=1}^{M} \sigma^m_{\alpha\beta}(\vec{r}'_P) + \sigma^{corr}_{\alpha\beta} \tag{3.7}$$

The second term of Eq. (3.7) accounts the physical boundary conditions, i.e. ensures satisfaction of these conditions. This article formulates a numerical scheme to find this

correction term in the presence of infinite screw dislocations around differently-shaped voids in a medium (the medium itself could be infinite, semi-infinite, or finite). Moreover, this correction term is a function of the dislocation positions in the medium with respect to the boundaries.

To illustrate this 2D problem, consider for now one simple void, a cylinder, with dislocations around it (Figure 1(a)). For any point on the void's free surface, the traction should be null, i.e. the stress traction vector $T = \boldsymbol{\sigma}\vec{n} = \vec{0}$, where $\boldsymbol{\sigma}$ is the stress tensor at the point and $\vec{n}$ is the unit vector normal to the surface (Fig. 3.1(c)).

Instead of annulling traction on all surface points, the current method ensures its annulment on collocation points on the surface (red dots in Figs. 3.1(b) and 3.1(c)). This is following the collocation point method presented by Khraishi et al. [15], [16], [17] and Siddique and Khraishi [18]. In this method, the collocation points represent the center of N fictitious (or mathematical) dislocation loops padding the surface (Figs. 3.1(b) and 3.1(c)). Such loops are rectangular loops having an unknown, and yet-to-be-determined Burgers vector, with two infinite screw segments/sides/lines and two edge dislocation segments/sides that are situated at $\pm\infty$. In this 2D problem, the two finite edge segments do not contribute anything to the stress field in the xy-plane shown in Fig. 3.1. Moreover, Figs. 3.1(b) and 3.1(c) each represents a cross-section through the two infinite screw dislocation lines. One of these dislocations will have a positive sign (i.e. its unknown bz and line sense are pointing in the same $+z$ direction) and the other a negative sign. Figure 3.1 (c) shows the cut through the loops, each shown as a polygon side, with the polygon vertices being a positive and negative screw dislocation. Note that each vertex has a positively and negatively signed dislocation from two contiguous loops. In this method, the more collocation points covering the surface (i.e. the higher their density), the more the numerical solution approaches the real solution (or analytical solution if one exists).

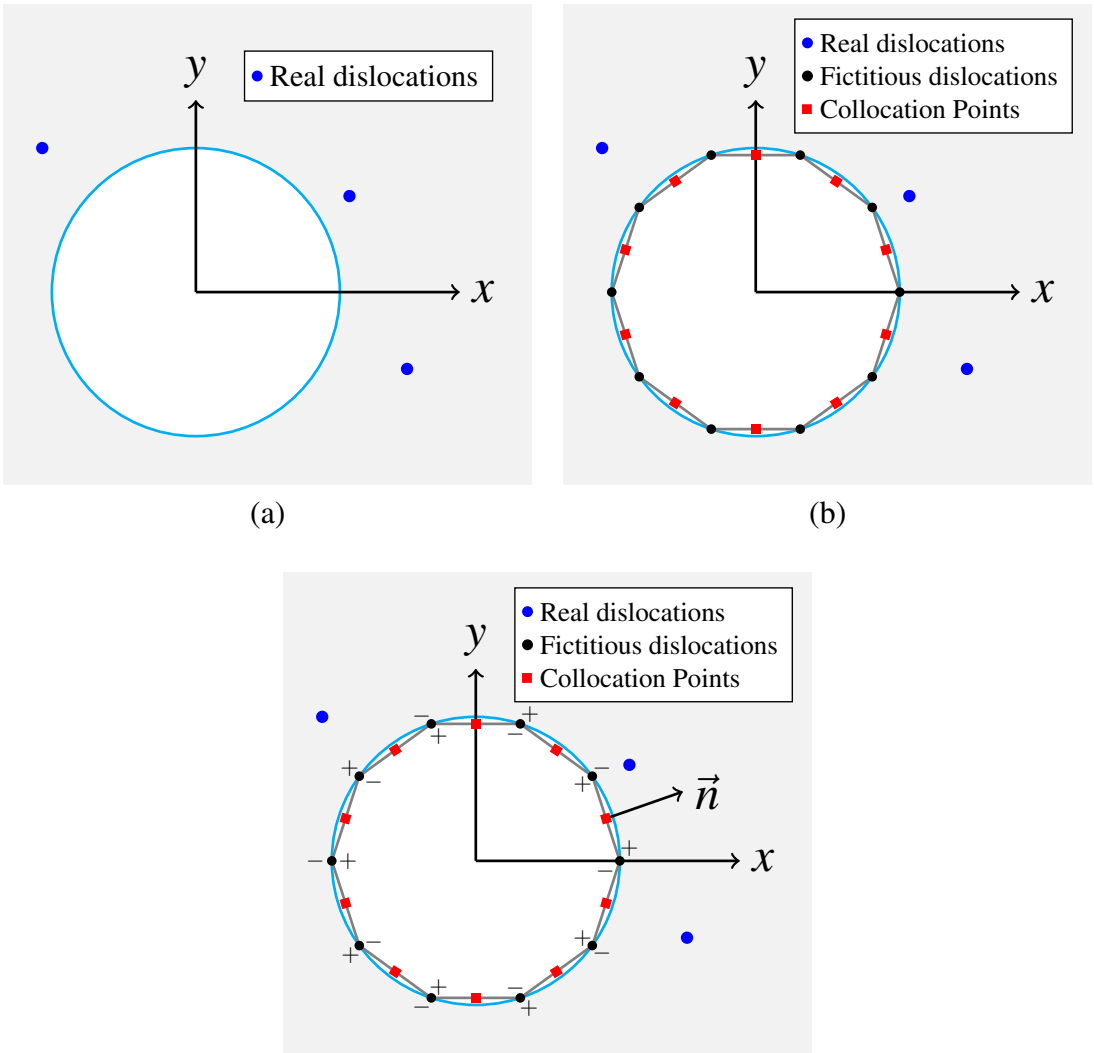

Figure 3.1: (a) Dislocations (real crystal dislocations) around a cylindrical hole in a medium, (b) Discretizing the free surface by a polygon with many sides. The midpoints of each side is a collocation point of the mathematical problem to be solved, i.e. satisfaction of the boundary condition, (c) The vertices of the polygon sides represent fictitious or mathematical dislocations. The plus sign indicates a positive screw dislocation, and the minus sign represents a negative screw dislocation. Dislocations around a cylindrical void and the development of the numerical method for the associated problem.

The above problem reduces to finding the Burgers vectors of the loops such that these loops collectively with the real dislocations satisfy the traction-free conditions on the col-

location points. Given this, Eq. (3.7) can be re-written explicitly for the $\sigma^{corr}_{\alpha\beta}$ term as,

$$\sigma_{\alpha\beta}\left(\vec{r}_P\right) = \sum_{m=1}^{M} \sigma^{m}_{\alpha\beta}\left(\vec{r}'_P\right) + \sum_{i=1}^{N} \sigma^{i}_{\alpha\beta}\left(\vec{r}'_i\right) \tag{3.8}$$

Where the correction term comes from the contribution of the surface loops to the stress state at any field point P. The reason dislocation loops are employed in this method is that they are a self-equilibrated source of stress for the correction term, and provide a compatible field with the exception of course at the dislocation point/location.

To formulate the problem numerically, we recognize that at any point on the void surface, $\vec{n} = (n_x, n_y, 0)$ and the traction $\vec{T} = (T_x, T_y, T_z) = (0, 0, \sigma_{xz} n_x + \sigma_{yz} n_y)$. This means that T_x and T_y are identically annulled. Only the T_z component needs therefore to be annulled. Now that there are $N+M$ sources of stress, the traction-free condition on collocation point $C(x,y)$ can be written as

$$T^C_z = \sum_{i=1}^{N} \left(\sigma^{i}_{xz}\left(\vec{r}'_C\right) n^C_x + \sigma^{i}_{yz}\left(\vec{r}'_C\right) n^C_y \right) + \sum_{m=1}^{M} \left(\sigma^{m}_{xz}\left(\vec{r}'_C\right) n^C_x + \sigma^{m}_{yz}\left(\vec{r}'_C\right) n^C_y \right) = 0 \tag{3.9}$$

where $\vec{r}'_C$ is the position vector between the dislocation and point C. Alternatively, Eq. (3.9) can be written as:

$$\sum_{i=1}^{N} \left(\sigma^{i}_{xz}\left(\vec{r}'_C\right) n^C_x + \sigma^{i}_{yz}\left(\vec{r}'_C\right) n^C_y \right) = - \sum_{m=1}^{M} \left(\sigma^{m}_{xz}\left(\vec{r}'_C\right) n^C_x + \sigma^{m}_{yz}\left(\vec{r}'_C\right) n^C_y \right) \tag{3.10}$$

The right-hand side of Eq. (3.10) is known from the problem configuration as it arises from the contribution of the real dislocations, and the left-hand side of Eq. (3.10) is a function of the unknown Burgers vectors of the N loops. For multiple interacting voids (see Fig. 3.2), we pad a total of N dislocation loops on the voids' surfaces. Each void surface can have a different number of padded loops, i.e. $N_1, N_2, \ldots$ etc. such that $N = N_1 + N_2 + \cdots$. This method is independent of the number of voids or their shape. In this

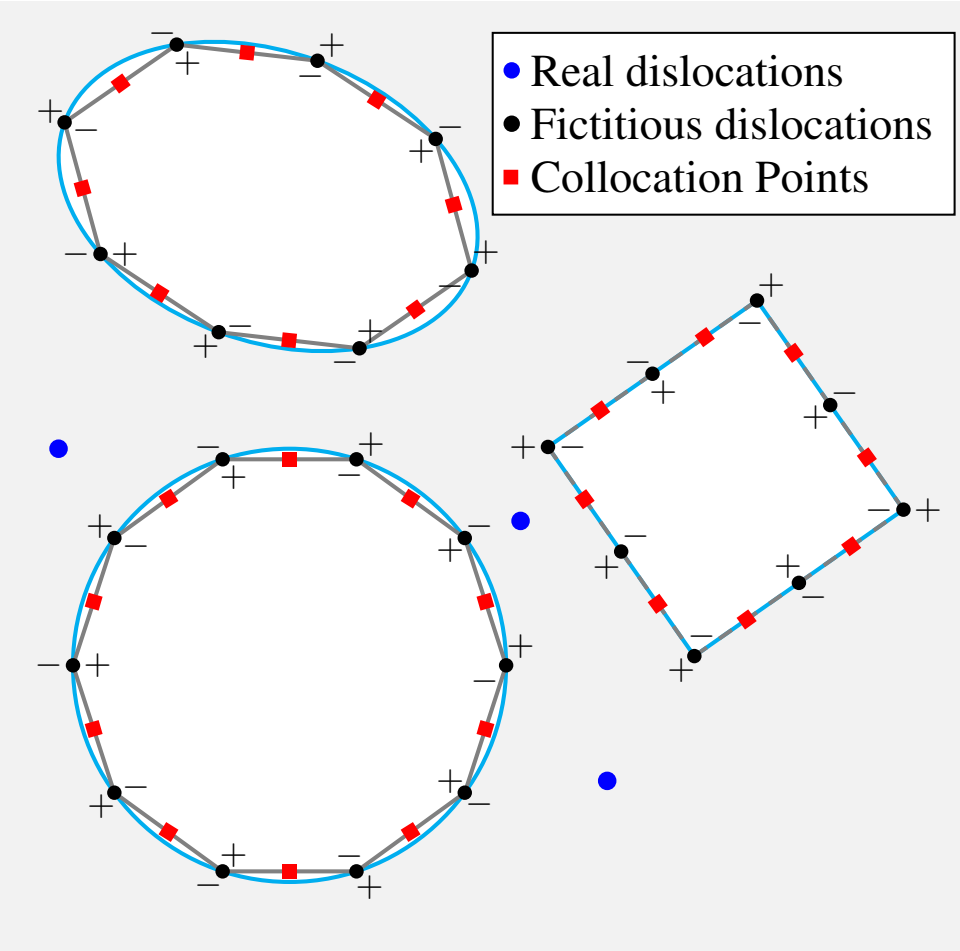

Figure 3.2: Multiple interacting voids of different shapes

light, Eq. (3.10) can be re-written for the case of interacting voids as:

$$\sum_{i=1}^{N_1}\left(\sigma_{xz}^{i}\left(\vec{r}_C'\right)n_x^C+\sigma_{yz}^{i}\left(\vec{r}_C'\right)n_y^C\right)+\sum_{l=1}^{N_2}\left(\sigma_{xz}^{l}\left(\vec{r}_C'\right)n_x^C+\sigma_{yz}^{l}\left(\vec{r}_C'\right)n_y^C\right)+\cdots = -\sum_{m=1}^{M}\left(\sigma_{xz}^{m}\left(\vec{r}_C'\right)n_x^C+\sigma_{yz}^{m}\left(\vec{r}_C'\right)n_y^C\right) \tag{3.11}$$

The traction component T_z for Loop j (or dislocation j in general) at collocation point $C(x,y)$ can be written as a linear combination of the unknown Burgers vector of loop j as,

$$\sigma_{xz}^{j\to C}(x,y)\,n_x^C+\sigma_{yz}^{j\to C}(x,y)\,n_y^C=\left[K_{xz}^{j\to C}(x,y)\,n_x^C+K_{yz}^{j\to C}(x,y)\,n_y^C\right]b_z^j=A_{Cj}b_z^j \tag{3.12}$$

where $\sigma_{xz}^{j\to C}$ is the xz-stress component of loop j evaluated at point C, b_z^j is the z- component of the Burgers vector for loop j, and $A_{Cj}(x,y)$ is the coupling term for loop j.

To find the coupling term, we find the kernel terms from Eq. (3.4) and then substitute it into Eq. (3.12). Equation (3.12) is substituted into the left-hand side of equation (10), which upon expansion yields N unknown Burgers vectors. However, equation (10) is applied N times for N collocation points. This yields a set of $N \times N$ linear equations. Once the unknown Burgers vectors are solved for they can then be substituted back into Eq. (3.8) to find the stress field.

For a screw dislocation around a void, the cut to generate the dislocation can be either from the void surface or from the infinity [12]. The numerical scheme presented here (involving the right-hand side of Eq. (3.10)) is developed based on the stress field of a screw dislocation formed by a cut from infinity.

3.3 Numerical Framework

Based on above, a set of linear equations can be written in matrix form as,

$$[A]\vec{B} = \vec{F} \tag{3.13}$$

Matrix $[A]$ is termed as coupling matrix, $\vec{B}$ is a column vector of unknown Burgers vectors of the dislocation loops and $\vec{F}$ is also a column termed as forcing vector evaluated at each collocation point by the real dislocations using the right-hand side of Eq. (3.10). The dimension of $[A]$ is $N \times N$, and $\vec{B}$ and $\vec{F}$ is N. As can be seen above, the elements of matrix $[A]$ are populated using Eq. (3.12) associated with the fictitious dislocation loops only, whereas vector $\vec{F}$ is associated with the real dislocations only, which is a known quantity. Elements of the matrix $[A]$ thus depends on the number of padded dislocation loops on the void surface, not on the density of real dislocations and elements of the quantities $\vec{F}$

depends on the number and location of the real dislocations and are independent of the fictitious dislocation density.

For the above problem, matrix $[A]$ is singular; hence the solution is not unique, and conventional decomposition techniques fail to solve Eq. (3.13). But the coupling matrix $[A]$ has marginal diagonal dominance meaning that the absolute value of the diagonal element of each row is equal to the sum of the absolute values of other elements, i.e. $|A_{ii}| = \sum_j |A_{ij}|$. This property of matrix [A] is needed for the convergence of iterative numerical linear equation solvers like the Gauss-Seidel method with successive over relaxations (SOR) [23]. In the current problem, Eq. (3.13) is solved using the Gauss-Seidel iteration technique with SOR parameter equal to 1.35, which expedited the solution convergence.

3.4 Results and Discussion

This article presents several verifications of the numerical method shown above. It also provides solutions to problems not available in the literature. Consider, for instance, a screw dislocation along the x-axis and away from a cylindrical hole center by $1.25R$ (where R is the radius of void). For this problem, the traction component T_z is computed at field points along $10°, 30°, 50°$, and $90°$ rays from the void center (see Fig. 3.1(c)). Figures 3.3(a) and 3.3(b) show such computations for the case of no proper treatment of the free-traction condition on the void surface and for the case of proper treatment using the above numerical method, respectively. Figure 3.3(a) shows the traction not terminating at zero on the free surface, whereas Fig. 3.3(b) shows how the employed numerical method satisfies the proper physical condition of the problem at-hand.

In dislocation theory, the thermodynamic force causing dislocations to glide is termed the Peach-Koehler (PK) force [11]. It is calculated using the following formula (which is

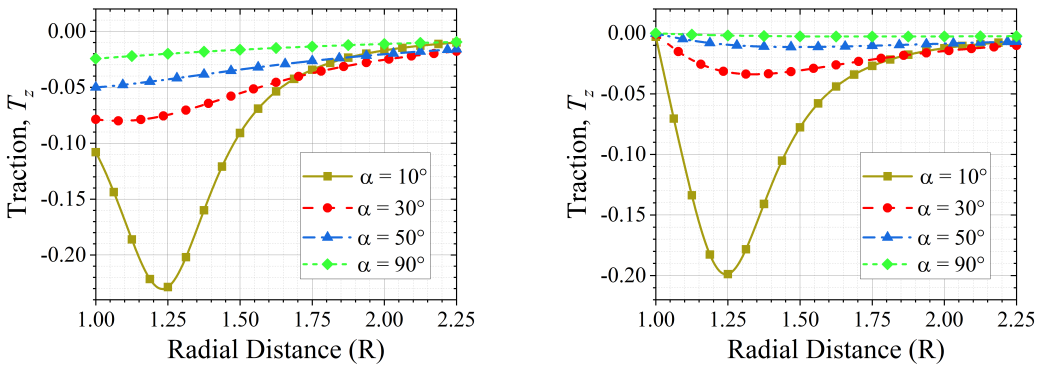

Figure 3.3: Plotted traction component T_z: (a) without proper treatment of the free-traction boundary condition, and (b) with proper treatment. Here $N = 150$.

applied here to the case of a screw dislocation):

$$\vec{F} = \left(\boldsymbol{\sigma}\vec{b}\right) \times \vec{t} = \left(\begin{bmatrix} 0 & 0 & \sigma_{xz} \\ 0 & 0 & \sigma_{yz} \\ \sigma_{xz} & \sigma_{yz} & 0 \end{bmatrix} \begin{Bmatrix} 0 \\ 0 \\ b_z \end{Bmatrix} \right) \times \begin{Bmatrix} 0 \\ 0 \\ 1 \end{Bmatrix} = \begin{Bmatrix} \sigma_{yz} b_z \\ -\sigma_{xz} b_z \\ 0 \end{Bmatrix} = \begin{Bmatrix} F_x \\ F_y \\ 0 \end{Bmatrix} \quad (3.14)$$

For dislocation near a free surface, this force has the effect of pulling the dislocation towards the surface for as the dislocation exits the material, the entropy reduces and the internal order of the crystal is restored.

Consider a screw dislocation lying on the x-axis near a cylindrical void (see Fig. 3.1(a)). In this case, the PK force pulling the dislocation towards the free surface (Eq. (3.14)) will only have an x-component and no y-component [9], [14]. In the above numerical method, the σ_{xz} and σ_{yz} stresses acting on the dislocation will emanate from the fictitious dislocation loops padding the surface. Hence one verification for the above numerical method is to compute the σ_{xz} stress from the loops along the x-axis ($y = 0$) to ensure that it is zero. Figure 3.4(a) shows that for several numbers of surface loops and provides verification of

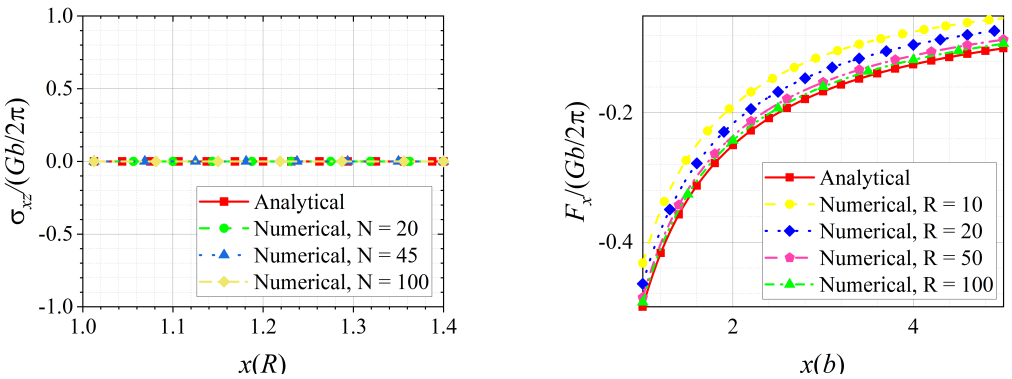

Figure 3.4: (a) normalized σ_{xz} emanating from the fictitious dislocations plotted along the x-axis (for any R), (b) normalized F_x emanating from the fictitious dislocations and acting on a real dislocation situated along the x-axis ($N = 500$, and R measured in b units).

the current method. Figure 3.4(b) shows another verification of the proposed method. The figure shows the normalized PK force component F_x produced by the fictitious dislocation loops on the free surface and felt by a screw dislocation along the x-axis. As the radius of the cylindrical void R increases, the numerical solution approaches the limiting case of a screw dislocation near an infinite flat free surface [18].

Another verification of the current numerical method is shown in Fig. 3.5. Here, the numerical solution is compared with the analytical solution derived by Lubarda [12] for a circular void. It can be seen from the figure that as the number of fictitious dislocation loops increase, the numerical solution approaches the analytical one. This represents a convergence test for the current collocation-point method. It is worth noting here that the numerical method does not need an excessive number of dislocation loops to match the analytical solution. Indeed, based on the previous works of [16], [17], [18], the numerical solution at a field point away from the free surface is accurate as long as the distance between the surface and the point is equal or more to the average spacing between the collocation points. This is actually exhibited in Fig. 3.5.

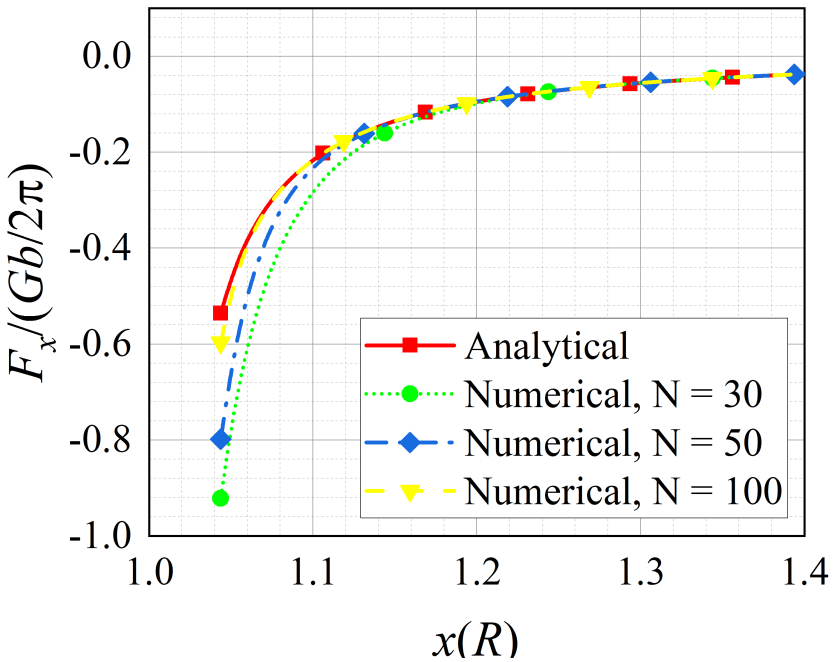

Figure 3.5: Peach-Koehler force exerted by the fictitious dislocations on a real dislocation situated along the x-axis ($R = 20b$). Also, the analytical solution is plotted.

The next figure illustrates the power of the current numerical method beyond available analytical solutions. The current method can easily handle voids of any shape and number, which is not currently available via analytical solutions, which have to be tightly prescribed in terms of the problem configuration. For Fig. 3.6, a dislocation is placed along the x-axis between two voids. These two voids can be of the same shape but of different diameters (Fig. 3.6(a)) or they can be of different shapes (circular cross-section versus a diamond one as in Fig. 3.6(b) or circular cross-section versus an ellipse as in Fig. 3.6(c)). An aspect ratio (AR) is defined as the maximum vertical dimension of the void on the right to the cylindrical void diameter on the left of the figures. In this problem, the elliptical and diamond shaped voids have the same horizontal dimension as the left cylinder diameter.

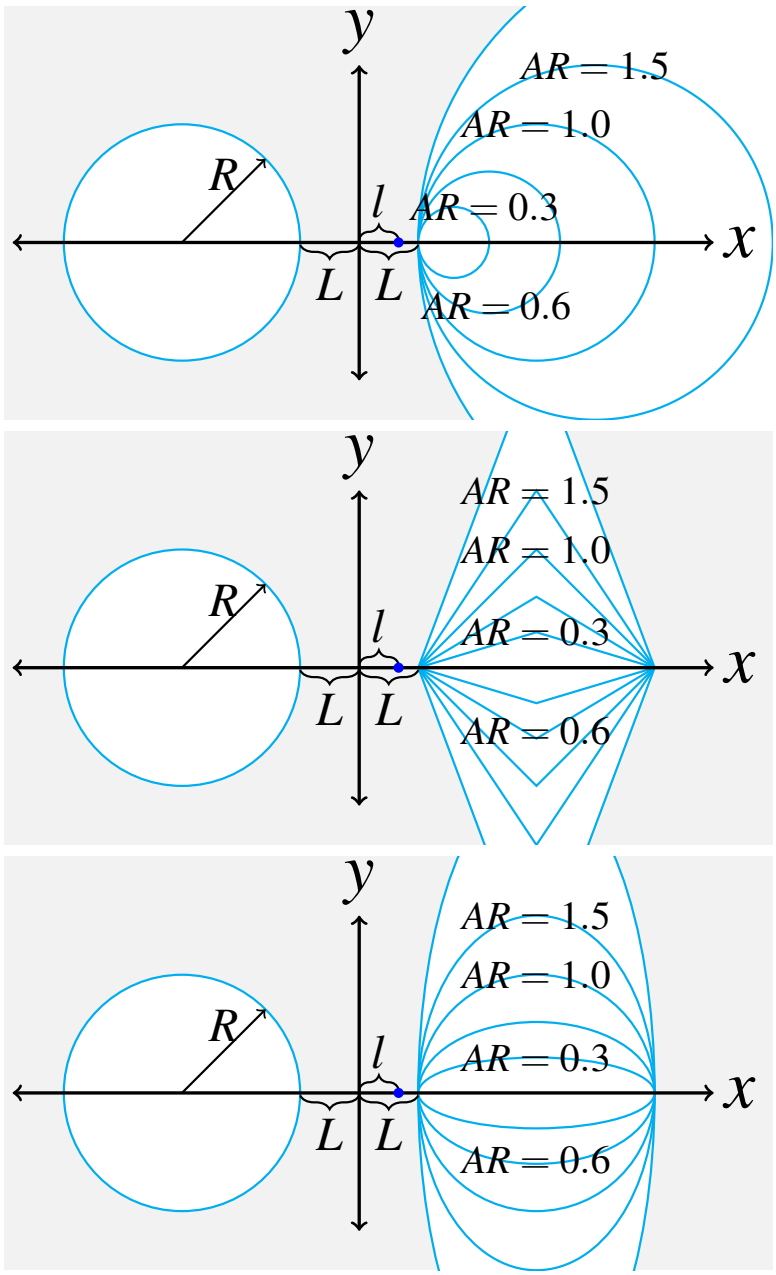

Figure 3.6: A screw dislocation between two differently-shaped voids.

For this problem configuration, the PK force by the fictitious dislocation loops from two voids of different shapes/sizes on a screw dislocation between them (on the x-axis) is com-

puted. Based on this computation, the position of equilibrium for the dislocation l, defined as the point where the net PK force (from the contributions of all fictitious dislocation loops on all voids) is zero, is determined. Moreover, one can normalize this position as:

$$\xi = \frac{l}{L} \tag{3.15}$$

where L is half the edge-to-edge distance between the voids. A plot of the equilibrium positions for the three configurations in Fig. 3.6 versus AR is shown in Fig. 3.7. As is expected, the smaller the void on the right compared to the one on the left, the more *xi* is positive, i.e. closer to the smaller void. Moreover, for the elliptical and the cylindrical voids on the right-hand side of Fig. 3.6(c) and Fig. 3.6(a), it is expected that ξ will be unity when AR is 1. This is another verification for the method and its implementation and Fig. 3.7 demonstrates that.

Here, it is worth discussing that other methods (besides the collocation point method presented here) could be employed to counteract the unphysical stress traction vectors on the free surfaces of a finite domain containing dislocations whose self-stress, which is a source of internal stress, is taken as that of a dislocation in an infinite domain. Specifically, the finite-element method (FEM) is used in coupling with a discrete dis- location (DD) dynamics simulation methodology: For 2D problems in [19] and for 3D problems in [24]. The main issue with coupling the FE methodology with the DD methodology is that they are two separate and different numerical methods. In the FEM, it is important to specify displacements as boundary (external or internal) conditions whereas in the DD method stresses are what is calculated for the movement and interaction of dislocations. And since the dislocations' self-stresses pose a non-uniform state of stress and deformation inside the finite computational domain, it is essentially impossible to know upfront what points in the solid need to be conditioned for what displacements in order to accommodate the FE methodology. Hence, the FEM method despite being able to exert a negative traction to counteract the unphysical stress tractions from the infinite-domain self-stress of dislocations, it grabbles with displacement conditions that could be unphysical in and by

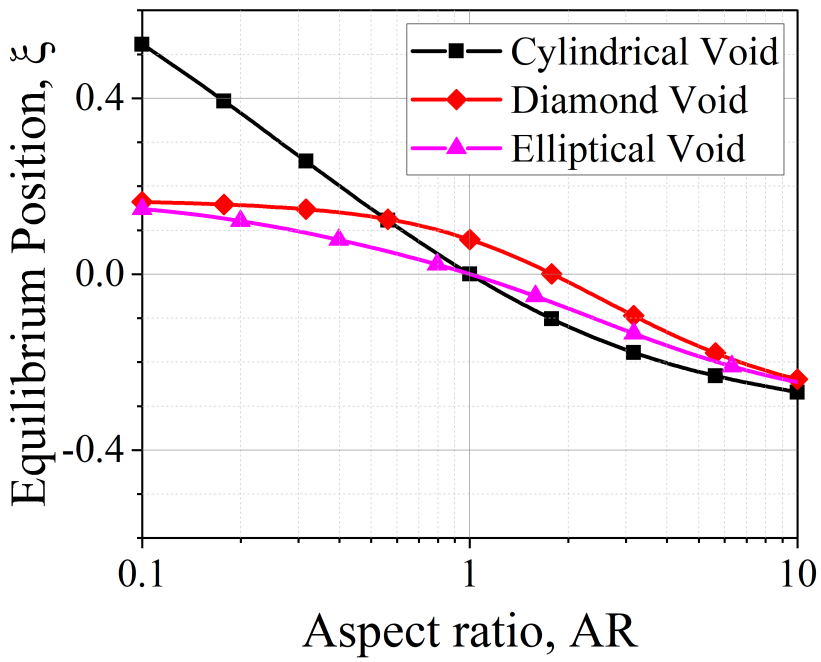

Figure 3.7: Equilibrium position for varying aspect ratios of the right-hand side voids of figures (6). $N = 500$.

themselves and hence defeat the original coupling idea between the two different simulation methodologies. The above method employed for the interaction of screw dislocations with holes could be extended to edge dislocations upon considering the T_x and the T_y stress traction components instead of the T_z traction component. This is because for an infinite edge dislocation the self-stress components are in the plane and not out of plane. This is something that the authors hope to accomplish in the future. Moreover, this collocation point method can be extended to 3D problems of dislocation-hole interactions. However, in this case, all stress traction components (i.e. T_x, T_y and T_z) at any collocation point need to be considered. As alluded to above, the collocation point method in 3D to treat dislocation-free sur- face problems was employed for flat or planar surfaces only [16], [17], [18]. However, for curved or non-planar surfaces, this method is yet to be developed

and would constitute a major development.

3.5 Conclusion

In this paper, the authors presented a generalized numerical method to find the stress field (which is easily convertible to strain field in isotropic elasticity) for the problem of screw dislocations (of any number) around voids. The voids can be of any number and any shape while maintaining the same formulation, something not attainable in analytical solutions. This method can be extended to edge dislocations as well but left for future developments. Moreover, since this dislocation problem is solved using other (fictitious) dislocations, the method is called a "self-consistent" method as it does not have to resort to a different solution methodology than the dislocation methods describing the initial problem.

Journal reference

Siddique, A. B., & Khraishi, T. A. (2021). Screw dislocations around voids of any shape: A generalized numerical approach. Forces in Mechanics, 3(October 2020), 100014. https://doi.org/10.1016/j.finmec.2021.100014

Chapter 4

A holed-plate with a material dislocation

Abstract

Standard text-book dislocation theory for the elastic fields of a dislocation are provided in an infinite medium. For problems involving free surfaces, or image stresses, the solution for such elastic fields is more complex. The current paper extends the state of knowledge for problems with free surfaces to address the stress field of a screw dislocation in a plate (two planar free surfaces) containing a hole/void. Such surfaces interact and thus affect the stress field of a dislocation in deviation of the infinite medium solution. The numerical solutions, based on reflective image stresses and the collocation-point method, provided herein have been verified to the extent available and such solutions allow for further applied problems. One main finding of the paper is that the equilibrium location of a screw dislocation is always closer to the hole/void surface than the planar free surface. Keywords: dislocation theory, hole, plate, void, collocation point method, image dislocations, image stresses

4.1 Introduction

The dislocations in a material are termed "carriers of plasticity." Any material experiences stress due to the presence of a dislocation inside it. In linear elastoplasticity, the stress field solution around a dislocation [5] in an infinite medium is a classic problem. Any discontinuity in the material affects the dislocation dynamics and the associated stress field. For example, a free surface (finite/infinite) close to a dislocation can significantly change the dynamics. To find the ensuing stress field, a classical solution [2], [11] (for the case of infinite material) along with a correction term is often used. Usually, this surface correction term is derived based on image dislocations, analogous to the solution of electrostatic problems presented by Jeans [25]. The additional surface correction term is used to ensure that the total stress field satisfies the zero stress traction boundary condition on a free surface.

Eshelby et al. [6] derived the 2D solution for an infinite straight screw dislocation in a thin plate, and Head [7] formulated the elastic interaction of a screw dislocation in a semi-infinite isotropic medium with a surface layer (i.e., oxide film). Later, Eshelby [8] derived the stress field of an eccentrically situated screw dislocation in a cylindrical rod. As another case of the curved (non-planner) free surface, Friedel [9] formulated the analytical solution of a screw dislocation near a cylindrical void. Yoffe [10] showed stress field calculations for a straight dislocation terminating at a free surface at an arbitrary angle.

A dislocation loop is formed when a dislocation line terminates into itself. The character of the dislocation in a glide loop varies from point to point. In a glide loop, the character of dislocation changes from edge to mixed and then to screw. The dislocation character is everywhere edge in a prismatic loop since the Burgers vector is normal to its slip plane. Kroupa [26], [27] derived the stress and deformation field of a prismatic circular loop in an isotropic infinite medium. Initially, Kröner [28] presented the stress field of a glide loop,

and the solution was later corrected by Marcinkowski et al. [29]. Later Khraishi et al. [30], [31] presented a comprehensive study on the displacement and stress fields of glide and prismatic circular dislocation loops. In recent works, Li et al. [32], [33] investigated the stress/strain field of rectangular dislocation loop in an infinite medium and parallel to a free surface of a half medium. A dislocation experiences an attraction force [11] by a free surface. This attraction force magnitude depends mainly on the relative distance between the free surface and the dislocation. The dynamics of the dislocation can be affected by this surface phenomenon. Lubarda et al. [12], [13], [14] formulated the image forces (attractive force by the free surface) on an infinite-length screw dislocation in an isotropic medium for multiple interacting free surfaces of different geometry/topology. Such solutions were strictly case-specific (i.e., they depended on the exact dislocation location and number and geometry of voids/free surface). In recent work, the authors of this article recently presented a versatile and adaptive numerical approach for finding the stress field solution for infinite straight screw dislocations near multiple interacting free surfaces of arbitrary geometry [34]. The numerical framework in this last reference was developed based on the collocation point method implemented by Khraishi et al. [15], [16], Yan et al. [17], and Siddique et al. [18], [35].

The works mentioned above investigated the stress field of a screw dislocation in an infinite medium. Some of these solutions also dealt with a half medium. None of the solutions dealt with a plate material and on-top one that has holes in it. In this current article, the authors present a generalized numerical framework for finding the stress field solution of a screw dislocation near a cylindrical void in a plate (free surfaces on both sides of the plate). The developed framework is scalable and can be used in 2D dislocation dynamics simulations to model the effect of free surfaces (external or internal) on dislocation glide and the ensuing crystal plasticity [19], [20]. Comprehensive theoretical development of the algorithm is presented in the Theory section. The Numerical Framework section discusses a numerical scheme to the stress field solution and an efficient algorithm for finding the

equilibrium points (points at which the screw dislocation is not feeling any force). In the Results section, the locus of the equilibrium points is presented and discussed for different problem parameters. The result is verified, for limiting cases, against previously published works.

4.2 Theory

The stress field component solutions for a screw dislocation inside an infinite medium is given by [2], [11],

$$\sigma_{xz} = -\frac{Gb_z}{2\pi}\frac{(y-C_y)}{(x-C_x)^2+(y-C_y)^2} \tag{4.1}$$

$$\sigma_{yz} = -\frac{Gb_z}{2\pi}\frac{(x-C_x)}{(x-C_x)^2+(y-C_y)^2} \tag{4.2}$$

Where, G is the shear modulus of the medium, b_z is the Burgers vector of the dislocation and (c_x, c_y) is the position of that dislocation with respect to the origin of a Cartesian coordinate system. This solution can be extended to half and finite media by adding a correction term to Eqs. ((4.1), (4.2)). The other four stress components are zero for a screw dislocation.

In this work, the authors are interested in screw dislocations in a finite material, specifically an isotropic plate with two parallel free surfaces (Fig. 4.1a). Consider the plate to have a thickness $2w$. For this problem, the zero stress traction boundary condition must be enforced on surfaces 1 and 2. Knowing that the unit normal ($\vec{n}$) to both surfaces is $(0,1,0)$, and that the equation of the traction $\vec{T}$ is given by: $\vec{T} = \sigma\vec{n}$, where σ is the 3×3 stress tensor at a material point, the traction vector is then given by: $\vec{T} = (T_x, T_y, T_z) = (0,0,\sigma_{yz})$. For a free surface, the traction must be null, and hence we must have $T_z = \sigma_{yz} = 0$. Here on both surfaces 1 and 2, we must then ensure $\sigma_{yz} = 0$ as a requirement for the physical boundary condition of the problem.

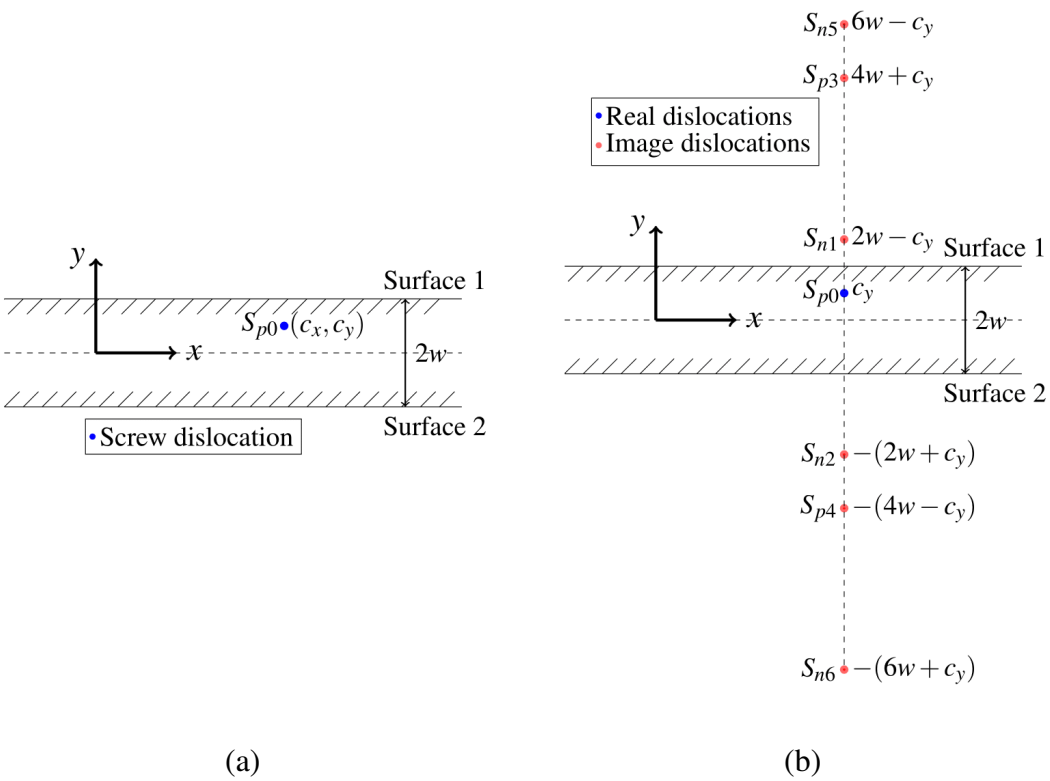

Figure 4.1: A crystal screw dislocation inside a plate, as well as image dislocations. (a) Screw dislocation inside a plate (b) Image dislocations to satisfy the boundary conditions

To illustrate the inappropriateness of the stress solution presented in Eqs. ((4.1), (4.2)), consider a real or crystal screw dislocation S_{p0} located at (c_x, c_y) in the plate (Fig. 4.1). Figure 4.2 shows the stress fields σ_{xz} and σ_{yz} using these two equations. The traction component, $T_z = \sigma_{yz}$ at any point $(x \neq c_x)$ on surface 1 $(y = w)$,

$$\sigma_{yz} = \frac{Gb_z}{2\pi}\left[\frac{(x-c_x)}{(x-c_x)^2+(w-c_y)^2}\right] \neq 0 \tag{4.3}$$

And at any point $(x \neq c_x)$ on surface 2 $(y = -w)$,

$$\sigma_{yz} = \frac{Gb_z}{2\pi}\left[\frac{(x-c_x)}{(x-c_x)^2+(-w-c_y)^2}\right] \neq 0 \tag{4.4}$$

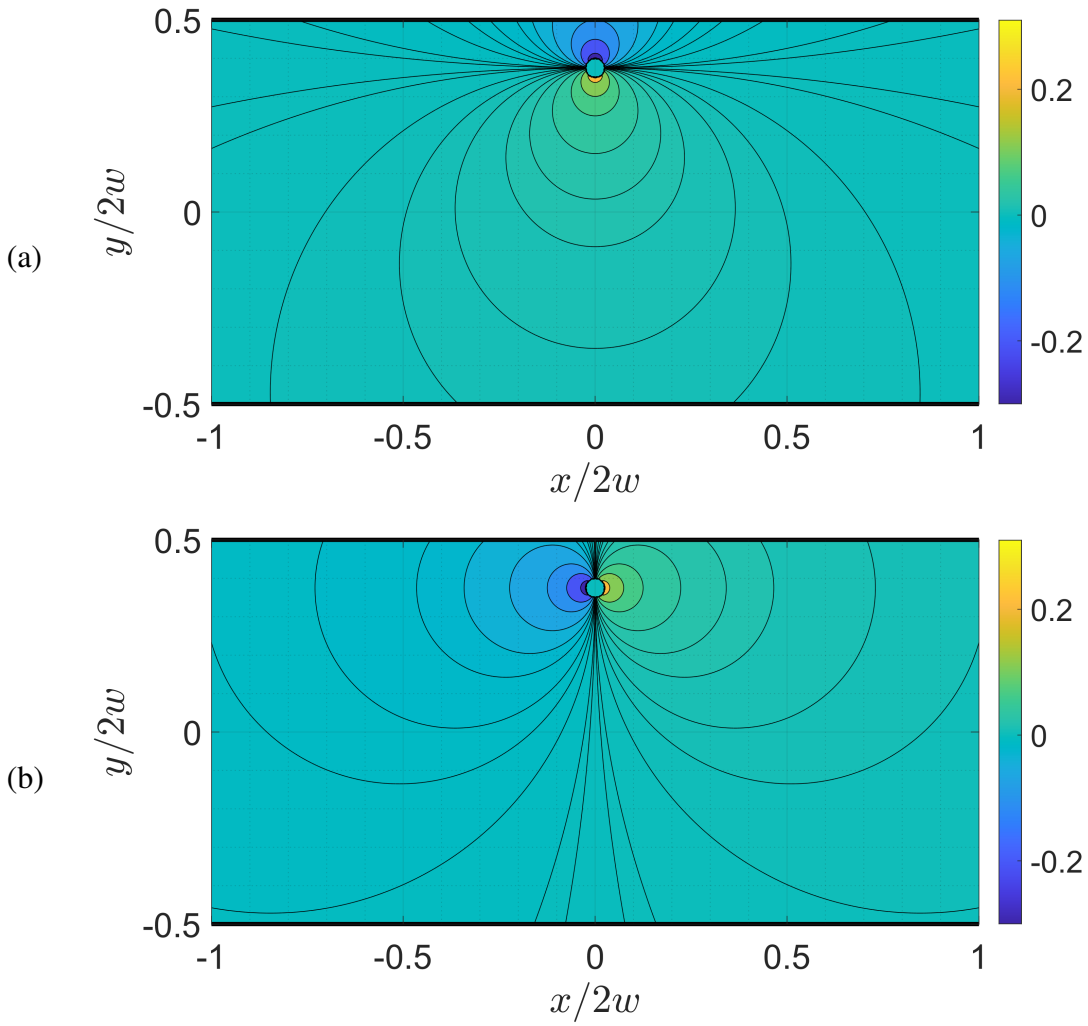

Figure 4.2: Contour plots of the stress field σ_{yz} and σ_{xz} in a plate (containing no hole/void) without considering any boundary conditions. (a) Contour plot for σ_{xz}/Gb, (b) Contour plot for σ_{yz}/Gb.

Equations ((4.3), (4.4)) and Fig. 4.2b clearly show that the stress traction component $T_z = \sigma_{yz} \neq 0$ on the two surfaces which is in direct violation of the physical boundary condition on these free surfaces. Hence, it is important to augment the stress solutions in Eqs. ((4.1), (4.2)) with additional surface correction terms that result in the satisfaction of the free surface boundary condition, i.e., to ensure that σ_{yz} is zero on both free surfaces.

To derive the surface correction term, we introduce fictitious or image dislocations. An image dislocation is an imaginary dislocation or a mathematical tool to formulate the correction terms needed to satisfy the boundary conditions for the classical solution (i.e., the infinite medium solution). An image dislocation is like any other dislocation: an equilibrated source of stress in the material. Image dislocations do not interact with each other since they are not physical dislocations. Here, we first add a fictitious negative ($b = -b_z$) dislocation S_{n1} at the mirror location from surface 1 (see Fig. 4.1b), in order to annul the traction component T_z on surface 1 [2], noting that y=w at surface 1:

$$T_z = \sigma_{yz} = \frac{Gb_z}{2\pi}\left[\frac{(x-c_x)}{(x-c_x)^2+(w-c_y)^2} - \frac{(x-c_x)}{(x-c_x)^2+(w-(2w-c_y))^2}\right] = 0 \quad (4.5)$$

As can be seen in Eq. (4.5), the free boundary condition is now satisfied on surface 1. But the zero traction boundary condition needs to be fulfilled simultaneously on all the free surfaces. If we consider surface 2 (where $y = -w$), the σ_{yz} is not zero on it:

$$T_z = \sigma_{yz} = \frac{Gb_z}{2\pi}\left[\frac{(x-c_x)}{(x-c_x)^2+(-w-c_y)^2} - \frac{(x-c_x)}{(x-c_x)^2+(-w-(2w-c_y))^2}\right] \neq 0 \quad (4.6)$$

This means that the fictitious/image dislocation S_{n1} is not sufficient by itself to fulfill the boundary condition on both free surfaces. Hence, we now turn our attention to surface 2. We have to add another fictitious negative ($b = -b_z$) dislocation S_{n2} at the mirror location of the real dislocation S_{p0} with respect to surface 2. Both S_{p0} and S_{n2} annul the traction on surface 2:

$$T_z = \sigma_{yz} = \frac{Gb_z}{2\pi}\left[\frac{(x-c_x)}{(x-c_x)^2+(-w-c_y)^2} - \frac{(x-c_x)}{(x-c_x)^2+(-w+2w+c_y)^2}\right] = 0 \quad (4.7)$$

However, one must also consider the effect of S_{n1} on surface 2 and not just the effect of S_{p0} and S_{n2}, i.e. all dislocations in the configuration need to be considered for their effect.

Considering all three dislocations on surface 2, one gets:

$$T_z = \sigma_{yz} = \frac{Gb_z}{2\pi}\left[\frac{(x-c_x)}{(x-c_x)^2+(-w-c_y)^2} - \frac{(x-c_x)}{(x-c_x)^2+(-w+2w+c_y)^2} - \frac{(x-c_x}{(x-c_x)^2+(-w-(2w-c_y))^2}\right] \neq 0 \tag{4.8}$$

Therefore, we need to add another fictitious positive ($b = b_z$) dislocation S_{p4} at the mirror location of image dislocation S_{n1} with respect to surface 2 (see Fig. 4.1b) to cancel the traction on surface 2:

$$\sigma_{yz} = \frac{Gb_z}{2\pi}\left[\frac{(x-c_x)}{(x-c_x)^2+(-w-c_y)^2} - \frac{(x-c_x)}{(x-c_x)^2+(-w-(2w-c_y))^2} - \frac{(x-c_x)}{(x-c_x)^2+(-w+2w+c_y)^2} + \frac{(x-c_x)}{(x-c_x)^2+(-w+4w-c_y)^2}\right] = 0 \tag{4.9}$$

Now the image dislocations S_{n2} and S_{p4} instigate non-zero traction component σ_{yz} on surface 1:

$$\sigma_{yz} = \frac{Gb_z}{2\pi}\left[-\frac{(x-c_x)}{(x-c_x)^2+(w+2w+c_y)^2} + \frac{x-c_x}{(x-c_x)^2+(w+4w-c_y)^2}\right] \neq 0 \tag{4.10}$$

To cancel the non-zero traction on surface 1, we again add one fictitious positive ($b = b_z$) dislocation S_{p3} at the mirror location of image dislocation S_{n2} from surface 1, and another fictitious negative ($b = -b_z$) dislocation S_{n5} at the mirror location of image dislocation S_{p4} from surface 1 (see Fig. 4.1b). As a result of these additional image dislocations, the traction component σ_{yz} on surface 1 now vanishes:

$$\sigma_{yz} = \frac{Gb_z}{2\pi}\left[\frac{(x-c_x)}{(x-c_x)^2+(w-c_y)^2} - \frac{(x-c_x)}{(x-c_x)^2+(w-(2w-c_y))^2} - \frac{(x-c_x)}{(x-c_x)^2+(w+2w+c_y)^2} + \frac{(x-c_x)}{(x-c_x)^2+(w+4w-c_y)^2} + \frac{(x-c_x)}{(x-c_x)^2+(w-4w-c_y)^2} - \frac{(x-c_x)}{(x-c_x)^2+(w-6w+c_y)^2}\right] = 0 \tag{4.11}$$

Again, these image dislocations S_{p3} and S_{n5} initiate non-zero traction on surface 2. It is

important to mention that the non-zero traction component on both free surfaces is now smaller in magnitude with the addition of more image dislocations than the previously calculated one in Eq. (4.3) or Eq. (4.4). So we keep adding image dislocations on either side of the free surfaces to balance the non-zero tractions on both free surfaces simultaneously (see Fig. 4.1b). The more fictitious/image dislocations added on either side of the plate, the more the magnitude of the non-zero traction component σ_{yz} tends to zero. From this trend, the addition of an infinite number of image dislocations on both sides of the plate will lead to satisfaction of the boundary condition of the problem. Based on all of the above, one can adjust the stress components in Eq. (4.1) and Eq. (4.2) by augmenting them to include an infinite series sum stemming from the image dislocations:

$$\sigma_{xz} = -\frac{Gb_z}{2\pi}\left[\frac{(y-c_y)}{(x-c_x)^2+(y-c_y)^2}+\sum_i^{\infty}\omega_i\frac{\left(y-c_y^{*i}\right)}{(x-c_x)^2+\left(y-c_y^{*i}\right)^2}\right] \tag{4.12}$$

$$\sigma_{yz} = \frac{Gb_z}{2\pi}\left[\frac{(x-c_x)}{(x-c_x)^2+(y-c_y)^2}+\sum_i^{\infty}\omega_i\frac{(x-c_x)}{(x-c_x)^2+\left(y-c_y^{*i}\right)^2}\right] \tag{4.13}$$

where, $\left(c_x, c_y^{*i}\right)$ are the coordinates of the i-th image dislocation. An image dislocation can be left-hand or right-hand screw dislocation with a Burgers vector equal to b_z, i.e. can be positive or negative dislocation. The y-coordinate c_y^{*i} is determined by the following relations:

$$\begin{aligned} c_y^{*i} &= (i+1)w+(-1)^{(i+1)/2}c_y \quad \text{and} \quad \omega_i = -1^{(i+1)/2} \quad \text{when } i \text{ is odd} \\ c_y^{*i} &= -\left(iw+(-1)^{(i+2)/2}c_y\right) \quad \text{and} \quad \omega_i = -1^{i/2} \quad \text{when } i \text{ is even} \end{aligned}$$

The infinite summation terms in Eqs. (4.12), (4.13) are the required correction terms to describe the correct stress profile in the plate in the presence of a real dislocation S_{p0}. These correction terms are not constant values but are functions of Burgers vector and the location of the real dislocation(s). This means that if the location of any real or crystal dislocation changes, then the correction terms need to be re-calculated. As a verification

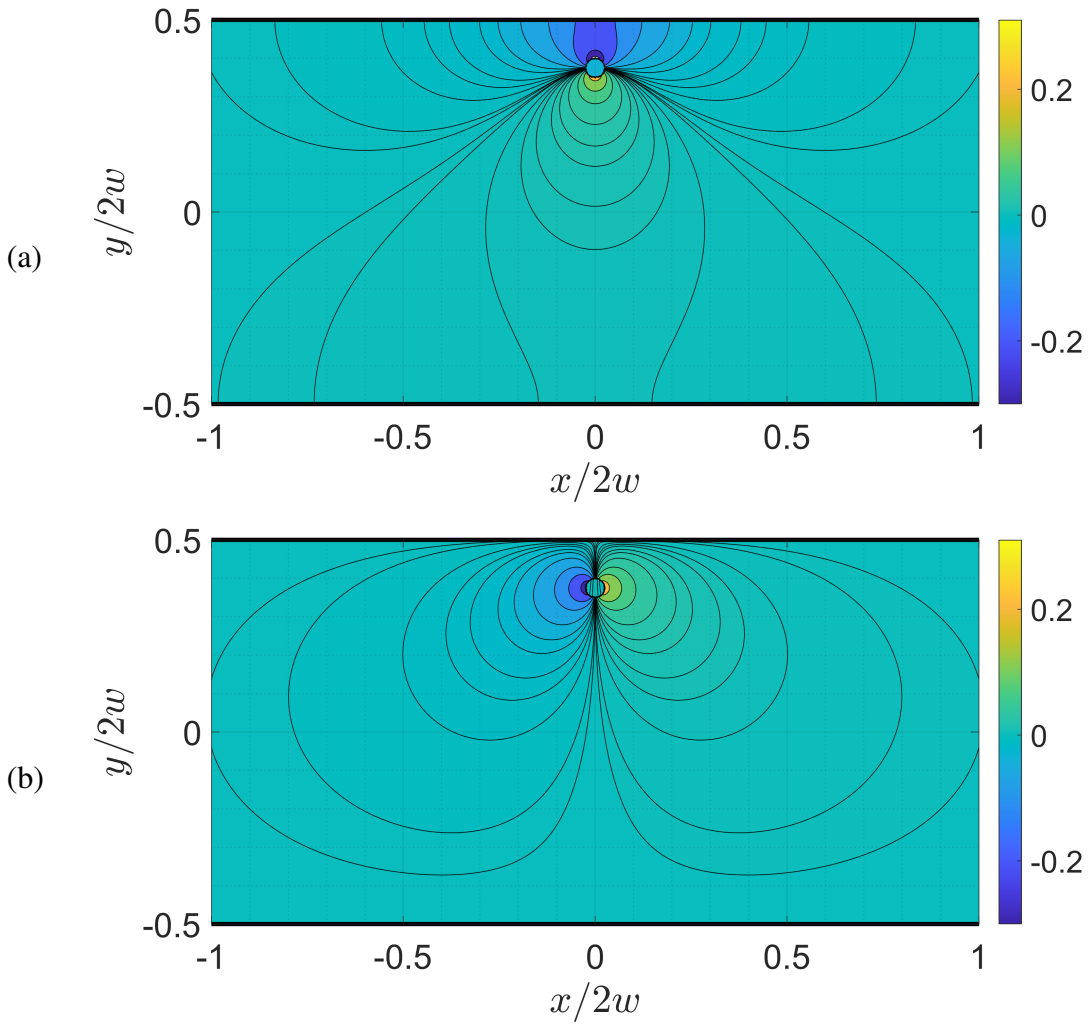

Figure 4.3: Contour plots of the stress $fields\sigma_{yz}$ and σ_{xz} in a plate (no hole/void) when enforcing the traction-free boundary condition (Eqs. (4.12), (4.13)). (a) Contour plot for σ_{xz}/Gb, (b) Contour plot for σ_{yz}/Gb.

of the developed Eqs. (4.12) and (4.13), we plot the field solution σ_{xz} and σ_{yz} using Eqs. (4.12) and (4.13) and show them in Fig. 4.3. For the sake of easy comparison, the levels of isolines in Fig. 4.2, Fig. 4.3, Fig. 4.6, and Fig. 4.7 are kept the same. Comparing Fig. 4.2 and Fig. 4.3, the effect of the boundary condition is easily visible. Figure 4.3 shows how the surface effect changes the stress field profile of σ_{xz} and σ_{yz}. Additionally, Fig. 4.3(b) shows the traction component σ_{yz} is zero on both surface 1 and surface 2, which verifies

the utilized method herein.

Now we extend the above-mentioned problem by including a cylindrical void of radius R in any arbitrary location inside it (for now let's take the center of the void to lie along the x-axis). A dimensionless parameter α is defined as $\alpha = w/R$ and $\alpha > 1$, where $2w$ is the width of the plate (see Fig. 4.1). The linear distance L between any point on a surface and the void center is given by $L = w/sin\theta = \alpha R/sin\theta$, where θ is the angle created by L and the horizontal reference axis (i.e, the positive x-axis), see Fig. 4.4. We label the equilibrium point distance from the void center as ξ, where $L > \xi \geq R$. At any equilibrium point *i*n the plate, the net force acting on the real dislocation is zero. In the presence of a void in a plate, we can incorporate the solution in Eqs. (4.12), (4.13) along with the collocation point method.

[34] to find the complete solution at any field point *i*n the plate. Thus, using the collocation point method in conjunction with the correction terms in Eqs. (4.12), (4.13), we derive another correction term for the stress field solution to satisfy the boundary conditions on all the free surfaces (the two planar or horizontal ones and the curved one(s) of the hole(s)):

$$\sigma = \sigma^c + \sigma_{corr} \tag{4.14}$$

where σ_{corr} is the correction term computed using the collocation point method, σ^c is the stress tensor from classical solution and the infinite series correction terms (Eqs. (4.12) and (4.13)), and σ is the stress tensor for the complete or total solution.

In the collocation point method, N fictitious or mathematical rectangular dislocation loops of unknown Burgers vector are padded on the void/hole surface. These loops are infinitely long in z-direction, and the Burgers vector has only a z-component. The Burgers vectors of these dislocation loops are determined in such a way to ensure the traction components are zero at the collocation points on the void surface. The collocation points are taken here

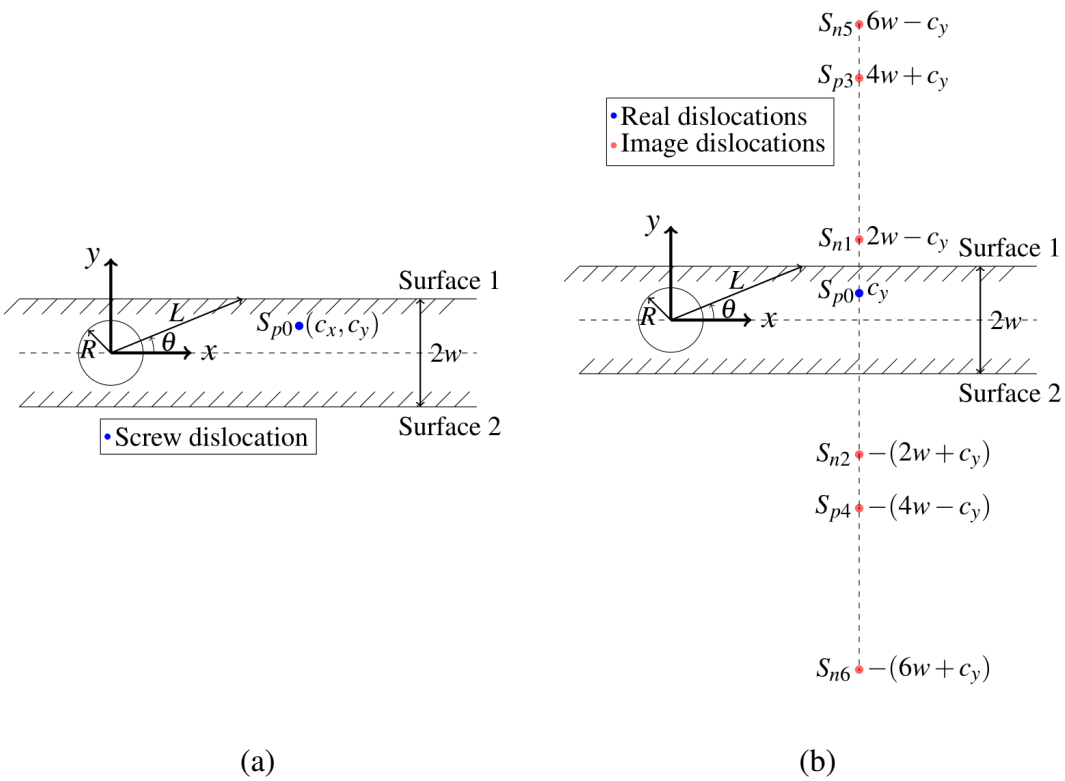

Figure 4.4: Methodology set up for a screw dislocation near a cylindrical void inside a plate. (a) Screw dislocation near a cylindrical void inside a plate (b) Image dislocations to satisfy the boundary conditions

as the geometric centers of the dislocation loops. Dislocation loops are employed in this method because they are a self-equilibrated source of stress for the correction term and provide a compatible field except at the dislocation point/location.

Each loop can be discretized into two infinite screw dislocations (direction parallel to z-direction, where the direction and Burgers vector are parallel) and two finite edge dislocations (dislocation direction/line sense normal to z-direction). Since the medium is infinite in z-direction we consider the problem as a 2D problem in an xy-plane. Here, the two edge dislocations do not contribute to the stress field in the xy-plane since their distance

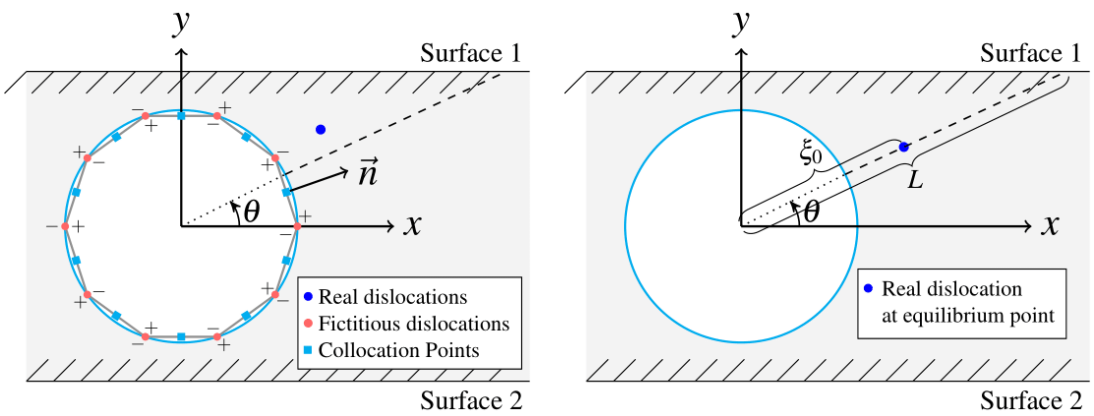

Figure 4.5: (a) Discretized surface loops. The + or − signs represent the direction of the infinite screw dislocations into the page, and the polygon sides are the edge dislocations. (b) A screw dislocation at an equilibrium point ($F_r = 0$), reflective image dislocations and collocation points are not shown here for simplicity.

from the plane is infinite. Now the two screw dislocations will have opposite direction/line sense vectors with respect to each other but the same Burgers vector. We assign + and – in Fig. 4.5(a) to differentiate them. Figure 4.5(a) shows how the discretized dislocations are oriented on the void surface. The polygon sides are the edge dislocations, and the vertices marked as + and – signs are the infinite screw dislocations. Note that each vertex has a positive and negative signed dislocation from two adjacent loops. It is interesting to see that both the + and – dislocations of a loop are adding to the total stress inside the loop but diminishing each other outside. It means that each collocation point experiences higher stress by its immediate surrounding dislocation loop than by any other loop on the void surface. Figure 4.5(b) shows the equilibrium point where the net force is zero on a dislocation.

In the collocation point method, it is important to know that a higher number of collocation points covering the surface will make the numerical solution approach the real solution (or analytical solution if one exists). Since the Burgers vectors of these image dislocations

are unknown, the stress values computed from all the image and real dislocations at each collocation point cannot be determined at this point. But the expression for stress components at a collocation point i (or any material point to that matter) can be written as a linear combination of all the unknown Burgers vectors:

$$\sigma_{pq}^{i} = \sum_{m=1}^{M} \sigma_{pq}^{\text{real dislocations}} + \sum_{j=1}^{N} \sigma_{pq}^{\text{image dislocations}} = \psi_{pq}^{i} + \sum_{j=1}^{N} \phi_{pq}^{j\to i} b_z^j \tag{4.15}$$

where $\psi_{pq}^{i} = \sum_{m=1}^{M} \sigma_{pq}^{\text{real dislocations}}$ is a known quantity (remember that these involve infinite sums for a plate as in Eqs. (4.12), (4.13) and $\phi_{pq}^{j\to i}$ can be computed for the dislocations padding the void/hole surface by putting $b_z = 1$ in Eqs. (4.12), (4.13). Note the double-sum that will ensue then in Eq. (4.15) as a result. Both the stress quantity ψ_{pq}^{i} and $\phi_{pq}^{j\to i}$ are evaluated at collocation point i. $\sum_{j=1}^{N} \phi_{pq}^{j\to i} b_z^j$ is the required correction term mentioned in Eq. (4.14). Equation (4.15) allows finding the expressions for the traction components at collocation point i as a linear combination of all the unknown Burgers vectors of the padded image discolorations on the void surface. Remembering the definition of stress traction from before as $\vec{T} = \sigma\vec{n}$, one obtains:

$$T_z^i = \sigma_{xz}^i n_x^i + \sigma_{yz}^i n_y^i = 0 \tag{4.16}$$

where $\vec{n}^i = (n_x^i, n_y^i)$ is the unit normal vector to the void surface at collocation point i. Now Eq. (4.16) can be written in light of Eq. (4.15) as:

$$\sum_{j=1}^{N} \left(\phi_{xz}^{j\to i} n_x^i + \phi_{yz}^{j\to i} n_y^i\right) b_z^j = -\left(\psi_{xz}^i n_x^i + \psi_{yz}^i n_y^i\right) \tag{4.17}$$

Equation (4.17) can be used to construct a set of linear equations using all of the collocation points, and the solution is the Burgers vector of the padded image dislocations along the void/hole surface. Once the Burgers vectors of these image dislocations on the hole perimeter are determined, then the correction term from the hole/void surface and the total stress tensor at any field point can be calculated using Eq. (4.15).

Peach-Koehler thermodynamic force $\vec{F}_{PK}$ acting on a dislocation can be expressed by [11],

$$\vec{F}_{PK} = \left(\boldsymbol{\sigma}\vec{b}\right) \times \vec{t} \tag{4.18}$$

where $\boldsymbol{\sigma}$ is the total stress tensor at a material point, $\vec{b}$ is the Burgers vector of such dislocation and $\vec{T}$ is the direction vector or line sense of this dislocation.

Since the stress tensor of any screw dislocation with $\vec{b} = (0,0,b_z)$ has only σ_{xz} and σ_{yz} components (with all other components vanishing), we simplify Eq. (4.18) for $\vec{b} = (0,0,b_z)$ and $\vec{T} = (0,0,1)$,

$$\vec{F}_{PK} = (F_x, F_y, F_z) = (\sigma_{yz}b_z, -\sigma_{xz}b_z, 0) \tag{4.19}$$

A dislocation starts to move in the slip plane when this Peach-Koehler force is larger than the internal lattice friction, and the speed of motion depends on the magnitude of the resolved shear stress. For the current configuration of the problem, one can compute the Peach-Koehler force in the radial direction as:

$$F_r = F_x \cos\theta + F_y \sin\theta \tag{4.20}$$

This was done using the first-rank tensor transformation rules for vector quantities. For the current problem configuration, the sign of the Peach-Koehler force can change depending on the location or position of the dislocation relative to the void free surfaces. When the dislocation is very close to the void, the direction of F_r is inward towards the void's center. When the dislocation is closer to the planar free surface, the direction of F_r or motion is outward with respect to the void. Since the stress field is continuous, there must be a point where $F_r = 0$. That point *i*s termed an equilibrium point (and exists at a radial distance ξ_0 per above). The calculation of ξ_0 is given below.

4.3 Numerical Framework

Based on the problem configurations, N number of linear equations can be constructed by employing Eq. (4.17) at N collocation points. The set of equations can be represented as a matrix equation:

$$[A]\vec{B} = \vec{F} \tag{4.21}$$

Matrix A is termed here as a "coupling matrix". $\vec{b}$ is a column vector of all the unknown Burgers vectors for which Eq. (4.21) is to be solved. $\vec{F}$ is also a column vector termed here as a forcing vector and is constructed from the left-side of Eq. (4.17). The dimension of matrix $[A]$ is N×N, and of vectors $\vec{b}$ and $\vec{F}$ is N. Any element A_{ij} of matrix $[A]$ represents the term in parenthesis on the left-side of Eq. (4.17) involving the j-th loop effect evaluated at collocation point i. Alternatively, matrix $[A]$ is populated from the stress contribution of the padded image dislocations only and the elements of vector $\vec{F}$ are associated with the real/crystalline dislocations (and the associated non-surface reflective image dislocations). The size of the linear system of equations in (4.21) is dominated by the number of padded image dislocations only, and not by the number of real/crystalline dislocations. The padded dislocations on the void surface, in combination with the reflective image dislocations in Fig. 4.4b, constructs the correction term in Eq. (4.14) to satisfy the boundary conditions at the collocation points and any point on the planar surfaces 1 and 2.

Equation (4.21) is solvable for a unique set of Burgers vectors if the matrix is non-singular. But for this problem configuration, matrix $[A]$ is singular which means that no unique set of Burgers vectors can be found as a solution. Also, no decomposition method for solving a system of linear equations is available for the current problem since matrix $[A]$ is singular. But matrix $[A]$ has marginal diagonal dominance meaning that the absolute value of the diagonal element of each row is equal, or slightly greater, than the sum of the absolutes of other elements, i.e., $Aii = \sum_j |A_{ij}|$. This feature of matrix $[A]$ directs us to try an iterative solver like the Gauss-Seidel [23] method with successive over-relaxation since diagonal

dominance of the coupling matrix ensures the solution will converge. In the current problem, Eq. (4.21) is solved using the Gauss-Seidel [23] iterative method with a Successive Over Relaxation (SOR) parameter equal to 1.35, which makes the solution convergence faster.

The Peach-Koehler force (Eq. (4.20)) is calculated in the radial direction from the void center out. A similar technique to the bi-section method for root-finding is used here to find the equilibrium point ($r = \xi_0$, see Fig. 4.5(b), where $F_r = 0$). Initially, for any angle θ, we choose a point $(r = \xi_1)$ close to the void surface and calculate the Peach-Koehler force. If $F_r(r = \xi_1) = 0$ there, then $r = \xi_1$ represents the equilibrium point. If not, then we choose another point $(r = \xi_2)$ that is halfway radially between the void surface and the external nearby free surface. From a previous work by the authors [34] [18], it is easily assumed the furthest distance of the equilibrium point from the void would be halfway from the void surface towards the planar free surface. We calculate the Peach-Koehler force there, and if $F_r(r = \xi_2) = 0$ then the equilibrium point *i*s there. If not, then we find the sign of $\omega_1 = F_r(r = \xi) \times F_r(r = \xi_2)$ The negative value of ω_1 ensures the location of the equilibrium point *i*s $\xi_1 < \xi_0 < \xi_2$. A positive value of ω_1 would indicate that the location of the equilibrium point lies outside this range, which is unlikely to happen based on the above discussion and if the first point $(r = \xi_1 \geq R)$ is chosen sufficiently close to the void surface. A verification of this is actually in the results below. Next, we compute the Peach-Koehler force, F_r at $r = \xi_3 = (\xi_1 + \xi_2)/2$. Again, compute $\omega_2 = F_r(r = \xi) \times F_r(r = \xi_3)$. If $\omega_2 = 0$, then equilibrium point *i*s $r = \xi_3$. Else if $\omega_2 < 0$ then the equilibrium point lies between $\xi_1 < \xi_0 < \xi_3$. And if $\omega_2 > 0$ then the equilibrium point lies between $\xi_3 < \xi_0 < \xi_2$. We repeat this process until we compute $|F_r(r = \xi_0)| \approx 0$. The finding of any equilibrium points is not a trivial process as it involves many iterations based on the scheme above. In each iteration, a system of N linear equations is solved in Eq. (4.21). Here, N was taken as 100. Each line of this system is based on Eq. (4.17). Equation (4.17) on its right-hand side can involve M real/crystal dislocations. Each of the M equations theoretically represents

a sum of infinite reflective image dislocations as equations (12) and (13) show. However, instead of summing an infinite number of image dislocations, 10,000 image dislocations were used in this sum. For a given angle θ, it could take up to 20 minutes to solve for an equilibrium point using a Matlab code on an average computer.

4.4 Results and Discussion

Figure 4.6 shows the stress profile due to a positive screw dislocation in a plate ignoring the effect of the cylindrical hole inside it, and Fig. 4.7 shows the resultant stress profile considering the effect of the cylindrical hole in it. As mentioned earlier, isoline levels of the contour plots in Figs. 4.2, 4.3, 4.6, and 4.7 are kept the same to track the changes due to the implementation of the boundary conditions. Figure 4.7(a) shows how the cylindrical hole surface affects the stress field σ_{xz}. Changes in the solution are clearly visible compared to Fig. 4.6(a) where the effect of the cylindrical hole is not considered. In Fig. 4.7(b), there is a verification of our proposed method. On the free surfaces 1 and 2, σ_{yz} is zero, which is a necessary boundary condition. However, σ_{yz} is not expected to be zero on every point of the cylindrical hole's surface because σ_{yz} is not equal to the traction T_z everywhere on the cylindrical hole's surface. σ_{yz} is equal to traction the T_z only on the two vertical points on the hole's surface where we find σ_{yz} is equal to zero in Fig. 4.7(b). Also, σ_{xz} is equal to the traction T_z only on two horizontal points on the hole's surface where we also find σ_{xz} is equal to zero in Fig. 4.7(a). Hence Fig. 4.7 presents a verification of our proposed numerical method.

The equilibrium points (where $F_r = 0$) for the current problem configuration are unstable (see Figs. 4.5(b) and 4.8(a)) since, at any radial location, other than the equilibrium point *i*tself, the dislocation tends to move toward the void surface or the external planar free surface. These equilibrium points divide the plate into two unstable regions (labeled regions

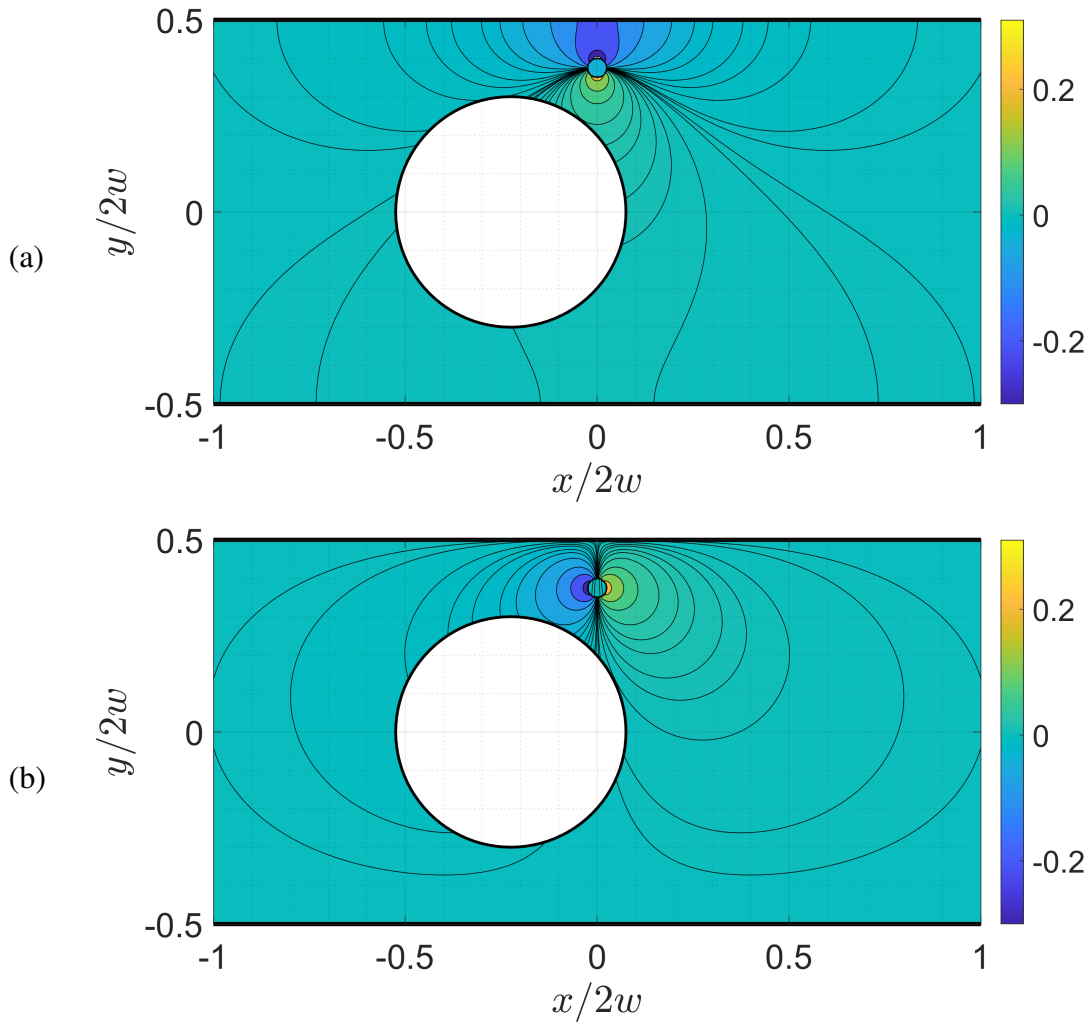

Figure 4.6: Contour plot of the stress field σ_{yz} and σ_{xz} in a plate with a hole/void but not considering its effect. (a) Contour plot for σ_{xz}/Gb. Contour plot for σ_{yz}/Gb

"1" and "2" in Fig. 4.8(b)). This figure indicates the direction of motion of the dislocation at a glance. In region 1, the direction of dislocation motion is dominated by the internal void surface (i.e., towards the void), and in region 2, it is dominated by the external nearby free surface.

It is worth emphasizing that our solution satisfies the boundary conditions on all the in-

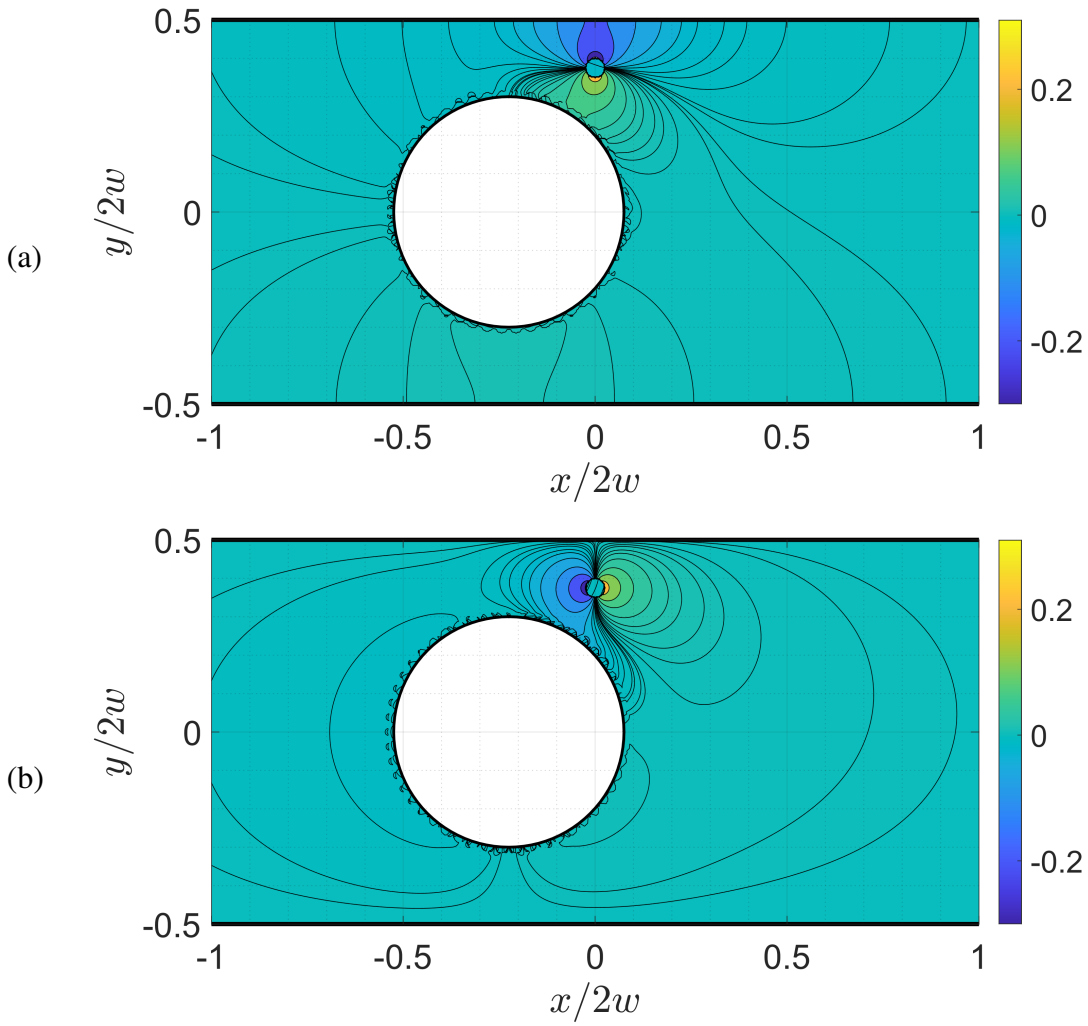

Figure 4.7: Contour plot of the stress field σ_{yz} and σ_{xz} in a plate with a hole/void considering all the boundary conditions. (a) Contour plot for σ_{xz}/Gb, (b) Contour plot for σ_{yz}/Gb.

ternal and external free surfaces. We computed a non-dimensional equilibrium distance ξ where $\xi = (\xi_0 - R)/(L-R)$ and $0 < \xi < 1$,. Since the quantity $(\xi_0 - R)/(L-R) \leq 0.5$, we can write the range of ξ for this problem configuration as $0 < \xi \leq 0.5$. Figure 4.9(a) shows the locus of ξ in the radial direction for different values of α, the ratio of plate width to void diameter. Figure 4.9(b) shows the locus of ξ in the radial direction for different values of θ, see Fig. 4.5b for the definition of angle θ. For any given angle θ, as α

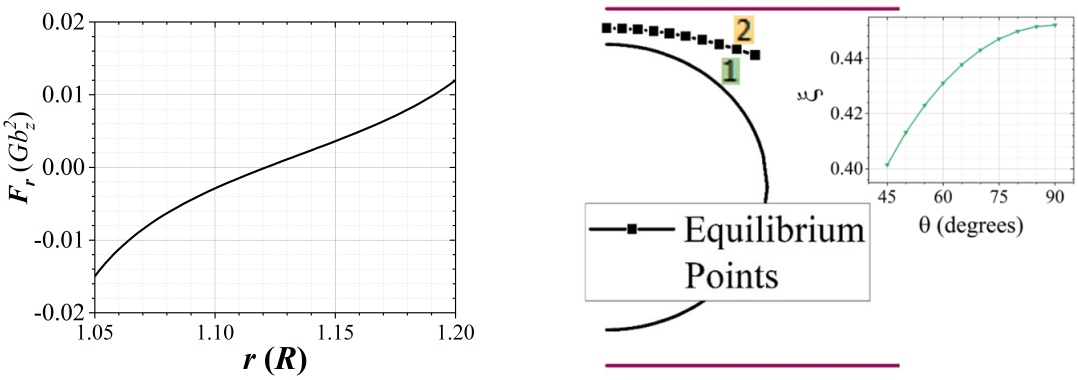

(a) (b)

Figure 4.8: Unstable equilibrium point and the unstable regions for a screw dislocation in a plate and near a void. (a) Shows the Peach-Koehler force along r for $\alpha = 1.25$ and $\theta = 80°$ (b) Equilibrium points shown here for $\alpha = 1.25$ and $45° \leq \theta \leq 90°$. Inset shows how ξ_0 is translated to the non-dimensional parameter ξ.

increases (or equivalently the width w of the plate increases for a constant R), the quantity L also increases but ξ decreases which means that the equilibrium point moves closer to the void surface (see Fig. 4.9a). For any given α, as the angle θ increases ξ increases, meaning that the equilibrium points move away from the void surface (see Fig. 4.9b). This is consistent with the previous statement because for the same α, quantity L and θ are inversely related (see Fig. 4.5(b)). Since L is high when θ is small, so for a smaller value of θ we see the equilibrium point moves closer to the void surface.

From Fig. 4.9 it is seen that the location of the equilibrium point ξ always remains between the void surface and less than halfway from the void surface and external free surface for any value of θ. This finding is consistent with the previous work of the authors [34], albeit for a different problem configuration than here. A comparison can be made in the outcomes between the current problem and the problem associated with Fig. 4.7 of the previous work [34] by the authors for $\theta = 90°$ and a very high value of α in the current configuration. Lastly, Fig. 4.10 shows the combined Figures 9a and 9b in a 3D plot. The

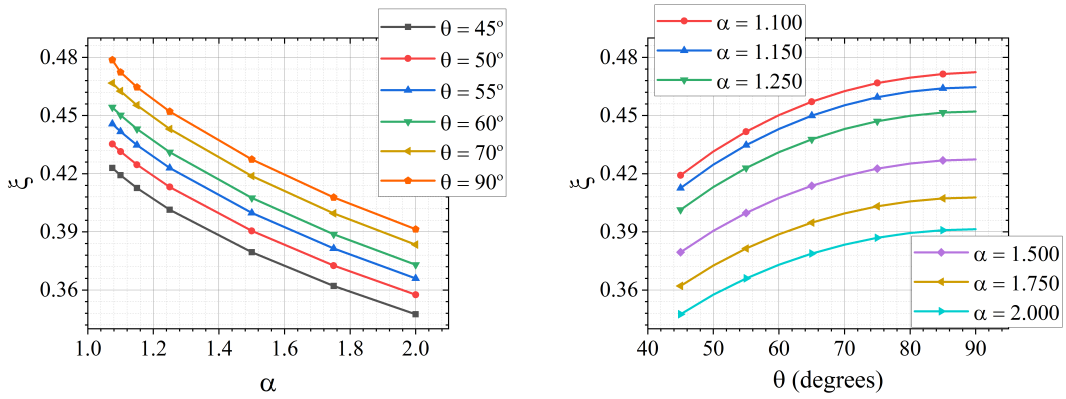

Figure 4.9: (a) Location of the equilibrium point vs the parameter α. α is the ratio of width of the plate to the diameter of the void. (b) Location of the equilibrium point vs angle θ

physical reason for the equilibrium point being closer to the void surface is that the real dislocation "sees" a smaller free surface with the curved void surface versus the planar or infinite surface (surface 1) and hence the pull towards the void is weaker since the image stresses pulling it are weaker than the planar surface image stresses.

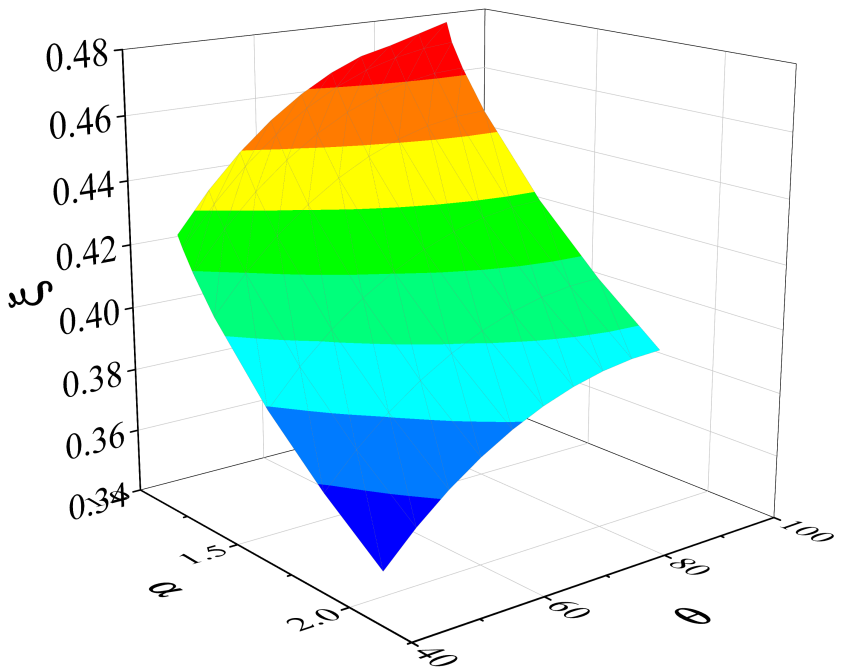

Figure 4.10: A 3D contour plot showing how the equilibrium position moves as a function of both α and θ

4.5 Conclusion

The current study presented a mathematical formulation for treating the traction-free boundary conditions of a plate with a hole/void inside it. The method is directly extendable to multiple holes or voids. The authors developed a numerical framework that combines the use of both the collocation-point method for the hole and the large array of image dislocations across the planar-free surfaces. The equilibrium points (where the Peach-Koehler force on a dislocation is zero) are unstable and always closer to the void surface. This is due to the curvature of the void versus the flatter plate surfaces resulting in weaker pull force towards the void. The results were partially verified with the authors' previous work for a limiting scenario. This method also can be extended for different shapes of void in a plate. Moreover, this method can be configured for a mode III crack inside a plate by using a collapsed ellipse for a void.

Journal reference

Siddique, A. B., & Khraishi, T. A. (2021). A holed-plate with material dislocations : Formulation and verification. Mathematics and Mechanics of Solids, 0(0), 10812865211053368. https://doi.org/10.1177/10812865211053369

Chapter 5

Static and dynamic dislocation problems near a free surface

Abstract

Simulation of dislocation dynamics enables researchers and scientists to explore the plastic behavior of crystalline materials under loading. Analytic solutions for the stress field due to a linear dislocation segment near a free surface are case-specific, e.g. dealing with either a horizontal segment or a vertical segment, and therefore hard to implement in time-dependent dislocation dynamics simulations as different dislocation segments could be differently oriented. This article presents a generalized numerical framework to find the stress field beneath a free surface due to the presence of a dislocation segment. The framework can be expanded to non-flat surfaces. Also, three-dimensional discrete dislocation dynamics simulations are performed here, which clearly show the effect of free surfaces on the flow stress of a material.

5.1 Introduction

Simulation of dislocation dynamics enables researches and scientists to explore the phenomena that happen during plastic deformation, which may not be observed in experimental work. Simulation of dislocation dynamics satisfying the physical boundary conditions in a 3D representative volume element is always a challenge.

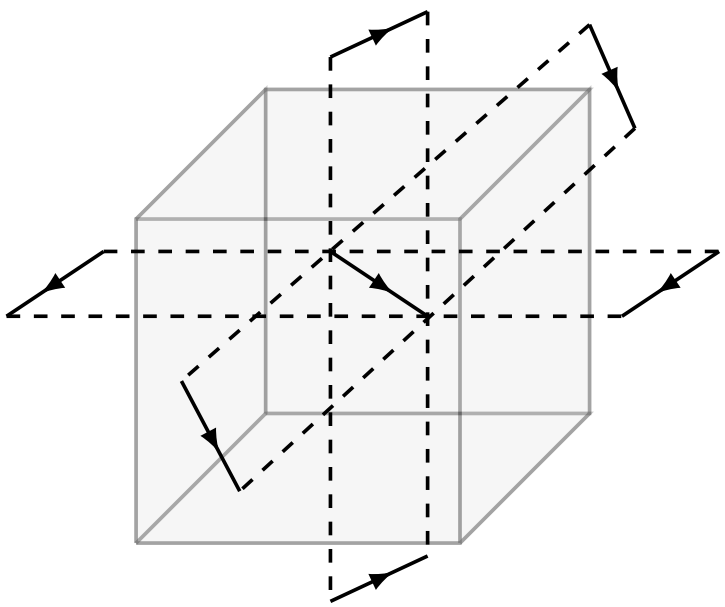

Figure 5.1: A dislocation segment in a DD computational box reflected off of the six external box surfaces

A dislocation segment causes stress in a crystalline material. Field stresses derived for an infinite medium are considered as classical problems in dislocation theory [2], [11]. The use of stress formulation derived for infinite medium needs an additional term to satisfy the physical boundary conditions in the cases of the semi-infinite and finite media. To derive/evaluate this additional correction term, researchers and scientists implemented different techniques in their work.

Yoffe [10] derived the elastic fields of a dislocation meeting a surface in an angle for an arbitrary choice of Burgers vector. Baštecká [36] formulated the field stress due to a pure edge circular dislocation loop near a free surface with Burgers vector normal to that free surface. Bacon and Groves [37], [38] showed the field displacements due to an infinitesimal dislocation loop of arbitrary shape, orientation, and Burgers vector in a semi-infinite isotropic medium. Maurissen and Capella [39], [40] derived the field stress correction terms of a dislocation segment parallel and perpendicular to a free surface in a semi-infinite elastic medium. Comninou and Dundurs [41] presented the formulations of the elastic field of an angular dislocation segment in isotropic half-space. For an anisotropic medium Lothe et al [42] derived an integral form of field stress for the case of a dislocation erminating at the free surface of an anisotropic half-space. Gosling and Willis [43] expressed the stresses due to an arbitrary dislocation in a semi-infinite medium as a line integral along the dislocation. Devincre [44] developed the expression of three-dimensional stress field for a straight dislocation segment in a global coordinate system. Also prior to that, Hirth and Lothe [11] developed the stress field of a linear dislocation segment in a segment-attached coordinate system.

Kubin et al [45] introduced the framework of 3D dislocation dynamics simulation in a finite medium. Later Canova et al [46] and Hartmaier et al [47] implemented different field correction methods in discrete dislocation dynamics simulations to incorporate the free surface effect. In a single crystal, El-Azab et al [48], [49] formulated traction and dislocation flux boundary conditions. Khraishi et al developed several methods for the treatment of traction-free boundary conditions in 3D dislocation dynamics [16], [17], [15]. In these referenced works, the dislocation field stress formulation developed in an infinite medium was augmented by image stress and surface correction terms, i.e. additional stress terms to satisfy the physical boundary conditions. In a recent article, Po et al [50] reviewed the nodal discrete dislocation methods for the investigation of plastic behavior in crystals with free surfaces.

In the works mentioned earlier [16], [17], [15], correction terms to mitigate the surface traction was developed locally and then transformed into a global coordinate system to compute the stress field due to the presence of a dislocation segment. Moreover, for each dislocation segment, the works just-mentioned required the placing of image dislocations in all six directions (across six free surfaces), see Fig. 5.1. In discrete dislocation dynamics simulations and during the evolution of dislocation segments, this reflection of image segments requires a substantial computational effort. For example, if the computational box includes 100 segments then the reflected image segments that have to be accounted for will be 600!

In this article, the authors present a generalized numerical framework to tackle traction-free boundary conditions using generally-prismatic rectangular dislocation loops padding the free surface. All the stress and correction terms are computed in the global coordinate system to save the effort of first-rank, and second rank, tensor local-to-global transformations and vice versa (as required in the case of Fig. 5.1). In the Theory section, the theoretical formulation for the problem of nullifying tractions on free surfaces is established. In the Numerical Considerations section, different numerical implementations particular to this problem are discussed. In the Results section, both static and dynamic computations are shown. The static for verification purposes against a known analytical solution involving an infinite plane, and the dynamic using dislocation dynamics simulations capable of modeling constant strain-rate loading.

5.2 Theory

A dislocation is a stress source in a crystalline material. Stresses in a field point P due to M dislocations in a medium, subject to linear elasticity, is written as,

$$\boldsymbol{\sigma}^P = \sum_i^M \boldsymbol{\sigma}^i \tag{5.1}$$

Where $\boldsymbol{\sigma}^P$ represents the total stress tensor at field point P due to stresses caused by the M dislocations and $\boldsymbol{\sigma}^i$ is the stress tensor at point P caused by dislocation i. Each $\boldsymbol{\sigma}$ is a 3×3 matrix of stress components. The field stress for a straight dislocation segment AB in an infinite medium is derived in [44] as,

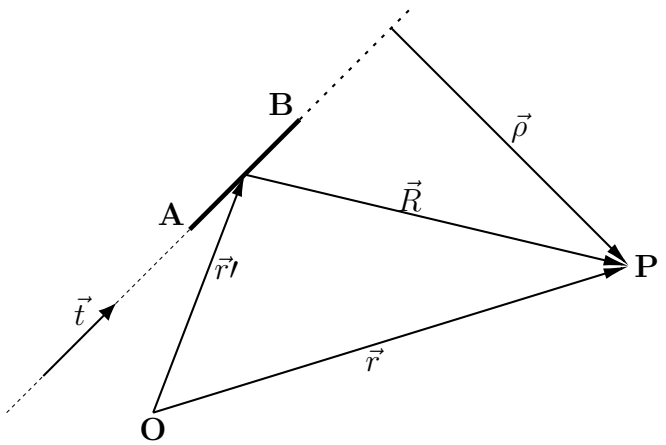

Figure 5.2: Vectors and scalars appearing in the definition of the stress component $\sigma_{\alpha\beta}$ generated by a dislocation segment AB. The stresses are evaluated at a field point P at a position vector $\vec{r}$ from the origin a of an xyz global coordinate system. $\vec{t}$ is the line sense unit vector of the dislocation segment.

$$\sigma_{\alpha\beta}^{AB} = \left(\sigma_{\alpha\beta}^{AB}\right)_{\vec{r}\prime=OB} - \left(\sigma_{\alpha\beta}^{AB}\right)_{\vec{r}\prime=OA} \tag{5.2}$$

where $\sigma_{\alpha\beta}^{AB}(\vec{r})$ is described in [44] and not reproduced here for brevity. At the free surfaces, the traction vector $\vec{t} = \sigma\vec{n}$ on each surface point must be zero which cannot be ensured from Eq. (5.2). In fact, it is violated since Eq. (5.2) was developed for an infinite medium. $\vec{n}$ is a unit vector perpendicular to the free surface and σ is the total stress tensor at the point. To meet this physical boundary condition, we need to add a correction term and rewrite eq (1) as

$$\sigma^P = \sum_i^M \sigma^i + \sigma_{corr} \tag{5.3}$$

Where, σ_{corr} is the required stress correction term to ensure zero traction on each field point of the free surface. The use of a correction term as in Eq. (5.3), as an approach to

satisfy a surface boundary condition, was used in the previously mentioned references.

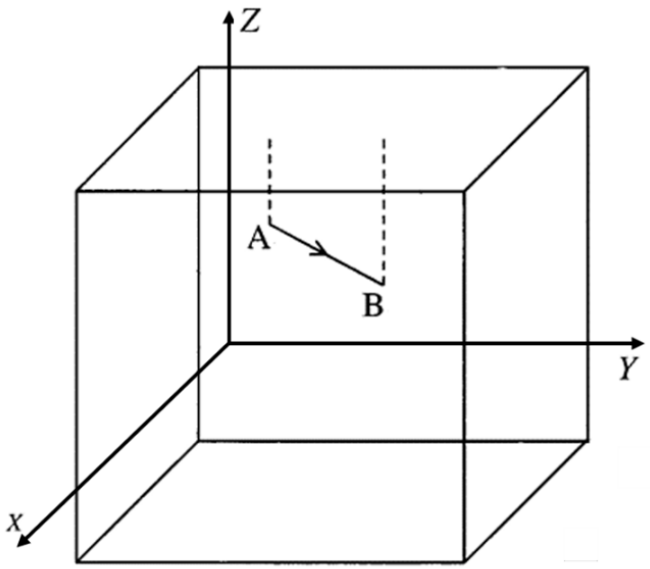

Figure 5.3: A finite Three-dimensional crystal with a linear dislocation AB in it.

Khraishi et al. [16], [17] introduced a collocation point method to derive σ_{corr}. In the collocation point method, it is sufficient to satisfy the boundary conditions at the distributed collocation points only as it is implied that an infinite number of collocation points will produce the exact analytic solution for the stress field if one existed.

In the collocation point method described in [16], [17] σ_{corr} is formulated using a local coordinate system i.e. the free surface is always considered as the local xy plane. Computed σ_{corr}in this method needs to be second-ranked tensor transformed to sum with the stress from the crystal dislocation segments computed in the global coordinate system (using [44]). Also, first-ranked tensor transformation is needed for coordinates of points (like points A and B in Fig. 5.2). In this article, we show a method to compute σ_{corr}in a global coordinate system so no further transformation is needed to compute Eq. (5.3).

For a dislocation segment inside a finite three-dimensional medium and beneath a free surface as shown in Fig. 5.3, we pad N generally-prismatic fictitious (i.e. non-crystalline) rectangular dislocation loops on the free surfaces where the collocation points are located at the center of these fictitious dislocation loops (see Fig. 5.4).

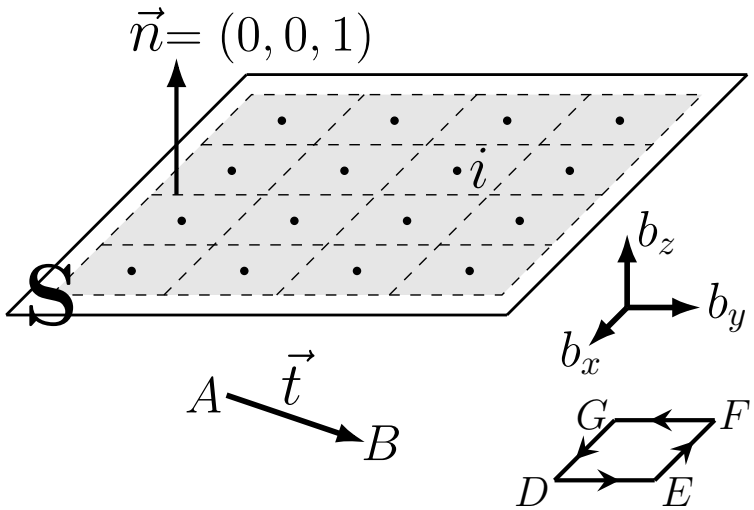

Figure 5.4: Dislocation Segment AB, with line sense vector $\vec{t}$, beneath a free surface. A mesh of rectangular elements representing generally-prismatic dislocation loops, covering area S upon which stress traction annulment is sought. Inset shows one of these loops $DEFG$ with Burgers vector components b_x, b_y and b_z. The elements' centers are the collocation points (N of them) for the problem at hand, e.g. point i in this figure is a collocation point.

As we compute the traction $\vec{T} = \sigma\vec{n}$ for the surface points, we find that the condition $\sigma_{xz} = \sigma_{yz} = \sigma_{zz} = 0$ must exist to ensure zero traction. Here, these three stress components are annulled on a set of N collocation points representing the generally-prismatic loops

padding the surface. Mathematically, the problem is formulated as follows:

$$\begin{aligned}
\sum_{j=1}^{N} \sigma_{xz}^{j\to i} &= -\sigma_{xz}^{AB\to i}, \qquad i = 1,2,\ldots N \\
\sum_{j=1}^{N} \sigma_{yz}^{j\to i} &= -\sigma_{yz}^{AB\to i}, \qquad i = 1,2,\ldots N \\
\sum_{j=1}^{N} \sigma_{zz}^{j\to i} &= -\sigma_{zz}^{AB\to i}, \qquad i = 1,2,\ldots N
\end{aligned} \tag{5.4}$$

where $\sigma_{\alpha\beta}^{j\to i}$ is the $\alpha\beta$ stress component of loop j evaluated or calculated at collocation point i (which is the center of Loop i). Also, $\sigma_{\alpha\beta}^{AB\to i}$ is the $\alpha\beta$ stress of segment AB evaluated at point i. We compute stress at any field point for any generally-prismatic dislocation loop in the global coordinate system as follows,

$$\sigma^{loop} = \sigma^{DE} + \sigma^{EF} + \sigma^{FG} + \sigma^{GD} \tag{5.5}$$

An examination of Eq. (5.2) shows that it is linear in the Burgers vector components b_x, b_y and b_z. This allows the following to be inserted into Eq. (5.4):

$$\sigma_{\alpha\beta}^{j\to i}(x,y,z) = K_{x\alpha\beta}^{j\to i}(x,y,z)\, b_x^j + K_{y\alpha\beta}^{j\to i}(x,y,z)\, b_y^j + K_{z\alpha\beta}^{j\to i}(x,y,z)\, b_z^j \tag{5.6}$$

where $\sigma_{\alpha\beta}^{j\to i}(x,y,z)$ is the $\alpha\beta$ stress component for Loop j (or dislocation j in general) at collocation point i, b_x^j is the x-component of the Burgers vector for the generally-prismatic dislocation loop, and $K_{x\alpha\beta}^{j\to j}(x,y,z)$ is the kernel term associated with x-component of the Burgers vector and evaluated at collocation point i. The kernels $K_{x\alpha\beta}$, $K_{y\alpha\beta}$ and $K_{z\alpha\beta}$ have been derived from the work of Devincre [44] and provided all of them for the first time in Appendix A. When inserting the last equation in the equation just before it, the following system of equations ensues:

$$\begin{aligned}
\sum_{j=1}^{N} b_x^j K_{xxz}^{j\to i} + b_y^j K_{yxz}^{j\to i} + b_z^j K_{zxz}^{j\to i} &= -\sigma_{xz}^{AB\to i}, \quad i = 1,2,\ldots N \\
\sum_{j=1}^{N} b_x^j K_{xyz}^{j\to i} + b_y^j K_{yyz}^{j\to i} + b_z^j K_{zyz}^{j\to i} &= -\sigma_{yz}^{AB\to i}, \quad i = 1,2,\ldots N \\
\sum_{j=1}^{N} b_x^j K_{xzz}^{j\to i} + b_y^j K_{yzz}^{j\to i} + b_z^j K_{zzz}^{j\to i} &= -\sigma_{zz}^{AB\to i}, \quad i = 1,2,\ldots N
\end{aligned} \tag{5.7}$$

The above system represents a system of $3N$ equations, which is more time consuming to solve than the previous system of N equations when an image segment was used in the last method [16]. The unknowns in this system, Eq. (5.7), are the Burgers vector components of the N loops. The last system of equations can be written in expanded form to show more clearly the ensuing kernel matrix:

$$\begin{bmatrix} K_{xxz}^{1\to1} & K_{yxz}^{1\to1} & K_{zxz}^{1\to1} & & K_{xxz}^{N\to1} & K_{yxz}^{N\to1} & K_{zxz}^{N\to1} \\ K_{xyz}^{1\to1} & K_{yyz}^{1\to1} & K_{zyz}^{1\to1} & \cdots & K_{xyz}^{N\to1} & K_{yyz}^{N\to1} & K_{zyz}^{N\to1} \\ K_{xzz}^{1\to1} & K_{yzz}^{1\to1} & K_{zzz}^{1\to1} & & K_{xzz}^{N\to1} & K_{yzz}^{N\to1} & K_{zzz}^{N\to1} \\ & \vdots & & \ddots & & \vdots & \\ K_{xxz}^{1\to N} & K_{yxz}^{1\to N} & K_{zxz}^{1\to N} & & K_{xxz}^{N\to N} & K_{yxz}^{N\to N} & K_{zxz}^{N\to N} \\ K_{xyz}^{1\to N} & K_{yyz}^{1\to N} & K_{zyz}^{1\to N} & \cdots & K_{xyz}^{N\to N} & K_{yyz}^{N\to N} & K_{zyz}^{N\to N} \\ K_{xzz}^{1\to N} & K_{yzz}^{1\to N} & K_{zzz}^{1\to N} & & K_{xzz}^{N\to N} & K_{yzz}^{N\to N} & K_{zzz}^{N\to N} \end{bmatrix} \begin{Bmatrix} b_x^1 \\ b_y^1 \\ b_z^1 \\ \vdots \\ b_x^N \\ b_y^N \\ b_z^N \end{Bmatrix} = \begin{Bmatrix} \sigma_{xz}^{AB\to1} \\ \sigma_{yz}^{AB\to1} \\ \sigma_{zz}^{AB\to1} \\ \vdots \\ \sigma_{xz}^{AB\to N} \\ \sigma_{yz}^{AB\to N} \\ \sigma_{zz}^{AB\to N} \end{Bmatrix} \tag{5.8}$$

Here the size of the kernel matrix is $3N \times 3N$ which equals $9N^2$. However and from dislocation theory ([16], [17]), the kernels for σ_{xz} and σ_{yz} associated with the b_z component of the Burgers vector are zero in the plane of the loop, i.e. the S area in Fig. 5.4 where $z = 0$. Moreover, from the same theory, the kernels for σ_{zz} associated with the b_x and b_y components of the Burgers vector are also zero. Also, any non-zero kernels on the surface where $z = 0$ can be written in simplified forms to speed up computations (see [16] and [17]). All of this means that the last system of equations can be written alternatively as:

$$\begin{aligned} &\sum_{j=1}^{N} b_x^j K_{xxz}^{j\to i} + b_y^j K_{yxz}^{j\to i} = -\sigma_{xz}^{AB\to i}, \quad i = 1,2,\ldots N \\ &\sum_{j=1}^{N} b_x^j K_{xyz}^{j\to i} + b_y^j K_{yyz}^{j\to i} = -\sigma_{yz}^{AB\to i}, \quad i = 1,2,\ldots N \\ &\sum_{j=1}^{N} b_z^j K_{zzz}^{j\to i} = -\sigma_{zz}^{AB\to i}, \quad i = 1,2,\ldots N \end{aligned} \tag{5.9}$$

The above represents two sets of decoupled systems of equations; one is 2N equations and the other is N equations. The size of the kernel matrices in these two systems is $2N \times 2N$ and $N \times N$, respectively, which equals $5N^2$. These two systems can be solved much faster

than the system of 3N linear equations (e.g. (8)). This can only be achieved by recognizing the decoupling between the prismatic and the shear components of the Burgers vectors in the plane of the dislocation loop i.e. the prismatic component of the Burgers vector b_z only has a non-zero normal stress σ_{zz} in the loop plane, and the shear components of the Burgers vector b_x and b_y only have a non-zero shearing stress σ_{xz} and σ_{yz} in the loop plane. Based on the above, Eq. (5.9) can be written in expanded form as:

$$\begin{bmatrix} K_{xxz}^{1\to1} & K_{yxz}^{1\to1} & & K_{xxz}^{N\to1} & K_{yxz}^{N\to1} \\ K_{xyz}^{1\to1} & K_{yyz}^{1\to1} & \cdots & K_{xyz}^{N\to1} & K_{yyz}^{N\to1} \\ \vdots & \vdots & & \ddots & \vdots \\ K_{xxz}^{1\to N} & K_{yxz}^{1\to N} & & K_{xxz}^{N\to N} & K_{yxz}^{N\to N} \\ K_{xyz}^{1\to N} & K_{yyz}^{1\to N} & \cdots & K_{xyz}^{N\to N} & K_{yyz}^{N\to N} \end{bmatrix} \begin{Bmatrix} b_x^1 \\ b_y^1 \\ \vdots \\ b_x^N \\ b_y^N \end{Bmatrix} = \begin{Bmatrix} \sigma_{xz}^{AB\to1} \\ \sigma_{yz}^{AB\to1} \\ \vdots \\ \sigma_{xz}^{AB\to N} \\ \sigma_{yz}^{AB\to N} \end{Bmatrix} \tag{5.10}$$

and

$$\begin{bmatrix} K_{zzz}^{1\to1} & & K_{zzz}^{N\to1} \\ \vdots & \ddots & \vdots \\ K_{zzz}^{1\to N} & & K_{zzz}^{N\to N} \end{bmatrix} \begin{Bmatrix} b_z^1 \\ \vdots \\ b_z^N \end{Bmatrix} = \begin{Bmatrix} \sigma_{zz}^{AB\to1} \\ \vdots \\ \sigma_{zz}^{AB\to N} \end{Bmatrix} \tag{5.11}$$

Once the Burgers vectors have been determined for all surface loops, one can evaluate the stress field at any point in the crystal. At field point P, the stresses can be computed as

$$\sigma_{\alpha\beta}^{P} = \sum_{i}^{M} \sigma_{\alpha\beta}^{i} + \sum_{j}^{N} \sigma_{\alpha\beta}^{j\to P} \tag{5.12}$$

Where, $\sigma_{\alpha\beta}^{i}$ is the stress due to real dislocation segments in the crystal and $\sigma_{\alpha\beta}^{j\to P}$ is the stress contribution by the generally-prismatic dislocation loops j at point P.

5.3 Numerical Considerations

Equations (5.10) and (5.11) describe two systems of linear equations where the left-hand matrix is termed the kernel matrix $[K]$. Elements of the Kernel matrix $[K]$ couple the Burgers vectors and the right-hand side vector, which acts as a forcing vector [F]. The Kernel

matrix is associated with the fictitious surface loops only, whereas the forcing vector is associated with real crystal dislocations or dislocation segments. The dimension of the kernel matrix depends on the areal loop density on a surface, and the elements of the kernel matrix are computed only taking into account the surface loops and not the dislocations inside the crystal. Elements of the forcing vector are computed at the collocation points, by only taking into account the dislocations or the dislocation segments inside the crystal. So, for the cases where more dislocations or dislocation segments are present, the Kernel matrices do not change, but the forcing vector does. In a simulation of dislocation dynamics, the Kernel matrix needs to be computed only once at the start of the simulation, but the forcing vector needs to be updated with every time step. The Burgers vectors of the fictitious surface loops thus change with every iteration depending on the positions of the dislocations or the dislocation segments relative to the surface. In a three-dimensional crystal volume, it is a must to ensure zero traction on all the free surfaces. For example, in a regular cube, traction-free boundary conditions need to be established on all the six cube surfaces. The stress at any material point is computed by summing the stresses from the dislocations in the crystal and all the fictitious loops from the six surfaces. For the uniform surface mesh in Fig. 5.4, the stress from loop i will dominate the state-of-stress computed at collocation point i, which makes the Kernel matrix $[K]$ diagonally dominant (i.e. $|k_{ii} \geq \sum_{j \neq i} |k_{ij}|$). Since matrix $[K]$ is diagonally dominant, it is possible to utilize an iterative method to solve the ensuing systems of linear equations (Eqs. (5.10) and (5.11)). Here a Gauss-Seidel iterative method [23] was adopted in conjunction with a relaxation parameter λ (to hasten the computations) equal to 1.35. This method is faster than the regular Gaussian elimination or any decomposition techniques [23]. For large matrices, any decomposition technique is complex and computationally expensive.

Moreover, for a curved dislocation, we divide it into linear segments and calculate the forcing vector using Eq. (5.2) for each segment. For multiple segments, their contribution is added together into the right-hand side of Eqs. (5.10) and (5.11). This discretization

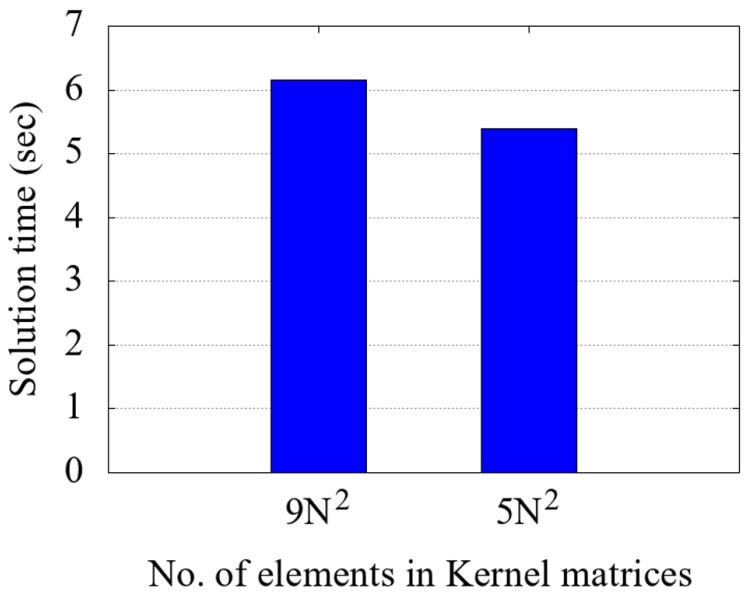

Figure 5.5: Computation time for equation (44) versus Eqs. (5.10) and (5.11). The $9N^2$ bar represents the time to solve equation (8) and the $5N^2$ bar represents the time to solve both Eqs. (5.10) and (5.11).

of the dislocation is still able to capture the correct physics of the problem. Again, this method can be readily implemented into the dislocation dynamics code by Khraishi et al. [16] and [17] and by Zbib et al. [51].

Figure 5.5 shows the time savings in solving the linear system of equations (8) versus the two systems of Eqs. (5.10) and (5.11). The figure shows a significant time improvement of approximately 14% for one surface mesh of 2500 (50×50) loops in one iteration. This time improvement is significant because, in a dislocation dynamics simulation, a hefty amount of time is saved over many time steps.

As a summary, to implement the above method, the following steps need to be executed

1. Create the surface mesh, e.g. pad the rectangular loops on the free surfaces and determine the collocation points.

2. Calculate the $[K]$ matrix using the equations presented in Appendix A.

3. Find the forcing vector $[F]$ using Eq. (5.2), adding contribution from as many existing segments

4. Solve Eqs. (5.10) and (5.11) to find the unknown Burgers vectors of the generally-prismatic loops on the free surfaces.

5. Compute stresses at any field point using Eq. (5.12)

5.4 Results

First, the current method is verified for the case of a horizontal subsurface linear segment AB parallel to the surface, see Fig. 5.6, as this case has an analytical solution [39]. The dimensions of the free surface are $20,000b \times 20,000b$, where b is the magnitude of the Burgers vector $\vec{b}$. The segment is located at a z-depth of 1,000b. Segment AB has a length L=100b. The coordinates for A and B are exactly (100b,0,0) and (0,0,0), respectively. The dislocation segment is placed at the middle of the finite volume so that the numerical solution is comparable to the analytical solution. The Burgers vector of the segment is set to $(1/\sqrt{3}, 1/\sqrt{3}, 1/\sqrt{3})$ for simplicity and Poisson's ratio $\nu = 0.383$. The stress field along a line parallel to the x-axis (y=0), with a z-depth of 400b from the free surface, was computed.

Figure 5.7 shows a comparison between the analytical solution by Maurissen and Capella [39] and the numerical solution from this work for an increasing number of surface loops. We see a gradual improvement in the numerical solution from, Fig. 5.7(a) to Fig. 5.7(f), as the number of loops or collocation points increases. We also observe that the numerical solution stabilizes after a certain number of surface loops (about 40×40), which can be explained via the Saint-Venant's principle. Saint-Venant's principle states that agreement

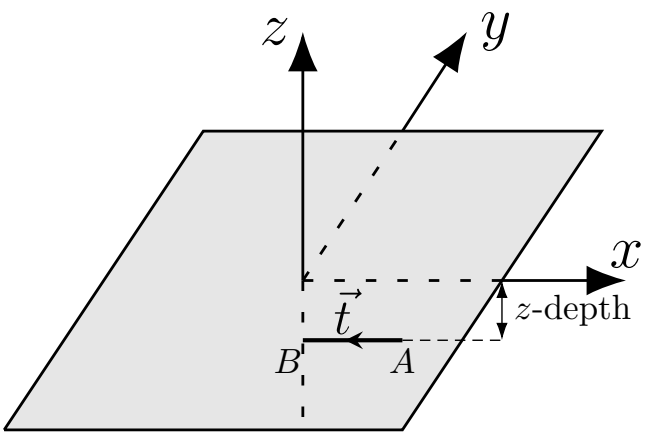

Figure 5.6: A Horizontal subsurface dislocation. Dislocation $\overrightarrow{AB}$ below a free surface at a depth of $1000b$ is shown. $\vec{t}$ represents the direction of dislocation $\overrightarrow{AB}$.

between an exact solution and an approximate one, but equipollent, at a boundary will be achieved for field points that lie more than a 'characteristic' distance away from the boundary. The characteristic distance, in this case, is the average separation distance between collocation points where the boundary condition is enforced (i.e. where the problem is solved). As we increase the surface loops, the characteristic distance becomes smaller, and the numerical solution has more matching to the analytical solution. Therefore, for field points closer to the surface than the characteristic length, the solution is not accurate and may exhibit oscillatory behavior with a wavelength equal to the characteristic length. It is worth mentioning here that although the solution might be oscillatory in this case, it still oscillates about a mean (obtained using least-squares curve fitting, for example) equal to the correct solution.

In the case of 3D discrete dynamics simulations, the dislocation segments are not always below the center of the free surfaces as their position evolves over time. In this case, the analytical solution in [39] is not expected to match the results of the numerical method presented here. To illustrate this point, let's consider a sub-surface segment near the edge

of a free surface as shown in Fig. 5.8(a). In this case, the analytical solution (Fig. 5.8(b)) does not match the numerical solution which is the proper solution in this case.

In addition to above static computations, we incorporated the current numerical method into the dislocation dynamics (DD) code by Zbib et al. [51] and Khraishi et al. [16], [17]. From classical dislocation theory, the stress field of a dislocation can be calculated accurately beyond its core distance of approximately $5b$ [52]. With this limit from elasticity theory, the Peach-Koehler force on a sub-surface segment cannot be determined within a core distance, or depth, from the surface. This is in harmony with other DD calculations as the overlapping of a subsurface dislocation segment with the core of a surface dislocation loop could trigger numerical problems. This is not a serious limitation by any means because the force acting to pull the segment towards the surface at these small depths is tremendously high and causes rapid vanishing of such segments into the surface. Moreover, since the plastic strain calculation from the computational cell is homogenized over the cell's volume, any inaccuracies in quantifying the motion of dislocation segments (e.g. occurring from not capturing image stresses, i.e. stress correction terms, accurately in the immediate vicinity of the free surface) will have practically no appreciable impact on such calculation.

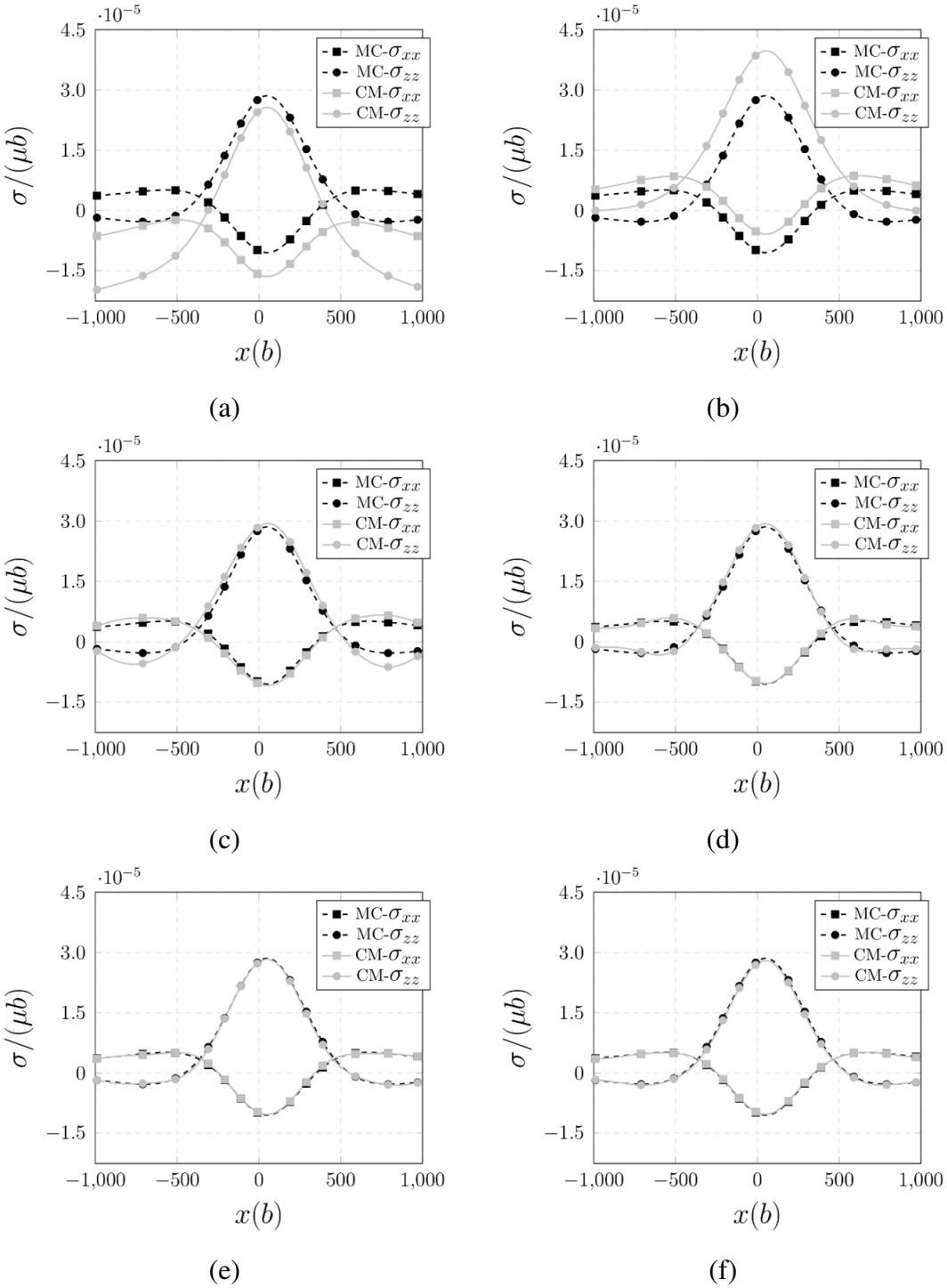

Figure 5.7: Stress field comparison with the analytical solution in reference [39] for an increasing number of surface loops. (a) Number of surface loops 5×5, (b) Number of surface loops 10×10, (c) Number of surface loops 20×20, (d) Number of surface loops 30×30, (e) Number of surface loops 40×40 and (f) Number of surface loops 50×50

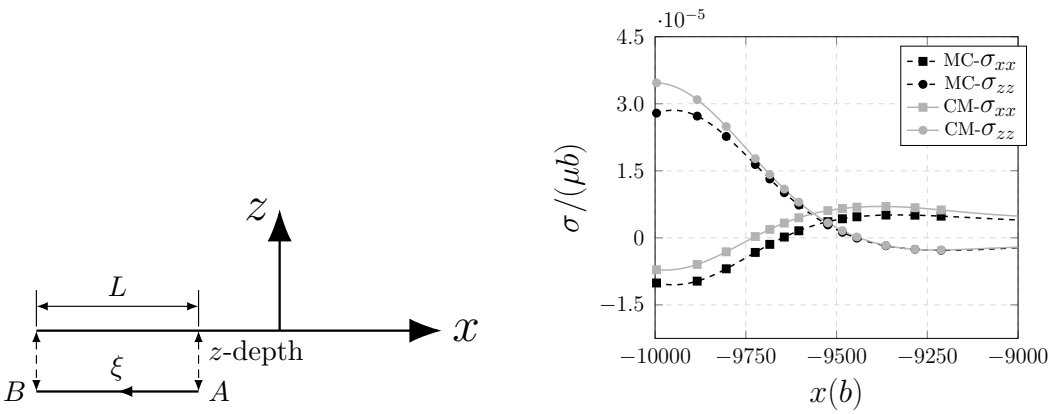

(a) (b)

Figure 5.8: The depth of the segment and the field points as above. (a) A sub-surface segment AB at the edge of a free surface. The segment is directly below the x-axis. (b) Stress field solution.

Here, we simulate a constant strain-rate experiment using a 3D crystal made of an isotropic material with dimensions of $10,000b \times 10,000b \times 10,000b$. Here, density $= 2,710$kg/m^3, Poisson's ratio $\nu = 0.33$, and the dislocation mobility equals 1000 $1/(Pa \cdot s)$. We place a Frank-Read source in the middle of the crystal along the x-axis with end nodal points coordinates equal to (-2000b,0,0) and (2000b,0,0) and a Burgers vector equal to (0,1,0) and with an applied strain-rate of $10s^{-1}$.

Figure 5.9 shows the effect of surface treatment on the stress-strain diagram obtained from simulations for different surface loop densities. For the case of no surface loops, i.e. no proper treatment of the traction-free surface condition, the stress-strain diagram is higher in values than any case of surface loops. For this diagram, as the Frank-Read (FR) source starts bowing it does so in a typical elastic fashion. Once the bowing reaches a critical stage (or size), further applied strain causes plasticity in the crystal. It takes multiple bows or looping by the source before the flow stress level basically stabilizes and hence the relatively flat plastic regime. For the case of surface loops, the loops actually cause the FR source to bow critically earlier than before, i.e. at an earlier applied strain amount, as the

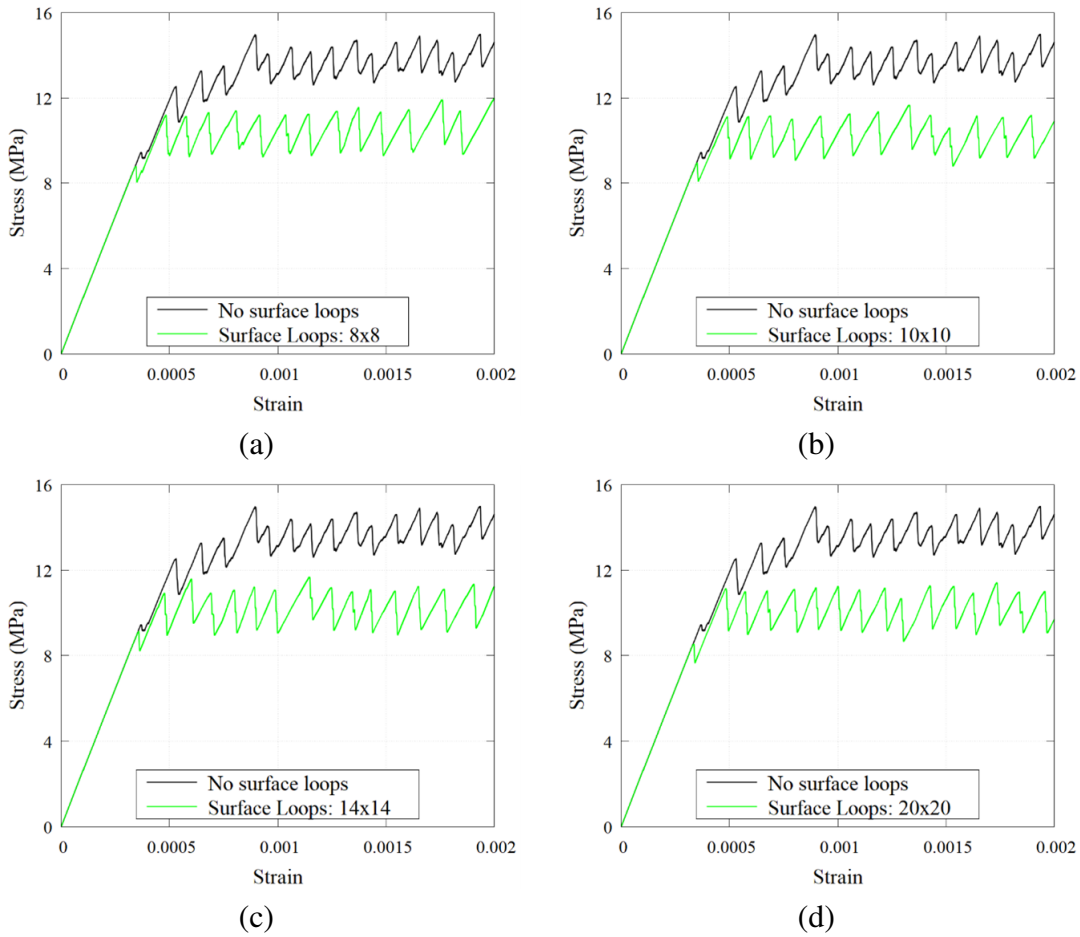

Figure 5.9: Simulations of a constant strain-rate loading experiment, i.e. stress versus strain, for a different number of surface loops. (a) Number of surface loops 8×8, (b) Number of surface loops 10×10, (c) Number of surface loops 14×14 and (d) Number of surface loops 20×20.

stress needed to cause this flowing is reduced thanks to a pulling force onto the dislocation coming from the surface loops. This pulling force accelerates the movement of the bowed source as well as the vanishing of the dislocation into the surface.

For this particular problem setup, there is a difference of about 40% between the two cases (loops versus no loops). This percent difference will change for different problems. For example, the image stress effect is expected to be lower for problems involving a lower

external surface area-to-volume ratio for the computational domain. This percentage will also change with the exact initial position of the dislocation source with respect to the interior of the computational domain (i.e. whether the source is initially close or far away from the free surfaces). See the discussions in [16] and [17].

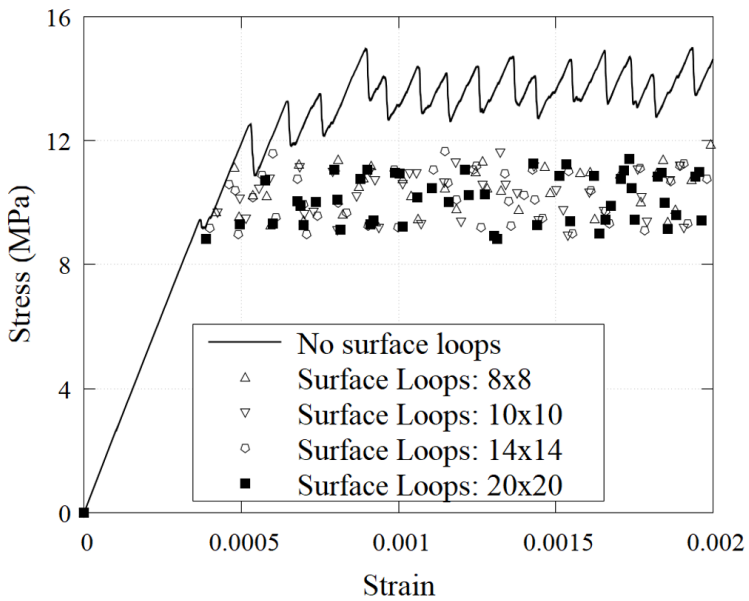

Figure 5.10: Stress-strain diagrams from dislocation dynamics simulations for one operational Frank-Read source in a cubic cell. The solid black line with a square symbol corresponds to no treatment of the traction free boundary condition, and the other lines correspond to an external surface loop density of 8×8, 10×10, 14×14 and 20×20.

In Fig. 5.10 we have superimposed all the stress-strain diagrams to accentuate the effect of surface loop density over the plastic behavior of the material. We observe no significant difference in the average stress-strain pattern for the different surface loop density, i.e. they all exhibit the same flow stress and flat plastic region on-average. This result allows the use of lower surface loop density to save significant computational time.

5.5 Conclusion

The current study has presented an efficient mathematical formulation for treating the traction-free boundary condition of a finite three-dimensional crystal. A numerical framework was developed to implement the theory in dislocation dynamics simulation. The method was implemented for a mesh of rectangular/square surface dislocation loops for both the static and dynamic cases. The DD simulations showed that incorporating the image stresses results into a different flow stress for the crystal (a significant difference in this case). The simulations also showed that they are not sensitive to the areal mesh density. This present method can be extended to other regular polygonal surface loops. Moreover, it could be extended to adaptive surface meshing on planar surfaces or even be generalized to treat non-planar free surfaces. Future works are planned to address the last two statements.

Journal reference

Siddique, A. B., & Khraishi, T. A. (2020). Numerical methodology for treating static and dynamic dislocation problems near a free surface. Journal of Physics Communications, 4(5). https://doi.org/10.1088/2399-6528/ab8ff9

Chapter 6

A mesh-independent brute-force approach

Abstract

Simulation of dislocation dynamics opens the opportunity for researchers and scientists to observe in-depth many plastic deformation phenomena. In 2D or 3D media, modeling of physical boundary conditions accurately is one of the keys to the success of dislocation dynamics (DD) simulations. The scope of analytical solutions is restricted and applies to specific configurations only. But in dynamics simulations, the dislocations' shape and orientation change over time thus limiting the use of analytical solutions. The authors of this article present a mesh-based generalized numerical approach based on the collocation point method. The method is applicable to any number of dislocations of any shape/orientation and to different computational domain shapes. Several verifications of the method are provided and successful implementation of the method in 3D DD simulations have been incorporated. Also, the effect of free surfaces on the Peach-Koehler force has been computed. Lastly, the effect of free surfaces on the flow stress of the material has

been studied. The results clearly showed a higher force with increased closeness to the free surface and with increased dislocation segment length. The simulations' results also show a softening effect on the flow stress results due to the effect of the free surfaces.

Keywords: free surfaces, dislocation theory, dislocation dynamics, Peach-Koehler force

6.1 Introduction

The dislocation is a type of defect and a source of stress in crystalline materials. Dislocation theory explains plastic deformation in a material. The stress field solution in an infinite medium due to dislocation is a fundamental problem of linear elastoplasticity [2] [11]. Eshelby and Stroh [6] extended this stress field solution in the case of a semi-infinite medium by adding a correction term. The correction term is derived by introducing image dislocations to treat the boundary condition of the free surface, which is analogous to the electrostatic problem of a line charge in a medium of non-homogeneous dielectric constant [25]. To derive this correction term for different boundary conditions, there have been many methods developed by researchers in the literature.

The earliest work dates back to 1961 by [10]. In this work, the problem of a terminating dislocation at a free surface was considered. Here, the dislocation was straight with any angle of incident or Burgers vector. In the case of a dislocation loop below a zero-traction surface, [36] found the stress solution in the case of a perpendicular Burgers vector to the surface. Later, [37] [38] derived the displacement field solution for an infinitesimal dislocation loop of arbitrary Burgers vector and orientation, and in a half-space, which can be extended to find the elastic fields of a finite dislocation loop. For a linear dislocation segment perpendicular and parallel to a free surface, [39] [40] derived the correction term in an isotropic medium that was half-infinite. Comninou and Dundurs [41] derived the

elastic field for an angular dislocation in a half-medium. This solution can be extended for an angular dislocation ending at the free surface in conjunction with the solution presented by [10]. In the case of a dislocation terminating at the free surface of a half-space, [42] derived an integral form for the field stress in an anisotropic medium. Using a line integral tracing the dislocation, [43] determined the stress solution for a dislocation in a half-medium. For a linear dislocation segment in an isotropic material, [44] found the stress field using a global coordinate system. Before that, [11] found the same stress field but using a coordinate system which was fixed to the dislocation segment.

Some of these developments enabled researchers to simulate dislocation dynamics in 2D and 3D space. Dislocation dynamics (DD) simulations brought to light many phenomena during plastic deformation, which are difficult, or sometimes impossible, to observe during real experiments. For three-dimensional dislocation simulations, the problem of dislocation interaction with surfaces or boundaries is always challenging. Nowadays, DD simulations are considered a valuable tool for plasticity research.

The first group to model three-dimensional dislocation motion and interaction in a simulation box was [45]. The effects of free surfaces were addressed using field correction methods in dislocation dynamics [46] [47]. Dislocation flux and traction boundary conditions were developed by [48] [49]. An image stress tensor to capture the effect of free surfaces was used by [53]. The effect of free surfaces on void strengthening was studied by [54]. Jing et al. [55] also studied the effect of voids on dislocation motion. Dislocation theory and molecular dynamics were used by [56] for sub-surface dislocation loops. Lastly, the development of methods to treat zero-traction boundaries for employment in three-dimensional dislocation simulations were presented by [15] [16] [17]. In the last works by [15] [16] [17], the developed methods revolved around a combination of image stresses and additional surface terms to correct for the proper physical boundary conditions. The corrections were needed since the employed dislocation stress fields in the

simulations were for an infinite domain, whereas the actual computation was done in a finite domain.

In the references indicated earlier [15] [16] [17], correction terms to satisfy the traction-free surfaces were generated for dislocation segments using a surface-attached coordinate systems. They were then transformed to a global coordinate system in order to calculate the stress evolution problem. More recent treatments for the effect of free surfaces has been provided by [18] for a flat surface in 3D space and for a curved one in 2D space [34].

In the proposed method for this article, all the stresses caused by the real and image dislocations/correction terms are calculated using a global coordinate system such that no first-rank or second-rank tensor transformations are required. Moreover, unlike previous collocation-point methods by [15] [16] [17] discussed above, the current method can utilize a structured or unstructured mesh on the free surface with any mesh element type (rectangular, triangular, etc.). This is for the purposes of satisfying zero traction condition on the free surface. The triangular mesh can, for example, save on computational time (see below). Below, the development of the correction terms is performed in the Theory section. Then the numerical model is established, along with any considerations, in the Numerical Considerations section. Lastly, dynamic and static dislocation problems are presented in the Results section. The static case verifies the solution against a known analytical result for a simple case. The dynamic case implements the method in a 3D dislocation dynamics simulation code that can generate a stress-strain curve.

6.2 Theory

A dislocation inside a crystalline material causes stresses in it. Stresses at any field point P due a linear dislocation segment AB in an unbounded space or medium was presented

by [44] as,

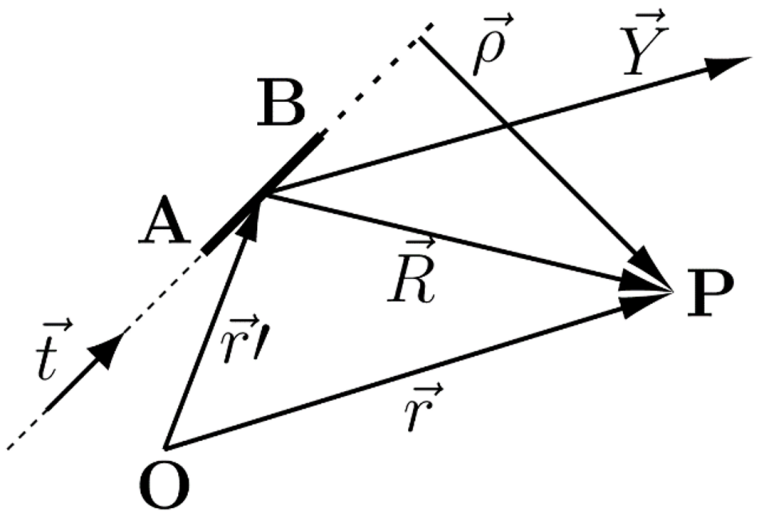

Figure 6.1: The figure defines the quantities used in calculating the $\sigma_{\alpha\beta}$ stress component due to a linear dislocation segment labeled AB. The vector $\vec{r}$ represents the position vector of an arbitrary field point P. The point O is the origin of a generally-situated global Cartesian coordinate system (*xyz*-system). The line sense vector for segment AB is denoted by the vector $\vec{t}$.

$$\sigma_{\alpha\beta}^{AB} = \left(\sigma_{\alpha\beta}^{AB}\right)_{\vec{r}\prime=OB} - \left(\sigma_{\alpha\beta}^{AB}\right)_{\vec{r}\prime=OA} \tag{6.1}$$

and $\sigma_{\alpha\beta}^{AB\vec{r}}$ is described in [44].

$$\begin{aligned}\sigma_{\alpha\beta}^{AB}(\vec{r}) = &\frac{\mu}{\pi Y^2}\left[\left[\vec{b}\vec{Y}\vec{t}\right] - \frac{1}{(1-\nu)}\left[\vec{b}\vec{t}\vec{Y}\right]^{s}_{\alpha\beta}\right. \\ &\left. - \frac{\left(\vec{b},\vec{Y},\vec{t}\right)}{2(1-\nu)}\left[\delta_{\alpha\beta} + t_\alpha t_\beta + \frac{2}{Y^2}\left[\rho_\alpha Y_\beta + Y_\alpha \rho_\beta + \frac{L}{R}Y_\alpha Y_\beta\right]\right]\right]\end{aligned} \tag{6.2}$$

where the material is isotropic with a modulus for shear μ and a Poisson ratio indicated by ν. In addition,

$$\begin{aligned}\vec{r} &= \vec{r} - \vec{r}' \\ L &= \vec{r} \cdot \vec{t} \\ \vec{\rho} &= \vec{r} - L\vec{t} \\ \vec{Y} &= \vec{r} + R\vec{t}\end{aligned} \tag{6.3}$$

Here, $(\vec{a}, \vec{b}, \vec{c})$ is called a scalar triple product and is given by:

$$(\vec{a}, \vec{b}, \vec{c}) = (\vec{a} \times \vec{b}) \cdot \vec{c} \tag{6.4}$$

and $\left[\vec{a}\vec{b}\vec{c}\right]^s_{\alpha\beta}$ is called symmetric tensor operator and is given by:

$$\left[\vec{a}\vec{b}\vec{c}\right]^s_{\alpha\beta} = \frac{1}{2}\left(\left(\vec{a} \times \vec{b}\right)_\alpha c_\beta + \left(\vec{a} \times \vec{b}\right)_\beta c_\alpha\right) \tag{6.5}$$

The total stress $\boldsymbol{\sigma}^P$, in linear elasticity, at P (any field point) due to a number of dislocations γ can be written as,

$$\boldsymbol{\sigma}^P = \sum_l^\gamma \boldsymbol{\sigma}^{l \to P} \tag{6.6}$$

Here, the stress of dislocation l is given by $\boldsymbol{\sigma}^{l \to P}$. The stress second-rank tensor is a 3×3 matrix, i.e. it has 9 components of stress.

The stress field formulation in Eq. (6.2) is not valid for a semi-infinite or finite medium since it does not ensure zero traction on the free surfaces. The traction vector $\vec{T} = \boldsymbol{\sigma}\vec{n}$ must be zero on the free surfaces of a semi-infinite or finite medium. The unit normal vector to the surface is indicated by $\vec{n}$, and the stress state at a surface point is given by $\boldsymbol{\sigma}$. To match this physical condition at any point M on the free surface, a correction term can be added by re-writing Eq. (6.6):

$$\boldsymbol{\sigma}^M = \sum_l^\gamma \boldsymbol{\sigma}^{l \to M} + \boldsymbol{\sigma}^M_{corr} \tag{6.7}$$

where $\boldsymbol{\sigma}^{M}_{corr}$ is the correction term for stress. This term ensures traction is null on any free surface point. This correction term is a spatial function of the dislocations and the field point. For example, any two field points in a material may have different correction terms depending on the spatial coordinates of the field points. Also, the correction terms change if the sub-surface dislocation changes position, say during a dynamics simulation.
The Peach-Koehler force at the center c of dislocation q as follows:

$$\vec{F}^{q} = \left(\left(\sum_{l \neq q}^{\gamma} \boldsymbol{\sigma}^{l \to qc} + \boldsymbol{\sigma}^{qc}_{corr} \right) \vec{b}^{q} \right) \times \vec{t}^{q} \tag{6.8}$$

where $\boldsymbol{\sigma}^{l \to qc}$ is the stress tensor at the center of dislocation q due to dislocation l. $\vec{b}^{q}$, $\vec{t}^{q}$ and $\boldsymbol{\sigma}^{qc}_{corr}$ are the Burgers vector, line sense and the correction term (evaluated at the center) of dislocation q, respectively. Also the total stress tensor at any field point P (not just surface points) is

$$\boldsymbol{\sigma}^{P} = \sum_{l}^{\gamma} \boldsymbol{\sigma}^{l \to P} + \boldsymbol{\sigma}^{P}_{corr} \tag{6.9}$$

A collocation point method was provided in [16] and [17] to capture $\boldsymbol{\sigma}_{corr}$. In this method, a number of collocation points on the surface in question are used to enforce the physical boundary conditions. As more points cover the surface, this numerical method is slated to match, in the limit of infinite collocation points, the correct analytical solution for the problem (if one existed of course).

The method introduced in [16] and [17] uses a local coordinate system to formulate $\boldsymbol{\sigma}_{corr}$. Specifically, the surface-attached xy-plane is the free surface. The correction terms in this method represent a second-rank tensor and need to be transformed as such since they need to be summed with the stresses from the crystal dislocations (which are computed with reference to a global coordinate system using the work of [44]). In addition to above, the coordinates or position vectors for points A and B (see Figs. 6.1 and 6.2) also require transformation as first-rank tensors (from global coordinates to local or surface-attached coordinate system). The method presented herein avoids such first-rank and second-rank

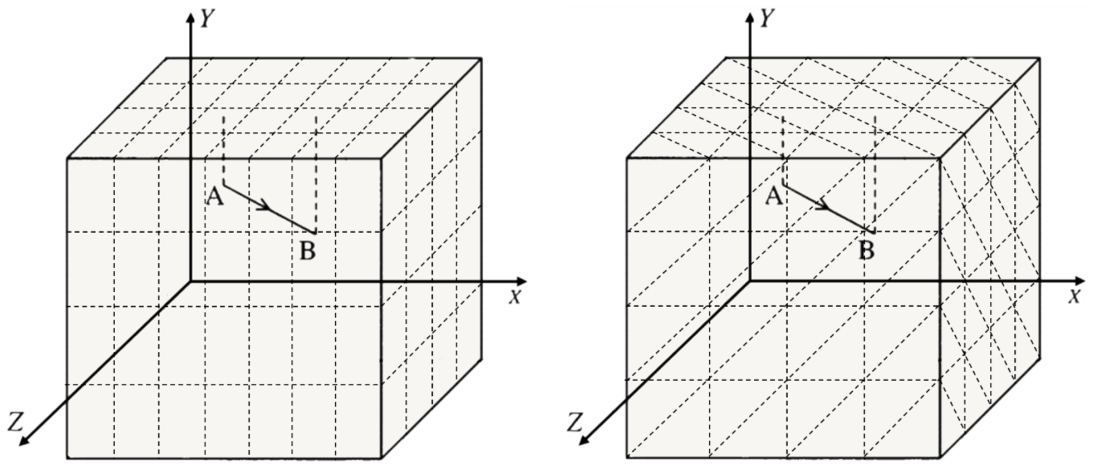

Figure 6.2: A cubic crystal used for the computation (showing surface loops) with segment AB shown inside of it. (a) Padded rectangular loops on the surfaces (b) Padded triangular loops on the surfaces

transformations, in order to find the correction terms $\boldsymbol{\sigma}_{corr}$, as a global system is used for all computations (such as Eq. (6.7) or Eq. (6.9)).

Figure 6.2 shows a sub-surface dislocation (or dislocation segment more specifically) below a traction-free surface. The dislocation is in a 3D domain of finite dimensions. The surface is meshed or padded by elements. Each surface element stands for a dislocation loop. Each dislocation loop *i*s called a generally-prismatic loop since its Burgers vector is angled with respect to the normal unit vector for the loop. Consider N such loops. These are not real dislocations, i.e. not crystal dislocations, but rather fictitious or mathematical dislocations used to solve the boundary-value problem at hand. These elements or loops can be rectangular or triangular in shape. As shown in Fig. 6.3, the collocation points represent the centers of the dislocation loops.

The condition $\vec{t} = \boldsymbol{\sigma}\vec{n} = \vec{0}$ for the surface traction translates to $\sigma_{yx} = \sigma_{yy} = \sigma_{yz} = 0$ for the surfaces in Fig. 6.3. The annulment of these stresses here happens on a set of N collo-

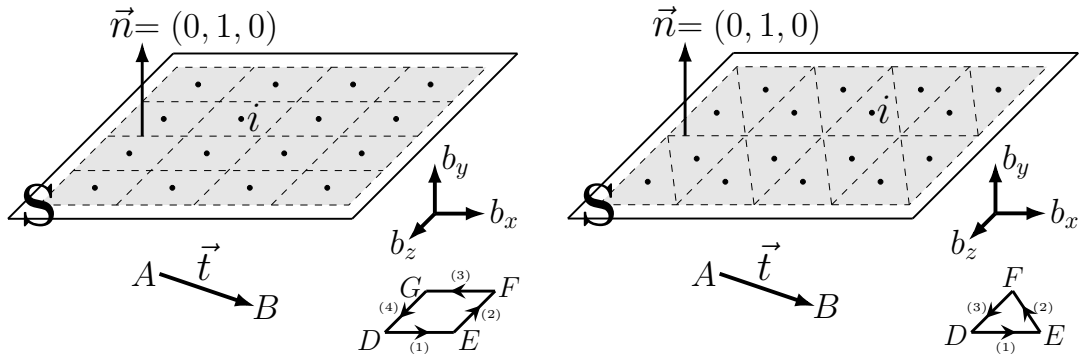

Figure 6.3: The figure shows a linear dislocation segment AB lying below a free surface. (a) This figure shows a meshing of the free surface with rectangular elements. In this method, each element is a dislocation loop with three Burgers vector components (b_x, b_y and b_z; see the inset). The area S covered by the mesh is where we are seeking to annul the traction in this problem. The inset also illustrates one of the dislocation loops, i.e. DEFG. (b) This figure is similar to (a) but the elements/dislocation loops here are triangular in nature. One such loop *i*s shown in the inset along with its Burgers vector components, i.e. loop DEF. The center of each element is a collocation point. There is N collocation points. For example, point *i* in the sketch is a collocation point.

cation points. These N points represent the centers of dislocation loops (all equilibriated sources of stress) meshing the surface. This condition on the surface can now be expressed as,

$$\left(\sum_{l}^{\gamma}\boldsymbol{\sigma}^{l\to i}+\sum_{j}^{N}\boldsymbol{\sigma}^{j\to i}\right)\vec{n}=\vec{0} \tag{6.10}$$

Where, $\boldsymbol{\sigma}^{l\to i}$ and $\boldsymbol{\sigma}^{j\to i}$ represent the stress tensor at surface collocation point i due to dislocation l and generally-prismatic surface loop j, respectively. After simplification, the

problem is formulated by rewriting equation (34) as follows:

$$\begin{aligned}
\sum_{j=1}^{N} \sigma_{yx}^{j\to i} &= -\sum_{l}^{\gamma} \sigma_{yx}^{l\to i}, \quad i = 1,2,\ldots N \\
\sum_{j=1}^{N} \sigma_{yy}^{j\to i} &= -\sum_{l}^{\gamma} \sigma_{yy}^{l\to i}, \quad i = 1,2,\ldots N \\
\sum_{j=1}^{N} \sigma_{yz}^{j\to i} &= -\sum_{l}^{\gamma} \sigma_{yz}^{l\to i}, \quad i = 1,2,\ldots N
\end{aligned} \tag{6.11}$$

where $\sigma_{\alpha\beta}^{j\to i}$ is the stress computed at point i due to loop j. Also, $\sigma_{\alpha\beta}^{l\to i}$ is the $\alpha\beta$ component of stress due to dislocation l and calculated at collocation point i on the surface. For a dislocation loop like $DEFG$ in Fig. 6.3(a), the stress is calculated at any (collocation) point i as the contribution of four segments in the loop. The calculation here being done with respect to a global coordinate system (using [44]):

$$\boldsymbol{\sigma}^{j\to i} = \boldsymbol{\sigma}^{j_{(1)}\to i} + \boldsymbol{\sigma}^{j_{(2)}\to i} + \boldsymbol{\sigma}^{j_{(3)}\to i} + \boldsymbol{\sigma}^{j_{(4)}\to i} \tag{6.12}$$

where $\boldsymbol{\sigma}^{j_{(1)}\to i}$ is the stress of dislocation segment (1) of loop j (shown as $DEFG$ in Fig. 6.3(a)) evaluated at collocation point i, and so forth. Similarly, for a generally-prismatic triangular dislocation loop (see Fig. 6.3(b)) in the global coordinate system one can write,

$$\boldsymbol{\sigma}^{j\to i} = \boldsymbol{\sigma}^{j_{(1)}\to i} + \boldsymbol{\sigma}^{j_{(2)}\to i} + \boldsymbol{\sigma}^{j_{(3)}\to i} \tag{6.13}$$

When one analyzes the segment stress solution by [44], see equation (2), it is apparent that is linear with respect to the Burgers vector components (b_x, b_y and b_z). Therefore, in Eq. (6.11), one can then insert:

$$\sigma_{\alpha\beta}^{j\to i}(x,y,z) = K_{x\alpha\beta}^{j\to i}(x,y,z)b_x^j + K_{y\alpha\beta}^{j\to i}(x,y,z)b_y^j + K_{z\alpha\beta}^{j\to i}(x,y,z)b_z^j \tag{6.14}$$

Here, the stress $\sigma_{\alpha\beta}^{j\to i}(x,y,z)$ is due to loop j acting on collocation point i. Also, the x-component of the Burgers vector is labeled here b_x^j for loop j. Lastly, the kernel term associated with this Burgers vector component is labeled $K_{x\alpha\beta}^{j\to j}(x,y,z)$. It is a field function evaluated at collocation point i. In this article, the kernels are computed using a "brute-force" method. This method is a straight-forward and generalized method to compute

kernels in Eq. (6.14). The desired kernels can be computed by canceling the other Burgers vector components in Eq. (6.14). For example, $K_{x\alpha\beta}$ can be calculated by putting $b_y = 0$, $b_z = 0$ and $b_x = 1$ in Eq. (6.14). In general,

$$\begin{aligned} K^{j\to i}_{x\alpha\beta}(x,y,z) &= \sigma^{j\to i}_{\alpha\beta}(x,y,z)\Big|_{b^j_x=1,\, b^j_y=0,\, b^j_z=0} \\ K^{j\to i}_{y\alpha\beta}(x,y,z) &= \sigma^{j\to i}_{\alpha\beta}(x,y,z)\Big|_{b^j_x=0,\, b^j_y=1,\, b^j_z=0} \\ K^{j\to i}_{z\alpha\beta}(x,y,z) &= \sigma^{j\to i}_{\alpha\beta}(x,y,z)\Big|_{b^j_x=0,\, b^j_y=0,\, b^j_z=1} \end{aligned} \tag{6.15}$$

Take Eq. (6.14) and insert it into Eqs. (6.11). The result is a system of linear algebraic equations (replacing equations (11)):

$$\begin{aligned} \sum_{j=1}^{N} b^j_x K^{j\to i}_{xyx} + b^j_y K^{j\to i}_{yyx} + b^j_z K^{j\to i}_{zyx} &= -\sum_{l}^{\gamma} \sigma^{l\to i}_{yx}, \quad i = 1,2,\ldots N \\ \sum_{j=1}^{N} b^j_x K^{j\to i}_{xyy} + b^j_y K^{j\to i}_{yyy} + b^j_z K^{j\to i}_{zyy} &= -\sum_{l}^{\gamma} \sigma^{l\to i}_{yy}, \quad i = 1,2,\ldots N \\ \sum_{j=1}^{N} b^j_x K^{j\to i}_{xyz} + b^j_y K^{j\to i}_{yyz} + b^j_z K^{j\to i}_{zyz} &= -\sum_{l}^{\gamma} \sigma^{l\to i}_{yz}, \quad i = 1,2,\ldots N \end{aligned} \tag{6.16}$$

Equations (6.16) has 3N equations. Such system requires increased solution time than the previously mentioned system of N equations which required the suspension of an image segment in air (e.g. [16]). However, the current method is more straight forward to implement. It also can be expanded to different types of meshes and saves time on the tensor transformations. For Eqs. (6.16), the sought after solution vector is composed of the different Burgers vectors for the N loops. Equations (6.16) can be re-written in matrix form

as:

$$\begin{bmatrix} K_{xyx}^{1\to1} & K_{yyx}^{1\to1} & K_{zyx}^{1\to1} & & K_{xyx}^{N\to1} & K_{yyx}^{N\to1} & K_{zyx}^{N\to1} \\ K_{xyy}^{1\to1} & K_{yyy}^{1\to1} & K_{zyy}^{1\to1} & \cdots & K_{xyy}^{N\to1} & K_{yyy}^{N\to1} & K_{zyy}^{N\to1} \\ K_{xyz}^{1\to1} & K_{yyz}^{1\to1} & K_{zyz}^{1\to1} & & K_{xyz}^{N\to1} & K_{yyz}^{N\to1} & K_{zyz}^{N\to1} \\ & \vdots & & \ddots & & \vdots & \\ K_{xyx}^{1\to N} & K_{yyx}^{1\to N} & K_{zyx}^{1\to N} & & K_{xyx}^{N\to N} & K_{yyx}^{N\to N} & K_{zyx}^{N\to N} \\ K_{xyy}^{1\to N} & K_{yyy}^{1\to N} & K_{zyy}^{1\to N} & \cdots & K_{xyy}^{N\to N} & K_{yyy}^{N\to N} & K_{zyy}^{N\to N} \\ K_{xyz}^{1\to N} & K_{yyz}^{1\to N} & K_{zyz}^{1\to N} & & K_{xyz}^{N\to N} & K_{yyz}^{N\to N} & K_{zyz}^{N\to N} \end{bmatrix} \begin{Bmatrix} b_x^1 \\ b_y^1 \\ b_z^1 \\ \vdots \\ b_x^N \\ b_y^N \\ b_z^N \end{Bmatrix} = - \begin{Bmatrix} \sum \sigma_{yx}^{l\to1} \\ \sum \sigma_{yy}^{l\to1} \\ \sum \sigma_{yz}^{l\to1} \\ \vdots \\ \sum \sigma_{yx}^{l\to N} \\ \sum \sigma_{yy}^{l\to N} \\ \sum \sigma_{yz}^{l\to N} \end{Bmatrix} \tag{6.17}$$

The matrix containing the kernel terms is labeled here the kernel matrix. Its size is $3N \times 3N \left(= 9N^2\right)$. The Burgers vectors for the padded surface loops can be found by solving Eq. (6.17). Once the Burgers vectors for the loops are found, the correction term $\boldsymbol{\sigma}_{corr}$ due to all the surface loops can be computed and substituted back into Eq. (6.9) to find the stresses at any field point inside the medium.

6.3 Numerical Considerations

Equation (6.17) can be expressed in matrix form as,

$$[K]\vec{B} = \vec{F} \tag{6.18}$$

The left-hand matrix $[K]$ is termed the kernel matrix, $\vec{B}$ is the solution Burgers vectors of the padded generally-prismatic dislocation loops and F is termed the forcing vector. Notice that $[K]$ and its elements couple $\vec{B}$ and $\vec{F}$. The elements of $[K]$ come from the surface loops. The elements of $\vec{F}$ come from the crystal dislocations. The surface loop density determines the dimension of $[K]$. The elements of $[K]$ are computed from the surface dislocation loops with no contribution from any crystal dislocations inside the computational domain/cell. For $\vec{F}$, however, its elements are computed (just like $[K]$ at the collocation points), from the effect of the real dislocations in the computational domain/cell. This

is important to observe since if more dislocations are present inside the crystal, this will affect only the calculation of $\vec{F}$ and won't affect the matrix $[K]$. This is very helpful in dislocation dynamics simulations as the kernel terms only need to be evaluated at the beginning of the simulation, whereas the elements of $\vec{F}$ need to be updated as time evolves, i.e. with every time stepping. Hence, as the dislocations glide in the crystal and change their configuration, so do the values for the $\vec{B}$ vector elements. Consider Fig. 6.2 which shows a computational box with six free surfaces. On each of these surfaces a zero stress-traction condition $\vec{T} = \vec{0}$ applies. Hence, to calculate the stress at any field point *i*n the box, one needs to sum stresses from all surface loops on all surfaces plus the stresses rising from internal stress sources such as real crustal dislocations (Eq. (6.9)).

Solving Eq. (6.18) is the most crucial part of this method. For each collocation point (like point *i* in Fig. 6.3), the state of stress from its own loop (loop *i* in this case) will dominate over stresses from other loops. This will make the Kernel matrix $[K]$ to be dominant on its diagonal. In other words $|k_{ii}| \geq \sum_{j \neq i} |k_{ij}|$. Iterative methods, like the Gauss-Seidel method ([23]), can be employed for cases when the matrix is diagonally-dominant. Also, successive relaxation can be utilized to solve the system of linear equations (see Eq. (6.18)). For faster computing, we have chosen a relaxation parameter λ such that $0 < \lambda < 2$. If b_f is a solution of Eq. (6.18) after iteration f then the new value of b_f is modified by a weighted average of the results from the previous and present iterations as

$$b_f^{new} = \lambda b_f^{new} + (1 - \lambda) b_f^{old} \tag{6.19}$$

In this study, the relaxation parameter λ is set equal to 1.35 (over-relaxation). This iterative method works faster than decomposition methods like Gaussian elimination for example (refer to [23]). In general, decomposition techniques in linear algebra tend to be expensive computationally especially for large matrices.

In the case of curved crystal dislocations, each of them can be divided into linear segments. The stress from each segment can be found using Eq. (6.1). The right-side of Eq.

(6.17) can add up the contribution of all these segments. Such dislocation curve segmentation or discretization is routine practice in dislocation dynamics simulation codes (see for example, [15] [16] [17] [57] [51]). The dislocation line discretization is capable of capturing the problem physics correctly.

Figure 6.4 shows a time comparison between two different shapes of surface loops (see

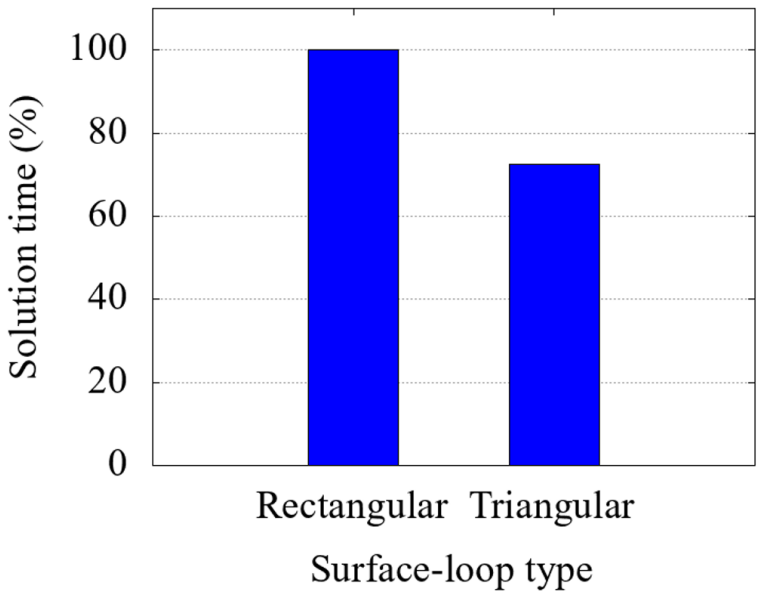

Figure 6.4: Computational time of any field stresses for two surface loop geometries used in computing the correction term.

Figs. 6.2 and 6.3) used to compute the correction term. The normalized time is recorded while computing the correction term using 2500 surface loops of both shapes. The figure shows about 30% time improvement for using a triangular surface mesh. This will make a remarkable time improvement in dynamic simulations by saving a significant amount of time over many time steps.

6.4 Results

First, the current brute-force method with rectangular and triangular surface loops is verified. Consider a situation of a horizontally-situated linear dislocation segment AB that is below and parallel to a free surface (refer to Fig. 6.5). This configuration has an analytical solution although the solution is for an infinite surface [39]. In this work, each side of the

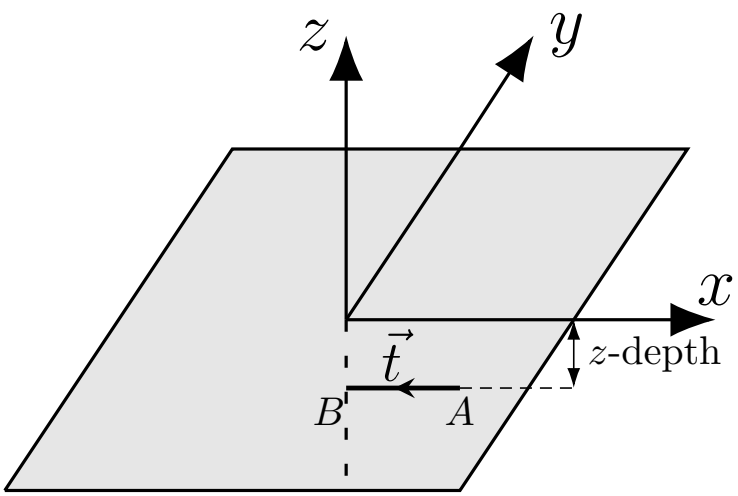

Figure 6.5: A Horizontal subsurface segment

finite-length square surface used here is 20,000b. The magnitude of the Burgers vector $\vec{b}$ is b. The depth of the linear segment below the surface is 1,000b. The length of the linear segment is 100b. For points A and B, the following exact coordinates were chosen (100b,0,0) and (0,0,0), respectively. Also, $\vec{b}$ for segment AB is chosen for simplicity as $(1/\sqrt{3}, 1/\sqrt{3}, 1/\sqrt{3})$. For the material, take Poisson ratio ν as 0.383. Consider a line, for field point calculations, beneath the surface and parallel to it at a depth of 400b (along $y = 0$ or the x-axis). See Figs. 6.6 and 6.7.

Second, the current brute-force method with rectangular and triangular surface loops is verified for a vertical segment AB beneath the free surface (see Fig. 6.5). This case is

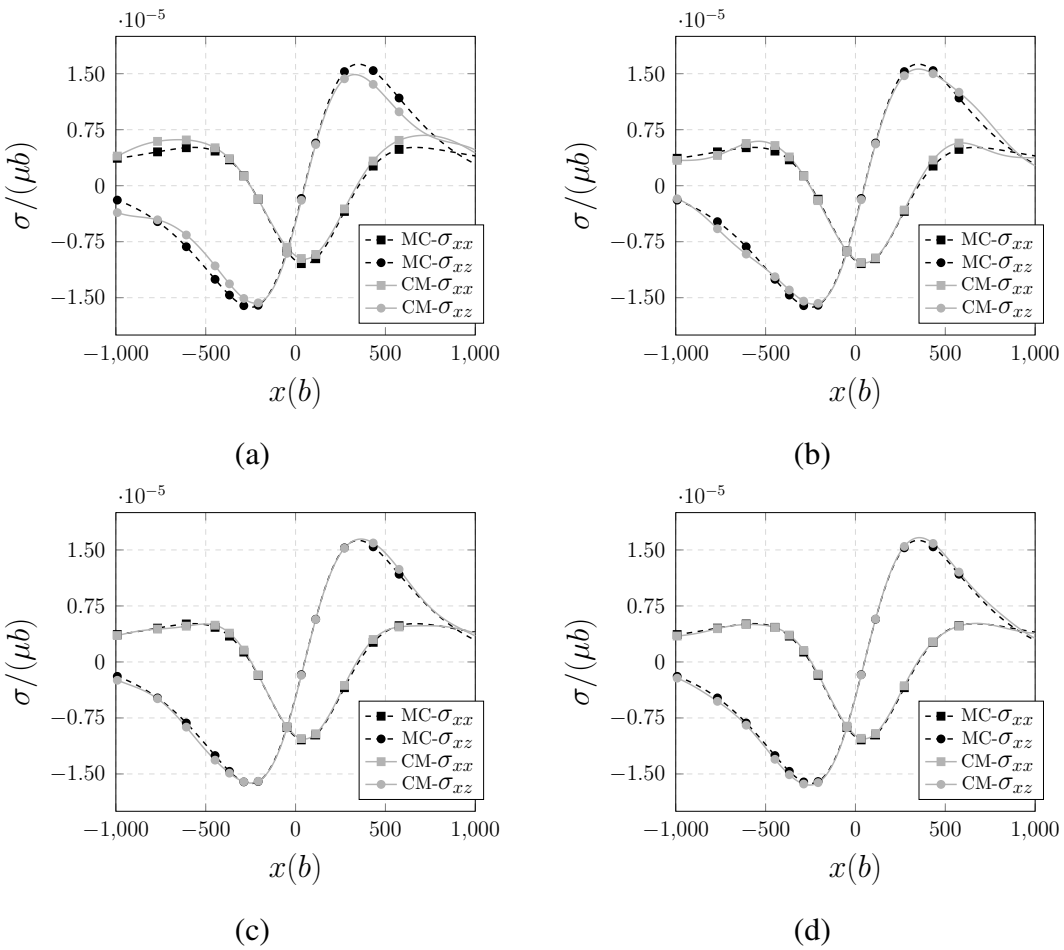

Figure 6.6: Stresses compared to the analytical solution found in Maurissen and Capella [39] as the number of rectangular surface dislocation loops is increased (see Fig. 6.3(a)). MC refers to Maurissen and Capella and CM refers to the current method. (a) Number of dislocation loops 400 (b) Number of dislocation loops 900 (c) Number of dislocation loops 1600 (d) Number of dislocation loops 2500

addressed analytically for an infinite surface dimensions by Maurissen and Capella [40]. Each side of the finite-length square surface used here is $20,000b$. The depth of point B is $1,000b$. Segment AB has a length $L = 100b$. For points A and B, the following exact coordinates were chosen $(0,0,-1,100b)$ and $(0,0,-1,000b)$, respectively. Also, $\vec{b}$ for segment AB is chosen as $(1/\sqrt{3},0,1/\sqrt{3})$. Poisson ratio $\nu is 0.38$. Consider a line, for field point calculations, beneath the surface and parallel to it at a depth of $400b$ (along $x = 0$ or

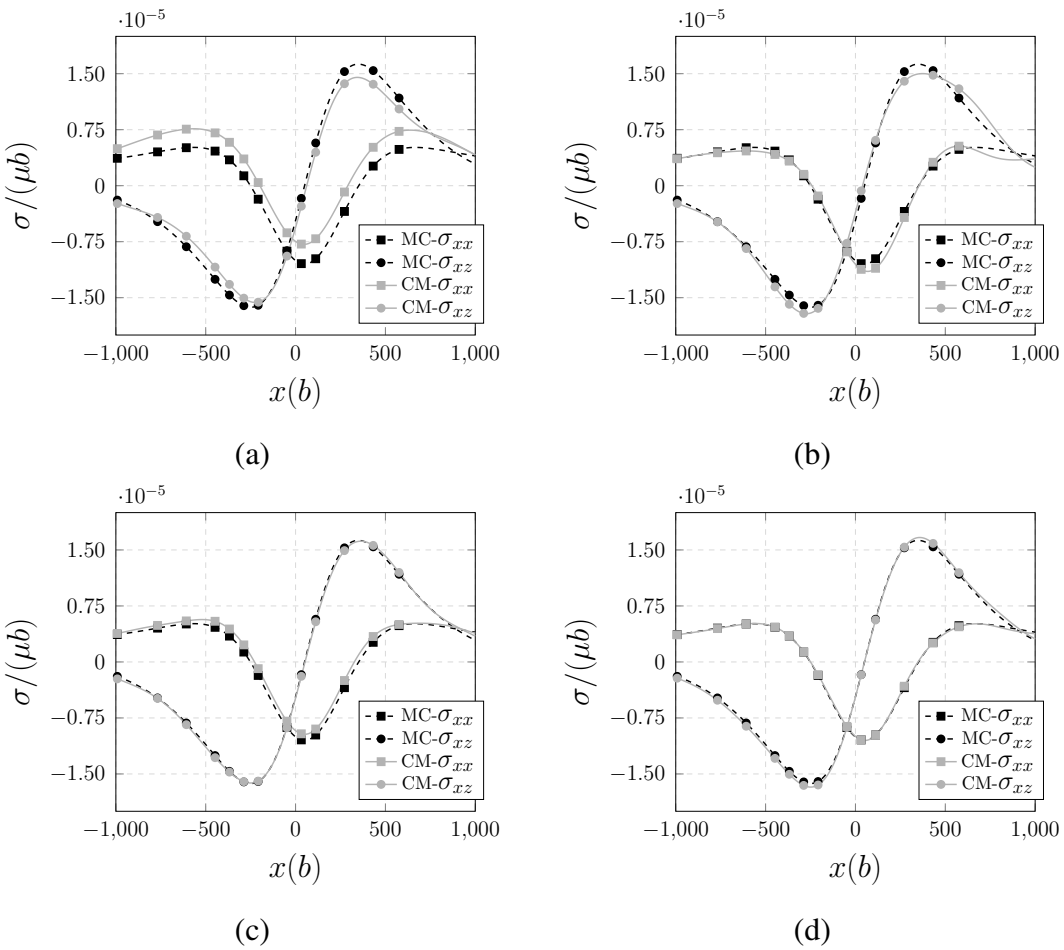

Figure 6.7: Stresses compared to the analytical solution found in Maurissen and Capella [39] as the number of triangular surface dislocation loops is increased (see Fig. 6.3(b)). MC refers to Maurissen and Capella and CM refers to the current method. (a) Number of dislocation loops 400 (b) Number of dislocation loops 900 (c) Number of dislocation loops 1600 (d) Number of dislocation loops 2500

the *y*-axis).

Figures 6.6 and 6.7 compare the analytical solution by Maurissen and Capella [39], for a horizontal sub-surface dislocation segment, and the solution from this numerical method as we increase the surface mesh density for the rectangular and triangular surface loops.

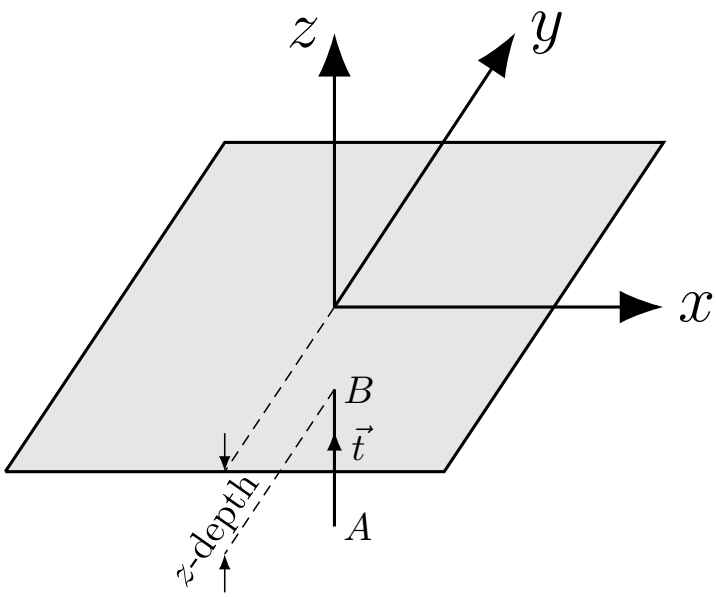

Figure 6.8: A Vertical subsurface segment

Figures. 6.9 and 6.10 compare the analytical solution by Maurissen and Capella [40], for a vertical sub-surface dislocation segment, and the solution from this numerical method as we increase the surface mesh density for the rectangular and triangular surface loops.

In the case of the horizontal sub-surface segment, the numerical solution approaches the analytical solution as the number of dislocation loops, i.e. collocation points, increase. Same goes to the vertical sub-surface segment. Saint-Venant's principle can be used to explain the stabilization of the numerical solution with increased number of surface loops (approximately 1,600). According to this principle, an approximate solution (but equipollent) at a boundary and an exact one will show agreement at field points that are positioned from the boundary a "characteristic" distance away. In this work, the characteristic distance is the spacing, on average, between the surface collocation points (where the solution is enforced or the problem solved). Therefore, an increase in the number of surface loops will result in a smaller characteristic distance and thus more matching between the nu-

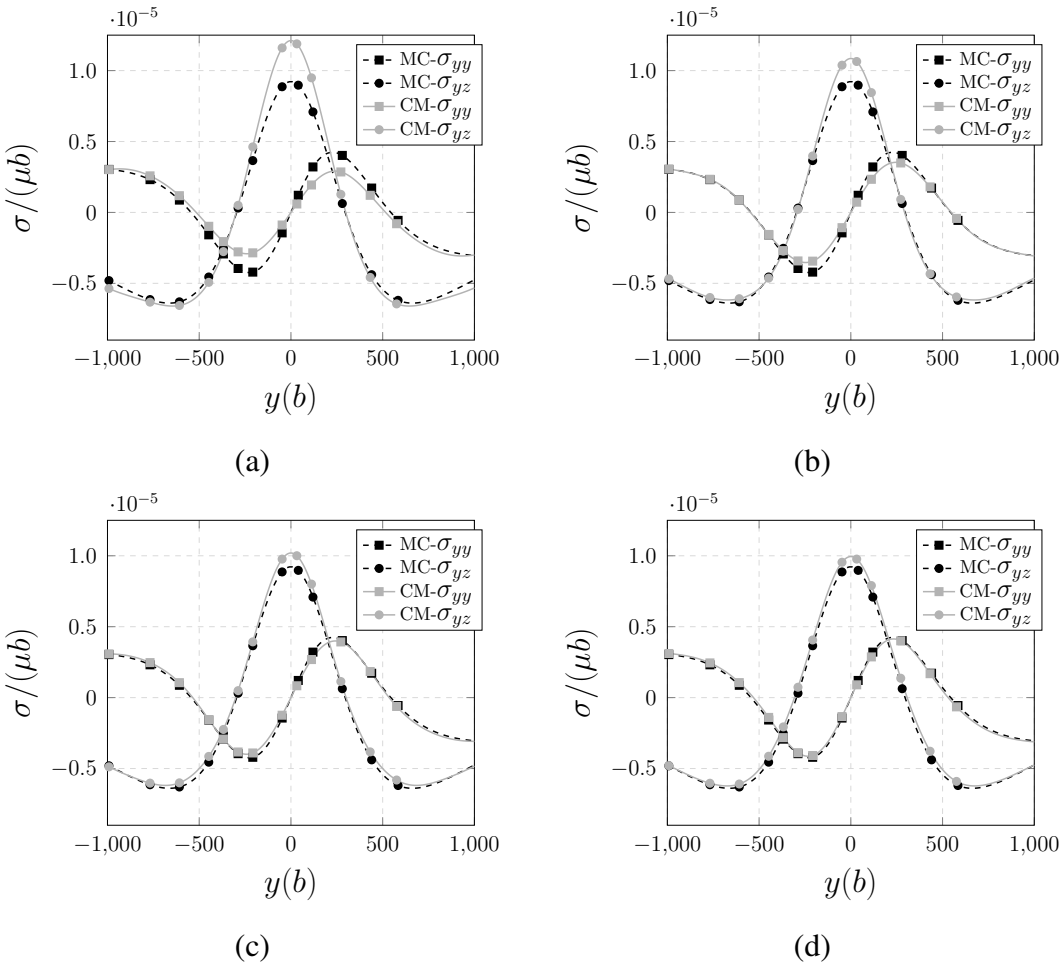

Figure 6.9: Stresses compared to the analytical solution found in Maurissen and Capella [40] as the number of rectangular surface dislocation loops is increased (see Fig. 6.3(a)). MC refers to Maurissen and Capella [40] and CM refers to the current method. (a) Number of dislocation loops 400 (b) Number of dislocation loops 900 (c) Number of dislocation loops 1600 (d) Number of dislocation loops 2500

merical and analytical solutions. The solution is not accurate for field points nearer to the surface than this characteristic distance. It may even exhibit oscillatory behavior in space with a wavelength equaling this distance. The mean value around the oscillations (e.g. by applying a least-square fit) will be equivalent to the correct solution.

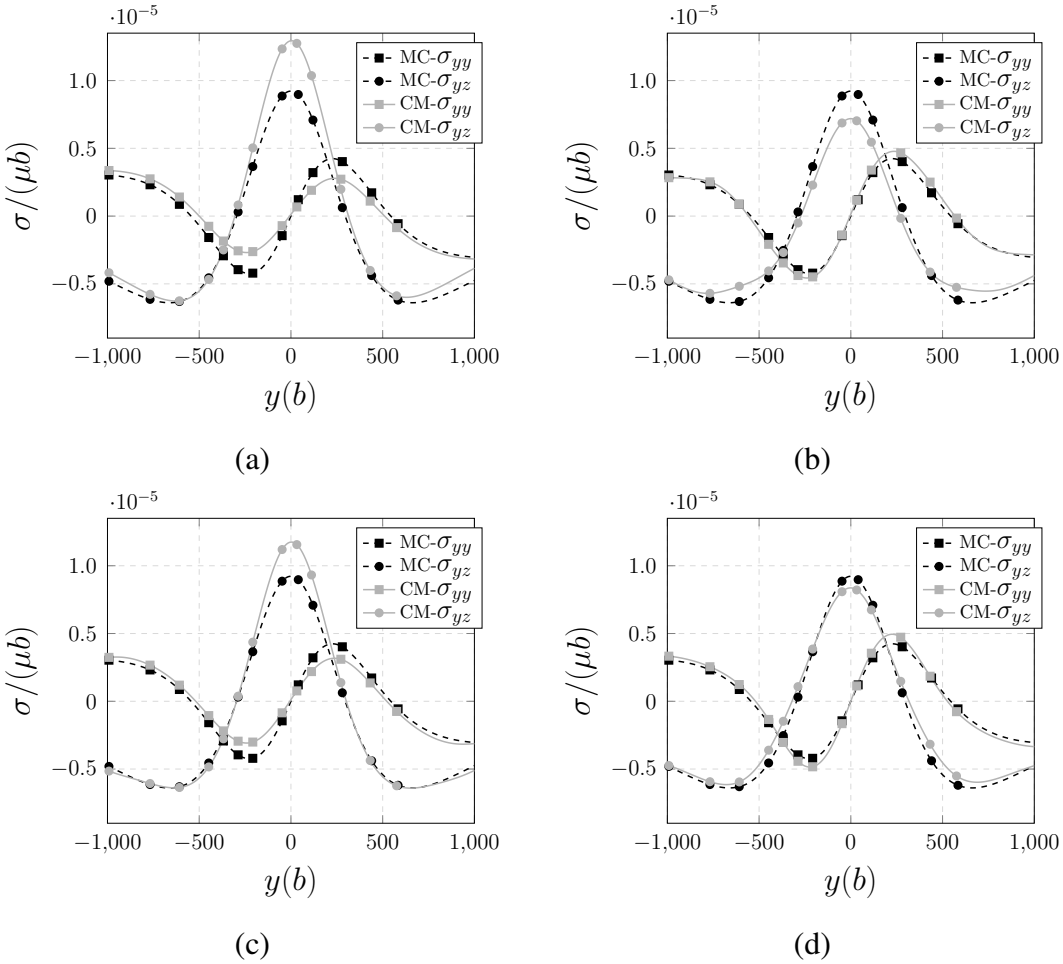

Figure 6.10: Stresses compared to the analytical solution found in Maurissen and Capella [40] as the number of triangular surface dislocation loops is increased (see Fig. 6.3(b)). MC refers to Maurissen and Capella [40] and CM refers to the current method. (a) Number of dislocation loops 400 (b) Number of dislocation loops 900 (c) Number of dislocation loops 1600 (d) Number of dislocation loops 2500

The above was verification of the method for static cases. For dynamic cases, we use the paper's method into a three-dimensional dislocation dynamics (or DD) code (see the works of [15] [16] [17] [18] [57] [51]). Dislocation theory dictates that stress calculations cannot be made closer to the dislocation line than a core radius. Meyers and Chawla [52], for example, define the core radius as 5b (where b is the magnitude of the Burgers vec-

tor). Therefore, when calculating the Peach-Koehler (PK) force on a crystal dislocation, it has to be below the surface by at least a core distance. This is a known problem in dislocation dynamics codes as the overlapping of a dislocation core (say for the surface loops) with a field point causes numerical problems. However, this is not a serious issue as the PK force is so high that it quickly pulls the segment into the free surface to vanish it. Below, a figure will be shown of such force. Also, since the plastic strain computation in DD codes is homogenized over the volume of the computational cell, this small area sweep close to the surface contributes negligibly to the total strain value, i.e. the error in not fully capturing the right image stresses (which are the correction terms emanating from the surface dislocation loops in the current case) is so minimal that it does not impact the overall computational results. This was shown in these preliminaries works referenced.

In what follows, constant strain-rate experiments are simulated for a three-dimensional crystal or cubic simulation box. The box has sides of 10,000b each. Each of the six box faces is padded with either rectangular or triangular generally prismatic surface dislocation loops (see Fig. 6.2). The mesh density on the six free surfaces is also varied. For these simulations, the density =2,710kg/m^3. Also, Poisson ratio $\nu = 0.3$, along with a dislocation mobility equaling 1000 1/(Pa·s) . A dislocation source (of the Frank-Read type) is placed along the x-axis. The coordinates for its end points are (-2000b,0,0) and (2000b,0,0). The Burgers vector was (0,1,0). Lastly, the applied strain-rate amount was 10 s$^(-1)$. For Figs. 6.11 and 6.12, the stress and strain are the yz-components.

To study the effect of surface loop number, or equivalently loop density, on the stress-strain curves, refer to Fig. 6.11 and to Fig. 6.12. The former uses rectangular surface loops for the surface correction terms, and the latter uses triangular surface loops. An averaging of the output stress-strain curve, i.e. smoothing, is done using a cubic spline fit between the two linear portions of the curve (after linear regression of the plastic deformation part) and presented in a solid line for each case. The cases of surface dislocation loops are com-

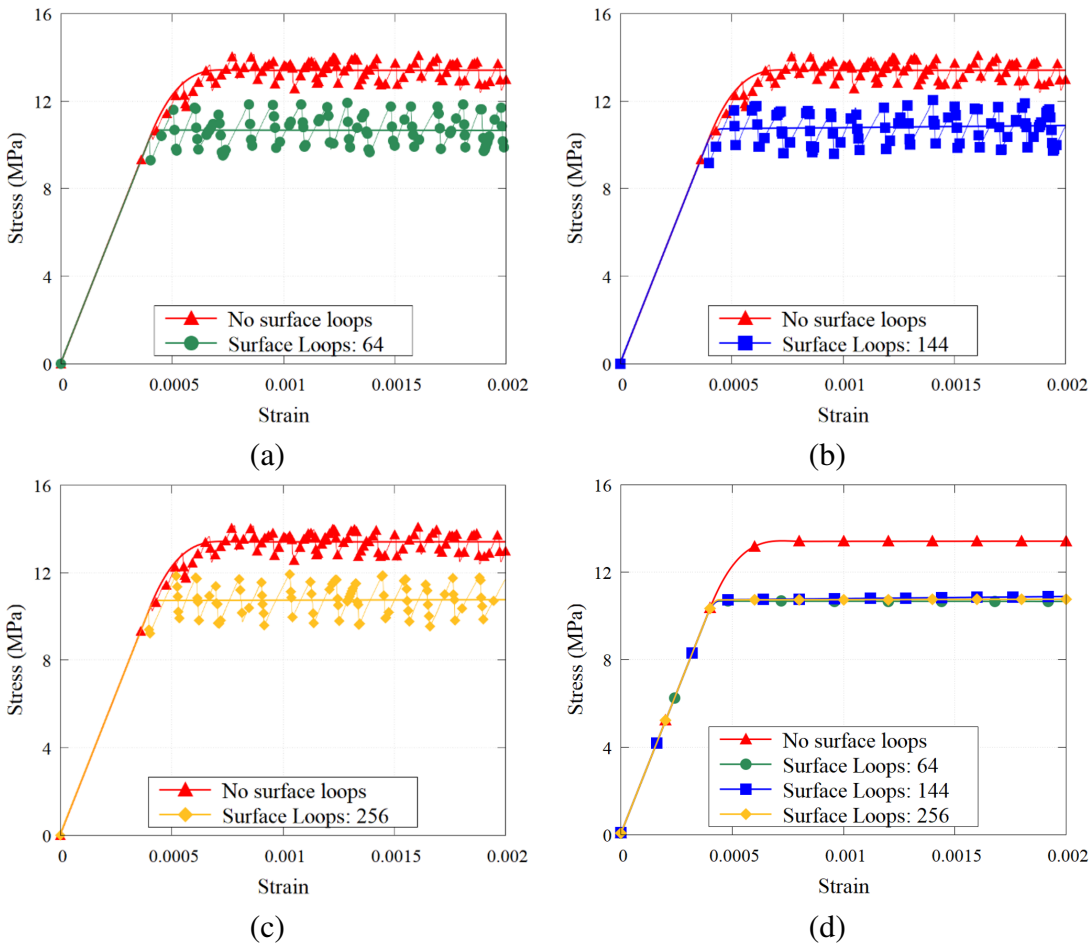

Figure 6.11: The effect of varying the number of surface dislocation loops on the stress-strain curve (using constant strain-rate loading). The correction term is calculated from rectangular surface loops. (a) Number of dislocation loops 64. (b) Number of dislocation loops 144 (c) Number of dislocation loops 256 (d) Effect of surface loop density.

pared to the base case of no surface loop, i.e. no treatment of the zero-traction boundary condition on the surface. The case of no surface loops shows higher flow stress than the cases of surface loops. This stress-strain diagram is typical in DD computations for an unobstructed Frank-Read source. The initial bowing of the FR source occurs in an elastic fashion (i.e. the source will bounce back to its original dislocation shape once load is removed). However, after a critical bow radius or size, the source then bows plastically in the material, i.e. irreversibly. That is when the stress-strain diagram starts bending from its

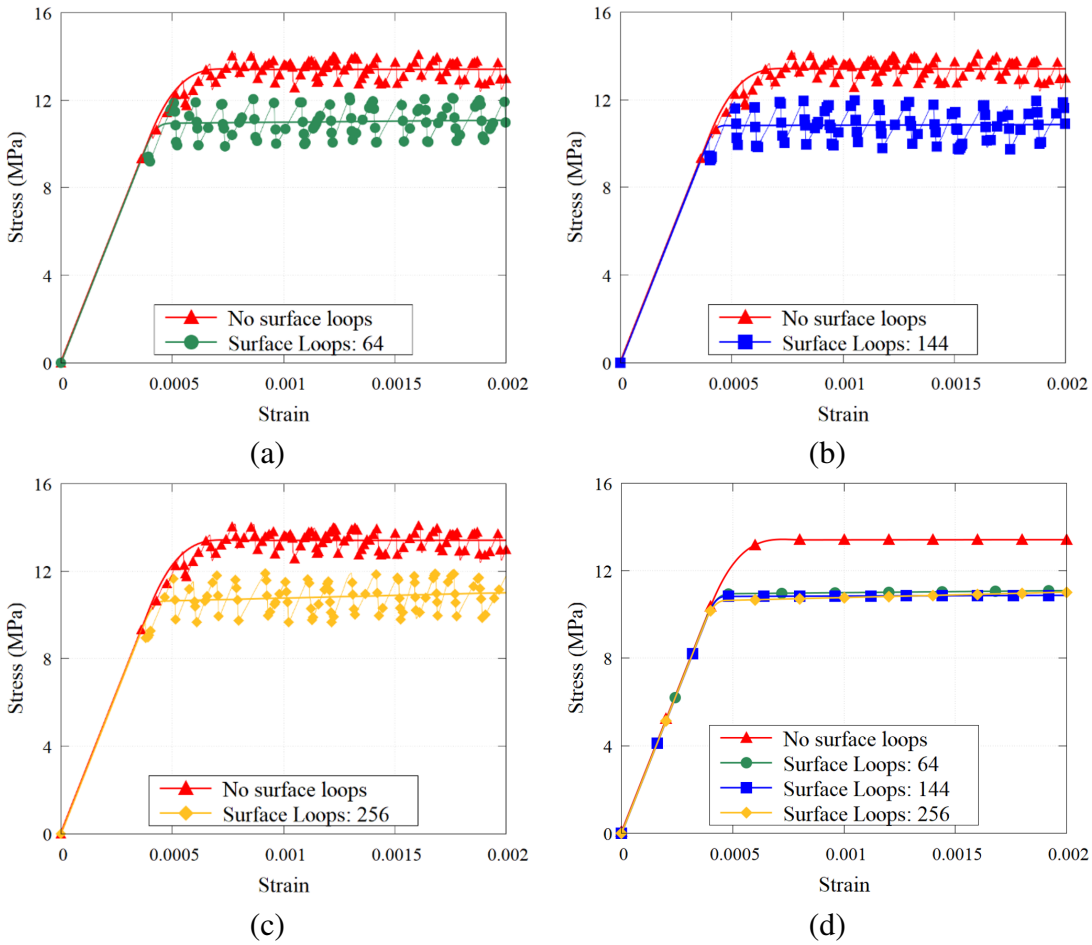

Figure 6.12: The effect of varying the number of surface dislocation loops on the stress-strain curve (using constant strain-rate loading). The correction term is calculated from triangular surface loops. (a) Number of dislocation loops 64. (b) Number of dislocation loops 144 (c) Number of dislocation loops 256 (d) Effect of surface loop density.

elastic region. It takes multiple bows or loops after the initial bowing for the stress-strain diagram to flatten, i.e. reach a flow stress value. When surface loops are present, they tend to pull on the dislocation source which causes it to bow earlier than the case of no surface loops. Meaning less applied strain is needed in the case of surface loops to reach critical bowing. This is due to the physical force that wants to pull on the dislocation and vanish it in the free surface to reduce the system's overall entropy, i.e. reduce the disorder in the crystal. This surface pull helps reduce the stress amount needed to cause this plastic flow

and hence the observation in Fig. 6.11 and 6.12.

If one measures the difference in flow stress for the above two cases of surface loops versus no surface loops, one finds this value approximately equal to 22%. The indicated percentage difference shall vary for different dislocation problems. If a problem has lower free surface area to volume ratio in the modeling cell then this percent amount should be lower due to lowered image stress effects. Another factor that will change this percentage is the exact initial position of the FR source inside the modeling cube/cell. Previous work has shown that the image stress effects depend on if the dislocation source is initially close to a free surface of the cube or far from it (i.e. positioned more internally in the cell). Discussions of this nature can be found in [16] and [17]. Figure 6.13 shows the effect of the

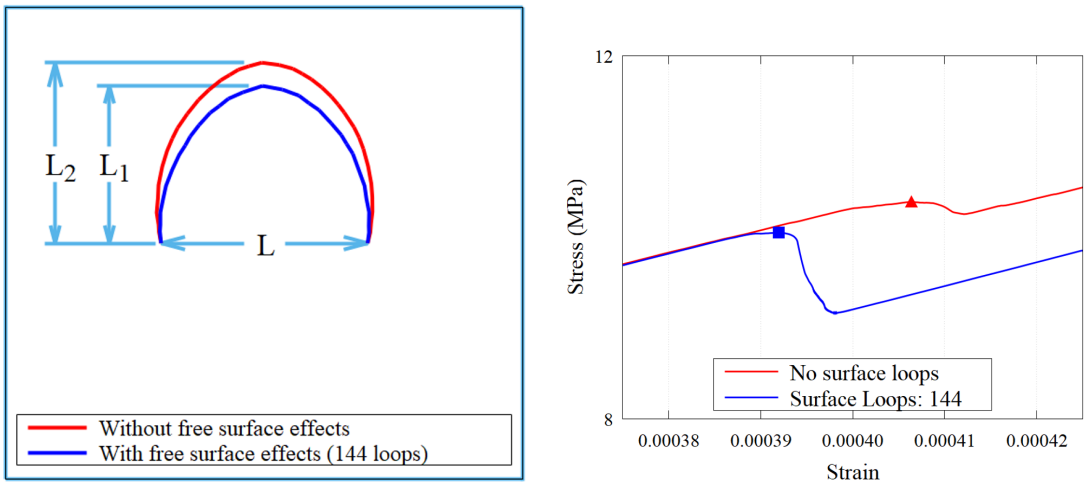

(a) (b)

Figure 6.13: Simulation snapshots at the critical bowing of a Frank-Read source of length L. (a) Illustration of the critical bowing of simulated Frank-Read sources. The view is perpendicular to the slip plane. (b) Markers showing the critical bowing stress and strain values, i.e. start of plasticity

free surfaces on the critical bowing of a Frank-Read source and the corresponding points on the stress-strain curves. Figure 6.13(b) is a zoomed-in figure from Fig. 6.11(b). As is known [2], at the critical bowing moment, the dislocation becomes unstable and starts

bowing quickly and irreversibly, i.e. plastic deformation ensues. From the simulations, the bowing dimension L_2 observed without surface effects is about 14 percent more than the bowing dimension L_1 when incorporating free surface effects. This is because the surface pulls the dislocation stronger as it gets closer to it. This causes the plastic flow to occur earlier than the case without free-surface effects (Fig. 6.13(b)). As is observed in Fig. 6.13, plastic flow started with a smaller radius of curvature for the dislocation source in the case where the free-surface effect is incorporated.

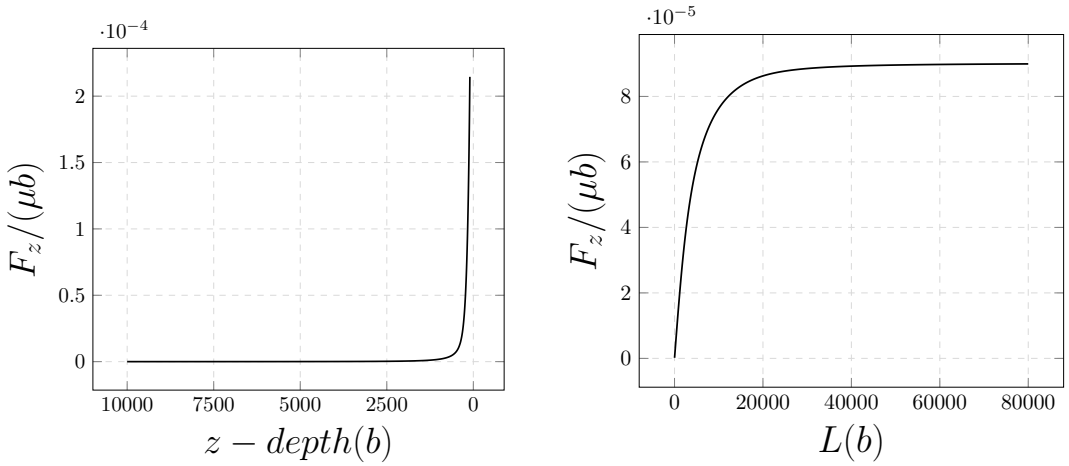

(a) (b)

Figure 6.14: The z-component of the Peach-Koehler force on a dislocation segment as the z-depth and length are varied. (a) Varying the dislocation depth (b) Varying the dislocation length

Figure 6.14(a) shows the z-component of the Peach-Koehler force acting at the center of a linear dislocation segment varying the dislocation depth from the free surface. The parameters for the calculations here are the same as those used earlier for a horizontal sub-surface segment with the exception of varying the depth (Fig. 6.14(a)) or the length (Fig. 6.14(b)). For Fig. 6.14(b), the segment was centered with respect to the z-axis. As the dislocation moves close to the surface, the Peach-Koehler force becomes stronger and pulls the dislocation towards it.

So it is very important to treat the boundary condition properly to model this problem accurately. Figure 6.14(b) shows the z-component of the Peach Koehler force (acting at the center of the dislocation) as it varies with the dislocation segment length where the stress reaches a limiting value as the dislocation segment length is sufficiently high.

6.5 Conclusion

The current study presented a generalized numerical technique to properly enforce zero-traction condition on a free surface of a three-dimensional crystal containing dislocations. A numerical method was generated adopting this generalized formulation and termed here as the "brute-force" method for implementation in dislocation dynamics (DD) simulations. The method uses dislocation loops, as self-equilibriated sources of stress, meshing the free surface. We have shown that such meshing could involve triangular or rectangular elements, i.e. dislocation loops. The method was illustrated for dynamic and for static dislocation problems. This "brute-force" method can be adapted to model non-planar free surfaces too. The stress correction term can also be computed using an unstructured random triangular surface mesh, which enables the possibility of modeling more complicated non-planar free surfaces. Lastly, we have shown using dislocation dynamics that the flow stress in the model is considerably different in the cases of image stress incorporation or not. The areal density of the surface mesh, or the mesh type, was not a riding factor for determining the flow stress. Hence, a lower mesh density can be used to save computational time. Due to the flexibility of the current method on the mesh type, future work can potentially utilize the developed collocation-point method to solve problems with curved free surfaces.

Journal reference

Siddique, A. B., & Khraishi, T. A. (2021). A Mesh-Independent Brute-Force Approach for Traction-Free Corrections in Dislocation Problems. Modeling and Numerical Simulation of Material Science, 11(01), 1–18. https://doi.org/10.4236/mnsms.2021.111001

Chapter 7

The treatment of singularities associated with a dislocation segment

Abstract

Quantification of the stress field around dislocations is important in dislocation theory and can have profound effect on computations involving dislocations such as in discrete dislocation dynamics (DDD) simulations. In this paper, the original work by Devincre (1995) on the stress field of a linear dislocation segment is carefully studied and based on three regions of space, a physics-based algorithm is presented to treat any singularity, weak or strong, associated with the self-stress of the segment. The paper shows several utilization of this method. Two of these utilization concern the 'collocation-point' method for capturing free-surface effects on dislocation forces and movement. In one, an on-the-fly mesh was utilized, and in the other an unstructured mesh was utilized. Results were validated where appropriate and both static and dynamic implementations are presented.

Keywords: dislocation dynamics, free surfaces, collocation-point method, flow stress

7.1 Introduction

Dislocation theory is a branch of materials science that is focused on the carriers of plasticity in crystalline solids or metals. Understanding how and why dislocation moves and interact between themselves and other micro-constituents will enable understanding of the plasticity phenomenon in crystals [2], [11], [3]. With many developments in dislocation theory, which were followed after by experimental evidence, the stage was set for developing plasticity models that take dislocations directly into account. Some of these models are based on dislocation densities as a field variable, i.e. a continuum approach [58], [59], [60] and some are based on modeling 3D discrete dislocations and their dynamics [45], [15], [61], [57], [62], [51].

The latter approach for modeling or simulating the dynamics of discrete dislocations was made possible by the ability to discretize a curved dislocation line into segments (similar to the finite element method which discretizes space into finite elements of different shapes). Hirth and Lothe [11] developed the stress field associated with a linear dislocation segment using a segment-attached coordinate system, where the z-axis coincides with the segment line. Devincre [44], building on the work of de Wit [21], developed expressions for the stress field of a linear dislocation segment based on an arbitrary located coordinate system. Cai et al. [63] developed the expression for the stresses of a dislocation segment using non-linear elasticity by spreading the Burgers vector of the line to avoid the common singularity. The result of this is more complex than the prior works, but it reduces to these prior works with no spreading (or zero spreading). Ghoniem and Sun [64] described a dislocation curve using general topological functions. All of the above works are within the realm of isotropic elasticity and apply to an infinite medium. The line singularity was also treated in the work of Jamond et al. [65] using the Discrete-Continuous Model (DCM) for the simulation of 3D dislocation dynamics which is based on a coupling between a Dislocation Dynamics (DD) code and a Finite Element (FE) code through eigenstrain theory.

The current chapter focuses on the leading work of Devincre [44] by closely looking at the spatial regions around a linear dislocation segment and properly treating the segment stresses in order to avoid singularities in the solution. This enables the regularization of the stress field. The space around the segment is divided into three distinct regions discussed below in the Methods section. By correctly placing a field point in the right region, the segment stress can then be calculated correctly or appropriately while avoiding singular calculations. Such regularization is important in dislocation dynamics simulations as the time-dependent solution can blow up or become unbounded if a field point lies in a singularity zone. To illustrate the method, including the accompanying algorithm developed here, a couple of applications are presented below in the Results and Discussion section. The examples revolve around the use of the distributed dislocation method, which can be used to solve crack problems [66], [67], [68], for solving the stress field of dislocations near a flat free surface [69], [16], [17], [18], [35] or near a curved surface [34]. These methods are "collocation point" methods where the zero traction physical boundary condition is enforced at a set of different surface points instead of an infinite number of them. These collocation points represent the centers of elements on a surface mesh whereby each element is represented by a multi-polygonal dislocation loop (which by itself is a self-equilibrated source of stress in the material). By figuring out the Burgers vectors of these surface fictitious/mathematical dislocation loops, the problem is then solved and the stress field at any sub-surface field point is the sum of the stress fields of surface loops plus the stress fields of the sub-surface dislocations.

The latest of these references [18] utilized a surface mesh of rectangular/square elements with each element composed of four linear dislocation segments whereby the whole computations are made in reference to an arbitrary-oriented global coordinate system. For this referenced work, the selection of collocation points had to be chosen carefully so as not to lie in the singularity zone, even the extended singularity zone, of any of the elements'

segments. More specifically, this structured surface mesh of elements had to look like a standard finite-element mesh in the sense that each element node has to be the node for four dislocation segments. In other words, a node for a dislocation segment cannot be a no node for an element. This severely restricts the meshing type used for the surface which can have ramifications on things like solution time for a static or dynamic problem. Of course, treating free surface problems can be attempted analytically [10], [36], [70], [37], [38], [39], [40], [41], [56], [71], [42], [32] but such treatment is severely restricted in scope and breadth since it has to be specific to a certain configuration of the domain and of the dislocation near the surface.

In this current chapter, we utilize the newly proposed non-singular stress field associated with a dislocation segment in application to new surface meshing of fictitious or mathematical dislocation loops. Specifically, we look at an irregular square/rectangular mesh, termed here "on-the-fly mesh" and also at an unstructured (or random) triangular-element mesh. Both of these meshes, albeit having their own advantages over a structured rectangular-element/square-element mesh, can run into singularity issues but are treated here with the newly developed method/algorithm. The "on-the-fly mesh" is illustrated here for static dislocation problems and the unstructured triangular mesh is illustrated here for dynamic dislocation problems.

In addition to the above, this current work looks closely at the extent of the dislocation core radius or size. There are different estimates in the literature for the radius of the core, r_c [2], [11], [52]. Based on the regularization of the segment stress introduced here, a rationale for the quantification of r_c is provided as well.

7.2 Methods

As mentioned above, this work builds on the work of Devincre [44] for the stress field of a linear dislocation segment in a linear-elastic isotropic infinite medium. For a segment AB of a dislocation line, shown in Fig. 7.1, the stresses at a field point $P(x,y,z)$ according to this last reference are provided with respect to a generally-oriented global coordinate systems centered at O by:

$$\sigma_{\alpha\beta}^{AB}(\vec{r}) = \left(\sigma_{\alpha\beta}^{AB}\right)_{\vec{r}'=\overrightarrow{OB}} - \left(\sigma_{\alpha\beta}^{AB}\right)_{\vec{r}'=\overrightarrow{OA}} \tag{7.1}$$

and $\sigma_{\alpha\beta}^{AB}$ is described as:

$$\begin{aligned}\sigma_{\alpha\beta}^{AB} =& \frac{\mu}{\pi Y^2}\left[\left[\vec{b}\vec{Y}\vec{t}\right]_{\alpha\beta}^{s} - \frac{1}{1-\nu}\left[\vec{b}\vec{t}\vec{Y}\right]_{\alpha\beta}^{s}\right. \\ & \left. - \frac{\left(\vec{b},\vec{Y},\vec{t}\right)}{2(1-\nu)}\left[\delta_{\alpha\beta} + t_\alpha t_\beta + \frac{2}{Y^2}\left[\rho_\alpha Y_\beta + Y_\alpha \rho_\beta + \frac{L}{R}Y_\alpha Y_\beta\right]\right]\right]\end{aligned} \tag{7.2}$$

where μ is the isotropic material shear modulus (also given by G in literature), ν is the Poisson's ratio and

$$\vec{R} = \vec{r} - \vec{r}' \tag{7.3a}$$

$$L = \vec{R}\cdot\vec{t} \tag{7.3b}$$

$$\vec{\rho} = \vec{R} - L\vec{t} \tag{7.3c}$$

$$\vec{Y} = \vec{R} + R\vec{t} \tag{7.3d}$$

Here, $(\vec{a},\vec{b},\vec{c})$ is called a "scalar triple product" and is given by:

$$(\vec{a},\vec{b},\vec{c}) = (\vec{a}\times\vec{b})\cdot\vec{c} \tag{7.4}$$

and $\left[\vec{a}\vec{b}\vec{c}\right]_{\alpha\beta}^{s}$ is called a "symmetric tensor operator" and is given by:

$$\left[\vec{a}\vec{b}\vec{c}\right]_{\alpha\beta}^{s} = \frac{1}{2}\left(\left(\vec{a}\times\vec{b}\right)_\alpha c_\beta + \left(\vec{a}\times\vec{b}\right)_\beta c_\alpha\right) \tag{7.5}$$

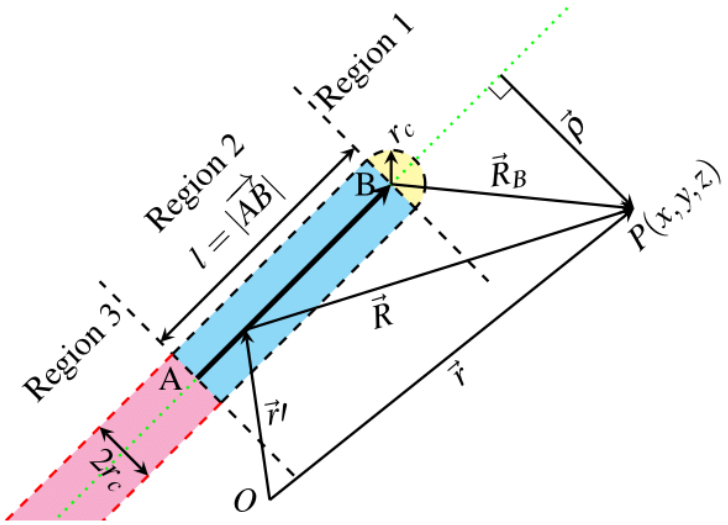

Figure 7.1: A dislocation segment AB with three identifiable regions in space. The line sense unit vector $\vec{t}$ points from A to B. Dislocation segment length: $l = |\vec{r}_B - \vec{r}_A| = |\overrightarrow{AB}|$.

Here, r_c is a cut-off radius delineating the core region of the dislocation (also called core radius for simplicity) where the self-stress of the dislocation shoots up to infinity under the use of linear-isotropic elasticity. The reason for this singular behavior is that the treatments of a dislocation viewed it as line defect experiencing a sudden displacement shift equal to the Burgers vector $\vec{b} = (b_x, b_y, b_z)$. The magnitude of the Burgers vector is indicated here as b. This discontinuous shift in the displacement field of the dislocation causes a singularity in the strain field, which is carried to the stress field via Hooke's law. The magnitude of r_c has been chosen differently in the literature, i.e. it has not been agreed upon or is a subject of debate. For example, Hirth and Lothe [11] took r_c as $1b$, Hull and Bacon [2] took it as $1b - 4b$, Meyers and Chawla [52] took it as $5b$, and so forth. One of the things provided or contributed by this work, as alluded to earlier, is an attempt at quantifying r_c in a fundamental way as seen below.

To better understand the behavior of stress around segment AB, contour plotting is used to give an overall look of stress distribution. Figure 7.2 shows contour plotting for two exem-

plary stress components σ_{11} and σ_{12}. Other stress components behave similarly. Taking a close look at Fig. 7.2 it is clear that stress values shoot up in value (indefinitely) immediately around the segment (labeled Region 2 in Fig. 7.1) and behind the segment (from point A opposite to the line sense, which is labeled Region 3 in Fig. 7.1). However, one would expect the stress around the mid-plane intersecting the segment center to be symmetric (i.e. Region 3 the mirror opposite of Region 1) or at least anti-symmetric which is not the case. This behavior is due to what Eq. (7.1) stands for. In Eq. (7.1), the stress from a half dislocation line extending from $-\infty$ to point B is subtracted from the stress from a half dislocation line extending from $-\infty$ to point A. This subtraction yields the stress of a dislocation line segment AB. Due to this subtraction process, it is recognized then that the stress at the dislocation line in Region 2 is strongly singular due to the issues discussed prior. It is also recognized that the stress at the dislocation line in Region 3 is expected to be weakly singular and right at the line itself due to the effect of the subtraction. Moreover, the stress in Region 1 seems to be (for the most part at least) non-singular and well behaving in values/distribution. In fact, in this figure a cut-off radius of $0.05b$ was utilized in Regions 2 and 3 to be able to do the plot, otherwise the stress would shoot to infinity there. Even with this implemented cutoff, the stress values are significant compared to the shear modulus.

Although the above was a visual investigation of the stress behavior, especially singularity behavior, of the dislocation segment, one can carefully examine Eq. (7.2), which feeds into Eq. (7.1), to see where the singularity exactly emanates from.

Consider point B of dislocation segment AB. From Eq. (7.3b), one can write:

$$L_B = (\vec{r}_P - \vec{r}_B) \cdot \vec{t} = \vec{R}_B \cdot \vec{t} \tag{7.6}$$

For any field point P, $\vec{\rho}$ is given by (Eq. (7.3c)):

$$\vec{\rho} = \vec{r}_B - L_B \vec{t} \tag{7.7}$$

Examining Eq. (7.2), it becomes unbounded if and only if either Y or R approaches zero. From the definition of $\vec{Y}$:

$$\vec{Y} = \vec{\rho} + L\vec{t} + |\vec{\rho} + L\vec{t}|\vec{t} \tag{7.8}$$

$Y = 0$ when, $\rho = 0$ and $L_B \leq 0$. This can happen in Regions 2 and 3 only and not in Region 1. In Region 1 therefore, there is no worry about singular stress behavior. However, special attention needs to be paid to the domed region around point B (see Fig. 7.1). In the following is an algorithm that checks against ρ approaching zero and then adjusts the stress calculation procedure accordingly.

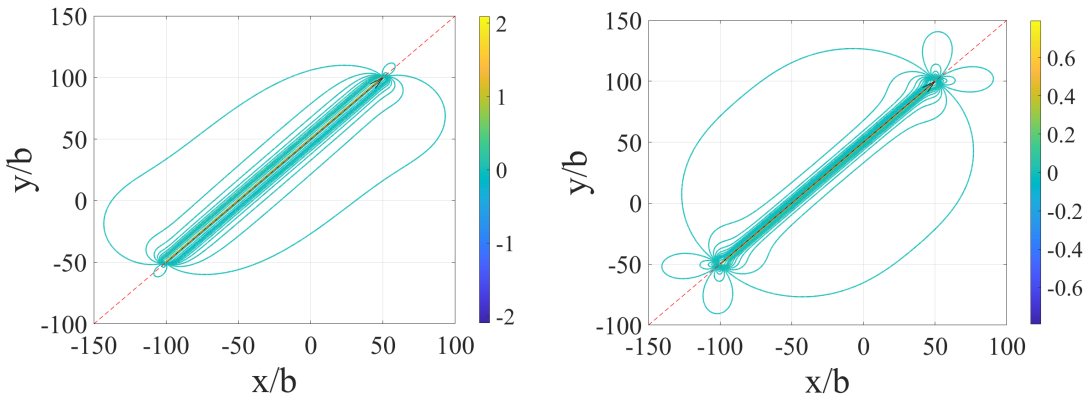

Figure 7.2: Contour plots around a linear dislocation segment lying in the xy-plane. These are made before implementing the algorithm in this paper (in the contour plots, points with $r_c < 0.05$ were ignored). The coordinates of point A are $(-100, -50, 0)$ and for point B are (50, 100, 0). Here, the Burgers vector = $(1/\sqrt{3}, 1/\sqrt{3}, 1/1/\sqrt{3})$ for simplicity. Here $\mu = G = 1$ and $\nu = 0.33$. (a) σ_{11}, (b) σ_{12}.

Algorithm

1. Calculate the quantity ρ per above. If $\rho \geq r_c$, no additional treatment is needed since point $P(x,y,z)$ lies outside the core region of the dislocation and therefore the stress equations (Eqs. (7.1) and (7.2)) are valid as is.

2. If $\rho < r_c$:

   (a) If $L_B > 0$ (Point $P(x,y,z)$ lies in Region 1 (yellow) in Fig. 7.1):

      i. If $R_B \geq r_c$ then no additional treatment is required (since $Y > r_c$).

      ii. If $R_B < r_c$ then the field point is within the domed area atop of point B. In this case, point P location has to be adjusted away from the dislocation line such that $\vec{\rho}$ is scaled up in magnitude to match r_c as shown in Fig. 7.3. Once $\vec{\rho}'$ (the new $\vec{\rho}$) is calculated (via $\vec{\rho}' = \vec{\rho} \times r_c/\rho$), a new adjusted location for point P (point P') can be determined (using equation 3.3, i.e. $\vec{r} = \vec{\rho} + L\vec{t}$). Now stress calculations can be performed at this new location.

   (b) If $L_B \leq 0$ and $|L_B| \leq l$ (Point $P(x,y,z)$ lies in Region 2 (cyan) in Fig. 7.1):

      To find the stress at this point, one needs to do a linear interpolation between 0 and σ_{ij}^{max}. More on this linear interpolation is given below in detail.

   (c) If $L_B \leq 0$ and $|L_B| > l$ (Point $P(x,y,z)$ lies in Region 3 (magenta) in Fig. 7.1):

      i. Reverse $\vec{t}$ and calculate segment stress and then multiply the obtained stress value by (-1) or a negative sign. In other words, calculate the stress for a directed segment from B to A instead of from A to B

      ii. Alternate to 2.c.i above, if $\rho \geq \varepsilon$, where ε could be as small as 10^{-10} or almost the computer machine zero, then one can proceed with normal stress calculations for the segment using Eqs. (7.1) & (7.2). This is possible due to the weak singular behavior in Region 3.

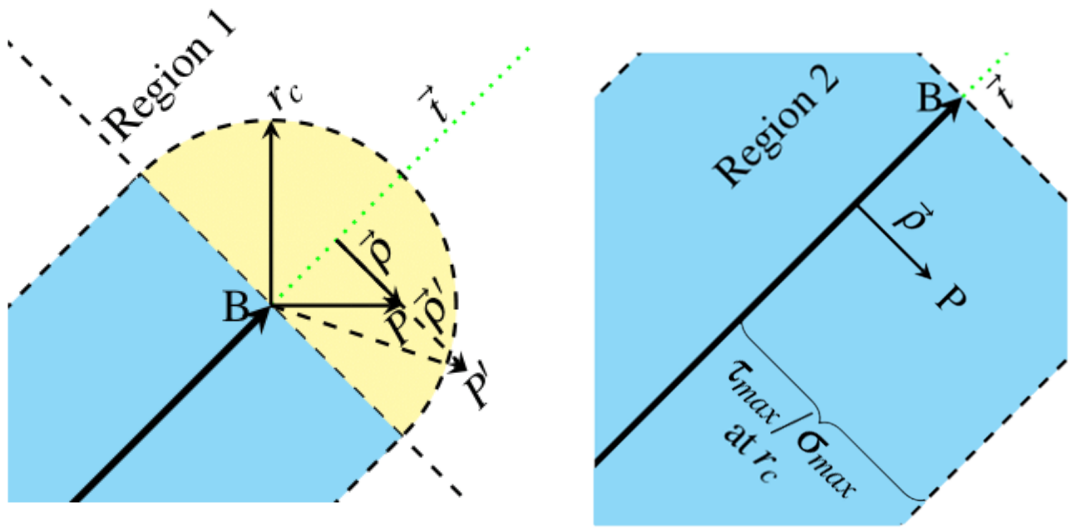

(a) (b)

Figure 7.3: Recommended location of P when (a) $L_B > 0$ and $R_B < r_c$ (b) Case 2.b in the algorithm. (a) Region 1, (b) Region 2

For the case 2.b above, the steps for linear interpolation are as follows (refer to Fig. 7.3(b)):

1. First, find the value of ρ for point P using Eq. (7.3c)
2. Multiply $\vec{\rho}$ with the quantity $\frac{r_c}{\rho}$, i.e. $\vec{\rho}' = \vec{\rho} \times \frac{r_c}{\rho}$ which extends to the core surface.
3. Find a new $\vec{r}_B$ value as such: $\vec{r}'_B = \vec{\rho}' + L_B\vec{t}$. From this, find a new $\vec{Y}$ value (equation 3.4).
4. Substitute back $\vec{\rho}'$ and $\vec{r}'_B$ (and the new $\vec{Y}$ value) into Eq. (7.2) and then Eq. (7.1) to find the limiting value of σ_{ij}^{max}
5. Now, the interpolated value of the stress is given by: $\sigma_{ij}(P) = \frac{\rho}{r_c} \times \sigma_{ij}^{max}$

The algorithm is shown below in Fig. 7.4 as a flow chart.

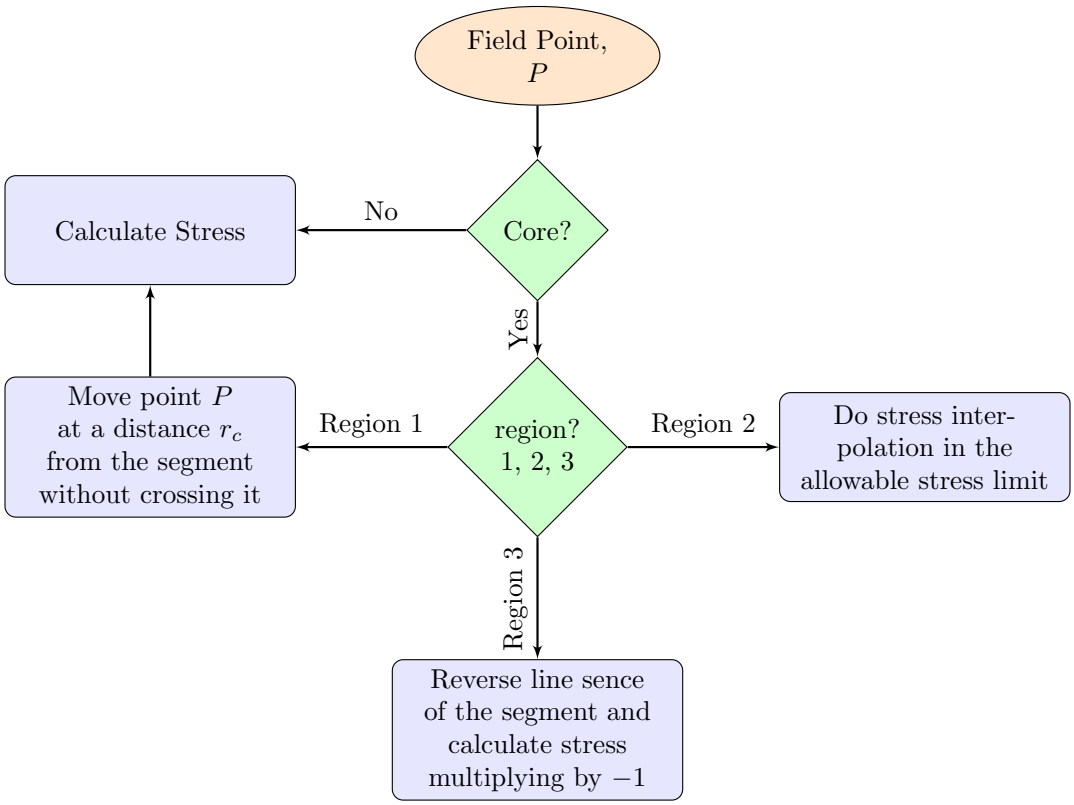

Figure 7.4: Flowchart of the algorithm

Lastly, it was mentioned above about the strong singularity occurring in Region 2. If one considers any plane containing the dislocation line segment and then plot any of the stress components σ_{ij} along a coordinate ξ perpendicular to the line, one gets a spatial behavior as shown in Fig. 7.5. In the schematic figure, the stress shoots to infinity as the dislocation line is approached. However, according to theory, stress must have a maximum theoretical value in a material that cannot be exceeded. According to Hull and Bacon [2], the maximum shear stress (indicated by the symbol taw or τ) is given by $\tau_{max} = G/2\pi$. In Meyers and Chawla [52], the maximum shear stress is given by: $\tau_{max} = G/5.1$. However, according to Hull and Bacon [2], a more realistic value for the maximum shear stress is given by: $\tau_{max} = G/30$. In addition, elementary mechanics of materials theory dictates

that for the simple case of uniaxial stress, the normal stress σ is double the shear stress τ in value, i.e. $\sigma_{max} = 2\tau_{max}$. Based on these maximum values for the different stress components, one can arrive at a calculated value for r_c per this figure. The figure also shows that within the core region in Region 2, the stress could be interpolated for values as the interpolation (linear interpolation is the most logical in this case) passes through zero at the dislocation line (i.e. the core center) due to the change in sign for the stress shown in the figure. The zero value at the dislocation center also makes physical sense since the dislocation cannot stress its own self. The exact steps to perform the interpolation were listed above.

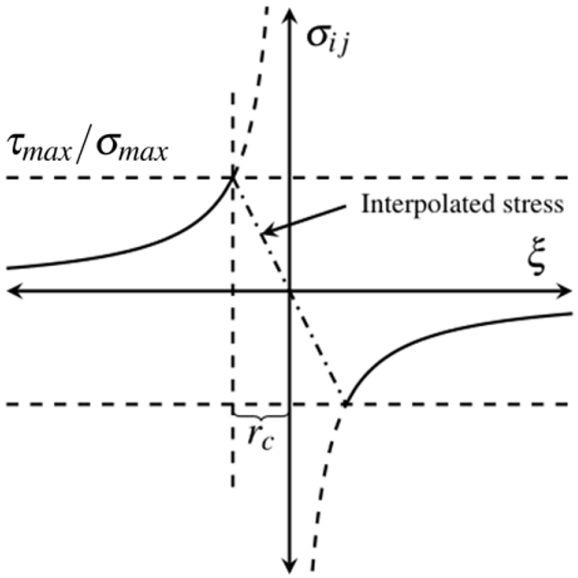

Figure 7.5: Schematic of stress behavior around a linear dislocation segment versus a coordinate traversing perpendicular to the segment (in Region 2).

7.3 Results and Discussion

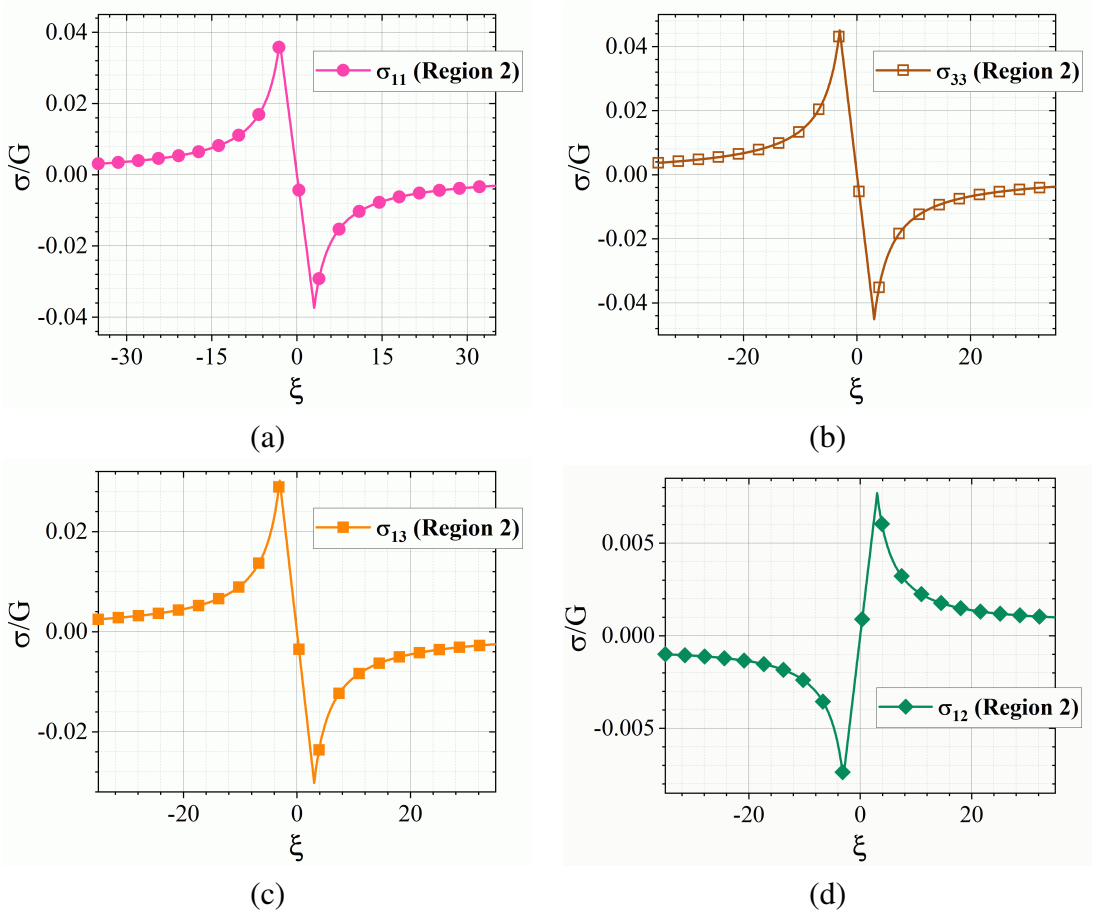

Figure 7.6: Plots of different stress components, in Region 2, along the ξ direction in an xy-plane containing a dislocation segment and passing through the center of the segment. Note that in all these plots, the curve passes through the (0,0) point. (a) σ_{11}, (b) σ_{33}, (c) σ_{13}, (d) σ_{12}

Upon implementation of the algorithm above, one can verify the produced results in several way. For example, let's take a segment AB of length $150\sqrt{2}$ lying in the $xy-$plane for simplicity. The coordinates of points A and B are $(-100b,-50b,0)$ and $(50b,100b,0)$, respectively. Let's also take a Burgers vector equal to: $1/\sqrt{3},1/\sqrt{3},1/\sqrt{3}$ for simplicity. The reason for choosing a Burgers vector with all three components not being zero is to

elucidate any possible contributions from these components to the different stress components. Here, $\mu = G = 1$ and $\nu = 0.33$.

Figure 7.6 shows plots for three stress components (σ_{11}, σ_{12}, σ_{13} and σ_{33}) versus coordinate ξ (expressed, and any coordinate, in units of b) which is perpendicular to the dislocation line and passing through the segment's center. The reason these components are chosen is that the first one (σ_{11}) is the same plot as σ_{22} and the third (σ_{13}) is the same plot as σ_{23}. In this figure, one can notice that all the stress components follow the schematic plot for stress distribution in Fig. 7.5. Per Fig. 7.5, the plots in Fig. 7.6 could be used to find a good estimate for r_c based on the reported values for the maximum shear stress provided in the textbooks of Hull and Bacon [2] and Meyers and Chawla textbook [52] (see above). Based on these three estimates for the maximum shear stress value, Table 7.1 can be generated and it shows estimates of r_c based on maximum shear stress values (or correspondingly maximum normal stress values from introductory mechanics of materials, see above). Based on the tabulated values, a conservative estimate for the core radius r_c is 2.75b (or $\sim 3b$). Notice that this value is between those reported in the literature (For example, Hirth and Lothe [11] took r_c as 1b, Hull and Bacon [2] took it as 1b-4b, Meyers and Chawla [52] took it as 5b, and so forth).

In addition to above, one now can do contour plots for the above dislocation segment example which lies in the *xy*-plane. Now that the above algorithm is implemented, Fig. 7.7 shows contour plots for all the stress components. Note that the plot for σ_{23} is the same as for σ_{13}. The plots are done using $r_c = 3b$ in Region 2. Notice that the stress levels in these contour plots is considerably less than those in Fig. 7.2 since (by employing the above algorithm) the stress levels are either capped in Fig. 7.2 based on theoretical grounds in Region 2 or the weak singularity completely removed/terminated in Region 3. Moreover, notice in these new figures, the perfect symmetry or anti-symmetry alluded to earlier around the plane perpendicular to the segment at is center. This is another indication of

	r_c based on: $\tau_{max} = \frac{G}{2\pi}$	r_c based on: $\tau_{max} = \frac{G}{5.1}$	r_c based on: $\tau_{max} = \frac{G}{30}$
σ_{11}	0.3620	0.2942	1.7423
σ_{22}	0.3620	0.2942	1.7423
σ_{33}	0.4299	0.3394	2.0478
σ_{23}	0.5770	0.4639	2.7492
σ_{13}	0.5770	0.4639	2.7492
σ_{12}	0.2828	0.2263	1.3463

Table 7.1: Calculation of r_c, in terms of b, based on the maximum shear stress or normal stress values using three different sources for the maximum value

the success of the above algorithm in attaining the goals of this work.

Another verification of the efficacy of the employed procedure or algorithm is shown in Fig. 7.8 which shows line plots for the different stress components, all for Region 3. All of these line plots are for the segment mentioned above which lies in the $xy-$plane (with b equal to unity here for simplicity). Here again, and for this particular segment, the plot σ_{23} is the same as for σ_{13}. The ξ parameter here is also normal to the dislocation line and lying in the $xy-$plane as before but it is perpendicular to the line (or really the line extension) in Region 3 and not in Region 2 like the plots in Fig. 7.6. For completeness sake, the ξ line was behind point A by 50b although the exact distance behind will only influence the values on the plotted stress components but not the shape of the curve. It is clear in Fig. 7.8, that by applying the above algorithm, that there are no singularities, not even the weak singularity, expected to be found in Region 3. Hence, the above method is working well again for eliminating the singularities associated with the core region of the dislocation segment. Notice that in Region 3 one can have a similar result to Fig. 7.8 by making $r_c \to \varepsilon$ and not just by flipping the line sense. This was pointed out in the procedure above.

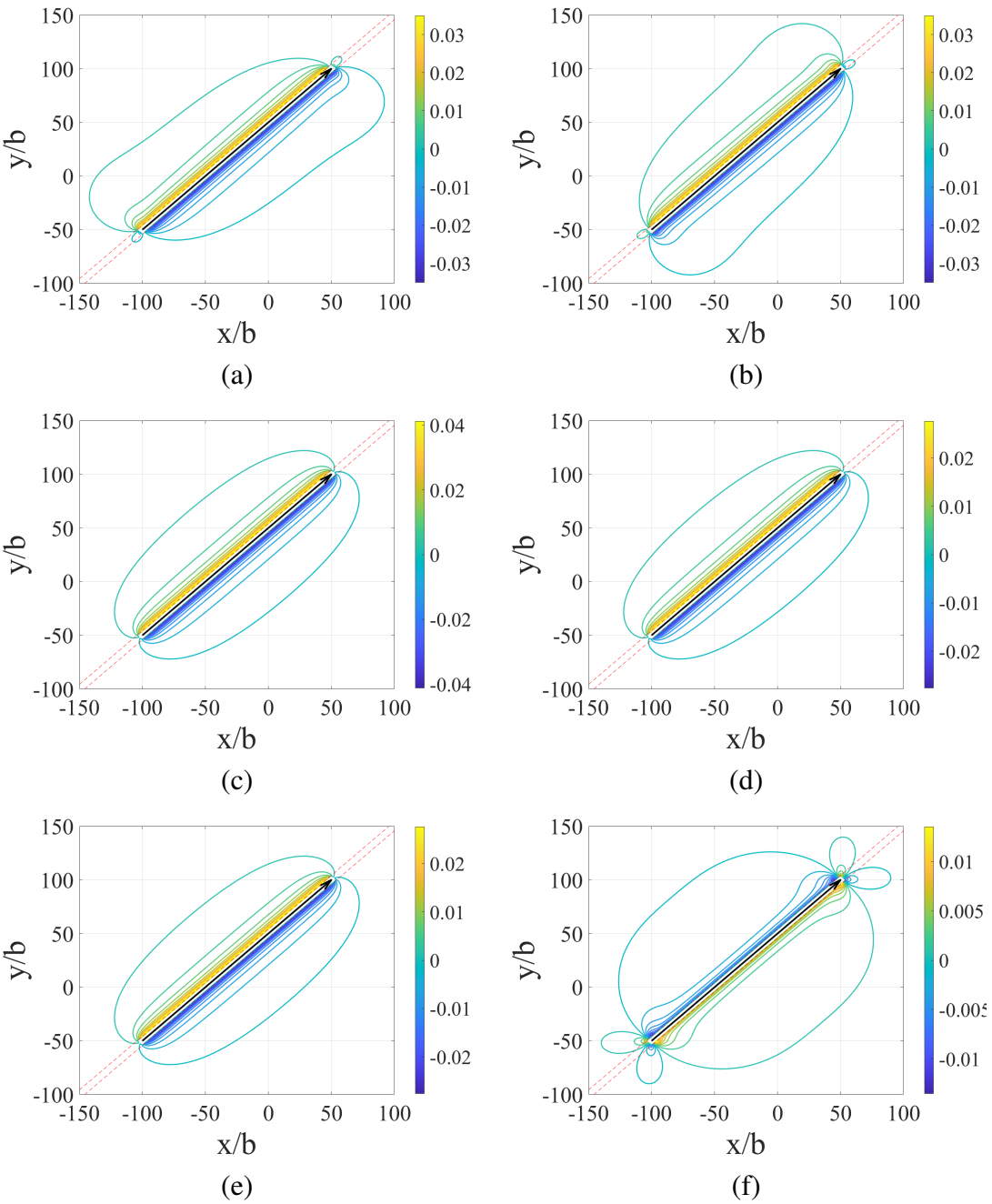

Figure 7.7: Contour plots around a linear dislocation segment lying in the $xy-$plane. These are made after implementing the algorithm in this paper. Applying the algorithm for the parameters: $r_c = 3b$, the coordinates of point A are (-100, -50, 0) and for point B are (50, 100, 0). Here, the Burgers vector = $(1/\sqrt{3}, 1/\sqrt{3}, 1/\sqrt{3})$ for simplicity. Here, $\mu = G = 1$ and $\nu = 0.33$. (a) σ_{11}, (b) σ_{22}, (c) σ_{33}, (d) σ_{23}, (e) σ_{13} and (f) σ_{12}

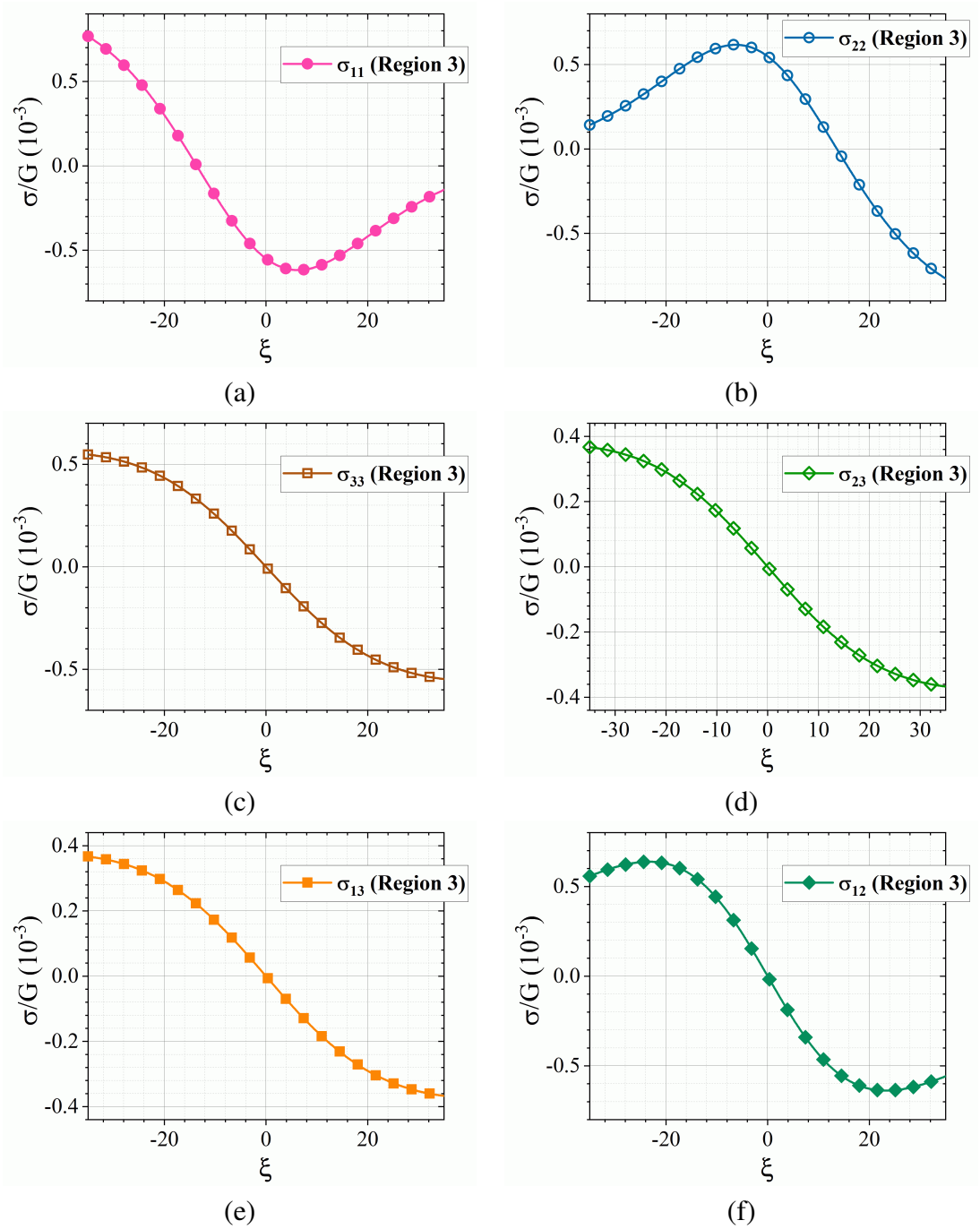

Figure 7.8: Line plots of stress showing the disappearance of the singularity in Region 3 with the application of the method in this paper. (a) σ_{11}, (b) σ_{22}, (c) σ_{33}, (d) σ_{23}, (e) σ_{13}, (f) σ_{12}

In addition to the above examples on the efficacy of the method or algorithm of this paper, another application of the method is presented here. In dislocation problems, both static and dynamic, the issue of dealing with the presence of a free surface in the computational domain frequently presents itself. Although there are different ways to deal with existence of free surfaces that can be found in the literature [46], [47], [48], [49], the focus here is on works that utilized the "collocation point method" to ensure that such surface is free from stress traction [69], [16], [17], [18]. The problem arises because analytical solutions for dislocation segments are provided (as in Eqs. (7.1) and (7.2) above, [11], or [63]) for infinite mediums. Such analytical solutions are the basis for discrete dislocation dynamics (DDD) simulations alluded to earlier [15], [61], [57], [51]. However, such DDD simulations are implemented in a finite or confined three-dimensional space or computational domain. When this domain contains free surfaces, additional stress terms (generally referred to historically as "image stresses") are needed to augment or complement the analytical dislocation segment solutions in order for the zero stress-traction condition to be met, even if partially, on the free surface. In the collocation point method, the zero traction condition is enforced on a collection of N surface points, called collocation points. As $N \rightarrow$ infinity, the solution approaches any analytical solution (if one existed). In the collocation point methods presented in [69], [16], [17], [18], the free surface is meshed by a contiguous uniform mesh or grid (see Fig. 7.9a), resulting in rectangular/square elements all of equal size, the center of each such element is a collocation point. Moreover, the extra "image stresses" at any crystal field point beneath the planar free surface come from the fact that each surface element in the mesh/grid stands for a generally-prismatic dislocation loop whose Burgers vector components are yet to be determined. The reason for choosing the elements as dislocation loops (which are fictitious or mathematical dislocation loops and not real or crystal ones) is two folds:

a Each such dislocation loop represents a self-equilibrated source of stress in the calculations and hence employing such loops does not disturb the spatial equilibrium

or even compatibility in the computational domain.

b Such dislocation loops can provide the extra or complementary stresses representing the "image stresses" mentioned above.

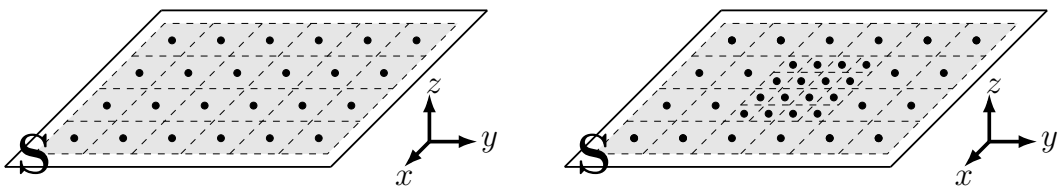

(a) (b)

Figure 7.9: Free surfaces (a) and (b) meshed by regular or irregular meshes with the dots representing collocation points. Dislocations lie beneath the surface in the material. (a) Regular mesh, (b) On-the-fly mesh

The problem of such mesh-based collocation method boils down to finding the Burgers vector components (bx, by, bz) of each loop on the surface. The way to find these Burgers vector components is equations that annul the traction $\vec{T}(\vec{T} = \sigma\vec{n}$, where $\boldsymbol{\sigma}$ is the stress state and $\vec{n}$ is a unit normal vector) at each of the N collocation points. For Fig. 7.9a, and using elementary continuum mechanics [4], the zero traction condition on the collocation points translates to enforcing $\sigma_{zx} = \sigma_{zy} = \sigma_{zz} = 0$ on each such point. Mathematically, the problem is formulated as such:

$$\sum_{j=1}^{N} \sigma_{xz}^{j\to i} = -\sigma_{xz}^{AB\to i}, \quad i = 1,2,\ldots N \tag{7.9a}$$

$$\sum_{j=1}^{N} \sigma_{yz}^{j\to i} = -\sigma_{yz}^{AB\to i}, \quad i = 1,2,\ldots N \tag{7.9b}$$

$$\sum_{j=1}^{N} \sigma_{zz}^{j\to i} = -\sigma_{zz}^{AB\to i}, \quad i = 1,2,\ldots N \tag{7.9c}$$

where $\sigma_{\alpha\beta}^{j\to i}$ is the $\alpha\beta$ stress component of loop j evaluated or calculated at collocation point i (which is the center of Loop i). Also, $\sigma_{\alpha\beta}^{AB\to i}$ is the $\alpha\beta$ stress of segment AB

evaluated at point i. Here the stress from all surface loops is counter-acting the stress of the subsurface dislocation segment(s) (which is given or provided as if the medium is infinite). On the right side of Eq. (7.9), although only the stress of one dislocation segment is displayed, it can instead be the sum of stresses from multiple dislocation segments (M of them) all under the free surface. Moreover, the above equations can be re-written as in Eqs. (7.10), where each loop stress is expressed as a linear combination of the loop's Burgers vector components and "kernel" terms which are functions of space and elastic constants. This separation of the Burgers vector components is attainable from basic linear elasticity dislocation theory (see [2], [11]). The recent work of Siddique and Khraishi [18] has explicitly provided the kernel terms in detail based on analysis of the Eqs. (7.1) and (7.2) above provided by Devincre [44].

$$\sum_{j=1}^{N} b_x^j K_{xxz}^{j\to i} + b_y^j K_{yxz}^{j\to i} + b_z^j K_{zxz}^{j\to i} = -\sigma_{xz}^{AB\to i}, \quad i = 1,2,\ldots N \tag{7.10a}$$

$$\sum_{j=1}^{N} b_x^j K_{xyz}^{j\to i} + b_y^j K_{yyz}^{j\to i} + b_z^j K_{zyz}^{j\to i} = -\sigma_{yz}^{AB\to i}, \quad i = 1,2,\ldots N \tag{7.10b}$$

$$\sum_{j=1}^{N} b_x^j K_{xzz}^{j\to i} + b_y^j K_{yzz}^{j\to i} + b_z^j K_{zzz}^{j\to i} = -\sigma_{zz}^{AB\to i}, \quad i = 1,2,\ldots N \tag{7.10c}$$

The above system represents a system of $3N$ equations, the unknowns of which are the Burgers vector components of the N loops. Once the Burgers vectors of the loops are solved for, the stress field at any material/field point P in the crystal below the surface can be calculated as follows:

$$\sigma_{\alpha\beta}^{P} = \sum_{i}^{M} \sigma_{\alpha\beta}^{i} + \sum_{j}^{N} \sigma_{\alpha\beta}^{j} \tag{7.11}$$

where the first sum on the right-hand side is for M dislocation segments under the surface and the second sum is for N dislocation loops meshing the free surface. In the [18] paper, and in reference to Fig. 7.9(a), the paper presented a rule of thumb based on Saint-Venant's principle, to determine the accuracy of the collocation-point method for calculating stress at any given field point. The rule of thumb states that the distance (z-distance in this case)

below the free surface needs to be equal or more than the average spacing between surface collocation points. For example, if each side of surface S in Fig. 7.9(a) is 20,000b (where b is the Burgers vector magnitude), then if the field point is 400b below the free surface that means that the average spacing between the surface collocation points need to be at max 400b. For the contiguous uniform mesh or grid in Fig. 7.9(a), that means that number of elements/loops lining up each side of the surface is 50 resulting in a 50×50 mesh, i.e. 2,500 elements/loops minimum covering the surface.

With the advent of this paper's method/algorithm above, a different way of meshing presented in Fig. 7.9(b) above can be utilized that would cut significantly on the computation time. Figure 7.9(b) shows a non-uniform mesh. This mesh is called here "on-the-fly" mesh because the idea is that one can start with a coarse (i.e. with few elements) uniform and contiguous mesh and then once a dislocation segment of a real crystal dislocation approaches the free surface in a dynamic simulation, and it is important to invoke the above-mentioned Saint-Venant's rule-of-thumb, then one or more of the large surface elements could be split into smaller elements in order to get back into compliance with the rule-of-thumb. For the sake of illustration, Fig. 7.9(b) shows that four large elements/loops in Fig. 7.9(a) were split into 4 smaller elements/loops each. Notice that in this new mesh, some of the new segments for the smaller loops can intersect, in their Region 3, a collocation point in bigger loops. This will cause a numerical issue, as pointed out above, if no proper treatment is utilized for Region 3 as introduced here in this work.

To illustrate the discussion above regarding Saint Venant's principle, on-the-fly meshing and the associated time savings when employing the collocation point method, consider a frontal view of Figs. 7.9(a) and 7.9(b) in Fig. 7.10.

In Fig. 7.10, a segment (called segment AB) is shown below a free surface. The two end points or nodes are labelled A & B. The segment is shown horizontal but could also be

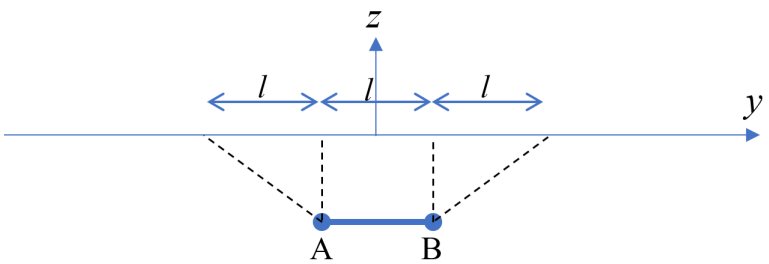

Figure 7.10: A segment below a free surface to illustrate the principles used for meshing the surface with dislocation loops the center of each is a collocation point.

inclined arbitrarily. The segment, or its closest point to the surface, is at a certain depth (z-depth) from the surface. If as above (Fig. 7.9), one considers a rectangular free surface such that each of its sides is 20,000b in length. Then according to Saint Venant's principle, in order for the collocation point method to work accurately it requires a spacing between the collocation points (centers of mesh elements/loops) to be equal to or less to the z-depth of the segment in this figure. Taking the z-depth to be 400b this means that the average spacing of collocation points should be 400b or less. Dividing 20,000b by 400b gives 50. Therefore, the size of each of the mesh surface elements/loops in the uniform contiguous mesh in Fig. 7.9(a) will be 400b or smaller. In other words, the total number of surface elements/loops is 2,500 (50×50 mesh) which is also the number of collocation points (N in Eqs. (7.9) or (7.10)).

However, another question begs itself. When the larger elements/loops are divided into smaller ones, how big is the size of the area to be divided as such? The authors hypothesize that another/second application of Saint Venant's principle can be made here. Specifically, by looking at Fig. 7.10, if the length of the segment is l (or its projected length on the free surface) then another length l should be added to each end of the surface projection for a total length of 3l (see Fig. 7.10). Now this ($3l \times 3l$) area can be divided into smaller elements/loops. This is the guideline to the creation of the "on-the-fly mesh". To test this new hypothesis, several figures/plots are created to verify it.

Figures 7.11, 7.12 and 7.13 show stress plots for the above-described segment AB which is here parallel to the free surface, by being also parallel to the x-axis, with the z-axis passing through the segment center. However, in these plots, the field points (all parallel to the x-axis with y=0) are at a z-depth = 400b. Specifically, the field line is from (-1,000b, 0, -400b) to (1,000b, 0, -400b). The z-depth for the segment in these figures is 1,000b. Also, the Burgers vector for the segment is taken as $(1/\sqrt{3}, 1/\sqrt{3}, 1/\sqrt{3})$. In all of these figures, we first start with a coarse mesh (25×25 elements/loops = 625 elements/loops). Secondly, we make the first application of St Venant's principle and thus have to use a mesh whose elements are at max 400b in size which generates a $50 \times 50 = 2,500$ loops/elements in the uniform mesh (see Fig. 7.9(a)). Third, we do an on-the-fly mesh by taking the center element in the 625 mesh and dividing it into four loops/elements (similar to Fig. 7.9(b)) to give a total of 628 loops/elements (625-1+4) in this non-uniform mesh. Fourth or lastly, we do an on-the-fly mesh by taking the center 9 elements (3×3) and divide each of them into four elements/loops (similar to Fig. 7.9(b)). This results into 652 (625-9+36) elements/loops total in this non-uniform mesh. In all of these figures, the collocation-point method using the segment algorithm described above, was compared to a known analytical solution by Maurissen and Capella [39] for a parallel dislocation segment in an isotropic half medium under an infinite surface plane. To make this comparison plausible with the finite surface employed in the numerical collocation point method, the dislocation segment is placed below the center of the surface and the surface dimensions or size is set to a large value, i.e. 20,000b.

Consider first Fig. 7.11. Here, Fig. 7.11(a) shows the 625 coarse mesh. Figure 7.11(b) shows the fine 2,500 elements/loops mesh. Figure 7.11(c) shows a non-uniform on-the-fly mesh with 628 elements, and Fig. 7.11(d) shows a non-uniform on-the-fly mesh with 652 elements/loops. For this figure, we consider a segment with length l = 100b (i.e. A coordinates are (-50b, 0 ,-1,000b) and B coordinates are (+50b, 0 ,-1,000b). For the 625 uniform mesh, the average spacing between the collocation points is 800b. Since the field

points depth is only 400b, the numerical solution is not expected to (nor does it) match the analytical solution in accordance with the first application of Saint Venant's principle. This is clearly reflected in Fig. 7.11(a). For the 2,500 mesh, the average collocation points spacing is 400b, so it is expected that the numerical solution matches the analytical solution for this case since the field points depth is 400b. Figure 7.11(b) shows such match. For the 628 non-uniform on-the-fly mesh, since the average collocation point spacing in the refined area right above the dislocation segment is 400b and the second application of Saint Venant's principle is valid (i.e. the refined mesh size of 800b is at least 3l = 300b here), it is expected to find a match between the analytical and numerical solutions. Figure 7.11(c) shows such match. Lastly, for the 652 non-uniform on-the-fly mesh, both applications of the Saint Venant's principle apply here and hence a match is expected between the numerical and analytical results. This is shown in Fig. 7.11(d).

Consider Figs. 7.12(a-d) which have 625 elements (uniform mesh), 2,500 elements (uniform mesh), 628 non-uniform on-the-fly mesh, and 652 non-uniform on-the-fly mesh, respectively. For these figures, we consider a segment with length l = 200b (i.e. A coordinates are (-100b, 0 ,-1,000b) and B coordinates are (+100b, 0 ,-1,000b). Figure 7.12(a) does not match the analytical solution because it fails to meet the first application of Saint Venant's principle whereas Fig. 7.12(b) does for these two uniform meshes. However, if one resorts to non-uniform meshing through on-the-fly meshing then Fig. 7.12(c) also shows disparity with the analytical solution since the second application of Saint Venant's fails here. However, if more larger elements than one element are sub-divided into smaller ones as in the 652 mesh in Fig. 7.12(d) then a match occurs between the analytical and numerical. This is so since the second application of Saint Venant's principle applies here. In this last figure, the finer mesh (i.e. sub-divided mesh) side length is 2,400b ($3 \times 800b$) which is greater than 3l (600b).

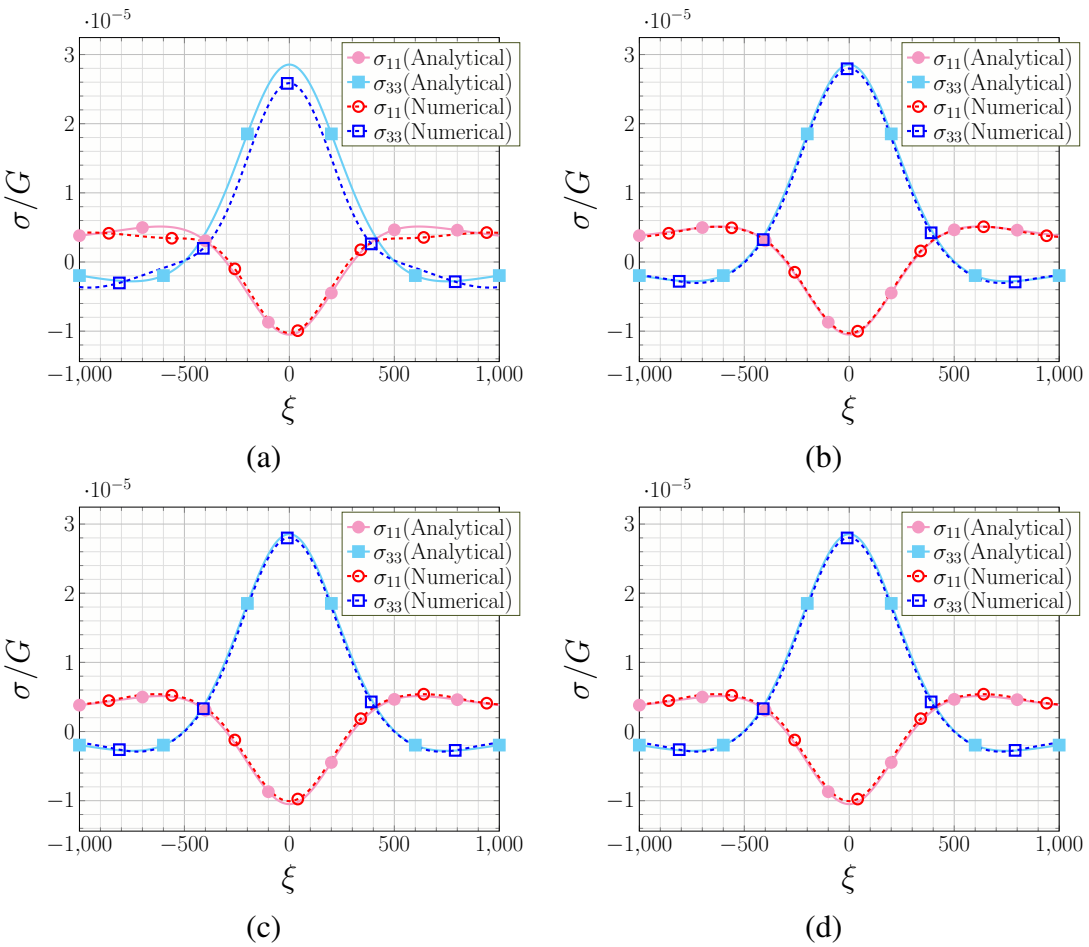

Figure 7.11: Comparison between the numerical collocation point method solution and analytical solution of Maurissen and Capella [39] for a horizontal segment beneath a free surface. Here, segment length l = 100b, i.e. A coordinates are $(-50b, 0, -1,000b)$ and B coordinates are $(+50b, 0, -1,000b)$. (a) Uniform surface mesh, 625 elements, (b) Uniform surface mesh, 2500 elements, (c) Non-uniform on-the-fly surface mesh, 628 elements, (d) Non-uniform on-the-fly surface mesh, 652 elements.

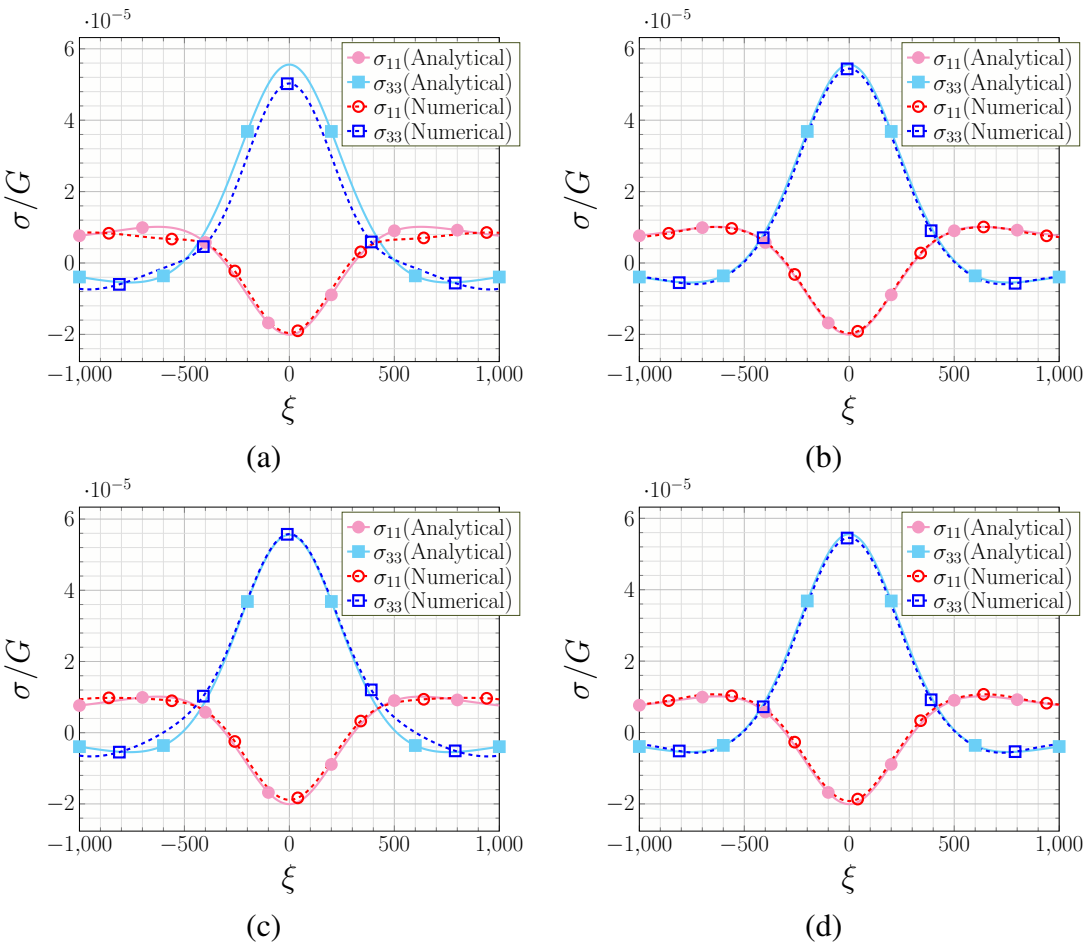

Figure 7.12: Comparison between the numerical collocation point method solution and analytical solution of Maurissen and Capella [39] for a horizontal segment beneath a free surface. Here, segment length l = 200b, i.e. A coordinates are (-100b, 0 ,-1,000b) and B coordinates are (+100b, 0 ,-1,000b). (a) Uniform surface mesh, 625 elements, (b) Uniform surface mesh, 2500 elements, (c) Non-uniform on-the-fly surface mesh, 628 elements, (d) Non-uniform on-the-fly surface mesh, 652 elements.

The mismatches above with the 625 mesh and the 628 mesh continues with increased segment length l for the rest of the fixed parameters above. Now consider Figs. 7.13(a-d) which also have 625 elements (uniform mesh), 2,500 elements (uniform mesh), 628 non-uniform on-the-fly mesh, and 652 non-uniform on-the-fly mesh, respectively. For these figures, we consider a segment with length $l = 800b$ (i.e. A coordinates are $(-400b, 0, -1,000b)$ and B coordinates are $(+400b, 0, -1,000b)$. According to the first application of Saint Venant's principle, the 625 and 628 should not show a match between analytical and numerical solutions and Figs. 7.13(a) and 7.13(c) reflect that. Also, for the 2,500 mesh there should still be a match between the two solutions and Fig. 7.13(b) reflect that. The small mismatch is due to the segment now being a significant percentage of the finite surface size of 20,000b which causes this situation to deviate even further from the infinite plane situation upon which the analytical solution is built. According to the second application of Saint Venant's, at this length l the 652 mesh which has a fine or sub-divided mesh equal to 3l ($3 \times 800b = 2,400b$) should be a borderline on-the-fly mesh case for seeking a match between analytical and numerical solutions. Looking at Fig. 7.13(d), it appears that this postulation is correct. Now if the segment length increases beyond 800b, it is expected that more mismatch will exist between the analytical and numerical solutions for the 652 mesh and that is indeed what is observed (figures are omitted here for brevity).

The above paragraphs illustrated the first and second applications of Saint Venant's principle in as far as the collocation point numerical method is concerned. Although the first application was introduced in prior works [69], [16], [17], [18], the second application introduced here was shown to be applicable and thus important for the on-the-fly meshing. The on-the-fly meshing was conceptualized in an effort to reduce computational time involving the system of equations above (Eqs. (7.9) and (7.10)). To show the amount of time savings in the computations, Table 7.2 lists the time it took to compute the stress field in the previous figures (Figs 7.11-7.13). The table shows that for the 625, 628 and 652 the computational time is similar. However, when employing the on-the-fly meshes (i.e.

Number of surface elements/loops/collocation points	Time (seconds) to compute stress field
625	32.26
628	35.88
652	38.67
2,500	452.34

Table 7.2: Comparison of the computational time for on-the-fly meshes with regular uniform meshes

628 and 652), a great reduction in computing time occurs compared to the fine mesh used in these prior references. For example, with the 652 mesh a time reduction from the fine mesh of 91.45% which is very significant since the outputted stress results are essentially the same.

With the new segment algorithm described above, other types of meshes on a free surface (besides ones shown in Fig. 7.9) are possible, like unstructured meshes (See Fig. 7.14). For such meshes, especially with a high number of elements, it is possible that numerical issues stemming from the Region 3 singularity pop up when evaluating the Kernel terms at collocation points representing the center of the elements/loops (see discussion above on the collocation-point method). For this random or unstructured triangular mesh, one can plot figures similar to Fig. 7.11-7.13 above, to show that the collocation-point method produces the correct surface correction terms ("image stresses") in compliance with the Maurrisen and Capella [39] analytical solution. However, such plots are not provided here for brevity. For the collocation-point method described above, the term $\sigma_{xz}^{j\to i}$ in Eq. (7.9a) becomes here equal to $\sum_{l=1}^{3}\sigma_{xz}^{jl\to i}$, where $\sigma_{xz}^{jl\to i}$ is the σ_{xz} stress component of the $l-$th segment of loop j acting at collocation point i. Similarly for Eqs. (7.9b) and (7.9c). For Eq. (7.11), $\sigma_{\alpha\beta}^{j}$ becomes for a triangular mesh with triangular loops/elements: $\sum_{l=1}^{3}\sigma_{\alpha\beta}^{jl}$, where $\sigma_{\alpha\beta}^{jl}$ is the $\sigma_{\alpha\beta}$ stress component of the $l-$th segment of loop j acting at at any material/field point P.

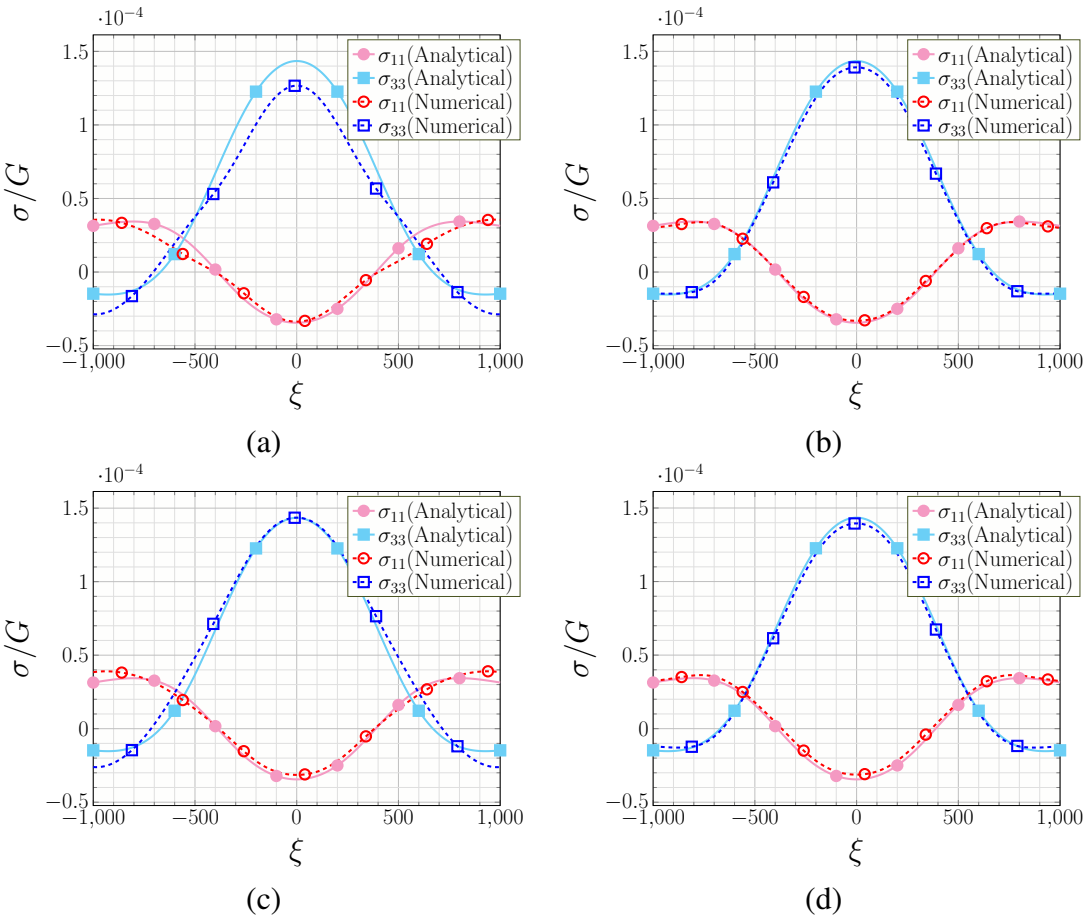

Figure 7.13: Comparison between the numerical collocation point method solution and analytical solution of Maurissen and Capella [39] for a horizontal segment beneath a free surface. Here, segment length l = 800b, i.e. A coordinates are (-400b, 0 ,-1,000b) and B coordinates are (+400b, 0 ,-1,000b). (a) Uniform surface mesh, 625 elements, (b) Uniform surface mesh, 2500 elements, (c) Non-uniform on-the-fly surface mesh, 628 elements, (d) Non-uniform on-the-fly surface mesh, 652 elements.

Alternatively, one can illustrate the use of this mesh in 3-D DDD simulations using the following parameters: constant strain-rate loading in the yz direction, applied strain-rate of $10s^{-1}$, one Frank-Read source lying on the x-axis with end point coordinates of (-2000b, 0, 0) & (2000b, 0, 0), Burgers vector $\vec{b} = (0,1,0)$, the computational box (or RVE) is $10,000b$ in each side of the cube, the shear modulus $\mu = G = 26.32$ GPa, ν = 0.33,

mass density =2,710 kg/m^3, and the dislocation mobility equaling 1,000 1/(Pa·s). In these simulations, the unstructured triangular mesh is used on each of the six surfaces of the computational box. Figure 7.15 compares the stress-strain results from the DDD simulations for two situations: one not accounting for the free surface effects, and one employing the collocation point method using the mesh in Fig. 7.14 to account for the effect of free surfaces. As can be seen in Fig. 7.15, the incorporation of correct free surface effects reduces the flow stress in the material by about 23%. This amount is considerable and its exact number depends on factors such as the source length, the surface-to-volume ratio, etc. Additionally to above, the new algorithm can also prevent the Region 2 or Region 3 singularities from talking place when an ensemble of dislocation segments are interacting in space inside the DDD computational domain/box.

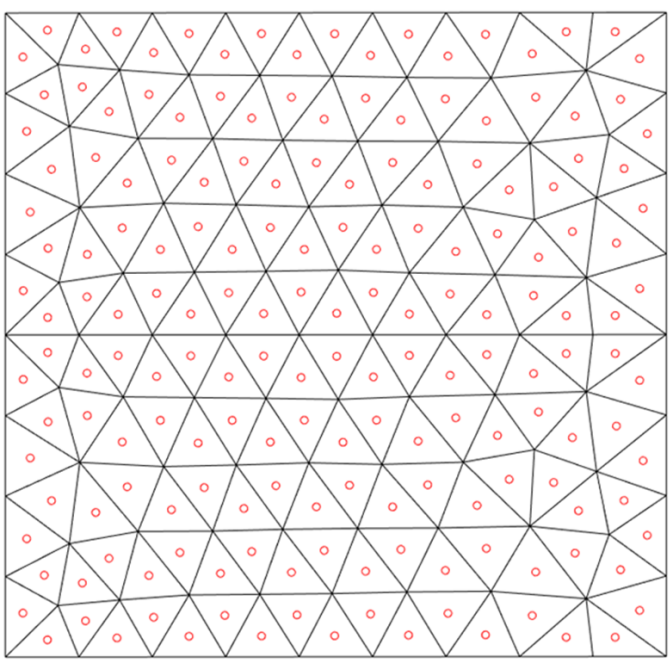

Figure 7.14: An unstructured triangular-element mesh used in the collocation-point method for properly treating free-surface problems in the presence of dislocations

Instead of using a constant-strain rate experiment, as in Fig. 7.15, a creep experiment can

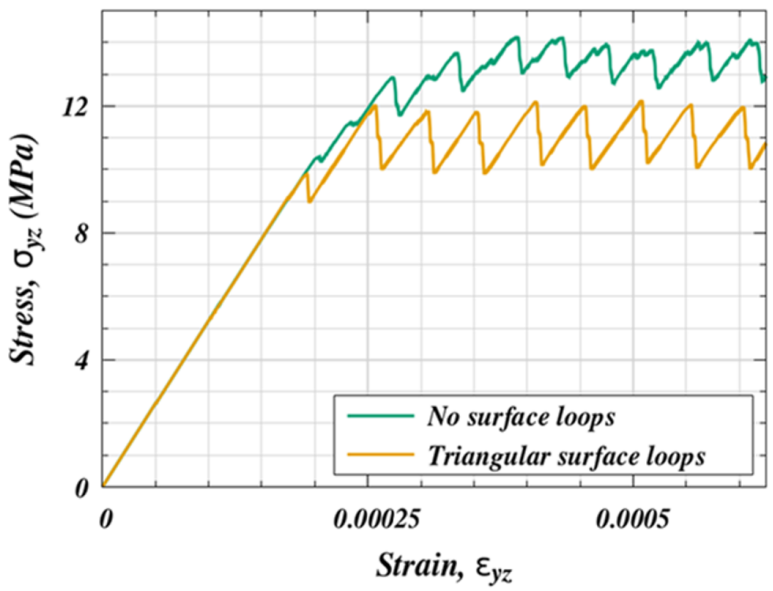

Figure 7.15: Stress-strain diagrams for a case with no free surface effects (No surface loops) and a case with free surface effects (Triangular surface loops). The computational box is subjected to constant strain-rate loading

be performed. If the source is placed parallel and closely beneath a free surface, the image stresses should be enough, once overcoming the lattice friction, to pull the dislocation out of the crystal. Figure 7.16 shows such simulation with the different colors showing different time shots or snaps in time. The initially straight dislocation bow outs until it gets absorbed in the surface at its middle region. The dislocation line continues to sink in the free surface until at the end only two screw segments remain on both ends.

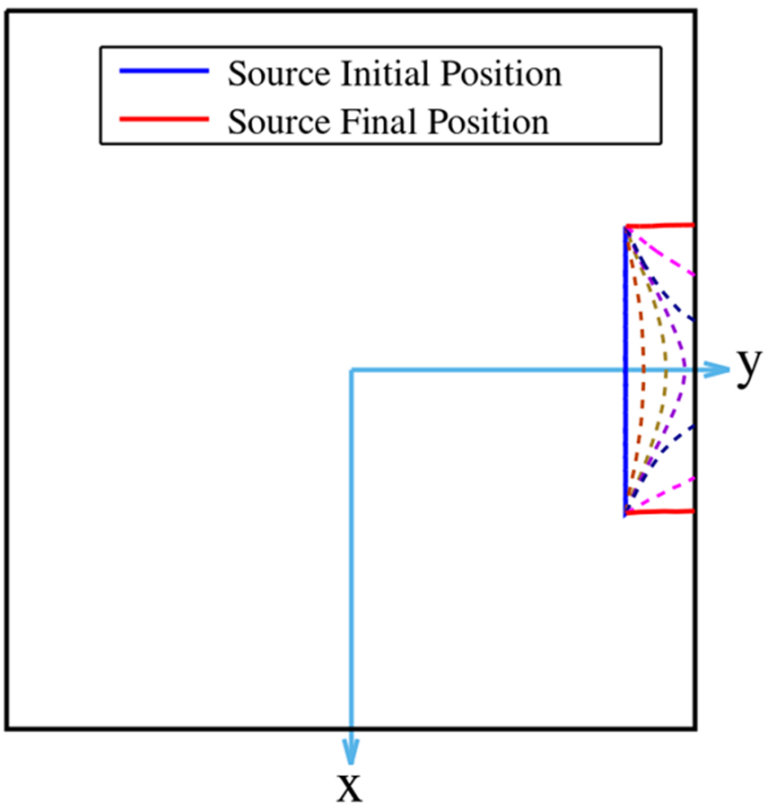

Figure 7.16: A dislocation source parallel and close to a free surface. The initially edge-character source gets absorbed into the free surface as shown by the time stills of the source (shown in dashed lines followed by the final source position

7.4 Conclusions

Based on this research which properly treats the stress field around a dislocation segment and its trailing line, i.e. its core region, to regularize it, the following conclusions can be made. The space around the segment can be partitioned into three regions: one regular region ahead of the segment, and one with a weak singularity in the trail of the segment and one immediately around the core of the segment with a strong singularity. Also, the r_c (cutoff radius or radius of the core region) is found to be $3b$ which is a recommendation stemming out of this work. Another conclusion is that the developed algorithm expands the type of surface meshes used in collocation-point methods by allowing on-the-fly meshing or unstructured meshes. This could generate time savings in the computations. The accuracy of the meshes' results is subject to St Venant's principle. Lastly, the research shows the importance of incorporating image-stress effects for a free surface as that could significantly impact the calculated flow stress of the material. The algorithm also could prevent problems in 3D DDD when dealing with ensembles of interacting and time-evolving dislocations in space.

Journal reference

Siddique, A. B., & Khraishi, T. A. (2021). The treatment of singularities associated with a dislocation segment with applications. Int. J. Theoretical and Applied Multiscale Mechanics, 3(4), 287–312.

Chapter 8

Dislocation multipoles in a crystal

Abstract

Plastic deformation in metals is dominated by the interactions among dislocations and other defects inside the crystal. A large number of dislocation multipoles (dipoles, tripoles, quadrupoles, etc.) can form during plastic deformation. Depending on the relative position and the orientation of the dislocations, interactions in and between multipoles can change the elastoplastic properties of a material. The authors of this article investigate the effect of dislocation multipoles on the elastoplastic properties of a material. This is performed analytically under different multipole configurations (i.e. the distance between active glide planes and the signs of the dislocations) as well as using a 3D Discrete Dislocation Dynamics (DDD) code. The simulations show that multipoles exhibit a hardening/softening effect when the sign of the dislocations involved is the same, and a hardening effect only when the dislocations are of opposite sign to nearby ones. The distance between the two neighboring dislocations was also affecting the proportional limit for the material. Such hardening or flow stress results, as in this study, can be incorporated into larger-scale modeling work.

8.1 Introduction

Dislocations are a type of defect in crystalline materials. They are labeled as “line defects.” In a typical crystal, many dislocations can exist and the dislocation density and structure will have an effect on the physical properties of the material. When two or more dislocations interact closely from same/different slip planes, they are labeled as ”multipoles.” Multipoles can be of edge or screw type.Depending on the proximity of the dislocations in the multipoles,interactions among the dislocations can affect the elastoplastic properties [72] . A material can be hardened or softened as a consequence of these interactions.Stokes and Olsen [73] and Kroupa [27] described the mechanism of dipole formation for both screw and edge dislocations. Gilman [72] and Neumann [74] studied the interaction between dislocations and dislocation dipoles, tripoles, and quadrupoles. In the two-dimensional study by Neumann [74], it was found that decomposition,i.e., splitting of the dipole usually occurs more often than trapping of the approaching dislocations.To understand dislocation phenomena in the plastic regime,researchers and scientists developed several codes that can simulate the dynamic behavior of dislocation interactions under simple to complex configurations, which are often not captured in real experiments.Kubin et al. [45] introduced a basic framework for three dimensional(3D) dislocation dynamics simulations and various features were introduced in more recent dislocation dynamics codes. In the current study, the simulations are performed on a dislocation dynamics code developed by Refs. [51], [75], [76], [17], [55], [15], [18], [35], [77].

The first work to look at dipole interactions using discrete dislocation dynamics(DDD) simulations is by Ref. [78]. In such work, it showed dynamic zipping and unzipping, i.e., dynamic coupling/de-coupling of dipole dislocations. Such dipole sources were initially remote from one another unlike the initial equilibrium stacking studied herein.The nature (stable/unstable) of the equilibrium points in a multipole configuration plays a vital role in the elastoplastic behavior.The authors of this article present an analytical/theoretical model

for stability analysis for any number of dislocations in a multipole configuration. This is something that was lacking from the literature.All the analytical/theoretical model cases presented in this article consider the dislocations as infinitely long. Although such studies can provide an understanding of multipole stability, the infinite length of the dislocation preclude the line tension effect, and the interplay between line tension and remote interactions, on elastoplasticity.To address this lacking knowledge, we therefore also show DDD simulation results of staggered Frank–Read (FR)sources [79] (pinned dislocation segments on different slip plane)in a 3D finite volume. These represent multipoles in real-world problems since both the medium and the dislocations are finite.Such simulations capture both the line tension and the interaction effects on a material's elastoplasticity.Detailed development of the interaction equations among the dislocations in a multipole configuration is shown in the Theory section, and the stability analysis is shown in the Stability of Multipoles section. The simulation setup is discussed in the Simulation Methodology section for the reproducibility of the results. A comprehensive discussion of the simulation results is presented in the Results and Discussion section.

8.2 Theory

The thermodynamic force $\vec{F}$ (also known as the Peach-Koehler force) acting on a dislocation can be calculated by [11]

$$\vec{F} = (\boldsymbol{\sigma}\vec{b}) \times \hat{e} \tag{8.1}$$

where $\boldsymbol{\sigma}$ is the stress tensor at a point on a dislocation line due to internal and externally-applied stresses, $\vec{b}$ is the magnitude and direction of the crystal distortion associated with that dislocation (also known as the Burgers vector) and $\hat{e}$ is a unit vector along the dislocation line (i.e. the line sense vector). Dislocations move in a slip plane when the Peach-Koehler (PK) force is high enough to overcome the internal friction in the crystal. A dislocation source multiplies when this force is large enough to overcome the line

tension of the dislocation. Line tension T of a dislocation is given by [2]

$$T = \alpha G b^2 \tag{8.2}$$

where $\alpha \approx 0.5 - 1.0$ and b is the magnitude of the Burgers vector. In the multiplication of an initially straight Frank-Read source, it is assumed that plastic flow occurs when the dislocation bows a half-circle [2]. This is also known as critical bowing. For critical bowing, the critical shear stress is calculated as,

$$\tau_{crit} = \alpha \frac{Gb}{R} \tag{8.3}$$

where R is the radius of the bowed dislocation. A similar derivation for the line tension and τ_{crit} is given in [3].

8.2.1 Dipole

Consider two infinite (along z) edge dislocations laying on slip planes parallel to the xz plane and separated by a distance d, as shown in Figures. 8.1 and 8.2. The glide force, F_x (PK force) acting on either dislocation due to their interaction when they both have the same sign (Fig. 8.1) can be derived by inserting $\vec{b} = (b_x, 0, 0)$ and $\hat{e} = (0, 0, 1)$ in Eq. (8.1),

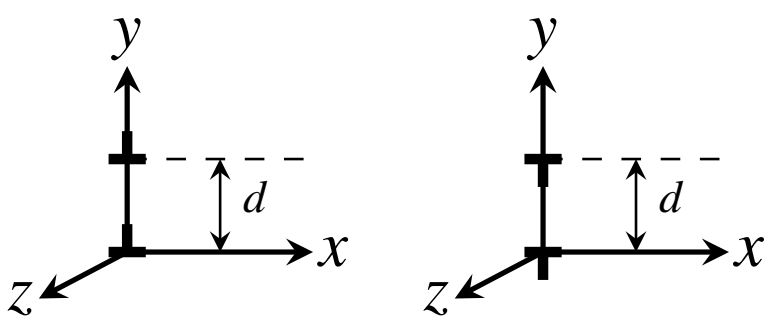

Figure 8.1: Dipole stable equilibrium (same sign dislocations)

$$F_x = \sigma_{xy} b_x \tag{8.4a}$$

$$F_x = \frac{G b_x^2}{2\pi(1-\nu)} \frac{x\left(x^2-d^2\right)}{\left(x^2+d^2\right)^2} \tag{8.4b}$$

$$\frac{F_x}{\kappa} = \frac{\left(\frac{x}{d}\right)\left[\left(\frac{x}{d}\right)^2-1\right]}{\left[\left(\frac{x}{d}\right)^2+1\right]^2} \tag{8.4c}$$

where, $\kappa = \frac{G b_x^2}{2\pi d(1-\nu)}$, G and ν are the shear modulus and the Poisson's ratio of the material. Equation (8.4)(b) was also provided in [2], [80], [81].

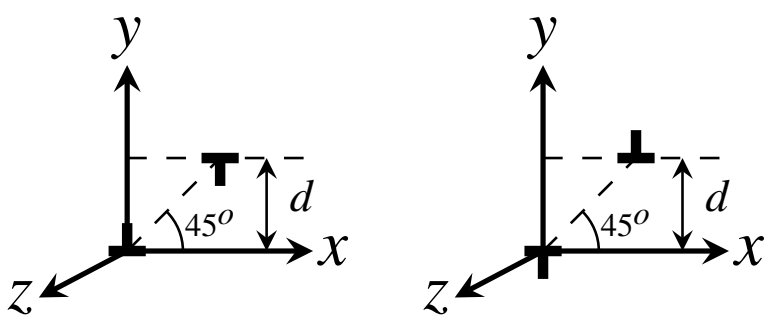

Figure 8.2: Dipole stable equilibrium (opposite sign dislocations)

When both dislocations have an opposite sign as in Fig. 8.2 (e.g. same Burgers vector but opposite line sense) one can insert $\hat{e} = (0,0,-1)$ in Eq. (8.1) and then write,

$$\frac{F_x}{\kappa} = -\frac{\left(\frac{x}{d}\right)\left[\left(\frac{x}{d}\right)^2-1\right]}{\left[\left(\frac{x}{d}\right)^2+1\right]^2} \tag{8.5}$$

8.2.2 Tripole

Tripoles can be formed in different configurations. Figure 8.3 shows two tripole arrangements where the dislocations lie on different slip planes. When all dislocations have the same sign (Fig. 8.3a), the glide force F_x at the top (or bottom) dislocation due to the interaction amongst the dislocations can be expressed as,

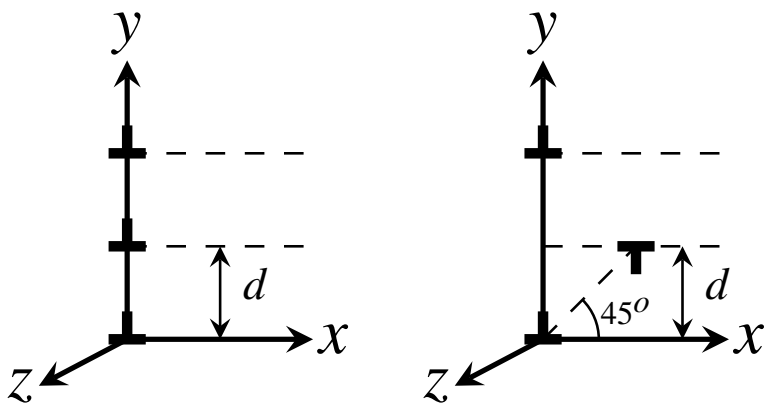

(a) (b)

Figure 8.3: Tripole configurations. (a) Same sign (b) Opposite sign in zigzag pattern

$$\frac{F_x}{\kappa} = \frac{\left(\frac{x}{d}\right)\left[\left(\frac{x}{d}\right)^2 - 1\right]}{\left[\left(\frac{x}{d}\right)^2 + 1\right]^2} + \frac{\left(\frac{x}{d}\right)\left[\left(\frac{x}{d}\right)^2 - 4\right]}{\left[\left(\frac{x}{d}\right)^2 + 4\right]^2} \tag{8.6}$$

And for the dislocation in the *middle*,

$$\frac{F_x}{\kappa} = 2\frac{\left(\frac{x}{d}\right)\left[\left(\frac{x}{d}\right)^2 - 1\right]}{\left[\left(\frac{x}{d}\right)^2 + 1\right]^2} \tag{8.7}$$

When the tripole dislocations are patterned in a zigzag (Fig. 8.3b) and are alternating in sign, the resulting glide force F_x at the top (or bottom) dislocation due to dislocation interactions is given by

$$\frac{F_x}{\kappa} = -\frac{\left(\frac{x}{d} - 1\right)\left[\left(\frac{x}{d} - 1\right)^2 - 1\right]}{\left[\left(\frac{x}{d} - 1\right)^2 + 1\right]^2} + \frac{\left(\frac{x}{d}\right)\left[\left(\frac{x}{d}\right)^2 - 4\right]}{\left[\left(\frac{x}{d}\right)^2 + 4\right]^2} \tag{8.8}$$

And for the dislocation in the middle,

$$\frac{F_x}{\kappa} = -2\frac{\left(\frac{x}{d}\right)\left[\left(\frac{x}{d}\right)^2 - 1\right]}{\left[\left(\frac{x}{d}\right)^2 + 1\right]^2} \tag{8.9}$$

8.2.3 General Multipole

In general, when all the dislocations have the same sign and are all lined up vertically, the glide force F_x on the top (or bottom) dislocation resulting from the interaction amongst the dislocations is given by

$$\frac{F_x}{\kappa} = \sum_{i=1}^{n-1} \frac{\left(\frac{x}{d}\right)\left[\left(\frac{x}{d}\right)^2 - i^2\right]}{\left[\left(\frac{x}{d}\right)^2 + i^2\right]^2} \tag{8.10}$$

And for the dislocation in the middle when the number of dislocations in the multipole n is an odd number,

$$\frac{F_x}{\kappa} = 2\sum_{i=1}^{(n-1)/2} \frac{\left(\frac{x}{d}\right)\left[\left(\frac{x}{d}\right)^2 - i^2\right]}{\left[\left(\frac{x}{d}\right)^2 + i^2\right]^2} \tag{8.11}$$

when n is even (middle is dislocation number $n/2+1$ counting from the bottom dislocation),

$$\frac{F_x}{\kappa} = \frac{\left(\frac{x}{d}\right)\left[\left(\frac{x}{d}\right)^2 - \left(\frac{n}{2}\right)^2\right]}{\left[\left(\frac{x}{d}\right)^2 + \left(\frac{n}{2}\right)^2\right]^2} + 2\sum_{i=1}^{n/2-1} \frac{\left(\frac{x}{d}\right)\left[\left(\frac{x}{d}\right)^2 - i^2\right]}{\left[\left(\frac{x}{d}\right)^2 + i^2\right]^2} \tag{8.12}$$

As for the top (or bottom) dislocation when all the dislocations in the multipole have a zigzag pattern (similar to Fig. 8.3b) and alternating in sign, the force is given by

$$\frac{F_x}{\kappa} = \sum_{i=1}^{n-1} (-1)^i \frac{\left(\frac{x}{d} - \xi_i\right)\left[\left(\frac{x}{d} - \xi_i\right)^2 - i^2\right]}{\left[\left(\frac{x}{d} - \xi_i\right)^2 + i^2\right]^2} \tag{8.13}$$

where, $\xi_i = \frac{1}{2} + \frac{1}{2}(-1)^{(n-i)}$. For the dislocation in the middle when n is an odd number,

$$\frac{F_x}{\kappa} = 2\sum_{i=1}^{(n-1)/2} (-1)^i \frac{\left(\frac{x}{d} - \xi_i\right)\left[\left(\frac{x}{d} - \xi_i\right)^2 - i^2\right]}{\left[\left(\frac{x}{d} - \xi_i\right)^2 + i^2\right]^2} \tag{8.14}$$

where, $\xi_i = \frac{1}{2} - \frac{1}{2}(-1)^{\frac{n-1}{2}-i}$ When n is even and for the middle dislocation (middle is dislocation number $\frac{n}{2}+1$ counting from the bottom dislocation)

$$\frac{F_x}{\kappa} = (-1)^{\left(\frac{n}{2}\right)} \frac{\left(\frac{x}{d}\right)\left[\left(\frac{x}{d}\right)^2 - \left(\frac{n}{2}\right)^2\right]}{\left[\left(\frac{x}{d}\right)^2 + \left(\frac{n}{2}\right)^2\right]^2} + 2\sum_{i=1}^{n/2-1}(-1)^i \frac{\left(\frac{x}{d}-\xi_i\right)\left[\left(\frac{x}{d}-\xi_i\right)^2 - i^2\right]}{\left[\left(\frac{x}{d}-\xi_i\right)^2 + i^2\right]^2} \tag{8.15}$$

where $\xi_i = \frac{1}{2} - \frac{1}{2}(-1)^{\left(\frac{n}{2}-i\right)}$ For a quadrupole and pentapole configurations, these are provided in Appendix B (the configuration, the glide force, and the glide force versus x).

8.3 Stability of Multipoles

Figure 8.4 shows the glide forces F_x for dipoles, as a function of x, and the equilibrium points (where $F_x = 0$) [2], [3]. For a dipole having same-sign dislocations (Fig. 8.1) there exists two unstable equilibrium points (at x = ±d) and one stable (middle) equilibrium point at the origin (at x = 0). The two unstable equilibrium points occur when the relative angle between the two dislocations is 45° and the stable equilibrium point occurs when the relative angle between the two dislocations is 0° (i.e. they are lined up vertically).

For the dipole with two oppositely-signed dislocations (Fig. 8.2), the dipole has two stable equilibrium points (at $x = \pm d$) and one unstable (middle) equilibrium point at the origin (at $x = 0$). %. The two stable equilibrium points occur when the relative angle between the two dislocations is 45° and the unstable equilibrium point occurs when the relative angle between two dislocations is 0° (i.e. they are lined up vertically).

For any perturbation from the equilibrium points, the glide force is directed towards the stable equilibrium points and away from the unstable equilibrium points. In other words, when any dislocation in a dipole configuration moves a little away from the stable equilibrium position, it feels a force that tends to bring it back to that stable equilibrium position.

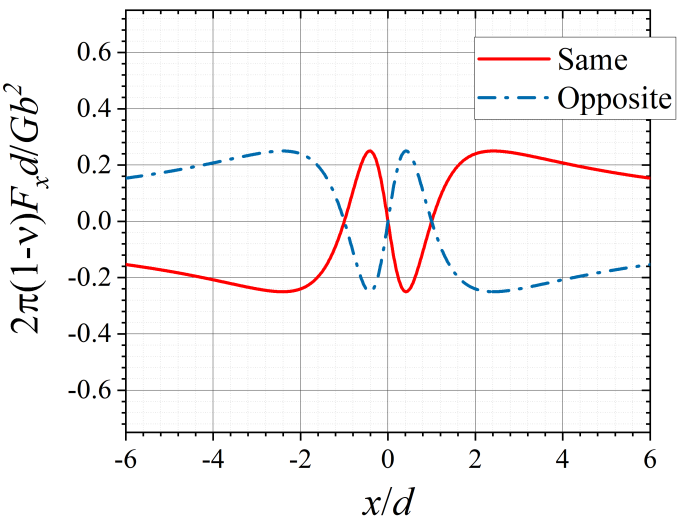

Figure 8.4: Normalized glide force between two parallel infinite edge dislocations of same and opposite signs

For an unstable equilibrium point, the opposite phenomenon occurs.

The region in space where a perturbation of the dislocation position tends to return it to an equilibrium point is termed a stable region, whereas a region in space where a perturbation of the dislocation position tends to move it away from an equilibrium point is termed an unstable region. The same sign dipole has stable and unstable regions (the stable region is $|x| < d$ and the unstable regions are $|x| > d$) but the opposite sign dipole has a stable region only (the stable region is $-\infty < x < +\infty$). Therefore, the opposite sign dipole should be resistant to dislocation flow on an extended range whereas the same sign dipole is only resistant to flow on a shorter range, and after that, it would not resist but rather assist in the dislocation flow.

Figure 8.5 shows the glide forces F_x for tripoles, as a function of x, and the equilibrium points (where $F_x = 0$). For a tripole having same-sign dislocations (Fig. 8.3a) there exists

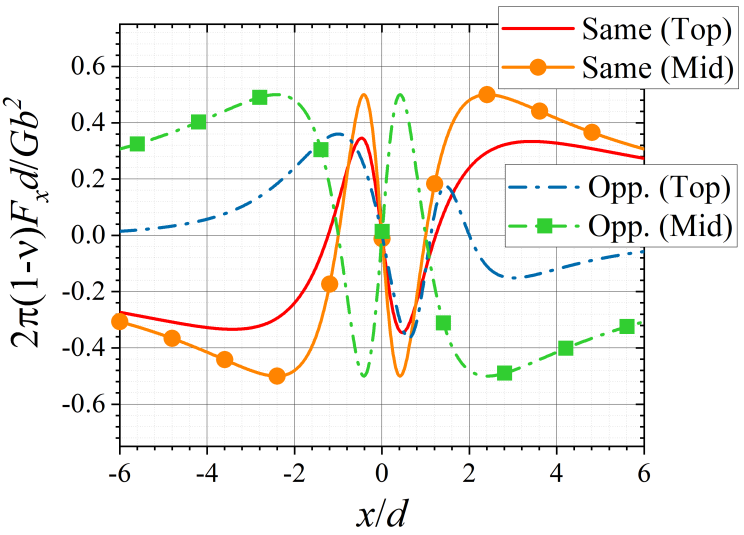

Figure 8.5: Normalized glide force for the tripole configurations in Fig. 8.3. "Same" refers to all dislocations in the multipole being of the same sign. "Opp." Refers to a zigzag pattern of the multipole where the dislocations alternate in sign. "Top" refers to the top dislocation and "Mid" refers to the middle dislocation.

two unstable equilibrium points and one stable (middle) equilibrium point at the origin. This is true for both the top (or bottom) dislocation and the middle dislocation although both have a relatively smaller region of stability. For Fig. 8.3b, there are also three equilibrium points with two being stable but with an infinite stability region. This is true for both the top/bottom and middle dislocations. Note that the force/stability curves for the tripole are more complex than for the dipole. For one reason, there are more of them to consider. Also for the tripole (or higher order poles), the curves are not always anti-symmetric which requires careful identification of peak or absolute peak values as shown in Appendix B.

From the stability figures (Fig. 8.5 and the Appendix B), it is evident that the top or outer dislocation in the multipole configuration is weakly coupled with other dislocations in the multipole and therefore subject to flowing first, i.e. detaching away first from the multipole. In other words, it is the weakest link in the multipole. The middle dislocation on the

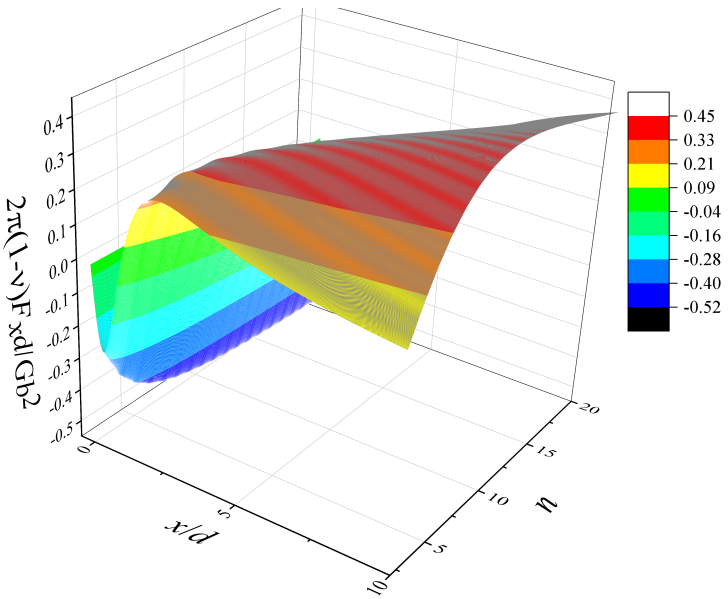

Figure 8.6: Surface plot of the top dislocation when all dislocations in the multipole are vertically stacked and of the same sign. Equation (8.10)

other hand seems to be more stable. With focus thus on the top/outer dislocation, Figs. 8.6 and 8.7 show surface plots based on Eqs. (8.10) and (8.13). Each surface point shows the PK force on the top dislocation of the multipole configurations. The force is a function of n and x. The figures show the complex dependence on n and x.

Figure 8.8 shows the maximum absolute PK force values acting on the top and middle dislocation. These maximum points are evaluated numerically, and each point shows the absolute maximum force irrespective of the x-location of this maximum point on the force curve. To get a curve for a middle dislocation at least three dislocation are required in a multipole. As seen in this figure, all the curves seem to plateau to some limiting value because the dislocation interaction has an inverse relationship to the separation distance between dislocations in the multipole configuration, i.e. the distances between the top dislocation and other dislocations will increase as n increases. Note in this figure that only when $n = 2$ or $n = 3$ that the absolute value of the glide force is the same whether one

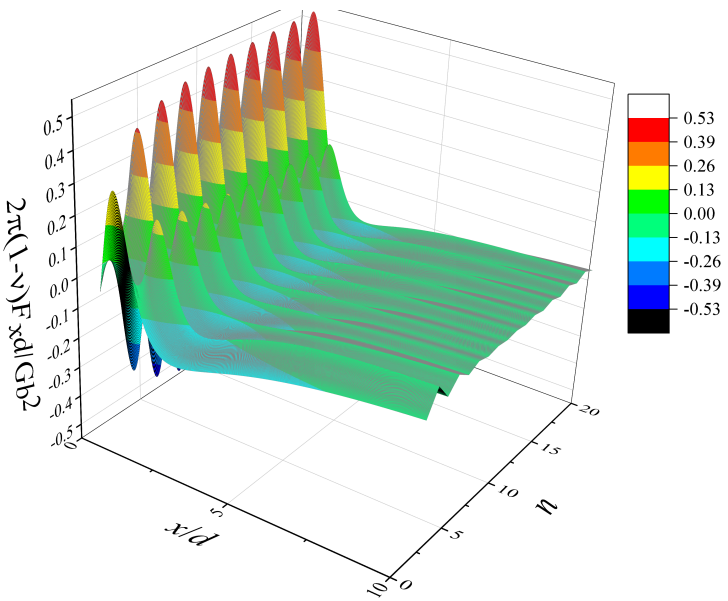

Figure 8.7: Surface plot of the top dislocation when all dislocations in the multipole are arranged in a vertical zigzag with their sign alternating between plus and minus. Equation (8.13)

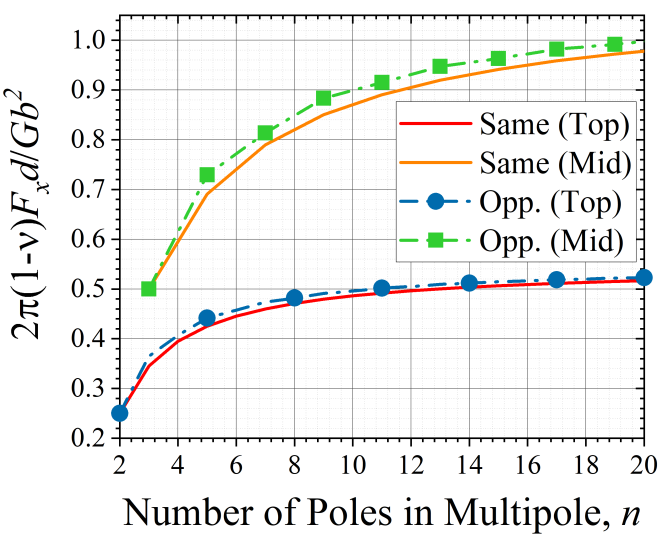

Figure 8.8: Absolute maximum force for each value of n.

considers a same sign multipole configuration (all vertically-aligned) or a vertical zigzag configuration with alternating dislocation signs. For any other n, the glide forces are not exactly the same. This figure shows that the middle dislocation could be twice as stable (factor of 2) as the top dislocation with this factor depending on n.

8.4 Simulation Methodology

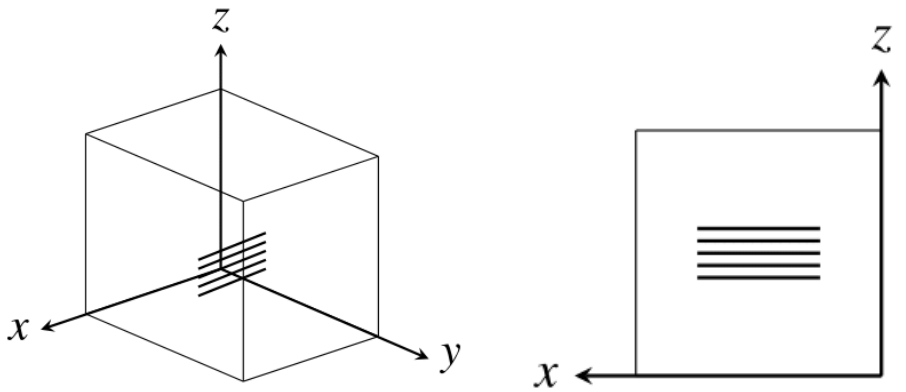

(a) (b)

Figure 8.9: Same-sign pentapole configuration. (a) Five Frank-Read sources inside an RVE (b) Front view of the RVE

To investigate the dislocation interactions mentioned in the Theory section in a three-dimensional finite-sized space, a number of simulations are performed by placing two, three, four, and five Frank-Read (FR) sources in different parallel slip planes (see Fig. 8.9 as an example) and applying constant strain-rate using the code developed by [6-14]. A main part of the simulations is to calculate the PK force experienced, at any time step, by the different dislocation segments in the computational box (Eq. (8.1)) and then applying a mobility law:

$$v_g = M_g F_g \tag{8.16}$$

where M_g is the glide mobility of the dislocations and F_g is the glide component of force $\vec{F}$ in Eq. (8.1). The study aims to understand how the initial multipole configuration affects the elastoplastic responses in the presence of external loading on the crystal. The shear modulus for the selected material (Aluminum) is taken at 26.32 GPa and Poisson's ratio is taken as 0.33. The dimension of the representative volume element (RVE) for these simulations is $60,000b \times 60,000b \times 40,000b$. The Burgers vector of the Frank-Read sources is taken as [0 1 0]. The shear load is applied in the yz-direction, and the applied strain rate is $10s^{-1}$. Dislocations lie parallel to the x-axis with a separation distance d. The length of each dislocation is $4,000b$.

The first group of simulations is conducted by changing the separation distance between active slip planes for the same-signed dislocations in the multipole (dipole, tripole, quadrupole and pentapole) configurations. Initially, all FR sources are placed on different slip planes as they make 0° angle with each other with respect to the vertical axis. This is a stable position for such multipoles, as mentioned in the Stability of Multipoles section.

Then in the second group of simulations, the dislocation sign was alternated between neighboring dislocations while the dislocations themselves are arranged in a vertical zigzag pattern. This is done for different multipoles (dipole, triple, quadrupole, and pentapole). To reverse the dislocation sign one can take opposite Burgers vectors for the neighboring dislocations, i.e. $[0\,1\,0]$ and $[0\,\bar{1}\,0]$. Here also, the separation between the dislocations on the different slip planes is varied and the result of this is obtained and studied. In other words, for the zigzag pattern each dislocation is making a 45° angle with respect to the vertical axis with the neighboring dislocations. See Fig. 8.3b and the quadrupole and pentapole figures in Appendix B.

At the start of each simulation, i.e. at time zero, the glide force F_y experienced by any dislocation, or dislocation segment, in the above multipole configuration can be obtained

using Eq. (8.1). For this simulation setup $F_y = \sigma_{yz} b$ since $\hat{e} = [1\,0\,0]$. Of course after the bowing of the FR sources commence, each dislocation segment can experience both glide components of the PK force, i.e. F_x and F_y.

8.5 Results and Discussion

Stress-strain diagrams are generated for each 3D DDD simulation. Although these diagrams were generated for different dipole, tripole, quadrupole and pentapole configurations, they are only shown here for the pentapole configurations for brevity and as exemplary figures of the results of the DDD simulations. Figures. 8.10 and 8.11 show the stress-strain responses of the RVE for different slip plane separations (normalized d) for pentapole configurations with the same and oppositely alternating dislocation signs, respectively. All the strain-stress diagrams are compared with a single FR source (labelled as "One FR") to capture any occurring hardening or softening phenomena associated with the different multipole configurations. The proportional limit (stress value at the end point of the elastic region) and the flow stress (averaged stress values over strain after any initial drop in stress beyond the elastic regime) are recorded for each simulation. Note that in Fig. 8.10, some stress-strain diagrams show a clear drop in stress value right after the elastic regime. This sudden drop is similar to the YPP (Yield Point Phenomenon) observed in low carbon steels, although the initial locking of dislocations here is due to the other dislocations in the multipole, unlike YPP in steels which is due to the solute carbon atoms.

Figures 8.12-8.15 show the proportional limit and flow stress for different multipoles as the separation distance d between any two slip planes is varied. The minimum d/b considered is 50. All the diagrams show both hardening and softening effects from the elastic interaction between two or more FR sources having the same sign.

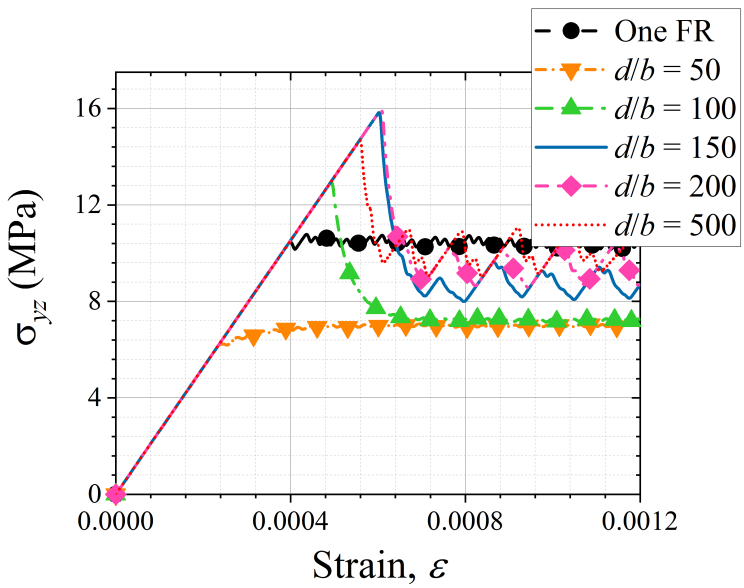

Figure 8.10: Stress-strain diagram for the material under different pentapole separations when all the dislocations have the same sign.

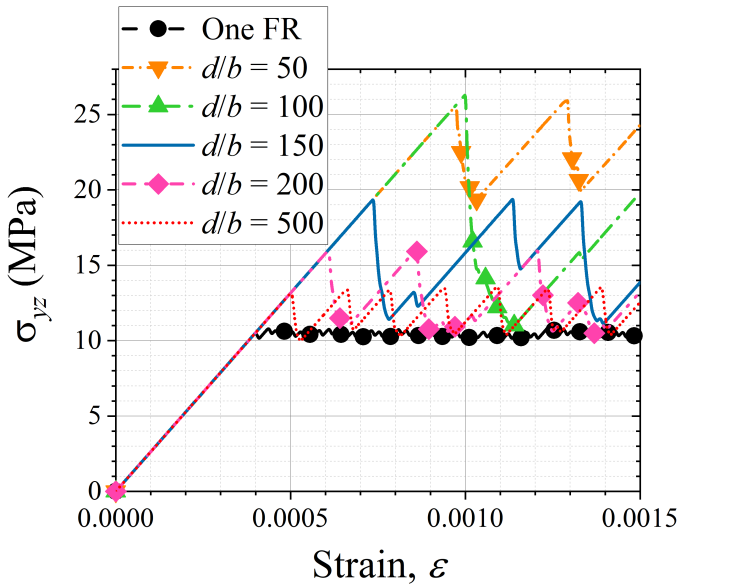

Figure 8.11: Stress-strain diagram for the material under different pentapole separations when the dislocation signs alternate between neighboring dislocations/sources.

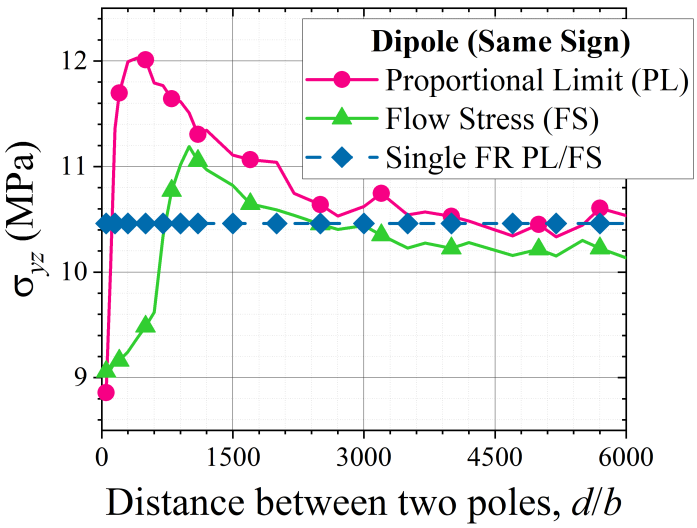

Figure 8.12: Comparison of Proportional Limit and Flow Stress of a dipole with a single Frank-Read source when both dislocations have the same sign

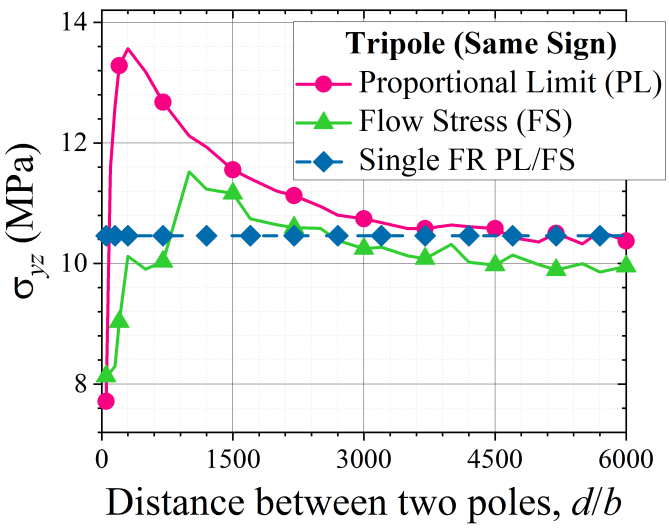

Figure 8.13: Comparison of Proportional Limit and Flow Stress of a tripole with a single Frank-Read source when the dislocations have the same sign

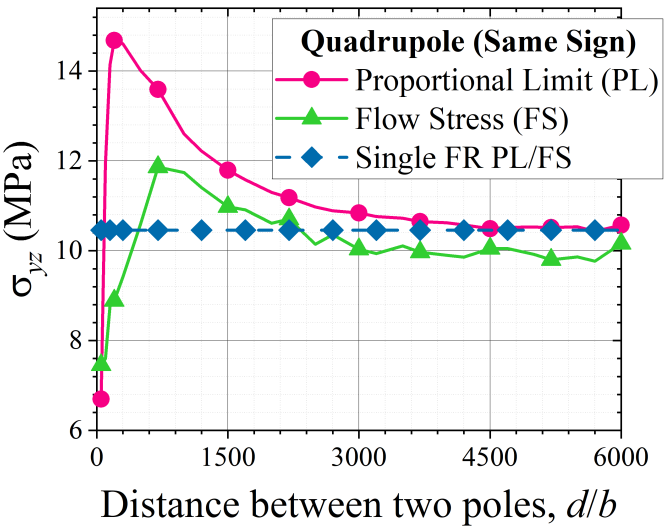

Figure 8.14: Comparison of Proportional Limit and Flow Stress of a quadrupole with a single Frank-Read source when the dislocations have the same sign

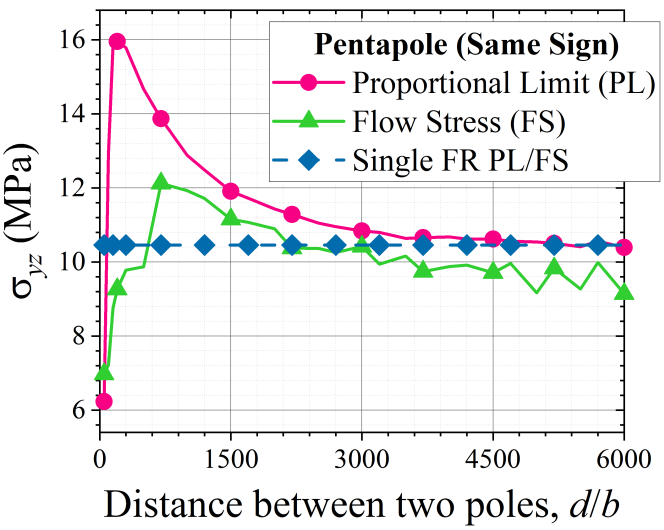

Figure 8.15: Comparison of Proportional Limit and Flow Stress of a pentapole with a single Frank-Read source when the dislocations have the same sign

This result shows good agreement with the information in the Theory/Stability of Multipoles sections regarding small source separations. For small separations, the sources bow together, trying to hold each other in equilibrium as they bow (Fig. 8.16). This raises the proportional limit (i.e. the critical bowing of source(s)) and thus the flow stress above a one source. However, as the distance between the sources increases more and more, the interaction effect of the sources on one another become less and less during bowing. This results in the proportional limit and flow stress eventually dropping to the same level as that of one source. For this kind of interaction, two parameters play an essential role in conjunction with one another: one is the separation distance between any two slip planes, and the other is the PK force due to the self-stress field created by the dislocations, i.e. the line tension of a dislocation. This force, with perturbations in the self-stress of the dislocations, can cause the same-signed dislocation sources to either take longer to critically bow (i.e. a hardening or strengthening effect) or bow critically quickly, i.e. at lowered strain value (i.e. a softening effect as seen in a stress-strain diagram). The reason for this softening effect at very small d values, is that the interaction force is very high and any perturbations in the bowing between the sources can at one point flip a stable position between any two nearby dislocations to an unstable position pushing the dislocations away from each other instead of pulling them to stay together. That will accelerate the production of strain at the same applied load value which is the exact definition of softening.

Another result from the simulations is that for any number $n \geq 3$, the DDD simulations show that the outer FR sources bow out critically first before the middle ones. Figure 8.16 shows a snapshot of a quadruple were the outer sources are starting to take off, i.e. break away from the pack, before the middle ones. This is in line with the stability discussions above regarding infinite-length dislocations that the outer dislocations are the least stable. This figure also shows how all the dislocations in a same-sign multipole initially bend/bow together while trying to maintain their vertical originally-stable configuration. This continuous attempt to align the dislocations in a vertical configuration produces resistance to

applied loading and hence a hardening effect that reflects itself on the PL results in Figures. 8.12-8.15.

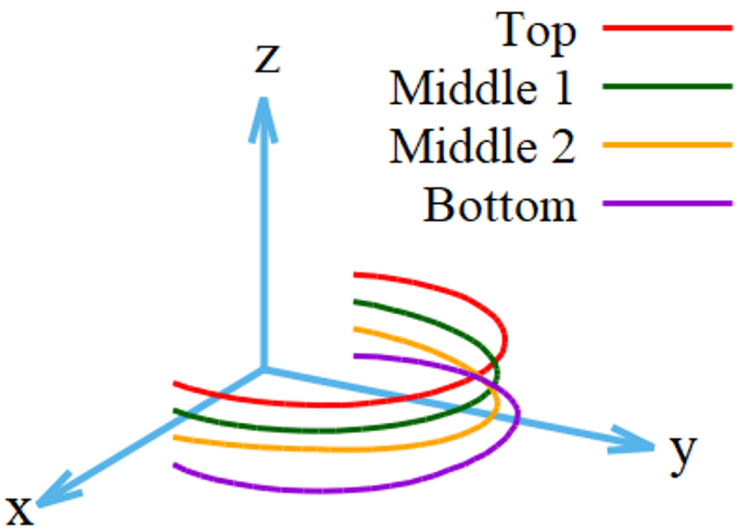

Figure 8.16: A snapshot of a bowing quadrupole with four FR sources. The outer sources are breaking away first from the pack.

Figures. 8.17-8.20 show different results for the oppositely-signed multipole configurations (in a zigzag pattern) compared to the same-signed multipoles having the same number n (Figures. 8.12-8.15). Here also, the minimum d/b considered is 50. For smaller separation distances in the oppositely-signed multipole configurations, both the proportional limit and the flow stress are significantly higher than for a single FR source. It can be as high as a factor of 3. For these multipole configurations, the entire slip plane acts as a basin of attraction for all the Frank-Read sources back to the equilibrium points, as shown in Figures. 8.4-8.5 (See Appendix B for higher-order multipoles). Thus one should not expect any softening effect from this configuration because this continuing stability of the configuration and continuous attraction to the equilibrium position hinders plastic flow. Figures. 8.17-8.20 also show a good agreement with the study hypothesis: as the separation distance increases, the stress-strain response mimics that of a single Frank-Read

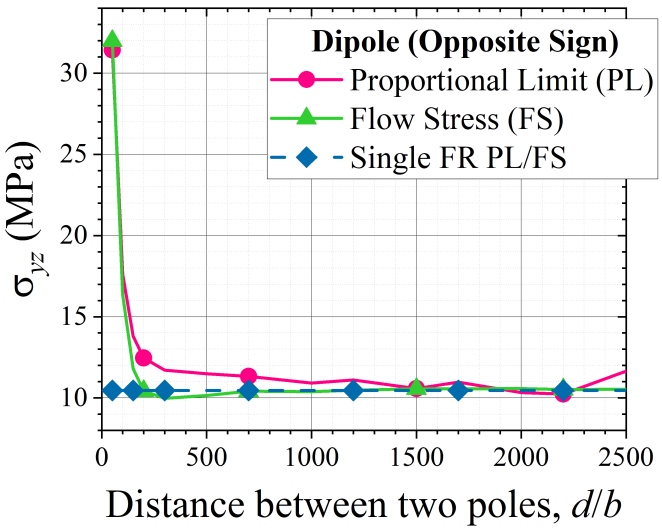

Figure 8.17: Comparison of Proportional limit and flow stress of a dipole with a single Frank-Read source when both dislocations have opposite signs

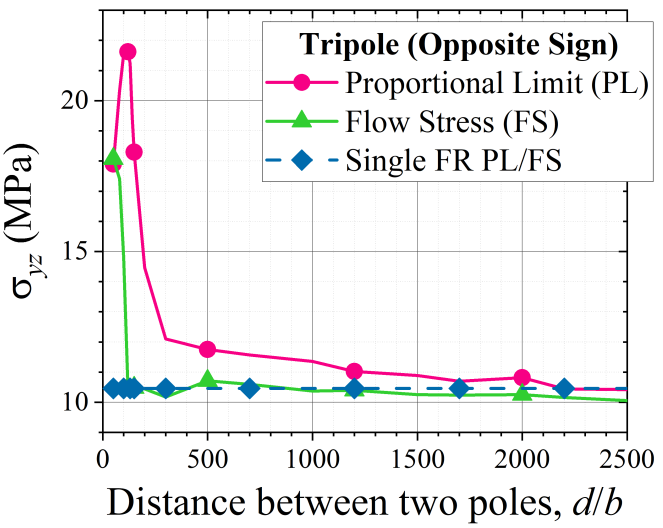

Figure 8.18: Comparison of Proportional limit and flow stress of a tripole with a single Frank-Read source when the dislocations have alternating opposite signs

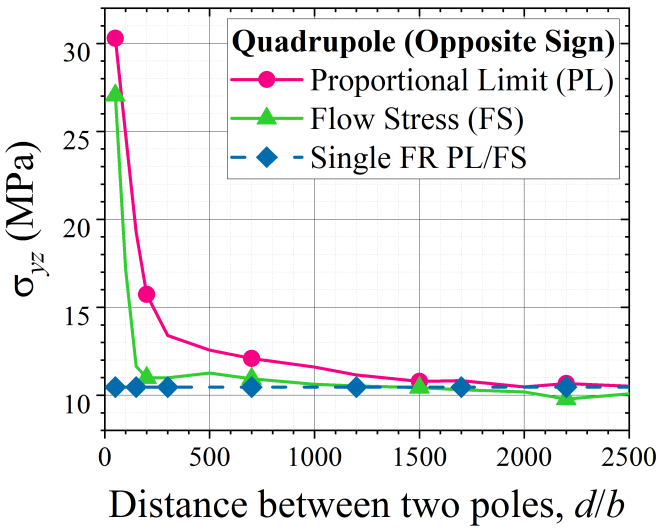

Figure 8.19: Comparison of Proportional limit and flow stress of a quadrupole with a single Frank-Read source when the dislocations have alternating opposite signs

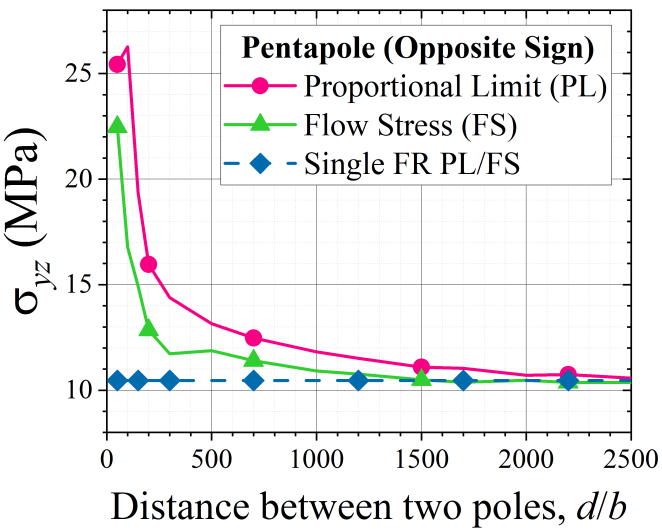

Figure 8.20: Comparison of Proportional limit and flow stress of a pentapole with a single Frank-Read source when the dislocations have alternating opposite signs

source response. This is true in the limit of high d values.

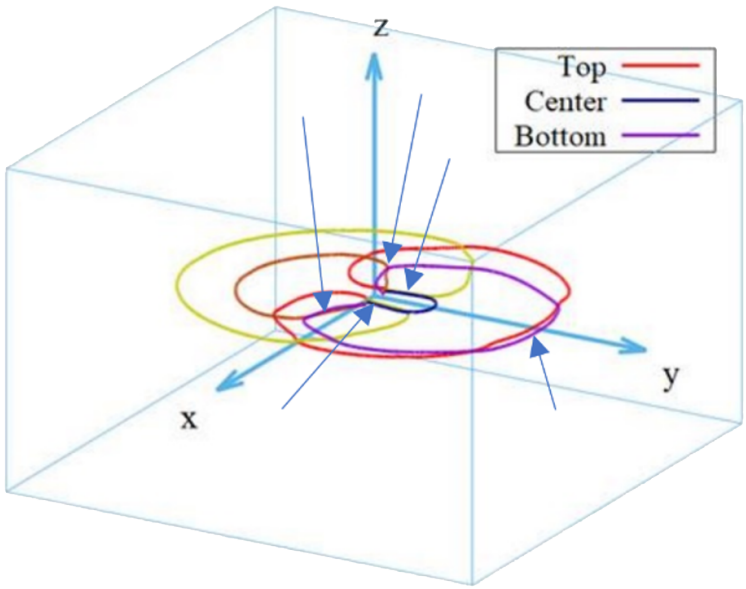

Figure 8.21: A snapshot in time of a pentapole (of the zigzag type) showing the interaction between the different active sources. Here, d/b = 200. The arrows are pointing towards dynamic dipoles.

It is important to note that in such simulations the ensuing dislocation microstructures can be complex as they evolve with strain. This complexity is a function of the source vertical separation (d/b) and the number of sources (n). To give one example of this complexity, consider Fig. 8.21. In this figure, a pentapole is shown at one strain value and as can be seen from the differently-colored dislocations/sources, their interaction is complex. This snapshot shows, for example, the formation of multiple dynamic dipoles at that instant of time. All such dynamics dipoles represent temporary pinning of dislocation motion/glide and thus cause an increase to the applied stress value needed to maintain plastic flow.

The peak (maximum) and minimum values for the proportional limit (PL) and flow stress (FS) from Figures. 8.12-8.15, independent of separation distance d, are plotted in Fig.

8.22. Figure 8.22 shows how added dislocations in the multipole contribute to dislocation

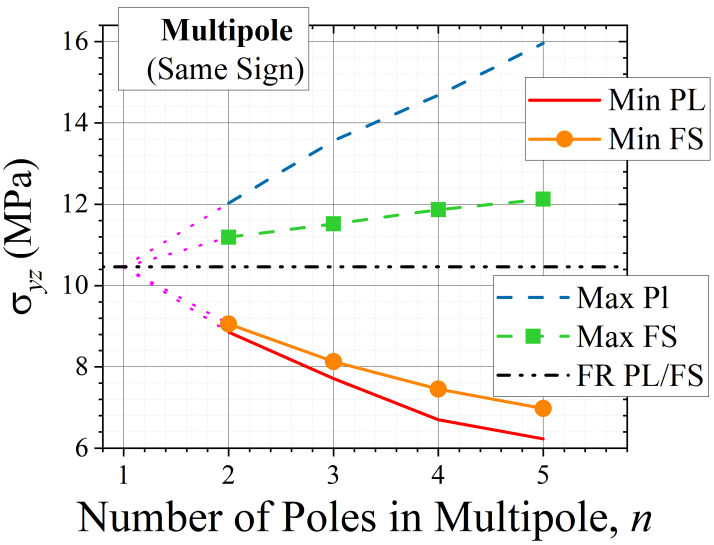

Figure 8.22: Comparison of Proportional Limit and Flow Stress of multipoles with a single FR source (last legend) when the dislocations all have the same sign. All curves are extrapolated to n = 1 (i.e. single FR source).

interactions that results in increased PL/FS with n. Given the prior discussion on the stabilizing effect of dislocations in a multipole, this result is not surprising. The curves in Fig. 8.22 seem to be reaching a plateau similar to what is seen in Fig. 8.6.

There are a few things to note about this Figure. First, the dislocation/source interactions are contributing to higher FS and PL than a single FR source (last legend in the figure). Indeed, at the highest n (i.e. $n = 5$), this increase from a single FR source is about 55% or a factor of 1.52 higher to critically bow a pentapole than to critically bow a single FR. A higher factor is possible if n is higher. Note that this increase in PL is due to dislocation interaction between sources and not due to line tension (which is driving the base value for a single FR source). Hence dislocation interactions are shown here as clearly significant for the elastoplasticity of a single crystal. Another thing to note about Fig. 8.22 is that

if one divides the increase in PL value from $n = 2$ to $n = 5$, the factor here will be 1.33 $(16/12)$. However, from Fig. 8.8 for the top dislocation (the least stable), the ratio of the breakaway force for $n = 5$ compared to $n = 2$ is 1.76 $(0.44/0.25)$. These values indicate the effect of dislocation interaction going from $n = 2$ to $n = 5$ and not the effect of line tension. Moreover, the reason the ratio from Fig. 8.8 is higher is that it considers infinite dislocations. Therefore, it appears that the theoretical analysis done in the Stability of Multipoles section is relevant to the analysis of finite-length sources arranged similarly as multipoles.

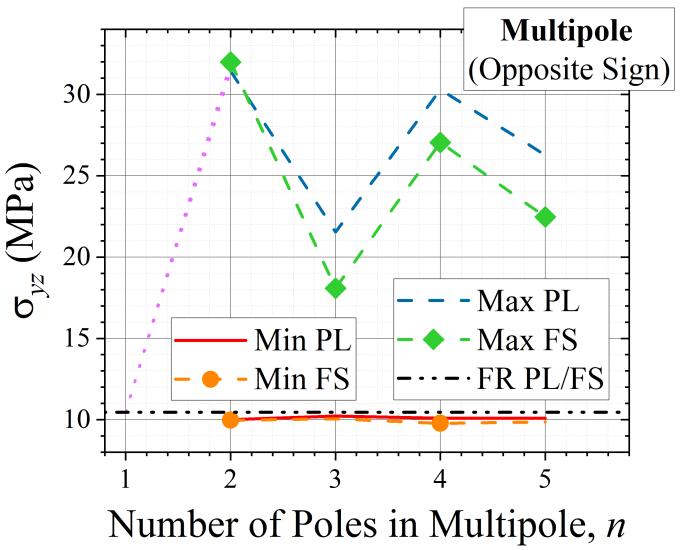

Figure 8.23: Comparison of Proportional Limit and Flow Stress of multipoles with a single FR source (last legend) when the dislocations are zigzag-arranged and alternating in sign.

The peak (maximum) and minimum values for the PL and FS from Figures. 8.17-8.20, independent of separation distance d, are plotted in Fig. 8.23. Figure 8.23 shows how added dislocations in the multipole contribute to dislocation interactions boosting the PL/FS over a single FR source. However, unlike Fig. 8.22 for dislocations of the same sign, Fig. 8.23 for dislocations of alternating sign shows an oscillating behavior. These oscillations are

similar to what is seen in Fig. 8.7 and should ultimately reach a limiting value with higher n. Notice that the PL and FS maximum values in Fig. 8.23 are higher than those in Fig. 8.22. The reason for this was discussed earlier. Note also that the minimum PL/FS values in this figure occur for large source separation d. An important outcome of these studies is that there were significant changes in the elastoplastic properties of a crystal not from a change in the dislocation density of that crystal but rather from changes in the configuration and relative position of the dislocations in the crystal. This is an important outcome of this work as dislocation density is a major parameter used in continuum plasticity models.

8.6 Limitations

The current study is limited to the hardening/softening of a crystalline material only due to the dislocation interactions in a multipole. Here dislocations are kept equally apart from each other in both same and opposite type multipole configurations. Moreover, the other aspects of material hardening processes (i.e., solid solution hardening and precipitation hardening) are not considered because the objective of this study is to understand the dislocation interactions in a multipole and its hardening or softening effect on the crystalline materials. In the analytical study, dislocations are considered to be infinitely long, so the line tension is neglected. Though the DDD simulations are done with finite dislocation sources considering line tension, the analytical prediction still reflects the results. Again the unequal separation between dislocations in the multipole may somewhat alter the trend of the current results. Simulations are done for a certain value of mobility constant, and the effect of dislocation mobility is not studied in this research.

8.7 Conclusions

In this article, the authors presented a study on dislocation multipoles, and presented analytical stability diagrams/equations and 3D DDD simulation outcomes. The simulations incorporated line tension effects whereas the analytical models did not since they assume infinite length of dislocations. Although the simulations used finite-length dislocation sources, the analytical models were still helpful in understanding the simulations. The simulations showed that both hardening and softening behaviors in the material can occur. One of the main findings of this study is that zigzagged multipoles with alternating dislocation sign only cause hardening. On the contrary, same-sign multipoles can exhibit either hardening or softening behavior depending on the separation distance between slip planes. At a separation distance of 4,500b, the sources act the same as a single FR source, i.e. the interaction between them diminishes. Another important finding is that the elasto-plastic properties of a crystal are dependent not just on dislocation density but also on the configuration and relative position of the dislocations in the crystal. Yet another finding is that dislocation interactions significantly contribute to the proportional limit and flow stress of a crystal and not just the line tension of the dislocations. In future studies, one could consider the initial source length as a parameter in the multipole configurations.

Journal reference

Siddique, A. B., Lim, H., & Khraishi, T. A. (2021). The Effect of Multipoles on the Elasto-Plastic Properties of a Crystal: Theory and 3D Dislocation Dynamics Modeling. Journal of Engineering Materials and Technology, 1–22.
https://doi.org/10.1115/1.4052168

Chapter 9

Multi-scale modeling of solute atom strengthening

Abstract

Discrete Dislocation Dynamics (DDD) codes enable researchers and scientists to explore the mechanical behavior of a material as impacted by its composition and microstructure. Understanding the strengthening mechanisms is very important for the development of new materials with improved and desired mechanical properties. One of the material strengthening/hardening mechanisms is solution hardening, and this method can be fundamentally understood from particle misfit models and the theory/implementation of dislocation dynamics. The overlapping of the eigenstrain fields of the misfit particles or solutes and the dislocations impedes the motion of dislocations and results in material hardening. This article incorporates the misfit particle model in a 3D DDD code in an attempt to capture this phenomenon and find the strength of solid solutions (for a binary Cu-Ni system) from the simulated stress-strain diagram. This study/research finds a good agreement between the simulation results and experimental data. The authors also corre-

late the strength differentials as a function of solute concentrations and compare them with relations in the literature.

9.1 Introduction

Line defects or dislocations are mostly responsible for plasticity in crystals. A dislocation causes stresses and strains in a solid material (called the self-stresses of a dislocation). The hardening o fa material can be explained by the difficulty of dislocations' movements and their interactions with other impurities or defects in a crystal. In general, a solid solution is designed to have a strength higher than its pure base element. In the process of solid solution hardening, interstitials or substitutional point defects are introduced in a solid matrix or crystal. A point defect, or an impurity, distorts the lattice and generates an associated stress and strain field (see Fig. 9.1). This stress and strain field interacts with the dislocations' stress and strain fields, impeding the motion of dislocations in the crystal, and thus hardening the material. The hardening behavior in a metallic material can vary depending on the composition of the solid solution.

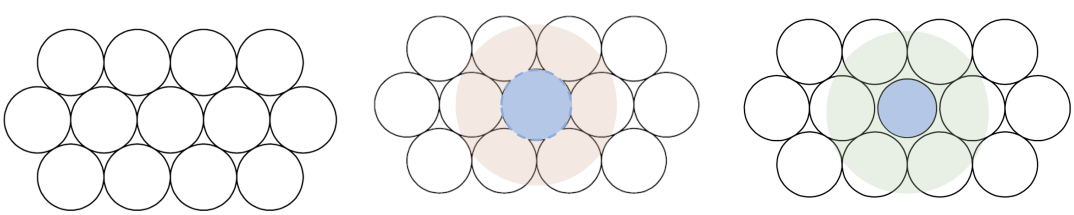

Figure 9.1: Deformation field due to a substitutional atom in a pure crystal. (a) Perfect crystal structure. (b) Crystal with a substitutional atom (solute atom is greater than matrix atom). The shaded region is in compression. (c) Crystal with a substitutional atom (solute atom is smaller than matrix atom). The shaded region is in tension.

Fleischer studied the atomic size effect and the modulus change effect on solution hard-

ening [82]. [83], [84], [85]. The size difference between the solute and matrix atoms can characterize the hardening effect of the solid solution. Riddhagni and Asimow [86] showed the effect of the size difference between solute and matrix atoms on solution hardening. This solid solution hardening can be understood in the context of the misfit particle model. Eshelby [87], [88] derived the elastic field around an ellipsoidal inclusion and described the method of generating the stress tensor atany point in the matrix due to a misfit particle. Weeks et al. [89] showed an approximate solution for the elastic energy due to the interaction between a straight dislocation and a bubble or particle at large separation distances. Mura [90] presented the eigenstrain method for solving particle problems, including misfit particle situations. However, the analytical solution must be reformulated every time the problem configuration changes.

Lerma et al. [91], [92], [93], [94] presented the solution of the elastic fields of misfit cylindrical and spherical particles, in infinite or semi-infinite mediums, using a dislocation-based numerical approach (the distributed-dislocation method),which can apply to different particle shapes as well.Scientists from several countries developed 2D and 3D Dislocation Dynamics codes to better understand the phenomena related to dislocation motion and interaction. These codes introducedthe opportunity to explore and understand many phenomena during plastic deformation, which are difficult or sometimes impossible to observe in real experiments. Kubin et al. [45] first introduced the 3D Discrete Dislocation Dynamics (DDD) simulation framework in a finite volume as a continuation of his work with Lepinoux [95].

Khraishi et al. [15], [76], [57] presented 3D simulation results of dislocation interaction with different types of hardening sources in metals. In a recent work, Liu et al. [96] presented a three-dimensional DDD framework for particle-strengthened materials that account for dislocation glide, cross-slip, and self-climb mechanisms.It is rare in the previous research works to find ones that emphasize comparisons to experimental data. In this arti-

cle, the authors introduce a method to simulate solid solution hardening using a multi-scale 3D dislocation dynamics code [51]. The Methodology section presents a detailed mathematical model and discusses different ways of dealing with the solute atoms. The Results and Discussion section shows a comparison between experimental tensile strength data for a binary Cu-Ni system, and flow stress computations captured from the DDD simulations. The comparison is important to establish the efficacy of this newly proposed method.

9.2 Methodology

9.2.1 Theory

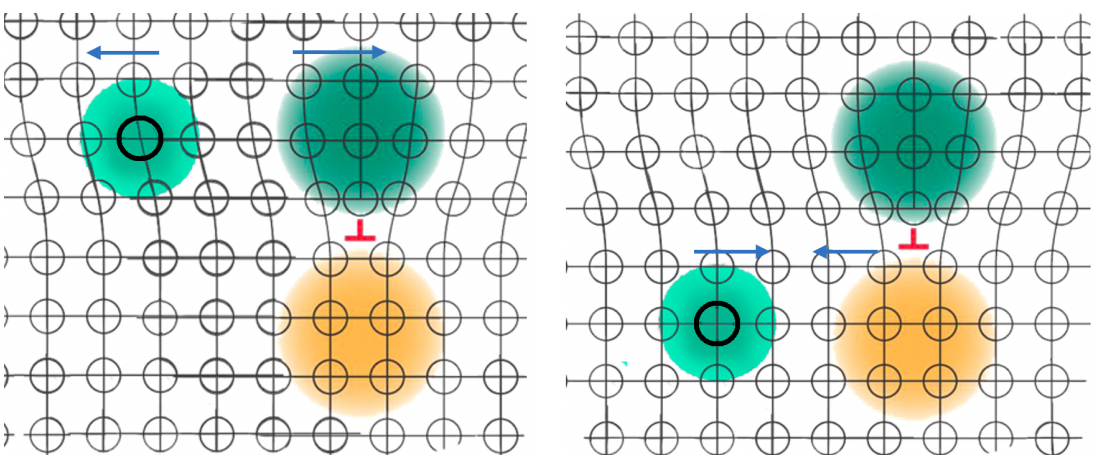

Figure 9.2: Interaction between an edge dislocation and a solute atom. The solute atom is shown using a thicker borderline. (a) Repulsion between dislocation and solute atom compressive fields, (b) Attraction between dislocation and solute atom fields (compression and tension, respectively).

An edge dislocation creates both tensile and compression zones in the material. When a dislocation moves, the region of tension and compression also moves with the dislocation line. When any dislocation approaches a substitutional atom, its strain field overlaps with

the strain field of the substitutional atom. If the interaction happens between the tensile zones of both dislocation and solute atom, then the solute atom repels, and thus impedes, the dislocation's motion. If the interaction occurs in the tensile region of a dislocation and the compressive region of a solute atom, then the solute atom attracts the dislocation, and this also impedes the dislocation's further motion. In both cases, the dislocation's motion is hindered. Hence, dislocations cannot move easily in the presence of solute atoms, and hardening increases with the presence of a solid solution.

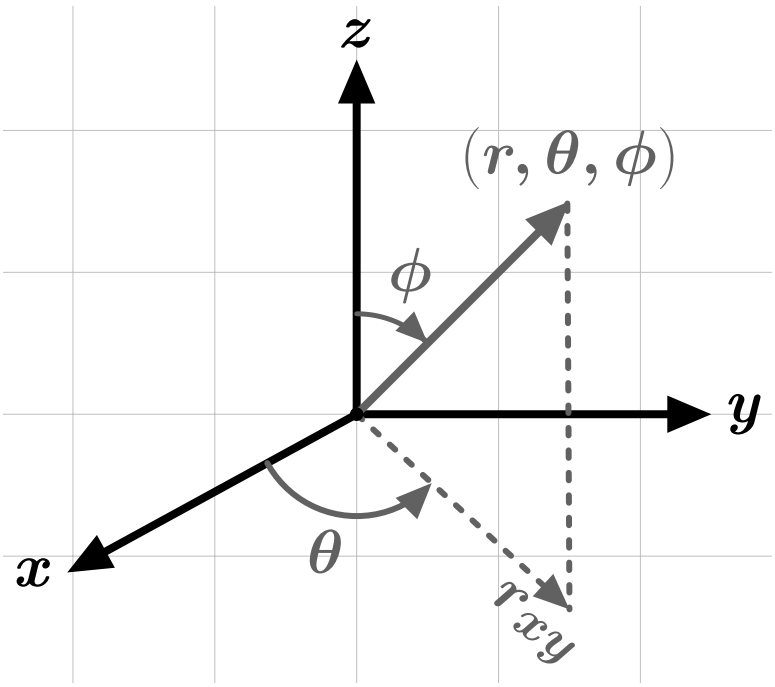

Figure 9.3: Spherical coordinates in relation to Cartesian coordinates.

We can make an analogy of the solute atom problem with the particle misfit problem (uniform radial-misfit particles of different elastic properties compared with their matrix materials) and can write from Eshelby [87], [88], Lerma et al. [93], using a spherical

coordinate system:

$$\sigma_{rr} = -\frac{4G_M C}{r^3} \tag{9.1a}$$

$$\sigma_{\theta\theta} = \sigma_{\phi\phi} = \frac{2G_M C}{r^3} \tag{9.1b}$$

$$\sigma'_{rr} = \sigma'_{\theta\theta} = \sigma'_{\phi\phi} = -\frac{4G_M C}{R_P^3} \tag{9.1c}$$

$$\sigma_{r\theta} = \sigma_{\theta\phi} = \sigma_{r\phi} = 0 \tag{9.1d}$$

$$\sigma'_{r\theta} = \sigma'_{\theta\phi} = \sigma'_{r\phi} = 0 \tag{9.1e}$$

where $C = \frac{\delta v'}{4\pi\left(1+\frac{4G_M}{3K_P}\right)}$, G_M is the shear modulus of the matrix material, r is the radial distance of a field point from the center of the misfit particle, $\delta v'$ is the volume difference between the matrix and the solute atom, K_P is the bulk modulus and R_P is the radius of the solute atom. Due to spherical symmetry, the shear stresses are zero as in Eqs. (9.1)(d) and (9.1)(e). Equations. (9.1)(a, b, d) are showing the stresses for the matrix and Eqs. (9.1)(c, e) are showing the stresses for the misfit particle. For relatively small $\delta v'$ ($\delta v' = V_P - V_M$, where V_P = Volume of a solute atom and V_M = Volume of a matrix atom), we can write:

$$\delta v' = 4\pi\left(R_P - R_M\right)R_P^2 \tag{9.2}$$

where R_M is the radius of the matrix atom. Note that Eq. (9.1) is developed for an isotropic medium. To transform Eq. (9.1) into the Cartesian coordinate system, we need a rotational transformation (see Fig. 9.3) matrix $[\beta]$, needed for second rank tensor transformations, where

$$[\beta] = \begin{bmatrix} \sin\phi\cos\theta & \sin\phi\sin\theta & \cos\phi \\ -\sin\theta & \cos\theta & 0 \\ -\cos\phi\cos\theta & -\cos\phi\sin\theta & \sin\phi \end{bmatrix} = \begin{bmatrix} \frac{r_x}{r} & \frac{r_y}{r} & \frac{r_z}{r} \\ -\frac{r_y}{r_{xy}} & \frac{r_x}{r_{xy}} & 0 \\ -\frac{r_z}{r}\frac{r_x}{r_{xy}} & -\frac{r_z}{r}\frac{r_y}{r_{xy}} & \frac{r_{xy}}{r} \end{bmatrix} \tag{9.3}$$

And,

$$\begin{bmatrix} x \\ y \\ z \end{bmatrix} = [\beta]^T \begin{bmatrix} r \\ \theta \\ \phi \end{bmatrix} \tag{9.4}$$

And,

$$\begin{bmatrix} \sigma_{xx} & \sigma_{xy} & \sigma_{xz} \\ \sigma_{xy} & \sigma_{yy} & \sigma_{yz} \\ \sigma_{xz} & \sigma_{yz} & \sigma_{zz} \end{bmatrix} = [\beta]^T \begin{bmatrix} \sigma_{rr} & \sigma_{r\theta} & \sigma_{r\phi} \\ \sigma_{r\theta} & \sigma_{\theta\theta} & \sigma_{\theta\phi} \\ \sigma_{r\phi} & \sigma_{\theta\phi} & \sigma_{\phi\phi} \end{bmatrix} [\beta] \tag{9.5}$$

As a verification of Eq. (9.3), one can find the third row of the transformation matrix $[\beta]$ by making a cross-product between rows 1 and 2. Similarly, the second row of the transformation matrix can be found from the cross-product of rows 3 and 1. The reason for needing to do the second-order stress transformations is that the DDD method employed here utilizes a Cartesian coordinate system.

9.2.2 Discrete Dislocation Dynamics (DDD)

The current study implements the above misfit particle model into the existing 3D DDD code originally developed by Zbib et al. [51]. The code first approximates a curved dislocation line by a piece-wise continuous (head-to-tail) set of mixed straight-line segments. The average glide velocity v_g of each dislocation segment is calculated using the following formula [51], [11]:

$$v_g = F_{eff} M_g \tag{9.6}$$

where F_{eff} is the effective force in the glide plane, and M_g is the temperature-dependent dislocation glide mobility. It is important to mention that the effective force F_{eff} is calculated at the center of each segment taking into account the line tension and force due to adjacent segments, the long-range interaction force (each segment with other remote segments), the force due to remotely applied stress, Peierls stress [97] and other sources of stress (e.g. micro-constituents [57], [61], [98], [19], inside interfaces [15], [99], [100], [101], free surface effects [18], [35], [34], [102], [49], [48], [54], etc.).

The resultant Peach-Koehler (PK) force (from all the interactions and applied load) on any segment j is calculated by the following Eq. [11]:

$$\vec{F}^{j} = \left(\left(\sum_{\substack{i=1 \\ i\neq j \\ i\neq j+1 \\ i\neq j-1}}^{N} \boldsymbol{\sigma}_i^D + \boldsymbol{\sigma}^a + \boldsymbol{\sigma}_j^* \right) \vec{b}_j \right) \times \vec{t}_j + \vec{F}^{j,j+1} + \vec{F}^{j,j-1} \tag{9.7}$$

where N is the total number of dislocation segments, $\boldsymbol{\sigma}_i^D$ is the stress tensor from remote segment i, $\boldsymbol{\sigma}^a$ is the applied stress tensor, $\boldsymbol{\sigma}^*$ is the stress tensor caused by other sources of stresses (i.e. free surfaces, solute atoms, micro-constituents, inside interfaces, etc.), $\vec{t}_j$ is the direction (or line sense) vector of dislocation segment j, and $\vec{F}^{j,j+1}$ and $\vec{F}^{j,j-1}$ are the interaction forces between segment j and $j+1$, and between j and $j-1$ respectively, i.e., the two immediate neighboring segments. In the current problem, the eigenstress tensor of a solute atom is calculated using Eqs. (9.1) utilizing a spherical coordinate system and then transformed, using Eq. (9.5), into a Cartesian system for use in σ^* in Eq. (9.7). This is so because the DDD coordinate system is Cartesian as shown in Fig. 9.4 below and discussed above.

A dislocation segment moves and increases in length depending on whether the acting PK force is large enough to overcome the lattice friction, line tension, and/or any other hindrances. Glide velocity for a segment is first calculated using Eq. (9.6) and then the nodal velocities are determined. It is important to mention that each segment contains two nodes and two adjacent segments have a common node. The nodal velocity is calculated by taking an average of two adjacent segments' velocities. Now the problem can be reduced to a set of non-linear first-order ordinary differential equations (ODEs) for the nodal position vectors:

$$\dot{\vec{X}}_j = \vec{f}_j \left(\vec{X}_1, \vec{X}_2, \vec{X}_3, \ldots, \vec{X}_k, \boldsymbol{\sigma}(t) \right) \tag{9.8}$$

where, k is the number of total nodal points and $\vec{f}_j$ is the force at node j which is a function of associated nodal vectors and the total stress. Solving Eq. (9.8), the nodal displacements are obtained. Each dislocation's motion contributes to material plasticity which is described via the plastic strain-rate tensor $\mathbf{D}^P$ [51].

$$\mathbf{D}^P = \sum_{j=1}^{N} \frac{-l_j v_{gj}}{2V} \left(\vec{n}_j \otimes \vec{b}_j + \vec{b}_j \otimes \vec{n}_j \right) \tag{9.9}$$

where l_j is the length of segment j, $\vec{n}_j$ is a unit normal vector to the slip plane and V is the volume of the simulated crystal.

9.2.3 Application of DDD to solution strengthening

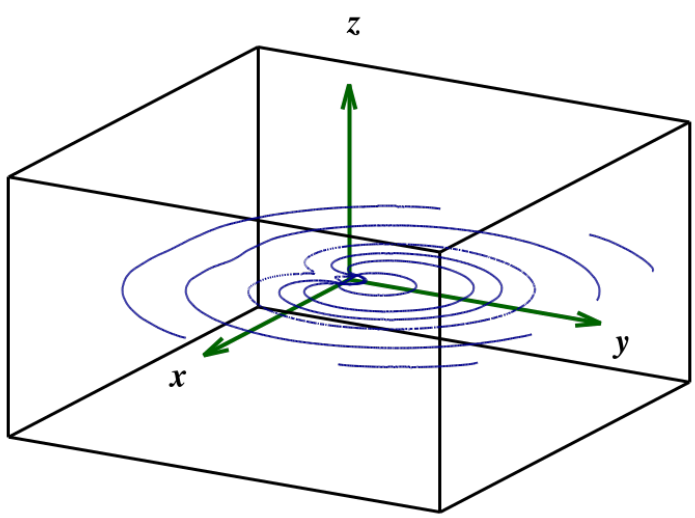

Figure 9.4: Multiplication of a single Frank-Read (FR) Source

Figure 9.4 shows the DDD simulated multiplication of a Frank-Read (FR) source [79] under external loading. Each line represents a snapshot in time of the expanding and multiplying source. To better visualize the different time snapshots of the FR source action, refer to Fig. 9.5. A dislocation source multiplies to a critical bow and instigates after that plastic deformation in the crystal, and then the multiplication continues and forms a series

	Copper	Nickel
Density (Kg/m^3)	8,960.0	8,908.0
Atomic radius (nm)	0.1278	0.1246
Atomic weight, A (amu)	63.50	58.69
Burgers vector magnitude, b (nm)	0.2556	0.2492
Shear Modulus (GPa)	46.0	76.0
Poisson's ratio	0.34	0.31

Table 9.1: Material properties of Copper and Nickel [103]. Note that, 1 amu = 1.66054×10^{-27}Kg.

of closed loops. Some of these loops move out from the representative volume element (RVE), or computational box, as they reach the boundary. During the multiplication process, the motion of a dislocation source is hindered by any solute atoms present in the crystal. As mentioned in the Theory sub-section, any substitutional atom restricts the dislocation motion by either repelling or attracting it, and as a result, the material hardens.

We simulate this solid solution strengthening phenomenon, conducting constant strain-rate experiments in a 3D crystal RVE by implementing the misfit particle model eqs. (1-5) in a 3D DDD code (by Zbib et al. [51]) to generate stress-strain curves and construct the strength vs. percentage of solute atoms curve. For simplicity, we assume the RVE to be isotropic. We chose the RVE or simulation volume/box for all the simulations to be centered on the coordinate system origin and of dimensions $60,000b \times 60,000b \times 40,000b$, where b is the magnitude of the Burgers vector. For Copper, $b = 0.2556$ nm. The material properties of pure Copper and Nickel used in the simulations are presented in Table 9.1.

Dislocation mobility is assumed 10,000 1/(Pa·s) in all the simulations, irrespective of the percentage of solute atoms in the solid solution. We pinned a Frank-Read (FR) source end-to-end at nodal point coordinates equal to $(-2,000b, 0, 0)$ and $(2,000b, 0, 0)$. The Burgers vector of the Frank-Read source is $(0, 1, 0)$, and the constant applied strain rate to the RVE is 10s^{-1} in all the simulations.

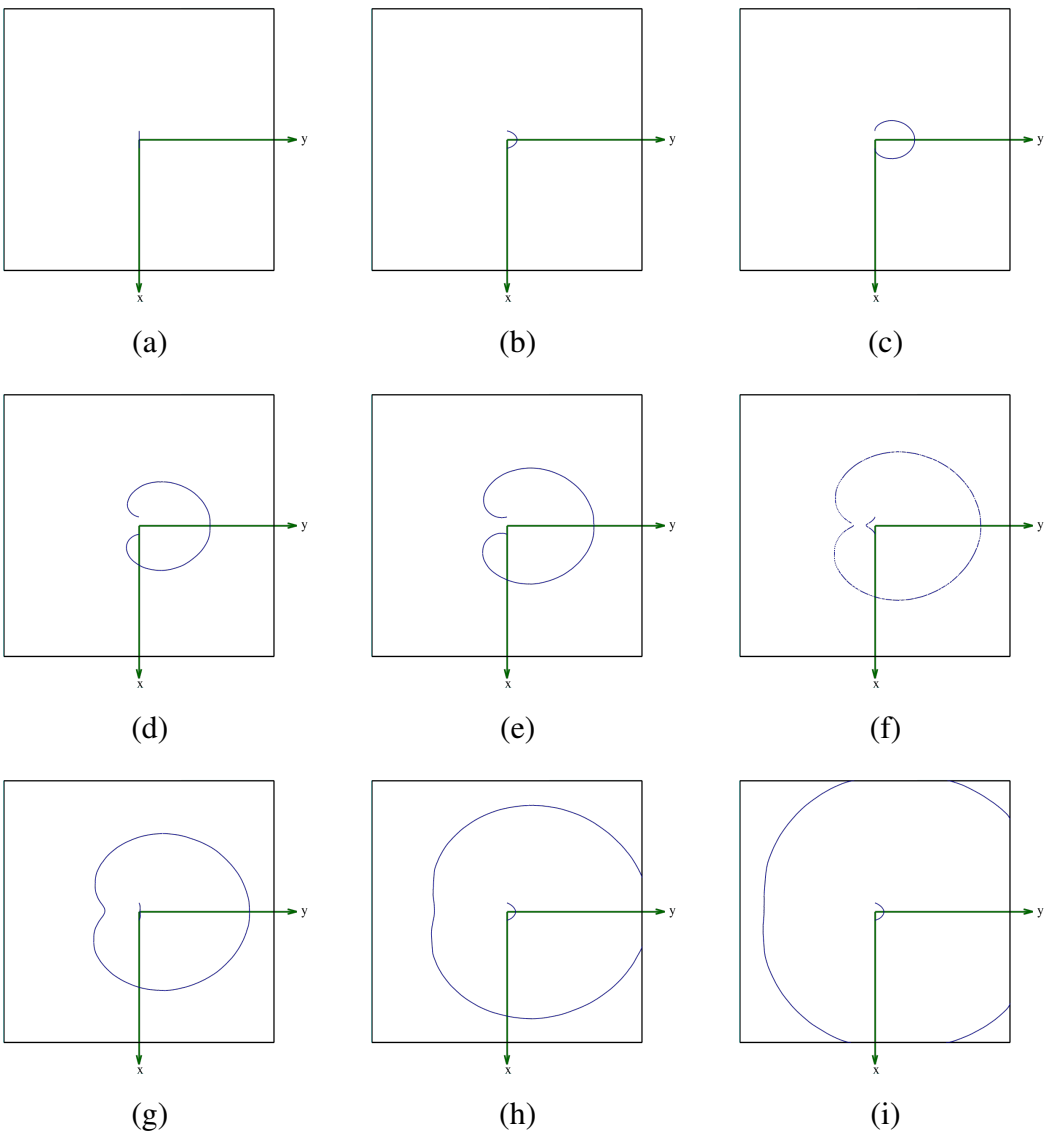

Figure 9.5: Timesteps ((a) – (i)) of a Frank-Read source multiplication shown in Fig. 9.4.

We have categorized the simulations based on the spatial arrangement of the substitutional particles or atoms in the solid solution. Chronologically, the modeling of the particle-misfit problem associated with solute atoms occurred as **Completely random order**, **Simple cubic (SC) structure**, and **Statistical** and described below.

Completely random order

We consider all the solute atoms (Ni atoms) to be randomly distributed in the Copper matrix as per the weight percentages without altering the Face Centered Cubic (FCC) lattice structure. The total volume of the RVE is $60,000 \times 60,000 \times 40,000 \times (0.2556 \times 10^{-9})^3 = 2.4046 \times 10^{-15}$ m^3. We calculate the weight of a pure Copper RVE (using Table 9.1) as $2.4046 \times 10^{-15} \times 8,960 = 2.1545 \times 10^{-11}$Kg. The total number of Copper atoms N in the RVE is equal to ($Wt_{RVE}/A_{Cu} = 2.1545 \times 10^{-11}/(63.5 \times 1.66054 \times 10^{-27}) = 2.0433 \times 10^{14}$) since the weight of one Copper atom is 63.5 amu ($63.5 \times 1.66054 \times 10^{-27}$ Kg). For any given weight percentage, say x% Nickel atoms in the Copper matrix, we can find the approximate number of Ni atoms, n, using the following relation [103]:

$$n = \frac{x \times A_{Cu}}{x \times A_{Cu} + (100 - x) \times A_{Ni}} \times N \tag{9.10}$$

where, A_{Cu} and A_{Ni} are the atomic weight of Copper and Nickel, respectively, and N is the total number of atoms present in the matrix. For 1% Ni atoms by weight, the number of Nickel atoms (eq. (10)) in the solid solution is approximately 2.2815×10^{12}. That means 2.2815×10^{12} Ni atoms can affect the dislocation motion. Since the atomic weight of Copper and Nickel are not significantly different, the number of Ni atoms increases almost linearly with the increase of Nickel weight percent in the solution (see Fig. 9.6a). The relationship between weight percentage and atom percentage is given in Eq. (9.11) [103]:

$$Wt\%_{Cu} = \frac{Atm\%_{Cu} \times A_{Cu}}{Atm\%_{Cu} \times A_{Cu} + Atm\%_{Ni} \times A_{Ni}} \times 100 \tag{9.11}$$

where, $Wt\%$ = Weight percentage, $Atm\%$ = Atom percentage, and A= Atomic weight.

We tried to simulate 1% Ni atoms in a Cu-Ni solid solution with the atom numbers/FR source info described earlier. As the simulation marched in time, we found sudden bowing of the dislocation source early in the simulations, which is unusual and unphysical for this problem. We investigated the issue and discovered that in the random distribution of the

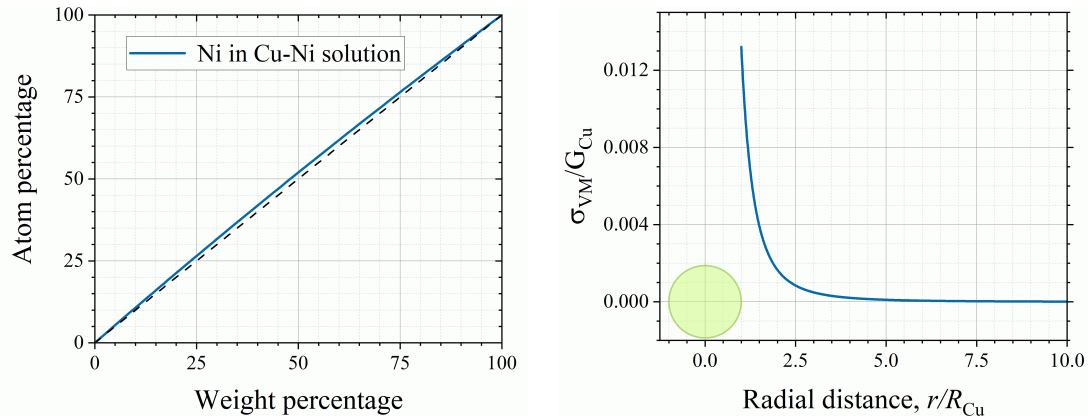

(a) (b)

Figure 9.6: (a) Atom percentage as a function of weight percentage. The dashed line is a 45° line to show the difference between atom percentage and weight percentage (i.e. they are not one-to-one) (b) Eigenstress (in terms of Mises stress) of a misfit particle (shown as a circle in the figure) as a function of normalized radial distance

solute atoms (per above), some atoms are very close to some dislocation segments and are causing very high local stress (see Fig. 9.6b). Figure 9.6b shows the von Mises stress [104] calculations which is given by this equation:

$$\sigma_{VM} = \sqrt{\frac{(\sigma_{xx}-\sigma_{yy})^2+(\sigma_{yy}-\sigma_{zz})^2+(\sigma_{zz}-\sigma_{xx})^2+6(\sigma_{xy}^2+\sigma_{yz}^2+\sigma_{zx}^2)}{2}} \tag{9.12}$$

Figure 9.6b plots the normalized von Mises stress versus radial distance from the solute atom center (the atom being shown in the figure as a circle). For example, a solute atom located $1.5R_{Cu}$ away $\left(\frac{\sigma_{VM}}{G_{Cu}} \approx 0.004\right)$ is causing a von Mises stress of about $0.004 \times 46.0 \times 10^9$Pa $= 184$ MPa. As a comparison, the yield stress of Copper at room temperature is about $80 \sim 100$ MPa [105]. This stress value, close to the solute atoms, is too high. Also, the minimum distance between two atoms in the crystal lattice is two atomic radii ($2R$). For this reason, the idea of the complete random distribution of solute atoms was abandoned.

Simple cubic (SC) structure

Next, we considered the solute atoms to be distributed randomly in the RVE, as per any studied weight percentages, but maintaining a SC lattice structure instead. Since both Copper and Nickel have FCC structures; we assumed here for simplicity that the Copper-Nickel solution obeys a SC structure. We know that in a SC structure, there is one full atom per unit cell. In a SC structure, the lattice constant $a = 2R = b$. So the volume of one unit cell is $b \times b \times b = b^3$ and in the current RVE, there can be $60,000 \times 60,000 \times 40,000 = 1.44 \times 10^{14}$ atoms. For 1% Nickel atoms in weight, the Copper-Nickel solution can have approximately 1.5567×10^{12} of Nickel atoms. This number is less than the previously calculated Nickel atoms (i.e. 2.2815×10^{12}) because the SC structure has a lower packing factor than the FCC structure. Therefore, in a simulation of 1% Nickel by weight, there are 1.5567×10^{12} atoms (still a large number of any simulation) that could affect the dislocation dynamics.

In a SC structure, the minimum distance between two atoms is $b = 2R$. Then the computed stress from the misfit model at $r = 2R$ is about 74 MPa, which is less than the yield stress of Cu but not significant. So for a high solute atom percentage, there could be the possibility of an early blowout of the dislocation source (i.e. high stresses driving the dislocation segments at high speeds to the outside of the RVE), and hence the model would still be unphysical. Since the eigenstress (stress not emanating from the applied loading) from the misfit particle model almost dies out after $5b$ (see Fig. 9.6b), we calculated in the dynamic simulations the eigenstress at the center of each dislocation segment only by considering the solute atoms within a $5b$ radius. This makes the simulation faster since we are not considering all the solute atoms in the DDD computational box and without a significant loss of accuracy from a stress calculation standpoint. Still, an average computer may take days to continue the simulation with 1% Nickel atoms in a Copper-Nickel solution to reach a strain of 0.15% in the DDD simulations. Some simulations may take

months depending on the weight percent of Nickel in the solution. Hence this approach has been abandoned as well.

Statistical approach

To mitigate the simulation time challenge, we took a statistical approach. In this approach, we considered a pseudo-RVE (not the original large simulation RVE) of dimensions equal to $20b \times 20b \times 20b$ as shown in Fig. 9.7, and considered the solute atoms in it placed randomly in a SC lattice (pertaining to whatever weight percentages of the two species). The random distribution of the solute atoms should be different for every dislocation segment and time-step of the dynamic simulation to mimic the actual random distribution of solute atoms in the larger material expanse. We computed the eigenstress at the center of the pseudo-RVE for all segments (with the center of the pseudo-RVE coinciding with the center of a segment) at each time step and fed the eigenstress tensor into Eq. (9.7) for calculation of the PK force in the 3D DDD code. This improved the simulation time over the previous method but was not significant and could not eliminate the possibility of the early blowout of the dislocation source during the simulation/multiplication.

In order to improve simulation time further, we want to find one stress tensor from the randomly distributed solute atoms rather than randomizing the solute atoms in a pseudo-RVE every time step. This stress tensor can be calculated before the simulation and can be thought of as the stress tensor at each field point of the larger simulation RVE. As can be seen from Eq. (9.7), the resultant PK force can be different for the same stress tensor when the direction vector, or line sense, of a dislocation segment is different. We added that stress tensor at the material or field points, representing segment centers, to the applied external shearing stress. This makes the simulation time impressively faster (around four to five hours on an average computer). However, the possibility of an early blowout of the dislocation source during the simulation/multiplication may still happen. Moreover,

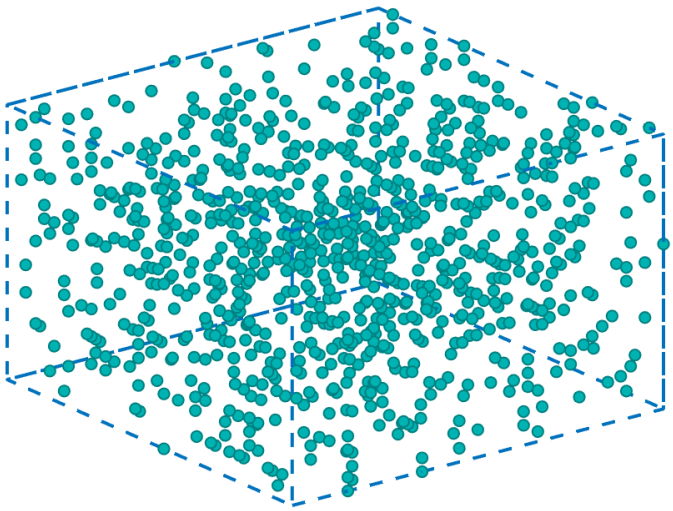

Figure 9.7: Randomly distributed Ni atoms (10% by weight) in a Cu matrix (dimension of the box: $20b \times 20b \times 20b$). Matrix atoms are not shown. The lattice structure of the solid solution is assumed to be a "Simple Cubic structure" here for simplicity. This box is termed a "pseudo-RVE" in this chapter

this raises a statistical argument of using one stress tensor for all time-steps. So to account for this issue, we find the eigenstress tensor by averaging stress tensors from many randomizations of solid atoms in the pseudo-RVE ($20b \times 20b \times 20b$). The use of this average tensor should be justified statistically. It is worth mentioning that the von Mises stress calculated from the average tensor is remarkably lower than one random stress tensor, and the possibility of an early source blowout is no longer an issue! Note that for the simulation of $x\%$ solute atoms by weight in the solution, we use in the DDD code the combined shear modulus of the solid solution, similar to the "rule of mixtures" [106] used in finding elastic properties in composite materials:

$$G_{Solution} = \frac{G_{solute} \times x + G_{matrix} \times (100 - x)}{100} \tag{9.13}$$

We also applied this rule of mixture to Poisson's ratio and the Burger vector magnitude.

9.3 Results and Discussion

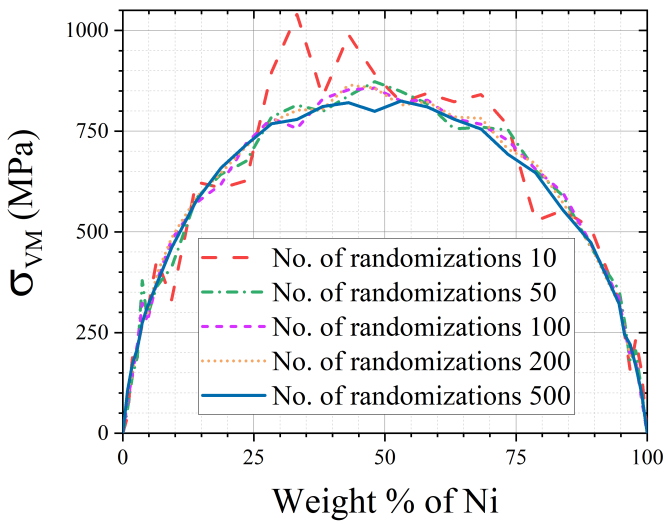

Figure 9.8: Average von Mises stress as the weight percentage of Nickel increases in a Copper-Nickel solid solution

Figure 9.8 shows the trend of the average von Mises stress introduced by the solute atoms as the weight percentage of the solute atom (Nickel) increases in the binary (Cu-Ni) solution. The average von Mises stress is calculated by averaging von Mises stress from the stress tensors of individual randomizations. That's why the average stress tensor from the randomizations (which is found by individually averaging every stress component to construct this average stress tensor) will not produce the average von Mises stress shown in the figure. The von Mises stress curve (see Fig. 9.8) becomes smoother as the randomization increases. The trend is quite symmetric, which *qualitatively* verifies the model. Another verification is the shape of this curve, which is parabolic in nature. This makes sense since at the midpoint; the slope is expected to tend to zero. This is because in a low percentage of the solute atoms, the eigenstress is low; and in a high percentage of the solute atoms, the eigenstress is also low because more overlapping in the tensile and compressive zones

occurs. If one switches the roles of Copper and Nickel atoms in terms of which one is the solute and which one is the matrix, Fig. 9.8 is still obtained due to the reasons discussed above. In other words, in the limit (or for pure Cu or pure Ni), it is not expected that the solute atoms randomizations would produce a net eigenstrain or eigenstress field and hence the corresponding zero von Mises stress expected from such field (as is captured in the figure). We see in Fig. 9.8, at a high percentage of the solute atoms, the calculated average von Mises stress is almost ten times the yield strength of pure Copper. This result is overestimated, or very high, because we see from Fig. 9.6b that the mathematical model (Eqs. (9.1)) overestimates the stress values.

In Fig. 9.9a, the flow stress of both Copper and Nickel is comparably smaller than the experimental(tensile) strength. This may happen for many reasons. We only considered a single Frank-Read source in the constant strain rate simulations and ignored the free surface effects [18], [35], [34], [102], [49], [48], [54], [17], [16], [69]. Since the simulations have only one dislocation source, the interactions from multiple dislocations [107] were not considered here. Again the simulations' RVE is monocrystalline(single crystal), whereas bulk materials are mostly polycrystalline. As a consequence, the grain size and grain boundary effects could [11], [100], [108] not be captured in the simulations. All the simulations ignored other kinds of dislocation interactions and phenomena that may hinder dislocation motion. As a result, the simulation flow strength is much lower than the experimental tensile strength of the bulk materials. Comparing the experimental strength [103] (see Fig. 9.9b) and the flow stress of Copper and Nickel from the simulation, we find the flow stress of both Copper and Nickel is about 11.89 times smaller than the experimental strength values. This result was assuring as this one factor related to both species (Cu and Ni). Based on this finding or result,the authors assumed that for any weight percentage of the solute atoms between the extremes of pure Cu or pure Ni, the results for flow stress from the DDD simulations should qualitatively (and not quantitatively) follow the experimental results for the tensile strength of this binary system (shown in Fig. 9.9b).

This hypothesis will be verified later on.

To produce a comparative tensile strength diagram (Fig. 9.9b), we took on the following approach. First, we pick any strength value σ_{xe} (the subscript e stands for "experimental") for a particular weight percentage (say $x\%$) of the Nickel atoms from the experimental tensile strength diagram [103], see Fig. 9.9b. Then we find another stress value σ_{xt} dividing σ_{xe} by 11.89. This σ_{xt} is our "target flow stress" in the DDD simulations for $x\%$ Nickel atoms in the Cu-Ni solution. The x here is any number between 0 and 100.

As described in the earlier section, we run the DDD simulation with the average eigenstress tensor, $\boldsymbol{\sigma}_{avg}$, for $x\%$ Nickel in the RVE. We find the flow stress from the simulation and compare it with σ_{xt}. The eigenstress tensor then may need to be scaled to match the target flow stress σ_{xt} for $x\%$ Nickel in Cu-Ni solution. This scaling factor can be chosen iteratively to match the flow stress σ_{xt} for $x\%$ of Nickel atoms in the Cu-Ni solution. Once we match σ_{xt}, we store that eigenstress tensor $\boldsymbol{\sigma}_{xs}$. We then employ the stress tensor $\boldsymbol{\sigma}_{xs}$ obtained for $x\%$ of Nickel in Cu-Ni solution for the other weight percentages of Ni in the solution using Fig. 9.8. For example, to find the eigenstress tensor for $y\%$ Nickel in Cu-Ni solution, we multiply the stress tensor $\boldsymbol{\sigma}_{xs}$ by a scaling factor equal to $\sigma^y_{VM}/\sigma^x_{VM}$, where σ^x_{VM} and σ^y_{VM} are the corresponding average von Mises stresses in Fig. 9.8 for $x\%$ and $y\%$ of Ni. This helps us run DDD simulations for all weight percentages of the solute atoms.

Figure 9.9a shows the stress-strain curves obtained via DDD simulations for different weight percentages of Ni in the Cu-Ni solutions via the process explained above. The flow stresses in Fig. 9.9b are captured from the stress-strain curves of Fig. 9.9a. Fig. 9.9b also demonstrates the comparison between the experimental strength for the different weight percentages of Ni (solute) atoms in the Cu-Ni solution [103]. Figure 9.9b is constructed with two different y-axes so the values of experimental tensile strength and flow stress from the simulations can be compared with a scale factor or qualitatively. Each

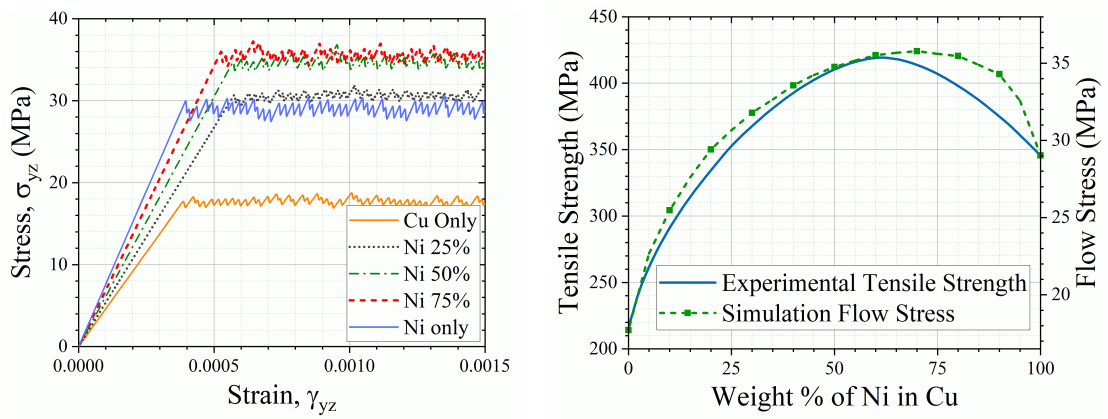

(a) (b)

Figure 9.9: (a) Stress-strain curves for different solute atom weight percentages. (b) Comparison between experimental strength and simulation flow stress for different weight percentages of solute atoms. The left y-axis is for experimental tensile strength, and the right y-axis is for the flow stress from the simulations.

DDD simulation for one weight percentage took around four to five hours on an average workstation. As we mentioned earlier, the flow stress values from the simulations are consistently 11.89 times smaller than the experimental tensile strengths. The left y-axis of Fig. 9.9b is for the experimental tensile stress, and the right y-axis is for the flow stress from the simulations. In Fig. 9.9b, we see an excellent *qualitative* agreement in experimental tensile strength values and the flow stress captured from the simulations. This proves the previously-stated hypothesis. Hence, this statistical approach for finding the eigenstress values and their effect on dislocations allows for faster and acceptable simulation results.

Next, we investigate the exponent of the flow stress, or change of flow stress, due to the addition of Ni (solute) atom in the Cu-Ni solid solution. We assume the relation to be,

$$\Delta\tau = a(bx)^c \tag{9.14}$$

where τ is the flow stress, x is the concentration (weight percentage) of solute atoms in the solution and the parameters a, b, c are determined by regression to get the highest coefficient of determination (R^2) as shown in Fig. 9.10a. Since the fit equation is nonlinear,

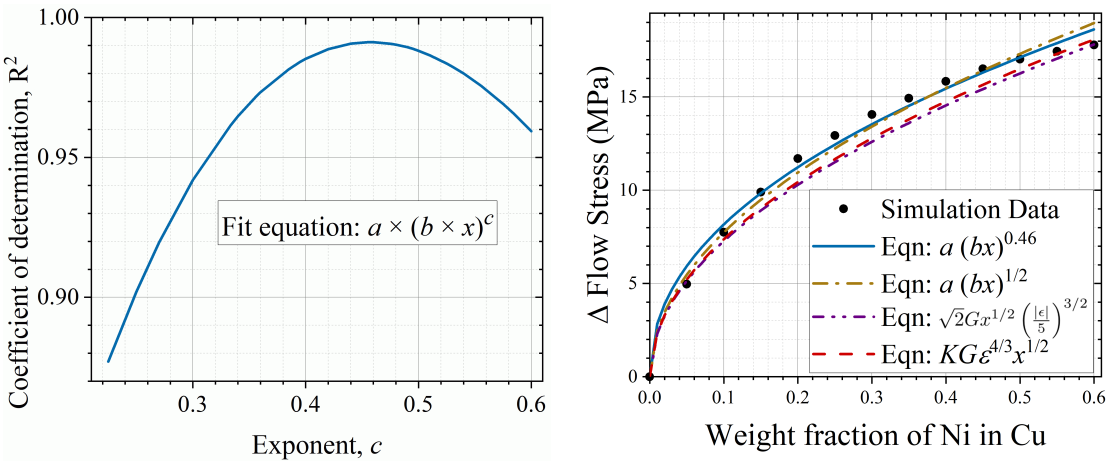

Figure 9.10: (a) The Coefficient of determination R^2 as a function of solute atom concentration. (b) Curve fitting of flow stress changes based on the simulation data, as well as plots of two known theoretical equations for flow stress changes

to avoid regression complications, we iteratively feed the value of parameter c and note the maximum coefficient of determination R^2 for a particular value of c and plot R^2 in Fig. 9.10a as a function of the solute atom concentration. The maximum value of R^2 that we found for the exponent (parameter c) is equal to 0.46 with the coefficient of determination being $R^2 = 0.9912$. Hull et al. [2] suggested the flow stress for $x\%$ solute atom as:

$$\Delta\tau = \sqrt{2}Gx^{\frac{1}{2}}\left(\frac{|\varepsilon|}{5}\right)^{\frac{3}{2}} \tag{9.15}$$

where G is the shear modulus and ε is the misfit strain equal to $\left(\frac{R_{solute}-R_{matrix}}{R_{matrix}}\right)$. Arsenault et al. [109] suggested another relation:

$$\Delta\tau = KG\varepsilon^{\frac{4}{3}}x^{\frac{1}{2}} \tag{9.16}$$

where ε is the misfit strain, and K is a constant and equal to 0.0694.

Figure 9.10b shows the curve fits, and the theoretical equations, imposed on the simulation flow stress data. As can be seen, the fit equation $a(bx)^{0.46}$ and $a(bx)^{0.5}$ matched closely to

the data points. For the exponent 0.46 and 0.50 we have presented parameters a, b, and R^2 (coefficient of determination) in table 9.2.

Exponent	a	b	R^2
0.46	1.164×10^5	1.031×10^5	0.9912
0.50	6.033×10^4	1.647×10^5	0.9881

Table 9.2: Fit parameters for Eq. (9.14) using different values of exponent c

In Fig. 9.10b, the suggested relations by Hull et al. and Arsenault et al. assume a constant value of the shear modulus, i.e. the shear modulus of the Copper matrix. The coefficient of determination for Hull et al. and Arsenault et al. are 0.9646 and 0.9739, respectively. However, it is more logical to take the shear modulus as a function of the solute atom concentration (Eq. (9.13)). We did the curve fit in Fig. 9.11a to see how much the relations suggested by Hull et al. and Arsenault et al., but with an adjusted shear modulus, match the simulation data. Both curves show improvement up to about 20% by weight of solute atoms, and then they both stray from simulation data as compared with the closer agreement in Fig. 9.10b which utilized a constant shear modulus value. We re-calculate the coefficient of determination: $R^2 = 0.6923$ for the Hull et al. relation in Eq. (9.15), and $R^2 = 0.6594$ for Arsenault et al. relation in equation. (9.16). Since the coefficients of determination R^2 for both relations are significantly lower than their previous fit (0.9646 and 0.9739 per above), we suggest using a constant value of the shear modulus G in Eqs. (9.15) and (9.16), and not use a variable shear modulus value that depends on the solute concentration. Also, since Eq. (9.14), with an exponent of 0.46 or 0.5 is providing the best fit with the highest coefficient of determinations, moving forward the authors will only focus on this fit equation and not Eqs. (9.15) and (9.16).

Let's turn our attention now to Fig. 9.11b. Although the chosen best-fit equation (Eq. (9.14)) nicely predicts the changes in the flow stress similar to the DDD predictions, this equation starts to deviate after 50% weight percent as it continues its upward-only trend.

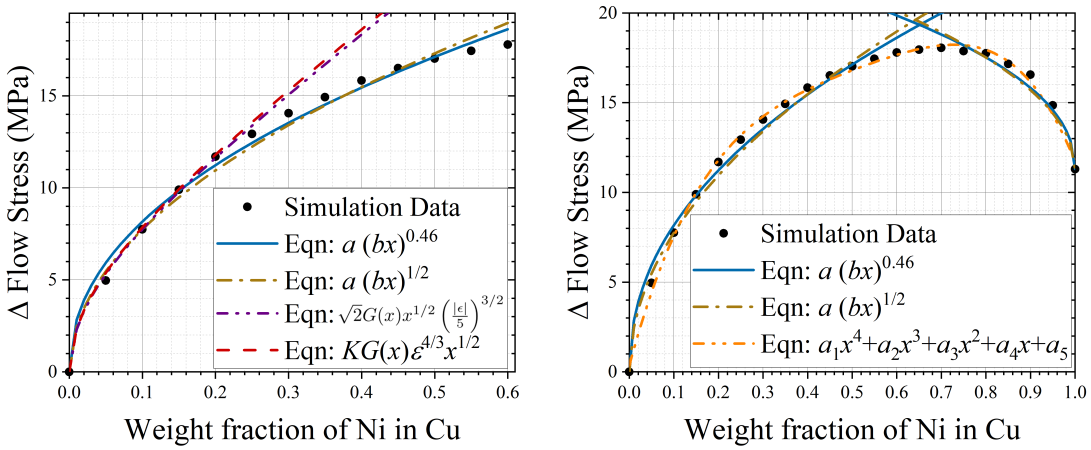

Figure 9.11: (a) Curve fits of flow stress changes with the shear modulus adjusted for the solute concentration, plus the simulation data points for solute concentrations from 0 to 0.6. (b) Curve fits of flow stress changes using Eq. (9.14) imposed on the simulation data points for solute concentrations from 0 to 1.

In other words, this equation cannot closely fit the whole range of data, i.e. 0% - 100% weight percents. However, this equation can be fit for high solute concentrations in reverse (see Fig. 9.11b). To fit high concentrations of Ni from $65\% - 100\%$ weight percents, we look at this problem in reverse. This means we now treat Ni as the base matrix and Cu as the solute. Doing so enables the curve fitting on the right-hand side of Fig. 9.11b.. Even when we employ fitting and reverse fitting, Eq. (9.14) still overshoots above the 3D DDD simulation data in Fig. 9.11b in the range between 50% and 75% weight percents. To overcome this issue, one can consider instead a polynomial fit to cover the whole range. The authors found out that the best polynomial fit is a fourth-order polynomial. For this polynomial fit, the coefficient of determination R^2 is equal to 0.9968 (for the whole range of solute atoms percentages) which is the best fit achieved in this study thus far. Specifically, the polynomial coefficients for this fit are: $a_1 = -1.355 \times 10^8$, $a_2 = -2.779 \times 10^8$, $a_3 = -2.228 \times 10^8$, $a_4 = 9.174 \times 10^7$, $a_5 = 3.634 \times 10^5$. As can be seen, the polynomial fitting allows for a natural fit equation that covers the whole range of data without having to piece together fit equations.

9.4 Conclusions

The current study presented several methods to simulate the solid solution strengthening using a 3D DDD code. Among the proposed methods, the statistical method is found to be the fastest and produces accurate simulations. Although the theoretical eigenstress model overestimates the generated stress by the solute atoms in the solid solution, the authors have shown a method, that relies on experimental input, to scale the computed stress tensor and use it in the simulations. The simulation results have shown good qualitative agreement with the experimental data and have proven the hypothesis that the shape of the flow stress data for binary solution systems mimics that of the tensile strength data. The authors therefore believe this approach can be expanded to other binary solution systems not studied here.

Journal reference

Siddique, A. B., & Khraishi, T. A. (2022). Multi-scale modeling of solute atom strengthening using 3D discrete dislocation dynamics. Journal of Materials Science.
https://doi.org/10.1007/s10853-022-07077-z

Appendices

Appendix A

Surface Kernels

A.1 Kernel Equations

$$
\begin{aligned}
K_{xxx} = & \frac{\mu}{2\pi Y^2(1-\nu)}\Bigg[\left(\varepsilon_{xxy}Y_y t_x + \varepsilon_{xxz}Y_z t_x + \varepsilon_{xxy}Y_y t_x + \varepsilon_{xxz}Y_z t_x\right)(1-\nu) \\
& - \varepsilon_{xxy}Y_x t_y - \varepsilon_{xxz}Y_x t_z - \varepsilon_{xxy}Y_x t_y - \varepsilon_{xxz}Y_x t_z - \left(Y_y t_z - Y_z t_y\right)\Bigg[\delta_{xx} + t_x t_x \\
& + \frac{2}{Y^2}\left[\rho_x Y_x + \rho_x Y_x + \frac{L}{R}Y_x Y_x\right]\Bigg]\Bigg] \\
= & -\frac{\mu}{2\pi Y^2(1-\nu)}\left[\left(Y_y t_z - Y_z t_y\right)\left[1 + t_x^2 + \frac{2}{Y^2}\left[2\rho_x Y_x + \frac{L}{R}Y_x^2\right]\right]\right]
\end{aligned}
\tag{A.1}
$$

$$
\begin{aligned}
K_{xxy} =& \frac{\mu}{2\pi Y^2(1-\nu)}\Bigg[\left(\varepsilon_{xxy}Y_y t_y + \varepsilon_{xxz}Y_z t_y + \varepsilon_{yxy}Y_y t_x + \varepsilon_{yxz}Y_z t_x\right)(1-\nu) \\
& - \varepsilon_{xxy}Y_y t_y - \varepsilon_{xxz}Y_y t_z - \varepsilon_{yxy}Y_x t_y - \varepsilon_{yxz}Y_x t_z - \left(Y_y t_z - Y_z t_y\right)\Bigg[\delta_{xy} + t_x t_y \\
& + \frac{2}{Y^2}\left[\rho_x Y_y + \rho_y Y_x + \frac{L}{R}Y_x Y_y\right]\Bigg]\Bigg] \\
=& \frac{\mu}{2\pi Y^2(1-\nu)}\Bigg[\varepsilon_{yxz}Y_z t_x(1-\nu) - \varepsilon_{yxz}Y_x t_z - \left(Y_y t_z - Y_z t_y\right)\Bigg[t_x t_y \\
& + \frac{2}{Y^2}\left[\rho_x Y_y + \rho_y Y_x + \frac{L}{R}Y_x Y_y\right]\Bigg]\Bigg] \\
=& \frac{\mu}{2\pi Y^2(1-\nu)}\Bigg[Y_x t_z - Y_z t_x(1-\nu) - \left(Y_y t_z - Y_z t_y\right)\Bigg[t_x t_y \\
& + \frac{2}{Y^2}\left[\rho_x Y_y + \rho_y Y_x + \frac{L}{R}Y_x Y_y\right]\Bigg]\Bigg]
\end{aligned}
\tag{A.2}
$$

$$
\begin{aligned}
K_{xxz} =& \frac{\mu}{2\pi Y^2(1-\nu)}\Bigg[\left(\varepsilon_{xxy}Y_y t_z + \varepsilon_{xxz}Y_z t_z + \varepsilon_{zxy}Y_y t_x + \varepsilon_{zxz}Y_z t_x\right)(1-\nu) \\
& - \varepsilon_{xxy}Y_z t_y - \varepsilon_{xxz}Y_z t_z - \varepsilon_{zxy}Y_x t_y - \varepsilon_{zxz}Y_x t_z - \left(Y_y t_z - Y_z t_y\right)\Bigg[\delta_{xz} + t_x t_z \\
& + \frac{2}{Y^2}\left[\rho_x Y_z + \rho_z Y_x + \frac{L}{R}Y_x Y_z\right]\Bigg]\Bigg] \\
=& \frac{\mu}{2\pi Y^2(1-\nu)}\Bigg[\varepsilon_{zxy}Y_y t_x(1-\nu) - \varepsilon_{zxy}Y_x t_y - \left(Y_y t_z - Y_z t_y\right)\Bigg[t_x t_z \\
& + \frac{2}{Y^2}\left[\rho_x Y_z + \rho_z Y_x + \frac{L}{R}Y_x Y_z\right]\Bigg]\Bigg] \\
=& \frac{\mu}{2\pi Y^2(1-\nu)}\Bigg[Y_y t_x(1-\nu) - Y_x t_y - \left(Y_y t_z - Y_z t_y\right)\Bigg[t_x t_z \\
& + \frac{2}{Y^2}\left[\rho_x Y_z + \rho_z Y_x + \frac{L}{R}Y_x Y_z\right]\Bigg]\Bigg]
\end{aligned}
\tag{A.3}
$$

$$
\begin{aligned}
K_{xyy} =& \frac{\mu}{2\pi Y^2(1-\nu)}\Bigg[(\varepsilon_{yxy}Y_y t_y + \varepsilon_{yxz}Y_z t_y + \varepsilon_{yxy}Y_y t_y + \varepsilon_{yxz}Y_z t_y)(1-\nu) \\
& - \varepsilon_{yxy}Y_y t_y - \varepsilon_{yxz}Y_y t_z - \varepsilon_{yxy}Y_y t_y - \varepsilon_{yxz}Y_y t_z - (Y_y t_z - Y_z t_y)\Bigg[\delta_{yy} + t_y t_y \\
& + \frac{2}{Y^2}\left[\rho_y Y_y + \rho_y Y_y + \frac{L}{R}Y_y Y_y\right]\Bigg]\Bigg] \\
=& \frac{\mu}{2\pi Y^2(1-\nu)}\Bigg[(\varepsilon_{yxz}Y_z t_y + \varepsilon_{yxz}Y_z t_y)(1-\nu) - \varepsilon_{yxz}Y_y t_z - \varepsilon_{yxz}Y_y t_z - \\
& (Y_y t_z - Y_z t_y)\left[1 + t_y^2 + \frac{2}{Y^2}\left[2\rho_y Y_y + \frac{L}{R}Y_y^2\right]\right]\Bigg] \\
=& \frac{\mu}{2\pi Y^2(1-\nu)}\Bigg[2Y_y t_z - 2Y_z t_y(1-\nu) - (Y_y t_z - Y_z t_y)\Bigg[1 + t_y^2 \\
& + \frac{2}{Y^2}\left[2\rho_y Y_y + \frac{L}{R}Y_y^2\right]\Bigg]\Bigg]
\end{aligned}
\tag{A.4}
$$

$$
\begin{aligned}
K_{xyz} =& \frac{\mu}{2\pi Y^2(1-\nu)}\Bigg[(\varepsilon_{yxy}Y_y t_z + \varepsilon_{yxz}Y_z t_z + \varepsilon_{zxy}Y_y t_y + \varepsilon_{zxz}Y_z t_y)(1-\nu) \\
& - \varepsilon_{yxy}Y_z t_y - \varepsilon_{yxz}Y_z t_z - \varepsilon_{zxy}Y_y t_y - \varepsilon_{zxz}Y_y t_z - (Y_y t_z - Y_z t_y)\Bigg[\delta_{yz} + t_y t_z \\
& + \frac{2}{Y^2}\left[\rho_y Y_z + \rho_z Y_y + \frac{L}{R}Y_y Y_z\right]\Bigg]\Bigg] \\
=& \frac{\mu}{2\pi Y^2(1-\nu)}\Bigg[(\varepsilon_{yxz}Y_z t_z + \varepsilon_{zxy}Y_y t_y)(1-\nu) - \varepsilon_{yxz}Y_z t_z - \varepsilon_{zxy}Y_y t_y \\
& - (Y_y t_z - Y_z t_y)\left[t_y t_z + \frac{2}{Y^2}\left[\rho_y Y_z + \rho_z Y_y + \frac{L}{R}Y_y Y_z\right]\right]\Bigg] \\
=& \frac{\mu}{2\pi Y^2(1-\nu)}\Bigg[(Y_y t_y - Y_z t_z)(1-\nu) + Y_z t_z - Y_y t_y - (Y_y t_z - Y_z t_y)\Bigg[t_y t_z \\
& + \frac{2}{Y^2}\left[\rho_y Y_z + \rho_z Y_y + \frac{L}{R}Y_y Y_z\right]\Bigg]\Bigg] \\
=& -\frac{\mu}{2\pi Y^2(1-\nu)}\Bigg[\nu(Y_y t_y - Y_z t_z) + (Y_y t_z - Y_z t_y)\Bigg[t_y t_z \\
& + \frac{2}{Y^2}\left[\rho_y Y_z + \rho_z Y_y + \frac{L}{R}Y_y Y_z\right]\Bigg]\Bigg]
\end{aligned}
\tag{A.5}
$$

$$
\begin{aligned}
K_{xzz} =& \frac{\mu}{2\pi Y^2(1-\nu)}\Bigg[\left(\varepsilon_{zxy}Y_y t_z + \varepsilon_{zxz}Y_z t_z + \varepsilon_{zxy}Y_y t_z + \varepsilon_{zxz}Y_z t_z\right)(1-\nu) \\
& - \varepsilon_{zxy}Y_z t_y - \varepsilon_{zxz}Y_z t_z - \varepsilon_{zxy}Y_z t_y - \varepsilon_{zxz}Y_z t_z - \left(Y_y t_z - Y_z t_y\right)\Bigg[\delta_{zz} + t_z t_z \\
& + \frac{2}{Y^2}\left[\rho_z Y_z + \rho_z Y_z + \frac{L}{R}Y_z Y_z\right]\Bigg]\Bigg] \\
=& \frac{\mu}{2\pi Y^2(1-\nu)}\Bigg[\left(\varepsilon_{zxy}Y_y t_z + \varepsilon_{zxy}Y_y t_z\right)(1-\nu) - \varepsilon_{zxy}Y_z t_y - \varepsilon_{zxy}Y_z t_y \\
& - \left(Y_y t_z - Y_z t_y\right)\left[1 + t_z^2 + \frac{2}{Y^2}\left[2\rho_z Y_z + \frac{L}{R}Y_z^2\right]\right]\Bigg] \\
=& \frac{\mu}{2\pi Y^2(1-\nu)}\Bigg[2Y_y t_z(1-\nu) - 2Y_z t_y - \left(Y_y t_z - Y_z t_y\right)\Bigg[1 + t_z^2 \\
& + \frac{2}{Y^2}\left[2\rho_z Y_z + \frac{L}{R}Y_z^2\right]\Bigg]\Bigg]
\end{aligned}
\tag{A.6}
$$

$$
\begin{aligned}
K_{yxx} =& \frac{\mu}{2\pi Y^2(1-\nu)}\Bigg[\left(\varepsilon_{xyx}Y_x t_x + \varepsilon_{xyz}Y_z t_x + \varepsilon_{xyx}Y_x t_x + \varepsilon_{xyz}Y_z t_x\right)(1-\nu) \\
& - \varepsilon_{xyx}Y_x t_x - \varepsilon_{xyz}Y_x t_z - \varepsilon_{xyx}Y_x t_x - \varepsilon_{xyz}Y_x t_z - \left(Y_z t_x - Y_x t_z\right)\Bigg[\delta_{xx} + t_x t_x \\
& + \frac{2}{Y^2}\left[\rho_x Y_x + \rho_x Y_x + \frac{L}{R}Y_x Y_x\right]\Bigg]\Bigg] \\
=& \frac{\mu}{2\pi Y^2(1-\nu)}\Bigg[\left(\varepsilon_{xyz}Y_z t_x + \varepsilon_{xyz}Y_z t_x\right)(1-\nu) - \varepsilon_{xyz}Y_x t_z - \varepsilon_{xyz}Y_x t_z \\
& - \left(Y_z t_x - Y_x t_z\right)\left[1 + t_x^2 + \frac{2}{Y^2}\left[2\rho_x Y_x + \frac{L}{R}Y_x^2\right]\right]\Bigg] \\
=& \frac{\mu}{2\pi Y^2(1-\nu)}\Bigg[2Y_z t_x(1-\nu) - 2Y_x t_z - \left(Y_z t_x - Y_x t_z\right)\Bigg[1 + t_x^2 \\
& + \frac{2}{Y^2}\left[2\rho_x Y_x + \frac{L}{R}Y_x^2\right]\Bigg]\Bigg]
\end{aligned}
\tag{A.7}
$$

$$
\begin{aligned}
K_{yxy} =& \frac{\mu}{2\pi Y^2(1-\nu)}\Bigg[\left(\varepsilon_{xyx}Y_x t_y + \varepsilon_{xyz}Y_z t_y + \varepsilon_{yyx}Y_x t_x + \varepsilon_{yyz}Y_z t_x\right)(1-\nu) \\
& - \varepsilon_{xyx}Y_y t_x - \varepsilon_{xyz}Y_y t_z - \varepsilon_{yyx}Y_x t_x - \varepsilon_{yyz}Y_x t_z - \left(Y_z t_x - Y_x t_z\right)\Bigg[\delta_{xy} + t_x t_y \\
& + \frac{2}{Y^2}\left[\rho_x Y_y + \rho_y Y_x + \frac{L}{R}Y_x Y_y\right]\Bigg]\Bigg] \\
=& \frac{\mu}{2\pi Y^2(1-\nu)}\Bigg[\varepsilon_{xyz}Y_z t_y\,(1-\nu) - \varepsilon_{xyz}Y_y t_z - \left(Y_z t_x - Y_x t_z\right)\Bigg[t_x t_y \\
& + \frac{2}{Y^2}\left[\rho_x Y_y + \rho_y Y_x + \frac{L}{R}Y_x Y_y\right]\Bigg]\Bigg] \\
=& \frac{\mu}{2\pi Y^2(1-\nu)}\Bigg[Y_z t_y\,(1-\nu) - Y_y t_z - \left(Y_z t_x - Y_x t_z\right)\Bigg[t_x t_y \\
& + \frac{2}{Y^2}\left[\rho_x Y_y + \rho_y Y_x + \frac{L}{R}Y_x Y_y\right]\Bigg]\Bigg]
\end{aligned}
\tag{A.8}
$$

$$
\begin{aligned}
K_{yxz} =& \frac{\mu}{2\pi Y^2(1-\nu)}\Bigg[\left(\varepsilon_{xyx}Y_x t_z + \varepsilon_{xyz}Y_z t_z + \varepsilon_{zyx}Y_x t_x + \varepsilon_{zyz}Y_z t_x\right)(1-\nu) \\
& - \varepsilon_{xyx}Y_z t_x - \varepsilon_{xyz}Y_z t_z - \varepsilon_{zyx}Y_x t_x - \varepsilon_{zyz}Y_x t_z - \left(Y_z t_x - Y_x t_z\right)\Bigg[\delta_{xz} + t_x t_z \\
& + \frac{2}{Y^2}\left[\rho_x Y_z + \rho_z Y_x + \frac{L}{R}Y_x Y_z\right]\Bigg]\Bigg] \\
=& \frac{\mu}{2\pi Y^2(1-\nu)}\Bigg[\left(\varepsilon_{xyz}Y_z t_z + \varepsilon_{zyx}Y_x t_x\right)(1-\nu) - \varepsilon_{xyz}Y_z t_z - \varepsilon_{zyx}Y_x t_x - \\
& \left(Y_z t_x - Y_x t_z\right)\Bigg[t_x t_z + \frac{2}{Y^2}\left[\rho_x Y_z + \rho_z Y_x + \frac{L}{R}Y_x Y_z\right]\Bigg]\Bigg] \\
=& \frac{\mu}{2\pi Y^2(1-\nu)}\Bigg[\left(Y_z t_z - Y_x t_x\right)(1-\nu) + Y_x t_x - Y_z t_z - \left(Y_z t_x - Y_x t_z\right)\Bigg[t_x t_z \\
& + \frac{2}{Y^2}\left[\rho_x Y_z + \rho_z Y_x + \frac{L}{R}Y_x Y_z\right]\Bigg]\Bigg] \\
=& -\frac{\mu}{2\pi Y^2(1-\nu)}\Bigg[\nu\left(Y_z t_z - Y_x t_x\right) + \left(Y_z t_x - Y_x t_z\right)\Bigg[t_x t_z \\
& + \frac{2}{Y^2}\left[\rho_x Y_z + \rho_z Y_x + \frac{L}{R}Y_x Y_z\right]\Bigg]\Bigg]
\end{aligned}
\tag{A.9}
$$

$$
\begin{aligned}
K_{yyy} =& \frac{\mu}{2\pi Y^2(1-\nu)}\Bigg[\left(\varepsilon_{yyx}Y_x t_y + \varepsilon_{yyz}Y_z t_y + \varepsilon_{yyx}Y_x t_y + \varepsilon_{yyz}Y_z t_y\right)(1-\nu) \\
& - \varepsilon_{yyx}Y_y t_x - \varepsilon_{yyz}Y_y t_z - \varepsilon_{yyx}Y_y t_x - \varepsilon_{yyz}Y_y t_z - \left(Y_z t_x - Y_x t_z\right)\Bigg[\delta_{yy} + t_y t_y \\
& + \frac{2}{Y^2}\left[\rho_y Y_y + \rho_y Y_y + \frac{L}{R}Y_y Y_y\right]\Bigg]\Bigg] \\
=& -\frac{\mu}{2\pi Y^2(1-\nu)}\left[\left(Y_z t_x - Y_x t_z\right)\left[1 + t_y^2 + \frac{2}{Y^2}\left[2\rho_y Y_y + \frac{L}{R}Y_y^2\right]\right]\right]
\end{aligned}
\tag{A.10}
$$

$$
\begin{aligned}
K_{yyz} =& \frac{\mu}{2\pi Y^2(1-\nu)}\Bigg[\left(\varepsilon_{yyx}Y_x t_z + \varepsilon_{yyz}Y_z t_z + \varepsilon_{zyx}Y_x t_y + \varepsilon_{zyz}Y_z t_y\right)(1-\nu) \\
& - \varepsilon_{yyx}Y_z t_x - \varepsilon_{yyz}Y_z t_z - \varepsilon_{zyx}Y_y t_x - \varepsilon_{zyz}Y_y t_z - \left(Y_z t_x - Y_x t_z\right)\Bigg[\delta_{yz} + t_y t_z \\
& + \frac{2}{Y^2}\left[\rho_y Y_z + \rho_z Y_y + \frac{L}{R}Y_y Y_z\right]\Bigg]\Bigg] \\
=& \frac{\mu}{2\pi Y^2(1-\nu)}\Bigg[\varepsilon_{zyx}Y_x t_y\left(1-\nu\right) - \varepsilon_{zyx}Y_y t_x - \left(Y_z t_x - Y_x t_z\right)\Bigg[t_y t_z \\
& + \frac{2}{Y^2}\left[\rho_y Y_z + \rho_z Y_y + \frac{L}{R}Y_y Y_z\right]\Bigg]\Bigg] \\
=& \frac{\mu}{2\pi Y^2(1-\nu)}\Bigg[Y_y t_x - Y_x t_y\left(1-\nu\right) - \left(Y_z t_x - Y_x t_z\right)\Bigg[t_y t_z \\
& + \frac{2}{Y^2}\left[\rho_y Y_z + \rho_z Y_y + \frac{L}{R}Y_y Y_z\right]\Bigg]\Bigg]
\end{aligned}
\tag{A.11}
$$

$$
\begin{aligned}
K_{yzz} =& \frac{\mu}{2\pi Y^2(1-\nu)}\Bigg[\left(\varepsilon_{zyx}Y_x t_z + \varepsilon_{zyz}Y_z t_z + \varepsilon_{zyx}Y_x t_z + \varepsilon_{zyz}Y_z t_z\right)(1-\nu) \\
& - \varepsilon_{zyx}Y_z t_x - \varepsilon_{zyz}Y_z t_z - \varepsilon_{zyx}Y_z t_x - \varepsilon_{zyz}Y_z t_z - \left(Y_z t_x - Y_x t_z\right)\Bigg[\delta_{zz} + t_z t_z \\
& + \frac{2}{Y^2}\left[\rho_z Y_z + \rho_z Y_z + \frac{L}{R}Y_z Y_z\right]\Bigg]\Bigg] \\
=& \frac{\mu}{2\pi Y^2(1-\nu)}\Bigg[\left(\varepsilon_{zyx}Y_x t_z + \varepsilon_{zyx}Y_x t_z\right)(1-\nu) - \varepsilon_{zyx}Y_z t_x - \varepsilon_{zyx}Y_z t_x \\
& - \left(Y_z t_x - Y_x t_z\right)\left[1 + t_z^2 + \frac{2}{Y^2}\left[2\rho_z Y_z + \frac{L}{R}Y_z^2\right]\right]\Bigg] \\
=& \frac{\mu}{2\pi Y^2(1-\nu)}\Bigg[2Y_z t_x - 2Y_x t_z\left(1-\nu\right) - \left(Y_z t_x - Y_x t_z\right)\Bigg[1 + t_z^2 \\
& + \frac{2}{Y^2}\left[2\rho_z Y_z + \frac{L}{R}Y_z^2\right]\Bigg]\Bigg]
\end{aligned}
\tag{A.12}
$$

$$
\begin{aligned}
K_{zxx} =& \frac{\mu}{2\pi Y^2(1-\nu)}\Bigg[\left(\varepsilon_{xzx}Y_x t_x + \varepsilon_{xzy}Y_y t_x + \varepsilon_{xzx}Y_x t_x + \varepsilon_{xzy}Y_y t_x\right)(1-\nu) \\
& - \varepsilon_{xzx}Y_x t_x - \varepsilon_{xzy}Y_x t_y - \varepsilon_{xzx}Y_x t_x - \varepsilon_{xzy}Y_x t_y - \left(Y_x t_y - Y_y t_x\right)\Bigg[\delta_{xx} + t_x t_x \\
& + \frac{2}{Y^2}\left[\rho_x Y_x + \rho_x Y_x + \frac{L}{R}Y_x Y_x\right]\Bigg]\Bigg] \\
=& \frac{\mu}{2\pi Y^2(1-\nu)}\Bigg[\left(\varepsilon_{xzy}Y_y t_x + \varepsilon_{xzy}Y_y t_x\right)(1-\nu) - \varepsilon_{xzy}Y_x t_y - \varepsilon_{xzy}Y_x t_y \\
& - Y_x t_y - Y_y t_x)\left[1 + t_x^2 + \frac{2}{Y^2}\left[2\rho_x Y_x + \frac{L}{R}Y_x^2\right]\right]\Bigg] \\
=& \frac{\mu}{2\pi Y^2(1-\nu)}\Bigg[2Y_x t_y - 2Y_y t_x(1-\nu) - \left(Y_x t_y - Y_y t_x\right)\Bigg[1 + t_x^2 \\
& + \frac{2}{Y^2}\left[2\rho_x Y_x + \frac{L}{R}Y_x^2\right]\Bigg]\Bigg]
\end{aligned}
\tag{A.13}
$$

$$
\begin{aligned}
K_{zxy} =& \frac{\mu}{2\pi Y^2(1-\nu)}\Bigg[\left(\varepsilon_{xzx}Y_x t_y + \varepsilon_{xzy}Y_y t_y + \varepsilon_{yzx}Y_x t_x + \varepsilon_{yzy}Y_y t_x\right)(1-\nu) \\
& - \varepsilon_{xzx}Y_y t_x - \varepsilon_{xzy}Y_y t_y - \varepsilon_{yzx}Y_x t_x - \varepsilon_{yzy}Y_x t_y - \left(Y_x t_y - Y_y t_x\right)\Bigg[\delta_{xy} + t_x t_y \\
& + \frac{2}{Y^2}\left[\rho_x Y_y + \rho_y Y_x + \frac{L}{R}Y_x Y_y\right]\Bigg]\Bigg] \\
=& \frac{\mu}{2\pi Y^2(1-\nu)}\Bigg[\left(\varepsilon_{xzy}Y_y t_y + \varepsilon_{yzx}Y_x t_x\right)(1-\nu) - \varepsilon_{xzy}Y_y t_y - \varepsilon_{yzx}Y_x t_x - \\
& \left(Y_x t_y - Y_y t_x\right)\left[t_x t_y + \frac{2}{Y^2}\left[\rho_x Y_y + \rho_y Y_x + \frac{L}{R}Y_x Y_y\right]\right]\Bigg] \\
=& \frac{\mu}{2\pi Y^2(1-\nu)}\Bigg[\left(Y_x t_x - Y_y t_y\right)(1-\nu) + Y_y t_y - Y_x t_x - \left(Y_x t_y - Y_y t_x\right)\Bigg[t_x t_y \\
& + \frac{2}{Y^2}\left[\rho_x Y_y + \rho_y Y_x + \frac{L}{R}Y_x Y_y\right]\Bigg]\Bigg] \\
=& -\frac{\mu}{2\pi Y^2(1-\nu)}\Bigg[\nu\left(Y_x t_x - Y_y t_y\right) + \left(Y_x t_y - Y_y t_x\right)\Bigg[t_x t_y \\
& + \frac{2}{Y^2}\left[\rho_x Y_y + \rho_y Y_x + \frac{L}{R}Y_x Y_y\right]\Bigg]\Bigg]
\end{aligned}
\tag{A.14}
$$

$$
\begin{aligned}
K_{zxz} =& \frac{\mu}{2\pi Y^2(1-\nu)}\Bigg[\left(\varepsilon_{xzx}Y_x t_z + \varepsilon_{xzy}Y_y t_z + \varepsilon_{zzx}Y_x t_x + \varepsilon_{zzy}Y_y t_x\right)(1-\nu) \\
& - \varepsilon_{xzx}Y_z t_x - \varepsilon_{xzy}Y_z t_y - \varepsilon_{zzx}Y_x t_x - \varepsilon_{zzy}Y_x t_y - \left(Y_x t_y - Y_y t_x\right)\Bigg[\delta_{xz} + t_x t_z \\
& + \frac{2}{Y^2}\left[\rho_x Y_z + \rho_z Y_x + \frac{L}{R}Y_x Y_z\right]\Bigg]\Bigg] \\
=& \frac{\mu}{2\pi Y^2(1-\nu)}\Bigg[\varepsilon_{xzy}Y_y t_z(1-\nu) - \varepsilon_{xzy}Y_z t_y - \left(Y_x t_y - Y_y t_x\right)\Bigg[t_x t_z \\
& + \frac{2}{Y^2}\left[\rho_x Y_z + \rho_z Y_x + \frac{L}{R}Y_x Y_z\right]\Bigg]\Bigg] \\
=& \frac{\mu}{2\pi Y^2(1-\nu)}\Bigg[Y_z t_y - Y_y t_z(1-\nu) - \left(Y_x t_y - Y_y t_x\right)\Bigg[t_x t_z \\
& + \frac{2}{Y^2}\left[\rho_x Y_z + \rho_z Y_x + \frac{L}{R}Y_x Y_z\right]\Bigg]\Bigg]
\end{aligned}
\tag{A.15}
$$

$$
\begin{aligned}
K_{zyy} =& \frac{\mu}{2\pi Y^2(1-\nu)}\Bigg[\left(\varepsilon_{yzx}Y_x t_y + \varepsilon_{yzy}Y_y t_y + \varepsilon_{yzx}Y_x t_y + \varepsilon_{yzy}Y_y t_y\right)(1-\nu) \\
& - \varepsilon_{yzx}Y_y t_x - \varepsilon_{yzy}Y_y t_y - \varepsilon_{yzx}Y_y t_x - \varepsilon_{yzy}Y_y t_y - \left(Y_x t_y - Y_y t_x\right)\Bigg[\delta_{yy} + t_y t_y \\
& + \frac{2}{Y^2}\left[\rho_y Y_y + \rho_y Y_y + \frac{L}{R}Y_y Y_y\right]\Bigg]\Bigg] \\
=& \frac{\mu}{2\pi Y^2(1-\nu)}\Bigg[\left(\varepsilon_{yzx}Y_x t_y + \varepsilon_{yzx}Y_x t_y\right)(1-\nu) - \varepsilon_{yzx}Y_y t_x - \varepsilon_{yzx}Y_y t_x \\
& - \left(Y_x t_y - Y_y t_x\right)\left[1 + t_y^2 + \frac{2}{Y^2}\left[2\rho_y Y_y + \frac{L}{R}Y_y^2\right]\right]\Bigg] \\
=& \frac{\mu}{2\pi Y^2(1-\nu)}\Bigg[2Y_x t_y(1-\nu) - 2Y_y t_x - \left(Y_x t_y - Y_y t_x\right)\Bigg[1 + t_y^2 \\
& + \frac{2}{Y^2}\left[2\rho_y Y_y + \frac{L}{R}Y_y^2\right]\Bigg]\Bigg]
\end{aligned}
\tag{A.16}
$$

$$
\begin{aligned}
K_{zyz} =& \frac{\mu}{2\pi Y^2(1-\nu)}\Bigg[\left(\varepsilon_{yzx}Y_x t_z + \varepsilon_{yzy}Y_y t_z + \varepsilon_{zzx}Y_x t_y + \varepsilon_{zzy}Y_y t_y\right)(1-\nu) \\
& - \varepsilon_{yzx}Y_z t_x - \varepsilon_{yzy}Y_z t_y - \varepsilon_{zzx}Y_y t_x - \varepsilon_{zzy}Y_y t_y - \left(Y_x t_y - Y_y t_x\right)\Bigg[\delta_{yz} + t_y t_z \\
& + \frac{2}{Y^2}\left[\rho_y Y_z + \rho_z Y_y + \frac{L}{R}Y_y Y_z\right]\Bigg]\Bigg] \\
=& \frac{\mu}{2\pi Y^2(1-\nu)}\Bigg[\varepsilon_{yzx}Y_x t_z\,(1-\nu) - \varepsilon_{yzx}Y_z t_x - \left(Y_x t_y - Y_y t_x\right)\Bigg[t_y t_z \\
& + \frac{2}{Y^2}\left[\rho_y Y_z + \rho_z Y_y + \frac{L}{R}Y_y Y_z\right]\Bigg]\Bigg] \\
=& \frac{\mu}{2\pi Y^2(1-\nu)}\Bigg[Y_x t_z\,(1-\nu) - Y_z t_x - \left(Y_x t_y - Y_y t_x\right)\Bigg[t_y t_z \\
& + \frac{2}{Y^2}\left[\rho_y Y_z + \rho_z Y_y + \frac{L}{R}Y_y Y_z\right]\Bigg]\Bigg]
\end{aligned}
\tag{A.17}
$$

$$
\begin{aligned}
K_{zzz} =& \frac{\mu}{2\pi Y^2(1-\nu)}\Bigg[\left(\varepsilon_{zzx}Y_x t_z + \varepsilon_{zzy}Y_y t_z + \varepsilon_{zzx}Y_x t_z + \varepsilon_{zzy}Y_y t_z\right)(1-\nu) \\
& - \varepsilon_{zzx}Y_z t_x - \varepsilon_{zzy}Y_z t_y - \varepsilon_{zzx}Y_z t_x - \varepsilon_{zzy}Y_z t_y - \left(Y_x t_y - Y_y t_x\right)\Bigg[\delta_{zz} + t_z t_z \\
& + \frac{2}{Y^2}\left[\rho_z Y_z + \rho_z Y_z + \frac{L}{R}Y_z Y_z\right]\Bigg]\Bigg] \\
=& -\frac{\mu}{2\pi Y^2(1-\nu)}\Bigg[\left(Y_x t_y - Y_y t_x\right)\Bigg[1 + t_z^2 + \frac{2}{Y^2}\left[2\rho_z Y_z + \frac{L}{R}Y_z^2\right]\Bigg]\Bigg]
\end{aligned}
\tag{A.18}
$$

Appendix B

Multipole

B.1 Quadrupole

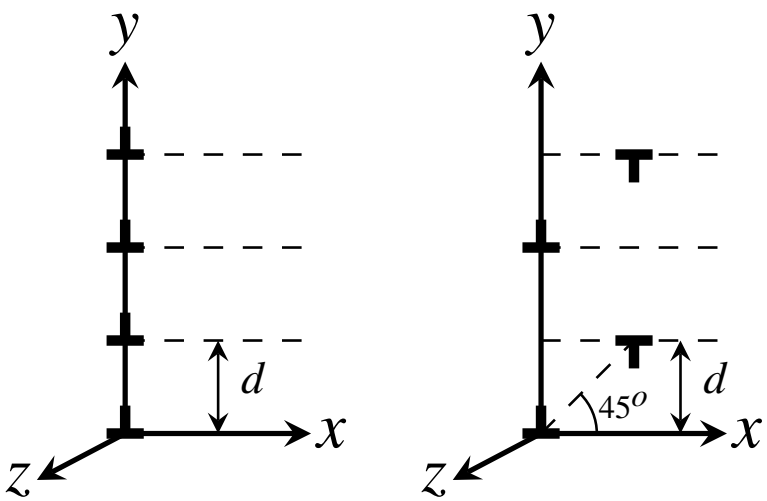

Figure B.1: Quadrupole configurations. (a) Same sign dislocations (b) Opposite sign dislocations

Same sign dislocations: For top dislocation

$$\frac{F_x}{\kappa} = \frac{\left(\frac{x}{d}\right)\left[\left(\frac{x}{d}\right)^2 - 1\right]}{\left[\left(\frac{x}{d}\right)^2 + 1\right]^2} + \frac{\left(\frac{x}{d}\right)\left[\left(\frac{x}{d}\right)^2 - 4\right]}{\left[\left(\frac{x}{d}\right)^2 + 4\right]^2} + \frac{\left(\frac{x}{d}\right)\left[\left(\frac{x}{d}\right)^2 - 9\right]}{\left[\left(\frac{x}{d}\right)^2 + 9\right]^2} \tag{B.1}$$

where $\kappa = \frac{Gb_x^2}{2\pi d(1-\nu)}$, d is the distance between two adjacent dislocations and ν is Poisson's ratio.

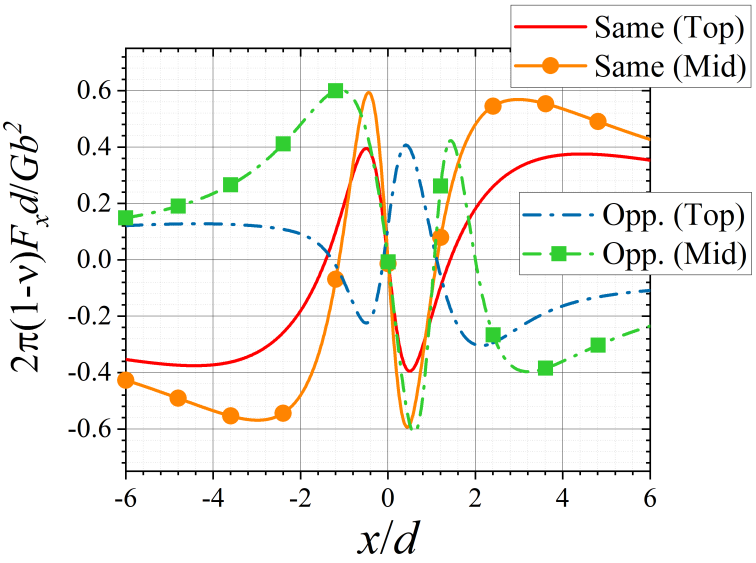

Figure B.2: Quadrupole: Normalized glide force between two parallel infinite edge dislocations of same and opposite signs

Same sign dislocations: For middle dislocation (3rd from bottom). The number of the middle dislocation in a multipole, counting from 1 at the bottom dislocation, is given by: $\left(\frac{n-1}{2}\right)+1$ if n is odd and $\frac{n}{2}+1$ if n is even.

$$\frac{F_x}{\kappa} = \frac{\left(\frac{x}{d}\right)\left[\left(\frac{x}{d}\right)^2 - 1\right]}{\left[\left(\frac{x}{d}\right)^2 + 1\right]^2} + \frac{\left(\frac{x}{d}\right)\left[\left(\frac{x}{d}\right)^2 - 1\right]}{\left[\left(\frac{x}{d}\right)^2 + 1\right]^2} + \frac{\left(\frac{x}{d}\right)\left[\left(\frac{x}{d}\right)^2 - 4\right]}{\left[\left(\frac{x}{d}\right)^2 + 4\right]^2} \tag{B.2}$$

Opposite sign dislocations: For top dislocation

$$\frac{F_x}{\kappa} = -\frac{\left(\frac{x}{d}\right)\left[\left(\frac{x}{d}\right)^2-1\right]}{\left[\left(\frac{x}{d}\right)^2+1\right]^2} + \frac{\left(\frac{x}{d}-1\right)\left[\left(\frac{x}{d}-1\right)^2-4\right]}{\left[\left(\frac{x}{d}-1\right)^2+4\right]^2} - \frac{\left(\frac{x}{d}\right)\left[\left(\frac{x}{d}\right)^2-9\right]}{\left[\left(\frac{x}{d}\right)^2+9\right]^2} \tag{B.3}$$

Opposite sign dislocations: For middle dislocation (3rd from bottom)

$$\frac{F_x}{\kappa} = -\frac{\left(\frac{x}{d}-1\right)\left[\left(\frac{x}{d}-1\right)^2-1\right]}{\left[\left(\frac{x}{d}-1\right)^2+1\right]^2} - \frac{\left(\frac{x}{d}-1\right)\left[\left(\frac{x}{d}-1\right)^2-1\right]}{\left[\left(\frac{x}{d}-1\right)^2+1\right]^2} + \frac{\left(\frac{x}{d}\right)\left[\left(\frac{x}{d}\right)^2-4\right]}{\left[\left(\frac{x}{d}\right)^2+4\right]^2} \tag{B.4}$$

B.2 Pentapole

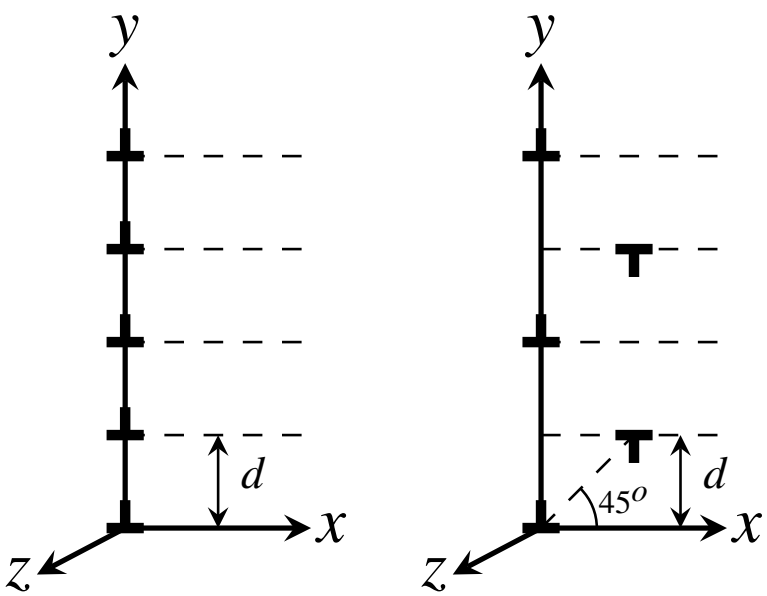

Figure B.3: Pentapole configurations. (a) Same sign dislocations (b) Opposite sign dislocations

Same sign dislocations: For top dislocation

$$\frac{F_x}{\kappa} = \frac{\left(\frac{x}{d}\right)\left[\left(\frac{x}{d}\right)^2-1\right]}{\left[\left(\frac{x}{d}\right)^2+1\right]^2} + \frac{\left(\frac{x}{d}\right)\left[\left(\frac{x}{d}\right)^2-4\right]}{\left[\left(\frac{x}{d}\right)^2+4\right]^2} + \frac{\left(\frac{x}{d}\right)\left[\left(\frac{x}{d}\right)^2-9\right]}{\left[\left(\frac{x}{d}\right)^2+9\right]^2} + \frac{\left(\frac{x}{d}\right)\left[\left(\frac{x}{d}\right)^2-16\right]}{\left[\left(\frac{x}{d}\right)^2+6\right]^2} \tag{B.5}$$

Same sign dislocations: For middle dislocation (3rd dislocation from bottom)

$$\frac{F_x}{\kappa} = \frac{\left(\frac{x}{d}\right)\left[\left(\frac{x}{d}\right)^2-1\right]}{\left[\left(\frac{x}{d}\right)^2+1\right]^2} + \frac{\left(\frac{x}{d}\right)\left[\left(\frac{x}{d}\right)^2-1\right]}{\left[\left(\frac{x}{d}\right)^2+1\right]^2} + \frac{\left(\frac{x}{d}\right)\left[\left(\frac{x}{d}\right)^2-4\right]}{\left[\left(\frac{x}{d}\right)^2+4\right]^2} + \frac{\left(\frac{x}{d}\right)\left[\left(\frac{x}{d}\right)^2-4\right]}{\left[\left(\frac{x}{d}\right)^2+4\right]^2} \tag{B.6}$$

Opposite sign dislocations: For top dislocation

$$\begin{aligned}\frac{F_x}{\kappa} =& -\frac{\left(\frac{x}{d}-1\right)\left[\left(\frac{x}{d}-1\right)^2-1\right]}{\left[\left(\frac{x}{d}-1\right)^2+1\right]^2} + \frac{\left(\frac{x}{d}\right)\left[\left(\frac{x}{d}\right)^2-4\right]}{\left[\left(\frac{x}{d}\right)^2+4\right]^2} - \frac{\left(\frac{x}{d}-1\right)\left[\left(\frac{x}{d}-1\right)^2-9\right]}{\left[\left(\frac{x}{d}-1\right)^2+9\right]^2} \\ &+ \frac{\left(\frac{x}{d}\right)\left[\left(\frac{x}{d}\right)^2-16\right]}{\left[\left(\frac{x}{d}\right)^2+16\right]^2}\end{aligned} \tag{B.7}$$

Opposite Burgers Vector: For middle dislocation (3rd dislocation from bottom)

$$\begin{aligned}\frac{F_x}{\kappa} =& \frac{\left(\frac{x}{d}\right)\left[\left(\frac{x}{d}\right)^2-4\right]}{\left[\left(\frac{x}{d}\right)^2+4\right]^2} - \frac{\left(\frac{x}{d}-1\right)\left[\left(\frac{x}{d}-1\right)^2-1\right]}{\left[\left(\frac{x}{d}-1\right)^2+1\right]^2} - \frac{\left(\frac{x}{d}-1\right)\left[\left(\frac{x}{d}-1\right)^2-1\right]}{\left[\left(\frac{x}{d}-1\right)^2+1\right]^2} \\ &+ \frac{\left(\frac{x}{d}\right)\left[\left(\frac{x}{d}\right)^2-4\right]}{\left[\left(\frac{x}{d}\right)^2+4\right]^2}\end{aligned} \tag{B.8}$$

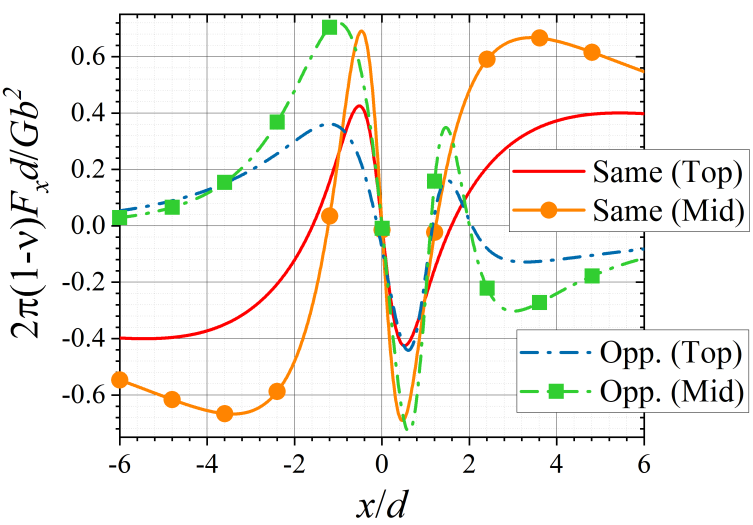

Figure B.4: Pentapole: Normalized glide force between two parallel infinite edge dislocations of same and opposite signs

References

[1] J. S. Koehler, "On the dislocation theory of plastic deformation," *Physical Review*, vol. 60, no. 5, pp. 397–410, 1941.

[2] D. Hull and D. J. Bacon, *Introduction to Dislocations*. Butterworth-Heinemann, 5th ed., 2011.

[3] J. Weeterman and J. R. Weeterman, *Elementary Dislocation Theory*. Oxford University Press, 1992.

[4] T. A. Khraishi and Y.-L. Shen, *Introductory Continuum Mechanics with Applications to Elasticity*. University Readers/Cognella, revised ed., 2011.

[5] V. Volterra, "Sur l'équilibre des corps élastiques multiplement connexes," *Annales scientifiques de l'École Normale Supérieure*, vol. 3e série, 24, pp. 401–517, 1907.

[6] J. D. Eshelby and A. N. Stroh, "CXL. Dislocations in thin plates," *The London, Edinburgh, and Dublin Philosophical Magazine and Journal of Science*, vol. 42, no. 335, pp. 1401–1405, 1951.

[7] A. K. Head, "X. the interaction of dislocations and boundaries," *The London, Edinburgh, and Dublin Philosophical Magazine and Journal of Science*, vol. 44, pp. 92–94, 1953.

[8] J. D. Eshelby, "Screw dislocations in thin rods," *Journal of Applied Physics*, vol. 24, pp. 176–179, 1953.

[9] J. Friedel, *Discolations*. Pergamon Press, 1st ed., 1967.

[10] E. H. Yoffe, "A dislocation at a free surface," *Philosophical Magazine*, vol. 6, pp. 1147–1155, 1961.

[11] J. P. Hirth and J. Lothe, *Theory of dislocations*. Krieger Publishing Company, 2nd ed., 1982.

[12] V. A. Lubarda, "On the non-uniqueness of solution for screw dislocations in multiply connected regions," *Journal of Elasticity*, vol. 52, pp. 289–292, 1998.

[13] V. A. Lubarda and X. Markenscoff, "The stress field for a screw dislocation near cavities and straight boundaries," *Materials Science and Engineering A*, vol. 349, pp. 327–334, 2003.

[14] V. A. Lubarda, "Image force on a straight dislocation emitted from a cylindrical void," *International Journal of Solids and Structures*, vol. 48, pp. 648–660, 2011.

[15] T. A. Khraishi and H. M. Zbib, "Dislocation dynamics simulations of the interaction between a short rigid fiber and a glide circular dislocation pile-up," *Computational Materials Science*, vol. 24, pp. 310–322, 2001.

[16] T. A. Khraishi and H. M. Zbib, "Free-surface effects in 3d dislocation dynamics: Formulation and modeling," *Journal of Engineering Materials and Technology*, vol. 124, pp. 342–351, 2002.

[17] L. Yan, T. A. Khraishi, Y.-L. Shen, and M. F. Horstemeyer, "A distributed-dislocation method for treating free-surface image stresses in three-dimensional dislocation dynamics simulations," *Modelling and Simulation in Materials Science and Engineering*, vol. 12, 2004.

[18] A. B. Siddique and T. A. Khraishi, "Numerical methodology for treating static and dynamic dislocation problems near a free surface," *Journal of Physics Communications*, vol. 4, no. 5, 2020.

[19] E. V. der Giessen and A. Needleman, "Discrete dislocation plasticity: A simple planar model," *Modelling and Simulation in Materials Science and Engineering*, vol. 3, pp. 689–735, 1995.

[20] S. M. Keralavarma and W. A. Curtin, "Strain hardening in 2d discrete dislocation dynamics simulations: A new '2.5d' algorithm," *Journal of the Mechanics and Physics of Solids*, vol. 95, pp. 132–146, 2016.

[21] R. de Wit, "Some relations for straight dislocations," *Physica Status Solidi (B)*, vol. 20, pp. 567–573, 1967.

[22] G. Mase, *Schaum's outline of continuum mechanics*. McGraw Hill Professional, 1970.

[23] S. C. Chapra and R. P. Canale, *Numerical Methods for Engineers*. McGraw-Hill Education, 7 ed., 2014.

[24] H. M. Zbib, T. D. D. la Rubia, and V. Bulatov, "A multiscale model of plasticity based on discrete dislocation dynamics," *Journal of Engineering Materials and Technology, Transactions of the ASME*, vol. 124, pp. 78–87, 1 2002.

[25] J. H. Jeans, *The mathematical theory of electricity and magnetism*. Cambridge University Press, 1911.

[26] F. Kroupa, "Circular edge dislocation loop," *Czechoslovak Journal of Physics*, vol. 10, pp. 284–293, 1960.

[27] F. Kroupa, "Dislocation dipoles and dislocation loops," *Le Journal de Physique Colloques*, vol. 27, pp. C3–154–C3–167, 1966.

[28] E. Kröner, *Kontinuumstheorie der Versetzungen und Eigenspannungen*. Springer-Verlag Berlin Heidelberg, 1958.

[29] M. J. Marcinkowski and K. S. Harsha, "Properties of finite circular dislocation glide loops," *Journal of Applied Physics*, vol. 39, pp. 1775–1783, 1968.

[30] T. A. Khraishi, J. P. Hirth, H. M. Zbib, and M. A. Khaleel, "The displacement, and strain-stress fields of a general circular volterra dislocation loop," *International Journal of Engineering Science*, vol. 38, pp. 251–266, 2000.

[31] T. A. Khraishi, J. P. Hirth, H. M. Zbib, and T. D. D. L. Rubia, "The stress field of a general circular volterra dislocation loop: Analytical and numerical approaches," *Philosophical Magazine Letters*, vol. 80, pp. 95–105, 2000.

[32] L. Li, T. A. Khraishi, and A. B. Siddique, "The strain/stress fields of a subsurface rectangular dislocation loop parallel to the surface of a half medium: Analytical solution with verification," *Journal of Applied Mathematics and Physics*, vol. 09, pp. 146–175, 2021.

[33] L. Li and T. A. Khraishi, "The stress field of a rectangular dislocation loop in an infinite medium : Analytical solution with verification," *Journal of Materials Science Research and Reviews*, vol. 7, pp. 47–59, 2021.

[34] A. B. Siddique and T. A. Khraishi, "Screw dislocations around voids of any shape: A generalized numerical approach," *Forces in Mechanics*, vol. 3, no. October 2020, p. 100014, 2021.

[35] A. B. Siddique and T. A. Khraishi, "A Mesh-Independent Brute-Force Approach for Traction-Free Corrections in Dislocation Problems," *Modeling and Numerical Simulation of Material Science*, vol. 11, no. 01, pp. 1–18, 2021.

[36] J. Baštecká, "Interaction of dislocation loop with free surface," *Cechoslovackij fiziceskij zurnal B*, vol. 14, no. 6, pp. 430–442, 1964.

[37] D. J. Bacon and P. P. Groves, "The dislocation in a semi-infinite isotropic medium," *Fundamental aspects of dislocation theory*, vol. 1, no. 317, pp. 35–45, 1970.

[38] P. P. Groves and D. J. Bacon, "The dislocation loop near a free surface," *Philosophical Magazine*, vol. 22, no. 175, pp. 83–91, 1970.

[39] Y. Maurissen and L. Capella, "Stress field of a dislocation segment parallel to a free surface," *Philosophical Magazine*, vol. 29, no. 5, pp. 1227–1229, 1974.

[40] Y. Maurissen and L. Capella, "Stress field of a dislocation segment perpendicular to a free surface," *Philosophical Magazine*, vol. 30, no. 3, pp. 679–683, 1974.

[41] M. Comninou and J. Dundurs, "The angular dislocation in a half space," *Journal of Elasticity*, vol. 5, no. 3-4, pp. 203–216, 1975.

[42] J. Lothe, V. L. Indenbom, and V. A. Chamrov, "Elastic Field and Self-Force of Dislocations Emerging at the Free Surfaces of an Anisotropic Halfspace," *Physica Status Solidi (B)*, vol. 111, no. 2, pp. 671–677, 1982.

[43] T. J. Gosling and J. R. Willis, "A line-integral representation for the stresses due to an arbitrary dislocation in an isotropic half-space," *Journal of the Mechanics and Physics of Solids*, vol. 42, no. 8, pp. 1199–1221, 1994.

[44] B. Devincre, "Three dimensional stress field expressions for straight dislocation segments," *Solid State Cmmmunications*, vol. 93, no. 11, pp. 875–878, 1995.

[45] L. P. Kubin, G. R. Canova, M. Condat, B. Devincre, V. Pontikis, and Y. Bréchet, "Dislocation Microstructures and Plastic Flow: A 3D Simulation," *Solid State Phenomena*, vol. 23-24, pp. 455–472, 1992.

[46] G. R. Canova and M. C. Fivel, "Developing rigorous boundary conditions to simulations of discrete dislocation dynamics," *Modelling and Simulation in Materials Science and Engineering*, vol. 7, no. 5, pp. 753–768, 1999.

[47] A. Hartmaier, M. C. Fivel, G. R. Canova, and P. Gumbsch, "Image stresses in a free-standing thin film," *Modelling and Simulation in Materials Science and Engineering*, vol. 7, no. 5, pp. 781–793, 1999.

[48] A. El-Azab, "The boundary value problem of dislocation dynamics," *Modelling and Simulation in Materials Science and Engineering*, vol. 8, no. 1, pp. 37—-54, 2000.

[49] J. Deng, A. El-Azab, and B. C. Larson, "On the elastic boundary value problem of dislocations in bounded crystals," *Philosophical Magazine*, vol. 88, no. 30-32, pp. 3527–3548, 2008.

[50] G. Po, M. S. Mohamed, T. Crosby, C. Erel, A. El-Azab, and N. M. Ghoniem, "Recent Progress in Discrete Dislocation Dynamics and Its Applications to Micro Plasticity," *Jom*, vol. 66, no. 10, pp. 2108–2120, 2014.

[51] H. M. Zbib, M. Rhee, and J. P. Hirth, "On plastic deformation and the dynamics of 3D dislocations," *International Journal of Mechanical Sciences*, vol. 40, no. 2-3, pp. 113–127, 1998.

[52] M. A. Meyers and K. K. Chawla, *Mechanical Behavior of Materials*. Cambridge, UK: Cambridge University Press, 2nd ed., 2009.

[53] C. Zhou, S. B. Biner, and R. LeSar, "Discrete dislocation dynamics simulations of plasticity at small scales," *Acta Materialia*, vol. 58, pp. 1565–1577, 2010.

[54] J. C. Crone, L. B. Munday, and J. Knap, "Capturing the effects of free surfaces on void strengthening with dislocation dynamics," *Acta Materialia*, vol. 101, pp. 40–47, 2015.

[55] P. Jing, T. A. Khraishi, J. A. Young, and B. D. Wirth, "Multi-scale simulations of the effects of irradiation-induced voids and helium bubbles on the mechanical properties of aluminium," *Philosophical Magazine*, vol. 85, pp. 757–767, 2005.

[56] P. Jing, T. A. Khraishi, L. A. Z. Ruiz, and B. D. Wirth, "The elastic fields of subsurface dislocation loops: a comparison between analytical continuum-theory solutions and atomistic calculations," *International Journal of Theoretical and Applied Multiscale Mechanics*, vol. 1, pp. 71–85, 2009.

[57] T. A. Khraishi, L. Yan, and Y.-L. Shen, "Dynamic simulations of the interaction between dislocations and dilute particle concentrations in metal-matrix composites (mmcs)," *International Journal of Plasticity*, vol. 20, pp. 1039–1057, 2004.

[58] K. Schulz, D. Dickel, S. Schmitt, S. Sandfeld, D. Weygand, and P. Gumbsch, "Analysis of dislocation pile-ups using a dislocation-based continuum theory," *Modelling and Simulation in Materials Science and Engineering*, vol. 22, no. 2, pp. 1–15, 2014.

[59] Y. Zhu and Y. Xiang, "A continuum model for dislocation dynamics in three dimensions using the dislocation density potential functions and its application to micro-pillars," *Journal of the Mechanics and Physics of Solids*, vol. 84, pp. 230–253, 2015.

[60] A. Acharya, "Driving forces and boundary conditions in continuum dislocation mechanics," *Proceedings of the Royal Society A: Mathematical, Physical and Engineering Sciences*, vol. 459, no. 2034, pp. 1343–1363, 2003.

[61] R. W. Leger, T. A. Khraishi, and Y. L. Shen, "A dislocation dynamics study of strength differential in particle-containing metals during cyclic loading," *Journal of Materials Science*, vol. 39, no. 11, pp. 3593–3604, 2004.

[62] B. Devincre, T. Hoc, and L. P. Kubin, "Dislocation mean free paths and strain hardening of crystals," *Science*, vol. 320, no. 5884, pp. 1745–1748, 2008.

[63] W. Cai, A. Arsenlis, C. R. Weinberger, and V. V. Bulatov, "A non-singular continuum theory of dislocations," *Journal of the Mechanics and Physics of Solids*, vol. 54, no. 3, pp. 561–587, 2006.

[64] N. Ghoniem and L. Z. Sun, "Fast-sum method for the elastic field of three-dimensional dislocation ensembles," *Physical Review B - Condensed Matter and Materials Physics*, vol. 60, no. 1, pp. 128–140, 1999.

[65] O. Jamond, R. Gatti, A. Roos, and B. Devincre, "Consistent formulation for the Discrete-Continuous Model: Improving complex dislocation dynamics simulations," *International Journal of Plasticity*, vol. 80, pp. 19–37, 2016.

[66] D. A. Hills, P. A. Kelly, D. N. Dai, and A. M. Korsunsky, *Solution of Crack Problems: The Distributed Dislocation Technique*, vol. 44. Springer-Science+Business Media, 1 ed., 1996.

[67] T. A. Khraishi and I. Demir, "On Cauchy singular integrals and stress intensity factors for 2D mode I cracks in an infinite solid," *Mechanics Research Communications*, vol. 30, no. 4, pp. 353–364, 2003.

[68] I. Demir and T. A. Khraishi, "The torsional dislocation loop and Mode III cylindrical crack," *Journal of Mechanics*, vol. 21, no. 2, pp. 109–116, 2005.

[69] T. A. Khraishi, H. M. Zbib, and T. D. De La Rubia, "The treatment of traction-free boundary condition in three-dimentional dislocation dynamic using generalized image stress analysis," *Materials Science and Engineering A*, vol. 309-310, pp. 283–287, 2001.

[70] Y. T. Chou, "The energy of circular dislocation loops in thin plates," *Acta Metallurgica*, vol. 11, pp. 829–834, aug 1963.

[71] L. Li and T. A. Khraishi, "Strain Field Development of a Rectangular Dislocation Loop in a Semi-Infinite Medium with Verification," *Physical Science International Journal*, vol. 25, no. 1, pp. 23–38, 2021.

[72] J. J. Gilman, "Influence of dislocation dipoles on physical properties," *Royal Society of Chemistry*, vol. 38, no. 0, pp. 123–137, 1964.

[73] R. J. Stokes and K. H. Olsen, "Dislocation interactions and dipole formation," *Philosophical Magazine*, vol. 8, no. 90, pp. 957–965, 1963.

[74] P. D. Neumann, "The interactions between dislocations and dislocation dipoles," *Acta Metallurgica*, vol. 19, no. 11, pp. 1233–1241, 1971.

[75] T. D. de la Rubia, H. M. Zbib, T. A. Khraishi, B. D. Wirth, M. Victoria, and M. J. Caturla, "Multiscale modelling of plastic flow localization in irradiated materials," *Nature*, vol. 406, no. 6798, pp. 871–874, 2000.

[76] T. A. Khraishi, H. M. Zbib, T. D. De La Rubia, and M. Victoria, "Localized deformation and hardening in irradiated metals: Three-dimensional discrete dislocation dynamics simulations," *Metallurgical and Materials Transactions B: Process Metallurgy and Materials Processing Science*, vol. 33, no. 2, pp. 285–296, 2002.

[77] A. B. Siddique and T. A. Khraishi, "The Treatment of SingularitiesAssociated With a Dislocation Segment With Applications," *International Journal of Theoretical and Applied Multiscale Mechanics*, 2021.

[78] M. Rhee, H. M. Zbib, J. P. Hirth, H. Huang, and T. De La Rubia, "Models for long-/short-range interactions and cross slip in 3D dislocation simulation of BCC single crystals," *Modelling and Simulation in Materials Science and Engineering*, vol. 6, no. 4, pp. 467–492, 1998.

[79] F. C. Frank and W. T. Read, "Multiplication processes for slow moving dislocations," *Physical Review*, vol. 79, no. 4, pp. 722–723, 1950.

[80] A. H. Cottrell, *Dislocations and plastic flow in crystals*. Oxford: Oxford University Press, 1953.

[81] D. J. Dieter, George Ellwood and Bacon, *Mechanical metallurgy*. New York: McGraw-hill New York, 3 ed., 1976.

[82] R. L. Fleischer, "The flow stress of body-centered cubic metals: inherent lattice hardening or solution hardening?," *Acta Metallurgica*, vol. 15, no. 9, pp. 1513–1519, 1967.

[83] R. L. Fleischer, "Solution hardening," *Acta Metallurgica*, vol. 9, no. 11, pp. 996–1000, 1961.

[84] R. L. Fleischer, "Solution hardening by tetragonal distortions: Application to irradiation hardening in F.C.C. crystals," *Acta Metallurgica*, vol. 10, no. 9, pp. 835–842, 1962.

[85] R. L. Fleischer, "Substitutional solution hardening," *Acta Metallurgica*, vol. 11, no. 3, pp. 203–209, 1963.

[86] B. R. Riddhagni and R. M. Asimow, "Solid-solution hardening due to the size effect," *Journal of Applied Physics*, vol. 39, no. 11, pp. 5169–5173, 1968.

[87] Eshelby, John Douglas, "The determination of the elastic field of an ellipsoidal inclusion, and related problems," *Proceedings of the Royal Society A: Mathematical, Physical and Engineering Sciences*, vol. 241, no. 1226, pp. 376–396, 1957.

[88] J. D. Eshelby, "The elastic field outside an ellipsoidal inclusion," *Proceedings of the Royal Society A: Mathematical, Physical and Engineering Sciences*, vol. 252, no. 1271, pp. 561–569, 1959.

[89] R. W. Weeks, S. R. Pati, M. F. Ashby, and P. Barrand, "The elastic interaction between a straight dislocation and a bubble or a particle," *Acta Metallurgica*, vol. 17, no. 12, pp. 1403–1410, 1969.

[90] Toshio Mura, *Micromechanics on defects in solids*. Martinus Nijhoff Publishers, 1987.

[91] J. D. Lerma, T. A. Khraishi, Y. L. Shen, and B. D. Wirth, "The elastic fields of misfit cylindrical particles: A dislocation-based numerical approach," *Mechanics Research Communications*, vol. 30, no. 4, pp. 325–334, 2003.

[92] J. D. Lerma, T. A. Khraishi, Y.-L. Shen, and B. D. Wirth, "A distributed-dislocation method for generalized eigenstrain problems," *High Performance Structures and Materials*, vol. 6, pp. 185–194, 2004.

[93] J. D. Lerma, T. A. Khraishi, and Y.-L. Shen, "Elastic fields of 2D and 3D misfit particles in an infinite medium," *Mechanics Research Communications*, vol. 34, no. 1, pp. 31–43, 2007.

[94] J. D. Lerma, T. A. Khraishi, S. Kataria, and Y.-L. Shen, "Distributed Dislocation Method for Determining Elastic Fields of 2D and 3D Volume Misfit Particles in Infinite Space and Extension of the Method for Particles in Half Space," *Journal of Mechanics*, vol. 31, no. 3, pp. 249–260, 2015.

[95] J. Lépinoux and L. P. Kubin, "The dynamic organization of dislocation structures: A simulation," *Scripta Metallurgica*, vol. 21, no. 6, pp. 833–838, 1987.

[96] F. X. Liu, A. C. F. Cocks, and E. Tarleton, "Dislocation dynamics modelling of the creep behaviour of particle-strengthened materials," *Proceedings of the Royal Society A: Mathematical, Physical and Engineering Sciences*, vol. 477, no. 2250, p. 20210083, 2021.

[97] J. J. Gilman, "The "peierls stress" for pure metals (evidence that it is negligible)," *Philosophical Magazine*, vol. 87, no. 35, pp. 5601–5606, 2007.

[98] C. Déprés, G. V. Prasad Reddy, C. Robertson, and M. Fivel, "An extensive 3D dislocation dynamics investigation of stage-I fatigue crack propagation," *Philosophical Magazine*, vol. 94, no. 36, pp. 4115–4137, 2014.

[99] J. Kacher, B. P. Eftink, B. Cui, and I. M. Robertson, "Dislocation interactions with grain boundaries," *Current Opinion in Solid State and Materials Science*, vol. 18, no. 4, pp. 227–243, 2014.

[100] M. Jiang, B. Devincre, and G. Monnet, "Effects of the grain size and shape on the flow stress: A dislocation dynamics study," *International Journal of Plasticity*, vol. 113, no. May 2018, pp. 111–124, 2019.

[101] Z. Shen, R. H. Wagoner, and W. A. Clark, "Dislocation and grain boundary interactions in metals," *Acta Metallurgica*, vol. 36, no. 12, pp. 3231–3242, 1988.

[102] A. B. Siddique and T. A. Khraishi, "A holed-plate with material dislocations : Formulation and verification," *Mathematics and Mechanics of Solids*, vol. 0, no. 0, p. 10812865211053369, 2021.

[103] W. Callister and D. G. Rethwisch, *Materials Science and Engineering An Introduction*. Wiley, 10 ed., 2017.

[104] R. v. Mises, "Mechanik der festen Körper im plastisch- deformablen Zustand," *Nachrichten von der Gesellschaft der Wissenschaften zu Göttingen, Mathematisch-Physikalische Klasse*, vol. 1913, no. 4, pp. 582–592, 1913.

[105] W. D. Jenkins, T. G. Digges, and C. R. Johnson, "Tensile Properties of Copper, Nickel, and 70-Percent-Copper-30-Percent-Nickel and 30-Percent-Copper- 70-Percent Nickel Alloys at High Temperatures," *Journal of Research of the National Bureau of Standards*, vol. 58, no. 4, pp. 201–211, 1957.

[106] A. K. Kaw, *Micromechanics of Composite Materials*. Taylor & Francis, 2nd ed., 2013.

[107] A. B. Siddique, H. Lim, and T. A. Khraishi, "The Effect of Multipoles on the Elasto-Plastic Properties of a Crystal: Theory and 3D Dislocation Dynamics Modeling," *Journal of Engineering Materials and Technology*, pp. 1–22, aug 2021.

[108] T.-H. Fang, C.-C. Huang, and T.-C. Chiang, "Effects of grain size and temperature on mechanical response of nanocrystalline copper," *Materials Science and Engineering: A*, vol. 671, pp. 1–6, 2016.

[109] R. J. Arsenault, S. Patu, and D. M. Esterling, "Computer simulation of solid solution strengthening in Fcc alloys: Part II. At absolute zero temperature," *Metallurgical Transactions A*, vol. 20, no. 8, pp. 1419–1428, 1989.